Charles University in Prague

Faculty of Science

Dissertation

2020   **Yong Zhou**

Charles University

Faculty of Science

Study program: Physical chemistry

Mgr. Yong Zhou

Design and catalytic application of novel nanostructured materials

Doctoral thesis

Supervisor: Dr. Maksym Opanasenko

Advisor: Prof. Ing. Jiří Čejka, DrSc.

Prague, 2020

Univerzita Karlova

Přírodovědecká fakulta

Studijní program: Fyzikální chemie

Mgr. Yong Zhou

Návrh a katalytické využití nových nanostrukturovaných materiálů

Disertační práce

Školitel: Dr. Maksym Opanasenko

Konzultant: Prof. Ing. Jiří Čejka, DrSc.

Praha, 2020

Prohlášení:

Dizertační práci jsem vypracoval na Přírodovědecké fakultě, Univerzity Karlovy.

Prohlašuji, že jsem závěrečnou práci zpracovala samostatně a že jsem uvedla všechny použité informační zdroje a literaturu. Tato práce ani její podstatná část nebyla předložena k získání jiného nebo stejného akademického titulu.

V Praze,

                                                       Podpis

Contents

Acknowledgements

List of publications

This thesis was composed according to the publications as follows:

1. Yong Zhou, Shashikant A. Kadam, Mariya Shamzhy, Jiří Čejka, Maksym Opanasenko. Isoreticular UTL-derived zeolites as model materials for probing pore size-activity relationship. ACS Catalysis, 9(2019), 5136-5146. doi.org/10.1021/acscatal.9b00950.

2. Yong Zhou, Naděžda Žilková, Mariya Shamzhy, Yamini Avadhut, Martin Hartmann, Jiří Čejka, Maksym Opanasenko. Novel approach towards Al-rich AFI for catalytic application. Applied Catalysis A: General, 577(2019), 62-68. doi.org/10.1016/j.apcata.2019.03.015

3. Hua Chen, Yong Zhou, Zdeněk Tošner, Jiří Čejka, Maksym Opanasenko. Synthesis of aggregation-resistant MFI nanoparticles. Catalysis Today, (2019). doi.org/10.1016/j.cattod.2019.10.026.

Abstract

Zeolites are crystalline aluminosilicates and environmentally friendly solid acid catalysts thanks to their non-toxicity, large surface area, excellent (hydro)thermal stability, and tunable acidity. Traditionally, zeolite catalysts are applied in industrial processes related to petrochemistry, but several studies have recently shown their high potential in fine chemicals production and volatile organic compounds (VOCs) elimination. Advanced materials based on newly developed layered and nanosized zeolites have exhibited further fascinating properties, e.g., a short diffusion pathway, tunable structure and morphology. However, the limited correlation between key parameters of zeolite synthesis and their properties (structural, textural, acidic) and catalytic performance, especially for new layered and nanosized zeolites, hinders the development and application of zeolite catalysts.

Considering the above, this thesis focused on the preparation of several sets of specific zeolite catalysts to gain further insights into the relationship between key properties of zeolites (structure, morphology, chemical composition, accessibility to acid sites or other functional groups, and organization of layers, among others) and their performance as catalysts, supports for other active phases or nanosized components of colloidal systems.

The structural, morphological and textural properties of these materials were characterized by XRD, electron microscopy and N_2 adsorption. The nature, number and location of catalytic active sites were investigated by ICP-OES, ^{27}Al NMR, FTIR with different probe molecules, diffuse reflectance UV/Vis, XPS, TG and TPD techniques. Catalytic performance over the developed catalysts was assessed in gas phase and liquid phase reactions, including ethanol dehydration, toluene alkylation, VOCs catalytic oxidation, tetrahydropyranylation of alcohols and p-xylene acylation.

The main achievements of this thesis are the following: (1) design of a group of isoreticular Al-IPC zeolites with gradually varied micropore size but with the same morphology, Al content and concentration of acid sites by selecting an appropriate set of synthesis parameters; as a unique set of model catalysts (lattice parameters can be adjusted independently of most

other properties), these isoreticular Al-IPC zeolites revealed a clear pore size-activity relationship in ethanol dehydration and tetrahydropyranylation reactions; (2) comparative analysis of the textural and catalytic properties of one-dimensional-pore zeolites synthesized using direct and post-synthetic alumination techniques; this strategy enabled us to optimize the incorporation of Al into zeolite frameworks typically considered Al-poor (e.g., **AFI** type); (3) correlation between the aggregation-resistant properties of nanosized zeolites prepared by surface modification of respective nanocrystals and the nature (denticity, polarity and size) of the functionalization agent. Compared with non-modified nanocrystals, materials containing optimized surface protection groups showed improved stability against aggregation both in suspension and under harsh catalytic conditions; (4) preparation of **MWW** zeolites with different layer arrangements (MCM-22/36/56) and chemical composition (Si/Al = 12 - 50) to understand the role of zeolites as supports in the elimination of VOCs; in particular, the Al content in the support significantly affects the dispersion and reducibility of the active phase (cobalt oxide) and thus the catalytic activity in toluene and propane oxidation reactions; the MCM-22 material with minimized external surface area and appropriate composition (Si/Al = 50) exhibited the highest catalytic activity for toluene and propane oxidation (the temperatures for 90% hydrocarbon conversion were 307 and 295 °C, respectively), demonstrating the high potential of this composite catalyst for its application in VOCs elimination.

Overall, (1) the catalytic activity studies over Al-IPC-n zeolites showed that both ethanol dehydration and tetrahydropyranylation of alcohols proportionally increased with pore size and concentration of external acid sites, thus demonstrating the potential of **UTL**-derived isoreticular zeolites as model catalysts to further our understanding of catalyst pore size-activity relationships. In addition, (2) the results from toluene alkylation demonstrated that post-synthetic isomorphous substitution of Al-poor one-dimension large pore zeolite can be used to efficiently tune the chemical composition of one-dimensional large-pore zeolites, thereby generating Al-enriched zeolite materials for appropriate catalytic applications. Furthermore, (3) surface silylation of **MFI**-nanosized zeolites reduced their aggregation and

improved their catalytic activity, hence partly solving their underlying activity and stability issues and enabling their application to a wider range of catalytic processes. Lastly, (4) the catalytic activity of cobalt-containing **MWW** zeolites in toluene and propane oxidation reactions increases with the Si/Al of the **MWW** supports and consequently with the dispersion and reducibility of the cobalt species. Thus, assessing the effects of specific properties of zeolites as supports on the dispersion and reducibility of the catalytic active phase and on the corresponding catalytic activity is crucial for the design of zeolite-supported catalysts with high activity in VOCs elimination.

Abstrakt

Zeolity jsou krystalické hlinitokřemičitany, které představují katalytické materiály šetrné k životnímu prostředí díky své netoxicitě, velkému povrchu, vynikající tepelné stabilitě a možnosti měnit jejich vlastnosti a aktivní centra. Zeolity se hojně používají v petrochemii a dalších průmyslových procesech. V poslední době nachází uplatnění i v nově vznikajících odvětvích, např. odstraňování těkavých organických látek (VOC) či výroba chemických specialit. Pokročilé materiály založené na vrstevnatých a nanočásticových zeolitech vykazují rovněž další zajímavé vlastnosti (vysoká plocha vnějšího povrchu, možnost cíleně upravovat jejich strukturu a morfologii), a byly použity v různých aplikacích. Chybí však vztah mezi klíčovými parametry syntézy zeolitů s jejich vlastnostmi (struktura, textura, kyselost) a také s katalytickými vlastnostmi, zejména u nových vrstevnatých a nanočásticových zeolitů, což brání využití a vývoji a zeolitových katalyzátorů.

Tato práce byla zaměřena na přípravu několika konkrétních typů zeolitových katalyzátorů, umožňujících pochopit vztah mezi důležitými vlastnostmi zeolitů (struktura, morfologie, chemické složení, přístupnost kyselých míst či jiných funkčních skupin, uspořádání vrstev atd.) a jejich katalytickou aktivitou, případně jejich využitím jako nosičů pro jiné aktivní fáze nebo nanočásticové složky koloidních systémů.

Struktura, morfologie a texturní vlastnosti připravených materiálů byly charakterizovány pomocí XRD, elektronové mikroskopie a adsorpce N_2. Povaha, množství a umístění působením aktivní fáze byly zkoumány pomocí ICP-OES, ^{27}Al NMR, FTIR s různými molekulami, difúzní reflektancí UV/Vis, XPS, TG a TPD a dalšími technikami. Katalytická aktivita připravených katalyzátorů byla studována v reakcích probíhajících v plynné i kapalné fázi; jmenovitě dehydratace etanolu, alkylace toluenu, katalytické oxidace VOC, tetrahydropyranylace alkoholů a acylace p-xylenu.

Hlavní závěry z této práce jsou následující: (1) skupina izoretikulárních Al-IPC zeolitů charakterizovaných postupně se měnící velikostí mikropórů při stejné morfologii, obsahu Al a koncentraci kyselých míst byla připravena vhodným výběrem syntetických parametrů. Jako

jedinečná modelová sada katalyzátorů (parametry mřížky lze upravit nezávisle na většině vlastností), izoretikulární zeolity Al-IPC ukázaly jasný vztah mezi velikostí pórů a katalytické aktivity při dehydrataci etanolu a tetrahydropyranylačních reakcích. (2) srovnání texturních a katalytických vlastností zeolitů s jednorozměrnými póry připravených pomocí přímé a postsyntetické aluminace umožnilo optimalizovat začlenění hliníku do zeolitových struktur chudých na hliník (např. typ **AFI**). (3) odolnost nanočásticových zeolitů vůči agregaci připravené povrchovou modifikací příslušných nanokrystalů byly korelovány s vlastnostmi (denticita, polarita, velikost) funkcionalizačního činidla. Ve srovnání s nemodifikovanými nanokrystaly, vzorek obsahující optimalizované skupiny chránící povrch vykazoval zřetelně lepší stabilitu proti agregaci v suspenzi i za tvrdých katalytických podmínek. (4) využití zeolitů **MWW** s různým uspořádáním vrstev (MCM-22/36/56) a chemickým složením (Si/Al = 12 - 50) umožnilo pochopit roli zeolitů jako nosičů při eliminaci VOC. Zejména obsah hliníku v nosiči má významný vliv na disperzi a redukovatelnost aktivní fáze (oxid kobaltu), a tím i na katalytickou aktivitu v oxidaci toluenu a propanu. Materiál MCM-22 s minimálním vnějším povrchem a vhodným složením (Si/Al = 50) vykazoval nejvyšší katalytickou aktivitu pro oxidaci toluenu a propanu (90% konverze při teplotě 307 °C a 295 °C), což otevírá možnosti pro využití při odstraňování VOC.

Celkově (1) studie katalytické aktivity u zeolitů Al-IPC-n ukázaly, že dehydratace ethanolu i tetrahydropyranylace alkoholů se úměrně zvyšovala s velikostí pórů a koncentrací vnějších kyselých míst, což demonstruje potenciál izoretikulárních zeolitů odvozených od UTL jako modelových katalyzátorů k dalšímu pochopení vztahů mezi velikostí a aktivitou pórů katalyzátoru. Kromě toho (2) výsledky alkylace toluenu prokázaly, že post-syntetická izomorfní substituce jednorozměrného zeolitu s velkými póry chudými na Al může být použita k účinnému vyladění chemického složení jednorozměrných zeolitů s velkými póry, čímž se vytvoří Al- obohacené zeolitové materiály vhodné pro katalytické aplikace. Dále, (3) povrchová silylace nano-zeolitů **MFI** omezila jejich agregaci a zlepšila jejich katalytickou aktivitu, čímž částečně vyřešila své základní problémy s aktivitou a stabilitou a umožnila jejich aplikaci na širší škálu katalytických procesů. A konečně (4) katalytická aktivita oxidů

kobaltu s nosiči na bázi **MWW** v toluenových a propanových oxidačních reakcích se zvyšuje se Si/Al nosiče zeolitů **MWW** a následně s disperzí a redukovatelností kobaltových látek. Hodnocení účinků specifických vlastností zeolitů jako nosičů na disperzi a redukovatelnost katalytické aktivní fáze a na odpovídající katalytickou aktivitu je tedy zásadní pro vývoj katalyzátorů na zeolitech s vysokou aktivitou při eliminaci VOC.

List of abbreviations

1ES	ethoxydimethylphenylsilane
3ES	triethoxyphenylsilane
A	acid dealumination
ADOR	Assembly-Disassembly-Organization-Reassembly
ACN	d_3-acetonitrile
BET	surface area according to Brunauer, Emmett and Teller theory
c_B	concentration of Brønsted acid sites
c_L	concentration of Lewis acid sites
CO-TPD	temperature programmed desorption of carbon monoxide
DR UV-Vis	diffuse reflection UV-Vis spectroscopy
DLS	dynamic light scattering
D4R	double four ring
DEE	diethyl ether
DHP	3,4-dihydro-2H-pyran
DTBPy	2,6-di-tert-butylpyridine
EDX	energy-dispersive X-ray spectroscopy
FCC	fluid catalytic cracking
FID	flame ionization detector
FTIR	fourier transform infrared spectroscopy
GC	gas chromatograph
HB	hydrogen bond
HMI	hexamethyleneimine
HRTEM	high resolution transmission electron microscopy
IZA	international zeolite association
IEZ	interlayer expanded zeolite
ICP-OES	inductively coupled plasma optical emission spectroscopy
i-PrOH	isopropyl alcohol
MR	member ring

MTO	methanol to olefin
NMR	nuclear magnetic resonance
PBU	primary building unit
Py	pyridine
S4R	single four ring
SBU	secondary building unit
SEM	scanning electron microscopy
SDA	structure directing agent
Si/Al	the molar ratio of silicon to aluminum
Si/Ge	the molar ratio of silicon to germanium
Sext	external surface area
TEM	transmission electron microscopy
TG	thermal gravimetric analysis
TPAOH	tetrapropylammonium hydroxide
TPD	temperature programmed desorption
TEOS	tetraethyl orthosilicate
TOF	turn over frequency
V_{mic}	micropore volume
V_{tol}	total pore volume
V_{meso}	mesopore volume
VOCs	volatile organic compounds
WHSV	weight hourly space velocity
XRD	X-ray diffraction

1. Aims of the study

Revealing of the structure-property-activity relationship for zeolite materials bridges the developing of highly efficient zeolite catalysts and understanding the mechanism of catalytic reactions. This thesis was focused on preparation of various zeolite catalysts, which are mainly based on layered and nanosized zeolites, and was aimed to study the insightful relationship between the properties of developed zeolite catalysts and their performance (activity, selectivity, stability) in different reactions.

This thesis aimed to achieve the following specific goals:

✓ To study pore size-catalytic activity relationship through a rational analysis of key factors affecting the synthesis of **UTL**-derived isoreticular zeolites as model systems

✓ To optimize the Al-AFI zeolite chemical composition for catalytic applications, synthesis of Al-enriched **AFI** zeolite

✓ To develop the method for suppressing of zeolite nanocrystals agglomeration while maintaining accessibility of acid sites, synthesis of silane functionalized **MFI** nanosized zeolites

✓ To correlate the textural and acid properties of zeolite supports to the performance of cobalt-containing **MWW** catalysts

✓ To characterize the developed catalysts using XRD, electron microscopy (SEM and TEM), adsorption, EDX and ICP-OES, NMR, FTIR, diffuse reflectance UV/Vis spectroscopy, TG, TPD and DLS etc.

✓ To assess catalytic properties of the designed catalysts by testing them in gas phase reactions (ethanol dehydration, toluene alkylation, catalytic oxidation of toluene and propane) and liquid phase reactions (tetrahydropyranylation of alcohols, acylation of p-xylene)

2. Introduction

2.1. Short overview on zeolite structures and applications in catalysis

2.1.1. Zeolite structures

Zeolites are crystalline aluminosilicates with regular three-dimensional frameworks and large surface area. To date, 248 zeolite structures have received respective three-letter code (e.g. **MFI**, **FAU**) from International Zeolite Association (IZA) [1]. The smallest structural unit to build zeolite frameworks is TO_4 tetrahedra (T = Si and Al). Individual tetrahedra is connected by sharing the bridge oxygen and further constitutes secondary building units (SBU) like 3-, 4-, 6- rings, spiro-5, and double four ring (D4R) etc.

Zeolites are microporous materials and the diameter of their pores and cavities is below 2 nm. According to oxygen atom number within the smallest pore entrance, zeolites are distinguished as 8- member ring (MR), small-pore zeolites (e.g., **CHA, CDO**); 10- MR, medium-pore zeolites (e.g., **MFI**, **MWW**); 12- MR, large-pore zeolites (e.g., **MOR**, **FAU**), and > 12- MR, extra-large-pore zeolites (e.g., **UTL**, **CFI**). In addition, based on the directions, at which a guest molecule can diffuse within zeolite channel system, zeolites are divided into one-dimensional (such as **MOR**, **AFI)**; two-dimensional (**MWW**, **FER**); and three-dimensional zeolites (**MFI**, **BEA, Figure 2-1**). When zeolites are used as catalysts, the differences in pore sizes, shapes and channel dimensions among zeolites will show great influences on their catalytic performances, which is well-known as shape-selective effect [2, 3].
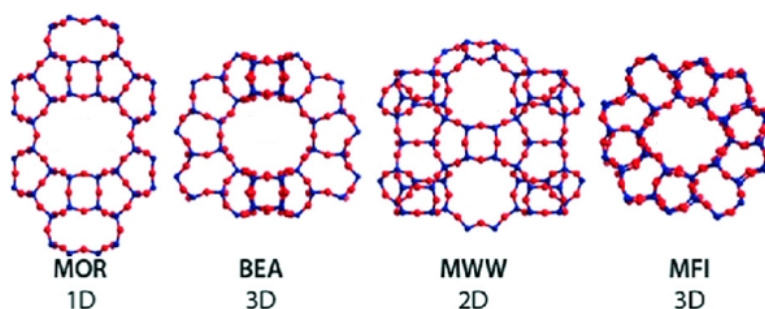
Figure 2-1. Zeolites with different topologies [4].

According to the interplay between the size or geometric shape of zeolite channels and kinetic diameters of guest molecules, there are three types of shape selectivity (**Figure 2-2**):

Reactant selectivity – only the reactant molecules possessing specific size and shape could enter zeolite channels;

Product selectivity – the initial products which are too bulky to leave the zeolite channels may decompose into final products with smaller size.

Transition state selectivity – only the certain intermediates (transition states) whose sizes and shapes match the channels or cavities could be formed.
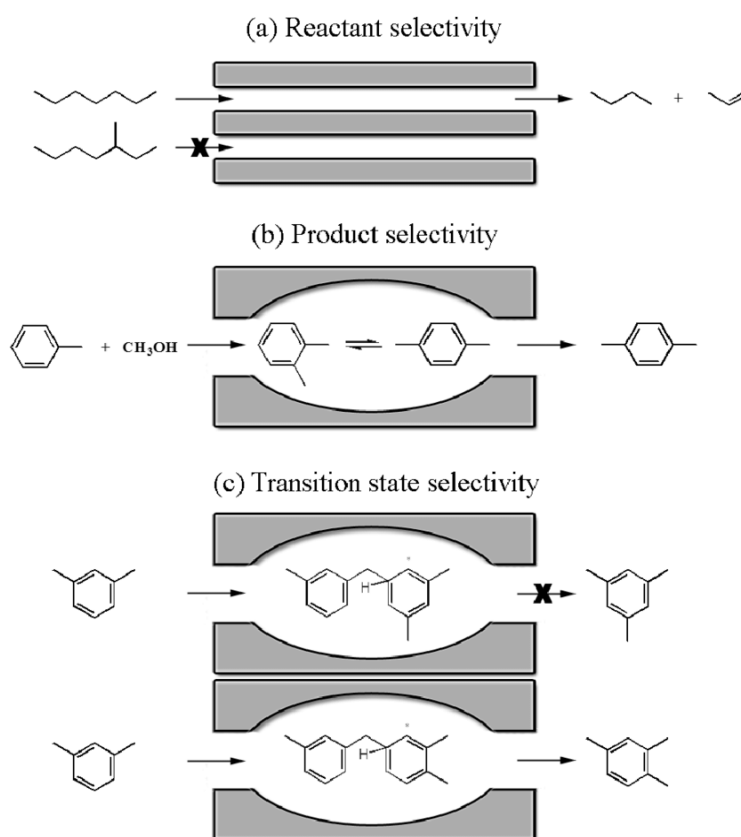
Figure 2-2. Three types of shape selectivity presented in zeolite catalysts [3].

Such formula $M_{x/n}[(AlO_2)_x(SiO_2)_y]$ could be used to describe chemical composition of zeolite frameworks. In the formula, M stands for the exchangeable extra-framework cations, e.g. Na^+, Ca^{2+}; n is the number of charges of cations; y/x is silicon to aluminum molar ratio (Si/Al) per unit cell. In aluminosilicates, each Al ion induces a framework negative charge and the

negative charges should be balanced with guest cations, such as H^+, Na^+ and K^+. Given the similarity in size and charge, the T atoms in zeolite frameworks can be isomorphously substituted by other atoms (so called heteroatoms), e.g. +4 (Ti^{4+}, Ge^{4+}, Sn^{4+}, etc.) or +3 (B^{3+}, Fe^{3+}, Ga^{3+}, etc.). The incorporated heteroatoms contribute to either Brønsted or Lewis acidity for zeolites (**Figure 2-3**). The acidic properties of zeolites, characteristic of amount, strength, types, and locations, can be conveniently assessed through FTIR with adsorption of specific probes (e.g. d_3-acetonitrile pyridine and 2,6-dialkyl pyridines) [5].
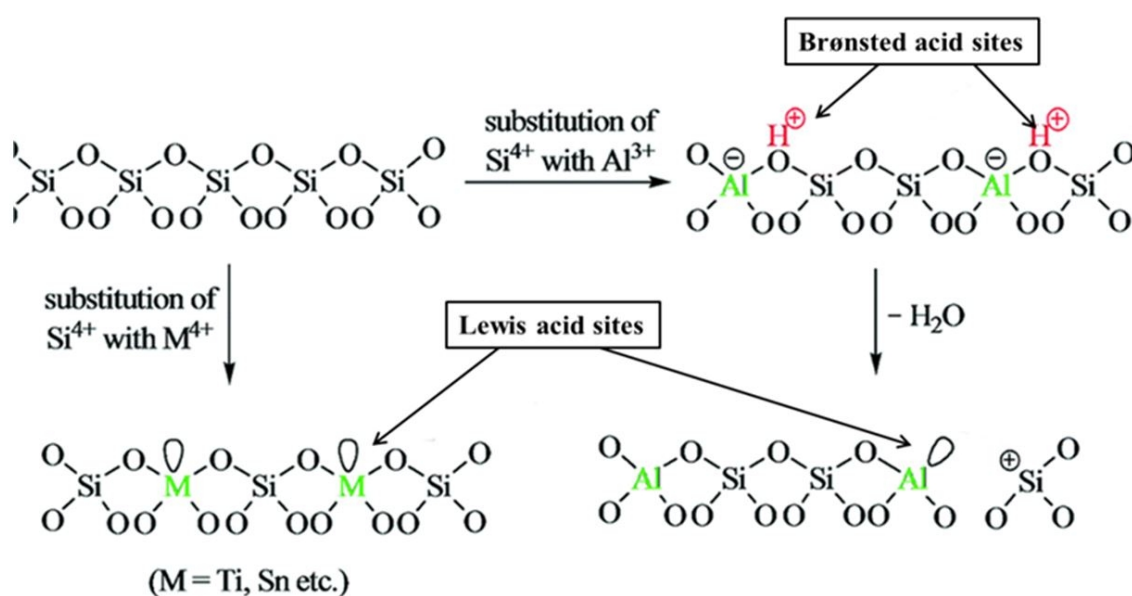
Figure 2-3. The schematic description of the nature and generation of Brønsted and Lewis acid sites on zeolite [6].

2.1.2. Zeolites in catalysis

Zeolites are traditionally applied to petrochemical related processes, such as fluid catalytic cracking (FCC) and hydrocracking, however, more and more emerging applications, such as fine chemicals production, biomass conversion and VOCs elimination etc. consider zeolites as perspective catalysts **(Figure 2-4)** [7].

Figure 2-4. Emerging applications of zeolites [7].

Benefits from chemical tunability and easy recyclability, zeolites are widely applied as heterogeneous catalysts. The development of zeolites as solid acid catalysts is associated with their successful application in oil refinery. In this field, zeolites have showed active roles in e.g., catalytic cracking, hydrogenation/dehydrogenation, skeletal isomerization, polymerization and aromatic alkylation with alkenes or alcohols etc. [8]. Several specific zeolites have shown high efficiency in these reactions, for example, rear earth ions-exchanged **FAU** zeolites are commonly used for fluid catalytic cracking [9]. **MFI** zeolites can be added for higher propylene production [10]. Zeolites are also useful for producing fine chemicals and have substituted some mineral acid catalysts[11]. Aromatic ketones are conventionally synthesized though Friedel-Crafts acylation of aromatics over homogeneous catalysts, e.g. HF, H_2SO_4, $FeCl_3$ or $AlCl_3$ [12]. However, using these catalysts is hazardous and shows difficulties in products separation. As alternative heterogeneous catalysts, various valuable products, like p-methylacetophenone, p-hydroxyacetophenones etc. could be produced by acylation of aromatics over zeolites catalysts [11].

With the development of global industrialization, we have to face more and more severe air

pollution issues. NO_x, NH_3, SO_2, H_2S and volatile organic compounds (VOCs), e.g. propane, toluene, formaldehyde etc., released from the industrial emission, are the main air pollutants. Developing techniques to eliminate the above pollutants is urgent and will decrease the harms to our health. Considering the adsorption and catalytic potentials, zeolites have been employed to many processes involving catalytic removal of air pollutant molecules. Among them, Fe- and Cu-SSZ-13 as active $deNO_x$ catalysts in NH_3-SCR reaction attract a lot of interest [13, 14]. Other zeolite frameworks such as ZSM-5 [15], Beta [16], UZM-35 [17] etc. also showed as appropriate candidates for catalytic treatment of NO_x. In addition, noble metal/ porous support hybrid materials showed high activity for complete conversion of VOCs at relatively low temperature [18]. However, design and development of transition metal-based catalysts is preferred considering their advantages in lower cost and higher abundance. Zeolites represent the materials with high surface area and pore volume, tunable hydrophobicity/hydrophilicity, high thermal stability. Therefore, zeolites are expected as desirable supports for loading catalytic active phase (both noble and non-noble metals) [19]. For example, Pt supported on the K-type Beta zeolite showed complete toluene conversion at 150 °C [20]. Similarly, cobalt-containing siliceous catalysts showed homogeneous distribution of Co_3O_4 on the dealuminated Beta supports, and compete converting of toluene to CO_2 and H_2O achieved at 325 °C. Moreover, Co/Beta catalyst was more active than some noble metal-containing Beta zeolites and zeolite-supported transition metals (Mn, Fe on clinoptilolite, ZSM-5) [21]. Another study showed that when pure silica Beta zeolite is used as support for Ag, respective catalysts outperformed other materials designed using oxide supports (CeO_2, TiO_2, γ-Al_2O_3, MnO_2) in catalytic combustion of HCHO at 70 °C [22].

The successful application of zeolites as catalysts is largely dependent on their properties. In order to promote the development of highly efficient zeolite materials for various processes and better understanding of catalytic reactions mechanism, it is crucial to further study the synthesis-property-activity relationships of zeolite materials.

2.2. Layered zeolites

2.2.1. Synthesis of layered zeolites

Layered zeolites consist of extended crystalline zeolitic sheets with thickness below a few nanometers [23, 24]. Layered zeolites could be synthesized by either bottom-up hydrothermal conditions or top-down structural transformation from specific germanosilicates [23-25]. One on side, layered zeolites with such as **MWW**, **FER, SOD** topologies can be produced from direct hydrothermal conditions with conventional structure directing agents (SDA) (**Figure 2-5 (a)**) [26-28]. Individual layers in layered precursors are connected through hydrogen bonds (HB) between the surface silanol groups. Upon calcination, SDAs are removed and simultaneously silanol groups are condensed into oxygen bridges, turning two-dimensional (2D) layered precursors into fully connected three-dimensional (3D) zeolites. Alternatively, under hydrothermal conditions, some layered zeolites, like **MFI** [29], **MOR** [30], could be prepared by designing specific structure directing agents (**Figure 2-5 (b)**). In this aspect, Ryoo et al. did pioneering work on the synthesis of stable single-unit-thickness **MFI** nanosheets using di-quaternary ammonium-type surfactants [29].
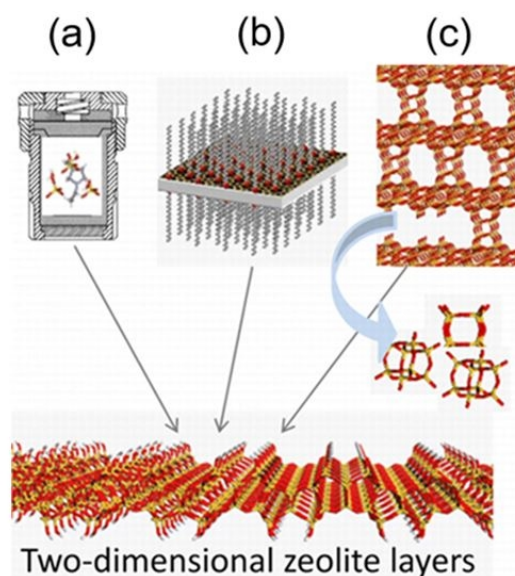
Figure 2-5. The scheme of three approaches to synthesize layered zeolites [23].

On the other side, the top-down approach to prepare layered zeolites is based on structural evolution of 3D germanosilicates, like **UTL**, ***CIF**, **IWW** etc. into 2D lamellae by post-synthesis treatments (**Figure 2-5 (c)**). Our group firstly established this top-down method and further developed it into a versatile strategy called ADOR [31, 32]. ADOR is the abbreviation for assembly–disassembly–organization–reassembly procedure. Step by step, firstly, a parent 3D germanosilicate characteristic of Ge-rich D4R is prepared hydrothermally (assembly); then it is hydrolyzed under appropriate conditions by removal of D4R units and consequently generates a layered precursor (disassembly); following is adjusting the arrangement of adjacent layers (organization) and lastly the layers are condensed into new 3D zeolite structures by calcination (reassembly). **Figure 2-6** shows a typic ADOR procedure exemplified by germanosilicate **UTL**. In which, layered precursor (named as IPC-1P) is produced after hydrolysis of **UTL** under low acidic or neutral mediums. And through manipulations of IPC-1P, a family of new zeolite frameworks including IPC-2, IPC-4 [33], IPC-6 [34, 35], IPC-7 [35], IPC-9 and IPC-10 [36] has been synthesized.
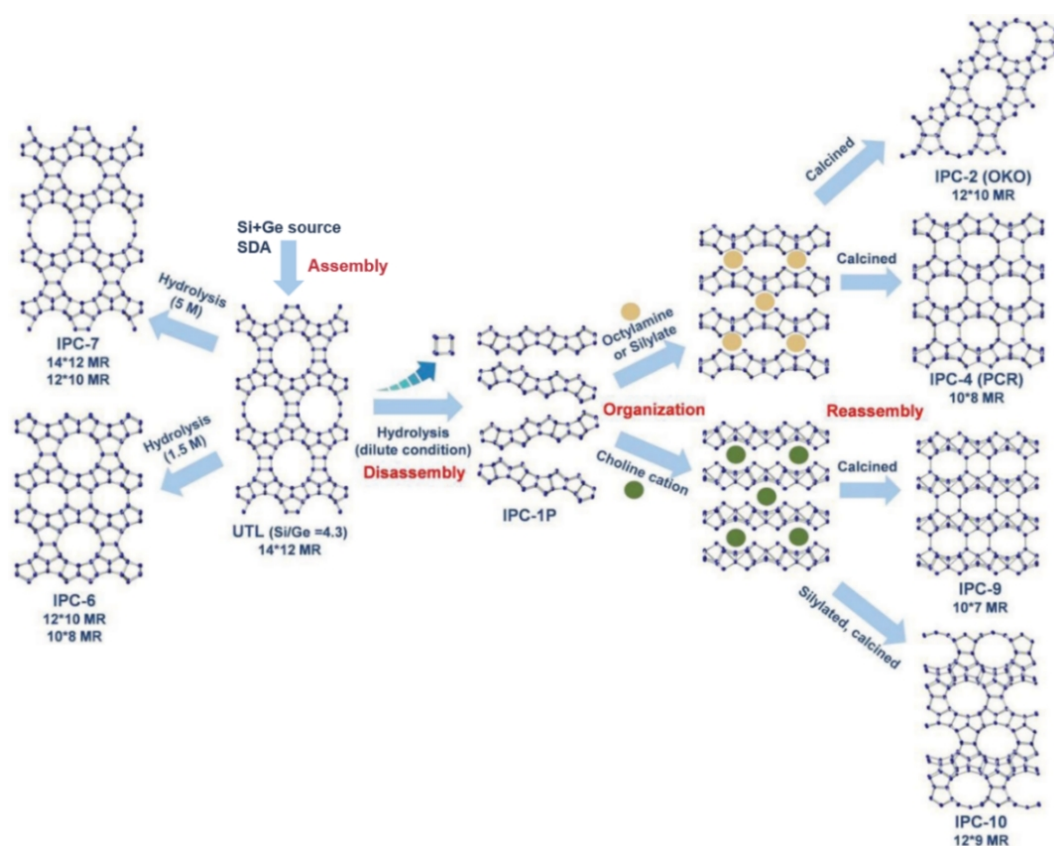
Figure 2-6. The ADOR strategy applied to **UTL** zeolite [25] [31].

2.2.2. Manipulation with zeolite layers

The layer zeolites offer rich possibilities for structural and chemical modifications on nanoscale level. A wide variety of post-synthetic modification methods have been reported to manipulate zeolite layers [25]. Here, layered zeolite precursor MCM-22P with **MWW** topology is taken as an example to illustrate some important post-synthetic modifications (**Figure 2-7**).

Firstly, upon calcination, the organic templates located at interlayer are eliminated and simultaneously two corresponding silanol groups on the surface of MCM-22P condense, forming oxygen bridge which connects the layers into 3D **MWW** zeolite, that is, MCM-22 [28].

In addition, interlayer silylation introduces additional tetrahedra units between the layers and thus results in enlarged interlayer space of layered precursors. In this process, the hydrolyzed silanes interact with surface silanol groups and then the neighboring layers are interconnected by intercalated silane linkers. The outcomes of interlayer expansion depend on the specific silanes. Monomeric [37], dimeric [38] or square-shaped single 4-ring (S4R) silanes [39] have been intercalated into the interlayer space. This versatile method has been applied to construct interlayer-expanded zeolites (IEZ) with different topologies, e.g., **MWW** [37, 38] or **FER** [39, 40]. Another example is zeolite IPC-2 (**OKO**) formed upon intercalation of the IPC-1P layered precursor with additional Si species [33, 41].

In contrast to IEZ materials, pillared zeolites also possess increased interlayer space than layered precursors while the nature of interlayer linkers is different. MCM-36 is one of the first and the most outstanding pillared zeolites [42]. Synthesis of MCM-36 consists of two steps: swelling MCM-22P with surfactant and then replacing the surfactant with amorphous silica pillars [42]. Cetyltrimethylammonium bromide (CTAB) is the most common surfactant for swelling. The final MCM-36 maintains the intralayer micropores from MCM-22P while forms additional mesoporosity by silica pillaring [43].

After swelling of MCM-22P, if further ultrasonic treatments are applied, delaminated **MWW**

materials with monolayered architecture could generate, such as ITQ-2 [44] and UCB-1 [45]. Furthermore, MCM-56 with disorder layers stacking can be synthesized either under hydrothermal conditions with shorter time than MCM-49 crystallization or treating the MCM-22P with mild acid solutions [43].
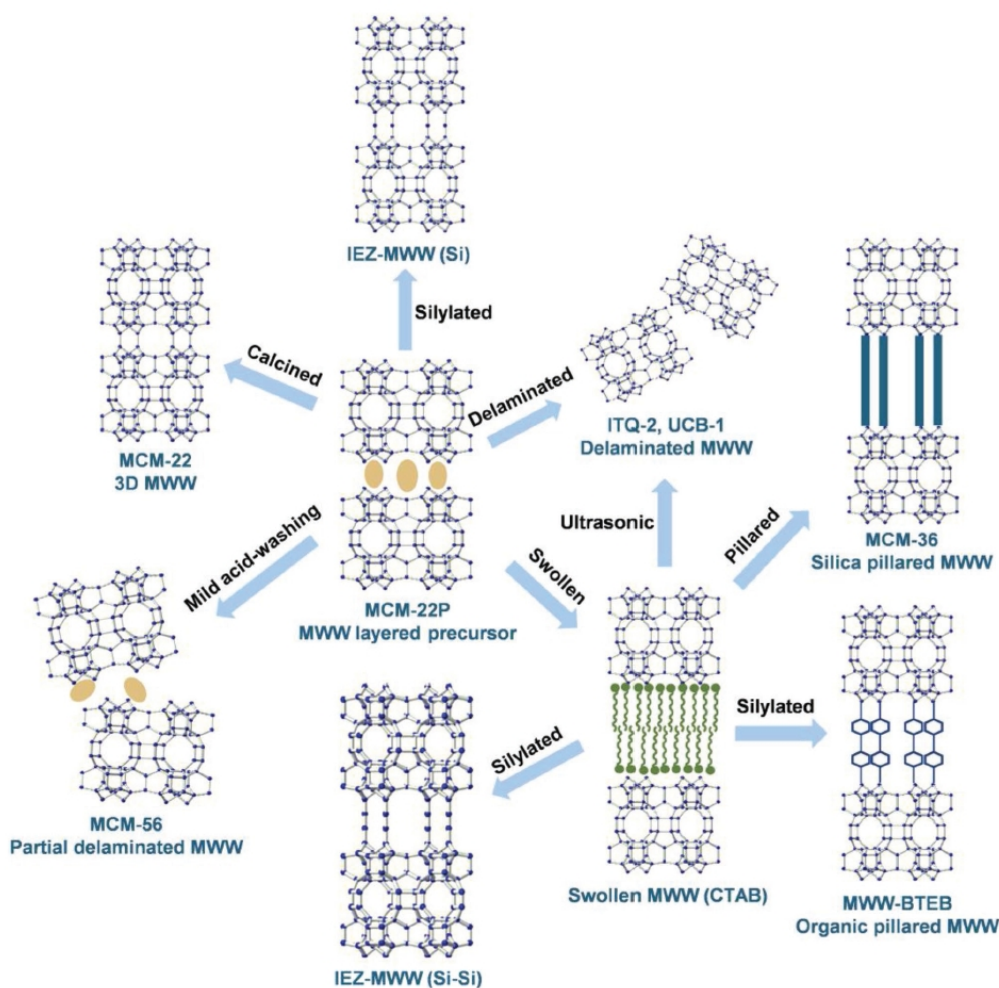
Figure 2-7. Representations of the post-synthetic modifications on MCM-22P zeolite [25].

2.2.3. Catalysis in layered zeolite materials

Layered zeolite precursors can be also viewed as new platform for designed synthesis of advanced catalysts by layers manipulations. Furthermore, layered zeolites have well-developed external surface and highly accessible acid centers which have shown advantages in reduction of the diffusion paths for the reactions involving bulky reactants [23, 24]. Given

the excellent physicochemical properties of layered zeolites, one can expect to improve the catalytic performances over layered zeolite catalysts for a wide variety of reactions, such as hydrocarbons transformation (cracking, alkylation, acylation etc.), gas-to-liquids processes, biomass conversion, red-ox catalysis and so on (**Figure 2-8**). In this aspect, MCM-22P derived materials and the **MFI** nanosheets are the most investigated catalysts regarding to layered zeolites. In addition, a family of isoreticular zeolites emerges recently, which are derived from **UTL** zeolite[46-48].
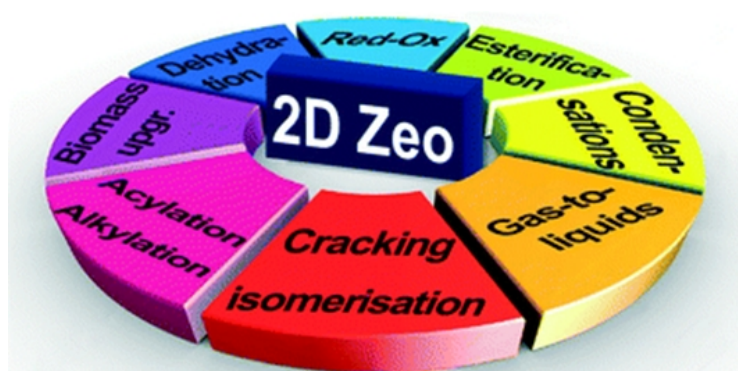
Figure 2-8. The typical reactions over layered zeolite-based catalysts [49].

A series of **MWW**-type zeolites, ITQ-2, MCM-36 and MCM-22, were compared in catalytic cracking reactions. Various reactants with increasing molecular size (n-decane, diisopropylbenzene and vacuum gasoil) were included [44, 50]. First of all, ITQ-2 did not show the advantage in the cracking of n-decane, which is due to the fast diffusion of n-decane over all the catalysts. However, larger fraction of liquid products was formed over ITQ-2 catalyst, suggesting fewer undesired cracking reactions occurred. When the size of reactant molecules increased, ITQ-2 showed higher conversion of diisopropylbenzene and vacuum gasoil than both MCM-22 and MCM-36. At the same time, ITQ-2 exhibited notable stability during the cracking tests due to the less pronounced formation of coke. In addition, in the cracking of vacuum gas oil, MCM-36 exhibited higher yields of liquid products than MCM-22 catalyst [50], which was explained that a higher concentration of acid sites located on the external surface of MCM-36. Furthermore, taking into account the advantages of abundant

acid sites on the external surface and decreased diffusion limitation, **MFI** nanosheets showed high efficiency in cracking of decaline [51] and naphthalene [52], methanol dehydration [53, 54] etc.

Incorporation of Ti or Sn into zeolite frameworks enables zeolites to catalyze important oxidation reactions. For example, a layered titanosilicate with **MFI**-type (named as LTS-1) and conventional TS-1 were compared in alkene selective oxidation to epoxide [55]. Various oxidants including H_2O_2, tert-butyl hydroperoxide and cumene hydroperoxide were used. In the epoxidation of cyclohexene with tert-butyl hydroperoxide and propylene with cumene hydroperoxide, LTS-1 outperformed conventional TS-1, indicating that layered **MFI** had advantages to treat bulky substances. In addition, the catalytic activity of Ti-MCM-56 and a series of benchmark titanosilicates (Ti-BEA, TS-1 and Ti-MCM-22) were evaluated in both epoxidation of alkenes with tert-butyl hydroperoxide and desulfurization of dibenzothiophene with H_2O_2. Ti-MCM-56 appeared to be the most active one among applied catalysts, which benefit from its more exposed acid sites [56]. Furthermore, a series of isoreticular titanosilicates was prepared from a Ti-UTL zeolite. Among them, Ti-IPC-1-PITi showed the highest activity in the selective oxidation reactions than others, which is related to its higher Ti content and less diffusion limitation [47]. In the Baeyer-Villiger (B-V) oxidation of 2-adamantanone [57], whatever the oxidants used, Sn-MCM-56 was more active than Sn-MCM-22, which is attributed to the disorderly of stacked MCM-22P layers in MCM-56 resulted in larger external surface area than MCM-22. Besides, Sn-MFI nanosheets with abundant and highly accessible Lewis acid sites also exhibited high activity in B-V oxidation [58].

The emerging layered zeolites have shown fascinating textural and acidic properties and been applied in different catalytic reactions. Regarding synthesis and application of layered zeolites, ADOR has proven to be a very efficient approach to produce new high silica zeolites and the derived isoreticular zeolites not only increase the number of available zeolite catalysts, but also could provide unique opportunity to study pore size-activity relationships of zeolite catalysts. In addition, layered zeolites have great potential to act as active phase

support due to high surface area and thermal stability. Whereas, comprehensively studying the effects of structure and acidity properties of layered zeolites on synthesis and catalysis of supported catalysts has not been sufficiently achieved.

2.3. Nanosized zeolites

2.3.1. Properties of nanosized zeolites

Conventional micron-sized zeolites are widely synthesized and applied in industrial catalysis processes. However, the large crystal size and limited pore size of micron-size zeolites cause significant diffusion restrictions for bulky reactants, intermediates and products, which results in a fast deactivation and reduced efficiency of zeolite catalysts [59]. To settle these drawbacks, many advanced zeolite materials have been prepared, such as hierarchical zeolite, extra-large pore zeolite, layered zeolites and nanosized zeolites [60, 61].

High quality nanosized zeolites have similar micropore volume to their micron-sized counterparts [62, 63]. However, nanosized zeolites exhibit apparently larger external surface areas than micron-sized zeolites and have shown advantages in catalyzing the reactions involving bulky reactants [63]. The short diffusion paths through nanosized zeolite channels is due to their small crystal size. **Figure 2-9** further summarizes the other advantages of nanosized zeolites [64].

Figure 2-9. Advantages of nanosized zeolites [64].

2.3.2. Synthesis of nanosized zeolites

The preparation of zeolite nanocrystals strongly depends on (1) the precursor source; (2) organic SDA; (3) solvent; (4) additives; and (5) crystallization conditions, such as temperature, time. (**Figure 2-10 (a)**) [65, 66]. Based on these key parameters, various methods have been reported to synthesize nanosized zeolites (**Figure 2-10 (b)**).

(a)
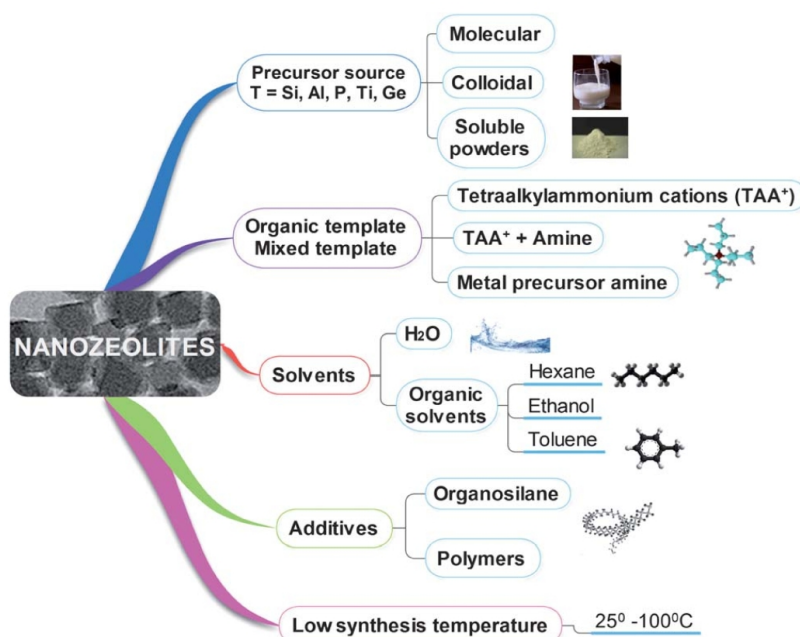
(b)
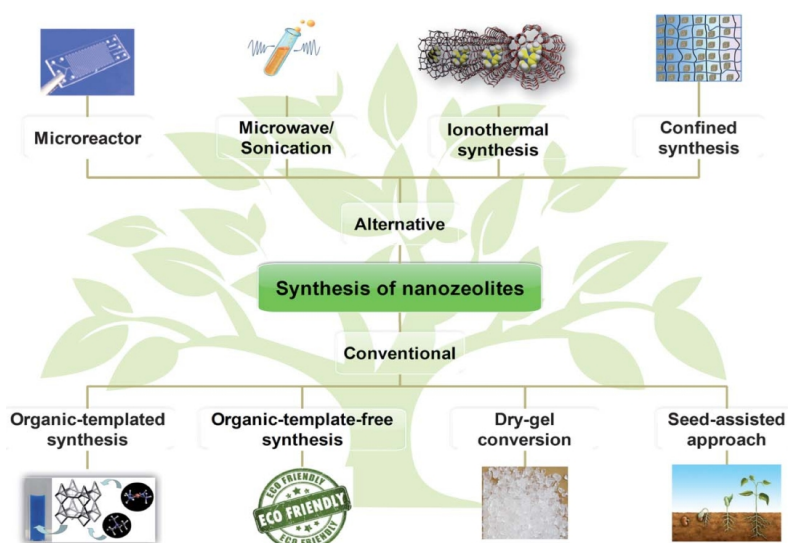
Figure 2-10. Key parameters (a) and approaches (b) to synthesize nanosized zeolites [65].

Several of synthesis methods for nanosized zeolites are highlighted in the following:

During the crystallization of zeolites, the temperature has significant effect on the nucleus formation and crystals growth. Compared to micron-sized zeolites synthesis, a lower crystallization temperature is essential for nanosized zeolites. In general, the decrease in temperature favors nucleation over growth. In addition, lower temperature inhibits Ostwald ripening of crystallites, which results in uniform small crystal size in the final product. In this aspect, Valtchev's group successfully prepared **LTA** zeolite (~200 nm) at room temperature [67]. Afterward, the same group further developed a two-step crystallization temperature method. In the first step, reaction mixture proceeds at room temperature and then the reaction continues at relative higher temperature, in the range of 35 to 65 °C. As a result, the crystal sizes of the **LTA** (30 ~ 400 nm) were controlled by adjusting the crystallization temperatures in the second step [68]. Recently, Ng et al. [69] successfully synthesized ultra-small **EMT** (6 ~ 15 nm) with high yields by controlling the growth kinetics using template-free method and low temperature (30 °C). Similarly, Awala et al. synthesized nanosized **FAU** with size of 10 ~ 15 nm using template-free method under low temperature conditions [70]. The nanosized **FAU** with Si/Al in the range of 1.1 to 2.1 can be synthesized with yields greater than 80%. Therefore, the template-free synthesis of nanosized zeolites represents a new green route to zeolite preparation, which avoid the use of costly SDA and further calcination treatment.

In addition, seed-assisted synthesis of nanosized zeolites is another environmentally friendly and efficient synthesis strategy. With the help of seeds, the crystallization time is shortened and crystal size is controllable. The size and dispersity of seed crystals play an important role in the morphology of nanosized zeolite products. For example, isolated seed crystals often resulted in zeolite crystals with regular morphology. Using seed-assisted strategy, nanosized zeolites with various structures, such as **MFI** [71], **MTW** [72], and **RTH** [73] have been prepared. Moreover, particular types of nanosized zeolites with optimized Si/Al can be obtained by seed-assistant synthesis. In this aspect, Mintova et al. reported the preparation of nanosized Beta zeolite with very low Si/Al of 3.9 [74]. Furthermore, the seed-assisted synthesis can effectively reduce the use of organic template agents, which is preferred for

industrial zeolite production.

2.3.3. Catalysis in nanosized zeolites

Compared to micron-sized zeolites, nanosized zeolites exhibit higher external surface acidity and improved mass transfer properties, which contributes to the increased catalytic activity of nanosized zeolites [75].

Nanosized zeolites have shown high activity, selectivity and stability in catalytic cracking, dealkylation, MTO and biomass conversion [76, 77]. For example, nanosized and commercial ZSM-5 zeolites with similar concentration of acid sites were compared in cracking of hydrocarbons (n-hexane, cyclohexane and methylcyclohexane) at 550 - 650 °C and atmospheric pressure [78]. When n-hexane was used as the reactant, initial yield was similar (~ 80%) over both ZSM-5 catalysts. However, nanosized ZSM-5 showed a more stable n-hexane conversion and product selectivity to olefins, in particular, $C_3=$, than micron-sized ZSM-5. With time, decreased reactant conversion and production of other hydrocarbons (paraffin, methane etc.) were observed over micron-sized ZSM-5 catalyst. In addition, increase in reactants size (cyclohexane or methylcyclohexane) results in lower cracking rates over micron-sized ZSM-5 catalyst. Moreover, benzene and toluene were detected in the products after cyclohexane or methylcyclohexane cracking, suggesting dehydrogenation reaction took place over micron-sized ZSM-5. Therefore, these results confirmed that diffusion limitations present in conventional large zeolite crystals, which leads to fast deactivation of the catalyst and formation of side products.

In addition, nanosized Y with distinct crystal size (Y-400, Y-70 and Y-10 composed of 400, 70 and 10 nm zeolite crystals respectively) were synthesized by organic-template-free method and were evaluated in dealkylation of 1,3,5-triisopropylbenzene [70]. Firstly, the conversions of 1,3,5-triisopropylbenzene over all nanosized Y catalysts were higher than commercial micron-sized Y sample, LZY-62 (crystal size of 1-2 μm). Furthermore, the selectivity to di-alkylated products (1,3 and 1,4-diisopropylbenzene) at 200 °C significantly depended on the crystal size of applied catalysts. LZY-62 with largest crystal size showed the lowest

selectivity. These results indicated that dealkylation of 1,3,5-triisopropylbenzene mainly occurred at the external surface of zeolites. Lastly, all nanosized Y catalysts showed superior stability after 12 h testing, suggesting the deactivation of the nanosized Y catalysts was almost absent.

Nanosized Y zeolites were also compared with micron-sized Y in H_2-free deoxygenation of triolein [79]. The micron-sized sample (Y2750) had large crystal size about 2.75 μm and was purely microporous. It exhibited the lowest triolein conversion than other nanosized Y zeolites and reached only 35% selectivity to hydrocarbons (gasoline, diesel and heavy hydrocarbons C_{19+}). In contrast, nanosized Y (Y-20, Y-65, Y-380 with crystal size of 20, 65 and 380 nm, respectively) catalysts showed higher hydrocarbon products selectivity (67-77 %). In addition, there is a clear linear relationship between rate constant of triolein deoxygenation and concentration of acid sites (Brønsted and Lewis) on external surface. As a result, Y-20 zeolite with the smallest crystal size and the highest external surface acidity outperformed other catalysts in triolein conversion (70%). A higher diesel to gasoline ratio and less heavy hydrocarbon products were achieved over Y-20 than other Y zeolites.

Similar to layered zeolites, nanosized zeolites have shown outstanding textural and acidic properties and have been applied in different catalytic reactions. In addition, the decrease in the zeolite crystal size extends the possible applications of nanosized zeolites, such as membrane and detectors etc. [80]. Though a lot of achievements have been made in both synthesis and application of new developed nanosized zeolite. However, nanosized zeolites crystals tend to agglomerate spontaneously due to a large number of surface defects (hydrophilic silanol groups) [81]. The aggregation of nanocrystals forming larger zeolite particles causes unfavorable intercrystal diffusion barrier (so called "internal diffusion barrier") and worse accessibility to acid sites [82], which fades away the advantages of nanosized zeolites. In this aspect, various methods have been reported to synthesize nanosized zeolites with decreased defects, for example, freeze drying [70], hierarchical assembly [83], isomorphous substitution (W, Mo incorporation into the zeolite framework) [81, 84], and silylation [85] etc., which address the necessities to improve the catalytic activity of nanosized

zeolites by design and construct aggregation-resistant zeolite materials though it is challenging.

2.4. Post-synthesis isomorphous substitution in zeolite framework

The diverse applications of zeolite materials commonly call for zeolites with wide range of chemical compositions (e.g., Si/Al). Generally, the chemical compositions of zeolites are outcomes of the direct hydrothermal synthesis and are strongly dependent on initial gel mixtures [86]. Post-synthesis isomorphous substitution is an alternative way to tune the chemical composition of zeolite frameworks for specific applications. Isomorphous substitution in zeolite frameworks is defined as replacing the framework T atoms with heteroatoms while preserving the initial zeolite structures.

As shown in **Figure 2-11,** the post-synthetic incorporation of heteroatoms into zeolite frameworks involves a partial removal of some framework atoms of the initial zeolite (e.g., Si, Al, Ge) resulting in the formation of so called "silanol nest" vacancies and then reinsertion of heteroatoms (e.g., Ti, Sn) to heal the vacancies [87].
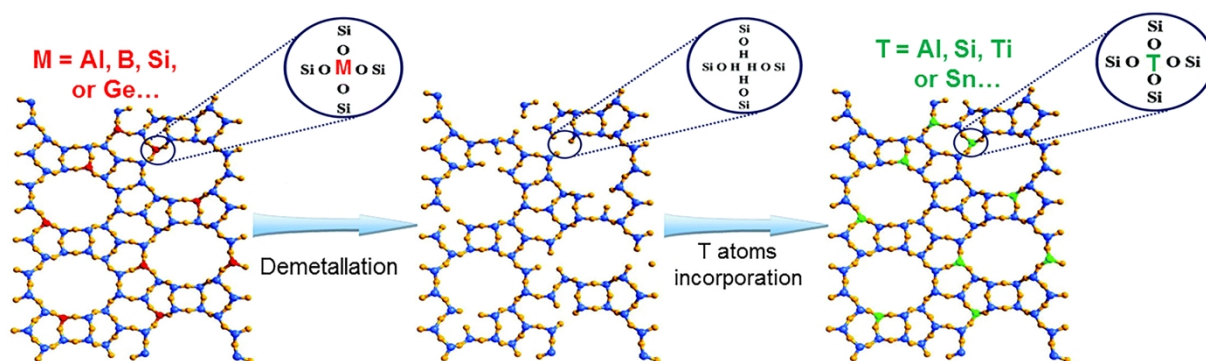
Figure 2-11. Schematic description of the isomorphous substitution process [87, 88].

Regarding post-synthetic isomorphous substitutions, alumination is an important and efficient way to tune the type, number and distribution of acid sites of zeolite. Both vapor and liquid solutions of Al source could be applied for incorporation of Al into zeolite frameworks. For example, treating high silica ZSM-5 and ZSM-11 with aluminum chloride vapor in N_2 steam

at high temperature, e.g. above 500 $^{\circ}$C, could generate strong acid sites [89]. In addition, when NaAlO$_2$ solution is used as Al source, it creates basic condition, which benefits to partially dissolve the Si atoms from zeolite framework and incorporate the Al into the framework at the same time [90, 91]. Al(NO$_3$)$_3$ is another commonly used Al source for alumination process. However, Chen etc. claimed that because the size of Al^{3+} hydrate is too large to go through the medium pore zeolite, e.g. ZSM-5 [91], therefore, the use of Al(NO$_3$)$_3$ as Al source may be inefficient for small and medium pore zeolites.

In addition, boron or germanium atoms are more chemically labile than silicon and aluminum in zeolite frameworks, which resulted in a lower stability of borosilicates or germanosilicates at various conditions (thermal or hydrothermal). However, this also can be considered as an opportunity to replace of B or Ge with other more catalytically active species, e.g., Al, Ti, Sn. Treating borosilicates or germanosilicates with HCl under appropriate conditions could lead to partial removal of B or Ge atoms without frameworks collapse, and the following alumination by Al(NO$_3$)$_3$ results in introduction of Al into the framework positions by healing the vacancies [91-93]. Reinsertion of Al into the zeolite frameworks to partially replace B or Ge improves the stability, acidity and thus catalytic performance of borosilicates and germanosilicates [94]. Furthermore, Ge is proved to be an efficient inorganic structure directing agent for large and extra-large pore zeolites [95, 96]. As a result, the Al(NO$_3$)$_3$ would work well as Al source for alumination of many germanosilicates [92, 93].

Regarding the diverse applications of zeolite materials, Al-rich or high silica zeolites have attracted more and more attentions because they have optimized acidity and hydrophobicity properties for certain applications. However, direct hydrothermal synthesis often cannot provide such Al- and Si-rich zeolites. Moreover, with the development of synthesis techniques, more and more new zeolite materials have been developed, for instance, large pore germanosilicates. Germanosilicates possess a great potential for catalysis applications, especially for bulky reactants conversion. Whereas, the intrinsic lack of strong (Brønsted) acidity and stability results in significant restrictions for their applications. Therefore, it has great significances to optimize the chemical composition of zeolites by isomorphous

substitutions, making them more suitable for specific catalytic applications.

With these, the investigation of synthesis-property-activity relationship of zeolite materials not only guides the developing of highly efficient zeolite catalysts but also helps the understanding of catalytic reactions mechanism. In particular, the emerging layered and nanosized zeolites offer fascinating textural and acidic properties for advanced applications. This thesis was focused on preparation of zeolite catalysts based on fully condensed ("3D"), layered ("2D") and nanosized ("0D") zeolites with regulated characteristics aimed to provide new insights into the relationship between important properties of zeolites and their catalytic performances. Following key properties of zeolites were carefully considered: structure, chemical composition, and accessibility of acid sites.

To fulfill these goals, **UTL**, **MWW**, **AFI**, **MFI** were used as model types of zeolites and they were tested in various liquid and gas phase reactions. The thesis is arranged as follows: **Section 3** outlines the materials synthesis, characterization, catalysis tests; **Section 4** describes the experimental results and discussion about designing different kinds of zeolites for catalytic applications; and **Section 5** offers a summary and concluding remarks.

3. Experimental part

3.1. Materials

Table 3-1: Reagents or solvents applied in the thesis.

Chemical name	Quality	Company	Formula
1,4-Dibromobutane	99%	Sigma-Aldrich	$Br(CH_2)_4Br$
cis-(2,6)-Dimethylpiperidine	98%	Sigma-Aldrich	$C_7H_{15}N$
2-ethylpiperidine	>98%	TCI	$C_7H_{15}N$
Hexamethyleneimine	99%	Sigma-Aldrich	$C_6H_{13}N$
Tetrapropylammonium hydroxide	40%	Sigma-Aldrich	$C_{12}H_{29}NO$
Cetyltrimethylammonium bromide	99%	VWR Chemical	$C_{19}H_{42}BrN$
Piperidine	99%	Alfa Aesar	$C_5H_{11}N$
Octylamine	99%	Sigma-Aldrich	$CH_3(CH_2)_7NH_2$
L-Lysine	>98%	Sigma-Aldrich	$C_6H_{14}N_2O_2$
Aluminum hydroxide	Reagent grade	Sigma-Aldrich	$Al(OH)_3$
Aluminum nitrate	>98%	Sigma-Aldrich	$Al(NO_3)_3 \cdot 9H_2O$
Germanium oxide	>99.99%	Sigma-Aldrich	GeO_2
Cobalt(II) nitrate hexahydrate	99.99%	Sigma-Aldrich	$Co(NO_3)_2 \cdot 6H_2O$
Sodium sulfate	>99%	Sigma-Aldrich	Na_2SO_4
Sodium hydroxide	98%	Penta	$NaOH$
Sodium hydroxide, 50% in water	50%	Merck	$NaOH$
Sodium aluminate		Sigma-Aldrich	$NaAlO_2$
Ammonium nitrate	99%	VWR Chemical	NH_4NO_3
Silica, fumed		Sigma-Aldrich	SiO_2
Triethoxyphenylsilane	98%	Sigma-Aldrich	$C_6H_5Si(OC_2H_5)_3$
Ethoxydimethylphenylsilane	>97%	Sigma-Aldrich	$C_{10}H_{16}OSi$
(4-biphenyl)triethoxysilane	98%	Gelest	$C_{18}H_{24}O_3Si$
3-(ethoxydimethylsilyl)propylamine	97%	Sigma-Aldrich	$C_7H_{19}OSiN$
LUDOX LS Colloid silica	30%	Sigma-Aldrich	SiO_2

Tetraethoxysilane	98%	Sigma-Aldrich	$Si(OC_2H_5)_4$
Hydrochloric acid	37%	Sigma-Aldrich	HCl
Nitric acid	69%	VWR Chemical	HNO_3
Acetic acid glacial	99.9%	VWR Chemical	CH_3COOH
Hydrofluoric acid	48%	VWR Chemical	HF
Chloroform	99.9%	Lachner	$CHCl_3$
Diethyl ether	99.9%	Lachner	$(C_2H_5)_2O$
Toluene	99.9%	VWR Chemical	$C_6H_5CH_3$
P-xylene	>99%	Sigma-Aldrich	$C_6H_4(CH_3)_2$
Methanol	99.9%	Lachner	CH_3OH
Ethanol Absolute		Penta	CH_3CH_2OH
1-Hexanol	98%	Sigma-Aldrich	$CH_3(CH_2)_5OH$
1-Decanol	99%	Sigma-Aldrich	$CH_3(CH_2)_9OH$
3,4-Dihydro-2H-pyran	99%	Sigma-Aldrich	C_5H_8O
Mesitylene	98%	Alfa Aesar	$C_6H_3(CH_3)_3$
Benzoyl chloride	99%	Sigma-Aldrich	C_6H_5COCl
Dodecane	99%	Sigma-Aldrich	$CH_3(CH_2)_{10}CH_3$
Acetonitrile-d_3	100%	Sigma-Aldrich	CD_3CN
Pyridine	Pure	Penta	C_5H_5N
Ambersep® 900(OH), ion exchange resin		Alfa Aesar	

3.2. Preparation of organic templates

6,10-dimethyl-5-azoniaspiro[4,5] decane hydroxide (DMAH) and 7-ethyl-6-azoniaspiro[5.5] undecane hydroxide (EAH) were templates for preparing germanosilicate **UTL** and Al containing **UTL** zeolites, respectively. They were prepared according to the methods reported in [97, 98]. For DMAH, firstly deionized water (140 g), NaOH (5.68 g), 1,4-dibromobutane (30.66 g) were successively added into a 1000 ml flask and stirred. After that, 2,6-

dimethylpiperidine (16.07 g) was added dropwise into the above mixture. They were stirred intensively overnight and until milk-like mixture was obtained. The mixture was cooled down by ice and then appropriate amount of sodium hydroxide was added under stirring. The addition of NaOH was finished until an oil phase started to form. Once the crystallization of oil phase was completed, the solid product was filtrated and then extracted by excess of chloroform. The solution was dehydrated by anhydrous sodium sulfate, after that the solution was partially evaporated. Finally, diethyl ether helped to precipitate the ammonium salt.

For 7-ethyl-6-azoniaspiro[5.5] undecane hydroxide (EAH), except of the replacement of the cyclic amine and bromo-derivative with 2-ethylpiperidine (16.07 g) and 1,5-dibromopentane (33.321 g), respectively, other reaction conditions were the same.

In addition, 7,11-dimethyl-6-azoniaspiro[5,6] undecane hydroxide was used as organic template for synthesizing germanosilicate **AFI**. The preparation procedure was similar to that for DMAH except that 1,4-dibromobutane was replaced by bromoderivative of 1,5-dibromopentane (32.65 g).

3.3. Synthesis of zeolite catalysts

Zeolite UTL.

Germanosilicate **UTL** zeolite was synthesized using DMAH as the template [97]. The reaction mixture was 0.8 SiO_2 : 0.4 GeO_2 : 0.4 DMAH : 30 H_2O. Al-UTL was prepared adopting EAH as template from the gel of 0.788 SiO_2 : 0.4 GeO_2 : 0.012 $AlO_{1.5}$: 0.4 EAH : 30 H_2O [99]. Typically, to obtain the hydroxide form of template, the bromide salt was ion-exchanged using anion exchange resin in the ratio of 8 mmol SDA/g resin. For the synthesis of germanosilicate **UTL**, firstly, Adding GeO_2 (0.84 g) into DMAH solution and stirring the mixture for 0.5 hour, GeO_2 was dissolved. Then, fumed silica (0.96 g) was added. Finally, the reaction mixture was charged into a 25 mL Teflon-lined stainless steel autoclave. Crystallization of zeolite was conducted at 175 °C for 7 days with agitation. For Al-UTL, firstly, Al(OH)$_3$ (0.02 g) was added into EAH solution and stirred for 0.5 h. Then, GeO_2 (0.84 g) and fumed silica (0.96 g) were added. The reaction mixture kept stirring to obtain a

homogeneous gel and was adjusted pH to 12. Al-UTL was crystallized with agitation at 175 °C for 22 days. Once crystallization was complete, solid outcomes were collected after filtration, thorough wash, and drying in an oven at 65 °C. To remove organic templates within zeolites, as-synthesized zeolites were calcined at 550 °C for 6 hours under air flow. The template-free **UTL** zeolites were used further as initial materials for synthesizing Al-IPC-n zeolites.

Zeolites Al-IPC-n.

Al-IPC-7: Al-IPC-7 was prepared by hydrolyzing the Al-UTL (1g) with 3.0 M Al(NO$_3$)$_3$ (100 mL) at 60 °C for 1 hour. Then, the mixture was filtrated and following dried.

Al-IPC-2: Al-IPC-2 was prepared by hydrolyzing the Al-UTL (1g) with 1.0 M Al(NO$_3$)$_3$ (100 mL) at room temperature (RT) for 1 hour. Then, the mixture was filtrated and following dried.

Al-IPC-6: Al-IPC-6 was prepared in a two-step procedure: germanosilicate **UTL** (Si/Ge = 2 in synthesis gel) (1g) was hydrolyzed in a mixture solution of 1.0 M acetic acid (150 ml) and 1.0 M Al(NO$_3$)$_3$ (100 mL) at 95 °C for 16 hours. Then, the collected solid after filtration and drying was treated with octylamine (50 g) at 60 °C for 16 hours.

Al-IPC-4: Al-IPC-4 was prepared in a two-step procedure: germanosilicate **UTL** (Si/Ge = 1.5 in synthesis gel) (1g) was hydrolyzed in a mixture solution of 1.0 M acetic acid (150 ml) and 1.0 M Al(NO$_3$)$_3$ (100 mL) at 95 °C for 16 hours. Then, the collected solid after filtration and drying was treated with octylamine (50 g) at 60 °C for 16 hours.

After alumination procedures, all IPC-n zeolites were thoroughly washed by very diluted HCl solution and water and were calcined at 550 °C for 6 hours prior other characterizations.

Zeolite AFI.

Ge-AFI. Germanosilicate zeolite with **AFI** topology (Ge-AFI) was prepared using 7, 11-dimethyl-6-azoniaspiro [5.6] undecane as structural-directing agent. The reaction mixture followed a molar ratio of x SiO$_2$: 0.24 GeO$_2$: 0.4 SDA : 30 H$_2$O (x = 0.9 and 0.96). Firstly, 7, 11-dimethyl-6-azoniaspiro [5.6] undecane hydroxide solution was prepared after ion-exchange of bromide-form SDA with resin. Germanium dioxide (1.26 or1.67 g) was added into the SDA solution and the mixture was stirred for 0.5 h. Then, fumed silica (2.88 g) was

added. Finally, reaction mixture was transferred into a 25 mL Teflon-lined stainless steel autoclave. Crystallization of zeolite was conducted with agitation at 175 °C for 7 days. Once the crystallization was complete, solid outcomes were collected after filtration, thorough wash and drying in an oven at 65 °C. To remove the SDA within zeolites, as-synthesized zeolites were calcined at 550 °C for 6 hours under the air flow.

Al-AFI. Ge-AFI zeolite (1 g) was added into 1.0 M $Al(NO_3)_3$ (100 ml), the suspension was stirred at 400 rpm at 80 °C for 48 hours. Solid product was referred to as Al-AFI.

deGe-Al-AFI. Ge-AFI zeolite (1 g) was first degermanated in 0.1 M HCl (100 ml) at 80 °C for 16 hours. Then, solid was separated and thoroughly washed by water to neutral. This intermediate was donated as deGe-AFI. Then the deGe-AFI was added into 1.0 M $Al(NO_3)_3$ (100 ml) for alumination, the suspension was stirred at 80 °C for 48 hours. The aluminated sample was noted as deGe-Al-AFI.

After alumination, all the samples were successive washed with 0.01 M HCl and water for several time and dried in an oven. Prior to further characterizations, all samples were calcined at 450 °C for 4 hours.

Zeolite MWW.

MCM-22. MCM-22 precursor (MCM-22P) with Si/Al of 15 in the synthesis gel followed molar ratio of reaction mixture：$2.5 Na_2O : Al_2O_3 : 30 SiO_2 : 10 HMI : 580 H_2O$ according to the procedures reported in [43]. It was synthesized using Ludox LS-30 (114.89 g), NaOH (50% in H_2O) (3.71 g), sodium aluminate (1.86 g), hexamethyleneimine (21.5 g). The gel was stirred intensively for 0.5 hour and transferred into a Teflon-lined stainless Parr reactor. Crystallization proceeded under agitation at 143 °C for 96 hours. Then the solid outcome was collected after filtration, thorough wash, and drying. The synthesis procedures of MCM-22P with Si/Al of 30 and 50 were similar to that for 15; only a proper amount of sodium aluminate was added.

MCM-36. MCM-36 was prepared by two-steps procedure: swelling and pillaring. MCM-22(P)(15) (5 g) was added to 25% C_{16}TMA-OH solution (100 ml). The resulted suspension was stirred at RT overnight. Swelling product (donated as MCM-22SW) was separated and

collected after centrifugation, wash and drying. After swelling, the weight of solid increased to 6.25 g. Pillaring was conducted with MCM-22SW (6.25 g) in TEOS (62.5 ml) firstly. The suspension was stirred at 85 °C for 24 hours. Solid product was separated by centrifugation and drying. After pillaring, the weight of the product increased to 8.05 g. Then, the dry powder was added into distilled water (800 ml) and stirred at RT for 24 h. Finally, the solid was obtained by filtration and drying.

MCM-56. MCM-56 was synthesized using Ultrasil silica (77.1 g), NaOH (50% in H_2O) (9.0 g), sodium aluminate (9.75 g), hexamethyleneimine (40.8 g) and water (396 g). The gel was stirred intensively for 0.5 hour and transferred into a Teflon-lined stainless steel autoclave. Crystallization proceeded under agitation at 143 °C for 33 hours. Then the solid outcome was separated and collected after filtration, wash and drying procedures.

Dealuminated MCM-22. 2.5 g MCM-22(50) was treated with 13 M HNO_3 solution (50 ml). The acid treatment was conducted at 80 °C for 4 hours. Then solid sample was recovered by filtration and washing with water to neutral and drying. The acid dealuminated MCM-22(50) was donated as MCM-22(50)-A.

Desilicated MCM-22. 1.0 g MCM-22(30) was added into 0.1 M NaOH (50 ml). Then, appropriate amount of piperidine was added. The amount of piperidine corresponded to 1.0 molar ratio relative to the SiO_2 in MCM-22(30). The desilication was conducted at 170 °C for 2 hours. Then solid sample was recovered by filtration and washing with water to neutral and drying. The base desilicated MCM-22(30) was donated as MCM-22(30)-B.

All as-synthesized **MWW**-type zeolites were calcined at 480 °C for 3 hours under nitrogen. Then calcination temperature increased to 540 °C and kept for 8 hours under air flow. In order to prepare the proton form **MWW** zeolites, calcined **MWW** zeolites were ion-exchanged four times with 1.0 M NH_4NO_3 (1 g zeolite per 100 ml solution), and calcined at 450 °C for 6 hours.

Co/MWW catalysts. 10% Co_3O_4 supported **MWW** catalysts were synthesized though incipient wetness impregnation of cobalt nitrate onto H-type **MWW** zeolites. Typically, 1 g of **MWW** zeolite was impregnated with 2 mL of cobalt nitrate aqueous solution (0.5717g

$Co(NO_3)_2 \cdot 6H_2O$). Then the suspension was dried at 80 °C. Finally, the dry powder was calcined at 400 °C for 3 hours.

Zeolite MFI.

Nanosized MFI. MFI zeolite with crystal size about 50 nm was prepared according to the reference [62]. The reaction mixture followed molar ratio of 1.0 SiO_2 : 0.45 TPAOH : 0.015 Na_2O: 0.003 Al_2O_3: 9 H_2O : 0.1 L-lysine. In a typical run, tetrapropylammonium hydroxide (40%, 2.288 g) was mixed with deionized water (1.62 g) at room temperature. Then, TEOS (2.083 g) was added under vigorously stirring for 6 h. Once the hydrolysis completed, sodium aluminate (0.006 g), sodium hydroxide (50%, 0.015 g) and L-Lysine (0.147 g) were added into the mixture. The gel was stirred at RT until appropriate water was remained and charged into a Teflon-lined stainless steel autoclave. Crystallization of zeolite was conducted initially at 80 °C for 48 hours and elevated the temperature to 170 °C for another 24 hours. As-synthesized solid was separated and purified by centrifugation with water and ethanol at 15000 rpm for 3 times, and then dried. Finally, the as-synthesized sample was calcined at 550 °C, 1 °C/min for 6 hours.

Silane modified MFI. The procedure of silane modification of nanosized **MFI** was performed as follows: 50 mg activated zeolite powder was suspended in acetone and then the suspension sonicated for 10 min. Then, in a ratio of 0.04 mmol silane/g zeolite, selected silane, triethoxyphenylsilane, ethoxydimethylphenylsilane, (4-biphenyl)triethoxysilane, or 3-(ethoxydimethylsilyl)propylamine, respectively, was added dropwise to the corresponding mixture under sonication. All the mixtures were further sonicated for 0.5 hour in ice bath. Once the reaction was completed, the samples were centrifuged and washed with acetone several times and dried at 60 °C overnight.

3.4. Characterization techniques

X-ray Diffraction. Structure and crystallinity of as-made, calcined and modified zeolites were evaluated by powder X-ray diffraction (XRD). The XRD measurements were performed on Bruker D8 Advance equipped with graphite monochromator and position sensitive

detector. The XRD measurements used CuKα radiation at 40 kV, 30 mA.

N₂ adsorption. Textural properties of calcined zeolites were assessed by N_2 adsorption at -196 °C. The measurements were performed on Micromeritics ASAP 2020. Except for silanes modified **MFI** samples, all the samples were degassed under vacuum at 250 °C for 4 hours. Silanes modified MFI samples were degassed at 150 °C.

Scanning Electron Microscopy. Morphological properties of zeolites were inspected by scanning electron microscopy (SEM) images. SEM measurements were performed on JEOL, JSM-5500LV microscope.

Transmission Electron Microcopy. TEM images and elements mapping were obtained from JEOL JEM2100 microscope.

Dynamic Light Scattering. Hydrodynamic diameters of nanosized **MFI** zeolites were estimated from dynamic light scattering (DLS) with scattering angle fixed at 173°. The DLS measurements were performed on Malvern Zetasizer Nano.

Inductively Coupled Plasma Optical Emission Spectroscopy. Chemical composition of zeolites is given by Inductively Coupled Plasma Optical Emission Spectroscopy (ICP-OES). The samples for ICP-OES were prepared by dissolving the zeolites in a mixture of acids (HF, HNO_3 and HCl). The ICP-OES measurements were performed on ThermoScientific iCAP 7000.

Solid State Nuclear Magnetic Resonance. Local coordinate state of Al and Si atom in zeolites were investigated by ^{27}Al and ^{29}Si solid nuclear magnetic resonance (NMR) at resonance frequencies of 99.30 and 130.24 MHz, respectively. ^{27}Al and ^{29}Si NMR chemical shifts were recorded using Agilent DD2 500WB spectrometer.

Fourier-Transform Infrared Spectroscopy. Type, concentration, strength and distribution of acid sites and nature of cobalt species on zeolites were assessed by FTIR adsorption of appropriate probes (d_3-acetonitrile (ACN), pyridine, 2,6-di-tert-butyl-pyridine (DTBPy), quinoline, CO etc.) using Nicolet 6700 FTIR with DTGS detector. Before the measurement, all the samples were prepared as self-supporting wafer and were outgassed at 450 °C overnight.

Diffuse Reflectance UV/Vis spectroscopy. DR-UV/Vis spectra of Co/MWW samples were recorded in the range from 175 to 800 nm. The DR UV-Vis measurements were performed on Cary 300 UV-Visible Spectrophotometer (Agilent Technologies).

Temperature Programmed Reduction. CO-TPR experiments were conducted at Université Lyon 1, IRCELYON. They were carried out under a gas flow of 3000 ppm CO balanced with He at 100 mL min^{-1}. In each test, samples were outgassed by He at 300 °C for 0.5 hour. Regarding the reduction process, temperature was increased from 50 °C to 750 °C with 5 °C/ min. The concentration of both CO and CO_2 were in-situ measured by Micro-GC (SRA % GC-R3000).

3.5. Catalytic tests

Tetrahydropyranylation of Alcohols. We performed the tetrahydropyranylation of alcohols over Al containing IPC zeolites in a Star-Fish workstation. This reaction took place in the two-neck flask at atmospheric pressure and at 60 °C, the temperature was monitored by thermocouple meter. All catalysts were activated in the oven at 450 °C for 90 minutes. During the experiment, 50 mg zeolite catalyst, 10 ml 3,4-dihydro-2H-pyran (as reactant and solvent) and 0.25 g methylene (as internal standard) were added into the flask, then once the temperature reached 60 °C, 4.5 mmol of appropriate alcohols (ethanol, 1-hexanol or 1-decanol) was added into the above mixture. Sample was taken out from the reaction mixture at planed time and was soon afterwards analyzed on Agilent 6859 gas chromatograph (GC) equipped with flame ionization detector (FID).

Ethanol Dehydration. Ethanol dehydration was performed by Shashikant Arun Kadam at J. Heyrovsky Institute of Physical Chemistry. This reaction took place in an IR-cell reactor [100] under atmospheric pressure and at 185 °C. All catalysts (about 20 mg) were firstly activated at 450 °C for 5 hours and then cooled down until 185 °C. Once the reaction temperature reached, the reactant was fed. Reaction products were in-situ inspected on Agilent 6850 gas chromatograph (GC) equipped with flame ionization detector (FID).

Toluene alkylation. Toluene alkylation with isopropyl alcohol experiments were performed

by Naděžda Žilková at J. Heyrovsky Institute of Physical Chemistry. This reaction took place in a fixed bed down-flow micro-reactor. at 250 °C under atmospheric pressure. All catalysts for toluene alkylation were firstly heated at 500 °C for 2 hours. During the experiment, toluene to isopropyl alcohol molar ratio (Tol/i-PrOH), was set to 9.6 in the feds to avoid a fast deactivation of catalysts. The weight hour space velocity was 10 h^{-1} based on toluene. The products were analyzed at planed time on Agilent 6890 gas chromatograph equipped with flame ionization detector (FID).

Catalytic total oxidation of toluene and propane. Catalytic total oxidation of toluene and propane were performed by Weidong Zhang at Université Lyon 1, IRCELYON. This reaction took place in a fixed-bed U-shape quartz reactor with inner diameter of 4 mm. K-type thermocouple was used to monitor the reaction temperature. Total flow rate was fixed at 100 ml/min. For toluene oxidation, the reactant gas was a mixture of synthetic air and 1000 ppm of toluene generated by bubbling synthetic air through the toluene saturator maintained at 5 °C. The products were analyzed online by a Rosemount Xtreme Gas Infrared Analyzer (Emerson Electric Co.). For propane oxidation, the feed gas was composed of 0.1 vol.% C_3H_8 and 21 vol.% O_2 balanced with He. The flow gas composition was monitored using a micro gas chromatograph (SRA % GC-R3000) equipped with a thermal conductivity detector. Reaction temperature program was set as follows: First, ambient temperature to 350 °C at 10 °C/min, stayed 350 °C for 2 hours, then decreased to 150 °C at a rate of 2 °C/min. The light-off profiles obtained upon cooling stage (from 350 °C to 150 °C) was used to compare the catalytic performance. To avoid overestimation of the catalytic performance due to the adsorption of reactants by high-surface area zeolites, CO_2 yield instead of hydrocarbons conversion was applied to establish the light-off curves.

Acylation of p-xylene. We performed acylation of p-xylene over **MFI** nanosized zeolites in a Star-Fish workstation. This reaction took place in the two-neck flask under atmospheric pressure at 130 °C. The temperature was monitored by thermocouple meter. Before the catalytic tests, all the catalysts were heated at 150 °C for 90 minutes. Then, 50 mg zeolite catalyst, 5 ml p-xylene (as reactant and solvent), and 0.5 g dodecane (as internal standard)

were added into reactor, then once the temperature reached 130 °C, 5 mmol of butyryl chloride (acylation agent) was added into the above mixture. Sample was taken out from the reaction mixture at planed time and was soon afterwards analyzed on Agilent 6850 gas chromatograph (GC) equipped with flame ionization detector (FID) detector.

4. Results and discussion

4.1. UTL-derived isoreticular zeolites

4.1.1. Synthesis of UTL-derived isoreticular zeolites

UTL-derived isoreticular zeolites possess similar crystalline layers inherited from parent **UTL** crystals along ab plane, but have distinct interlayer linkers along c axis. According to the variation of interlayer connections, this series of UTL-derived isoreticular zeolites includes IPC-2 (**OKO**), IPC-4 (**PCR**), IPC-6 (***PCS**), and IPC-7. UTL-derived IPC zeolites cover a wide range of pore sizes, from 14-MR in IPC-7 to 8-MR in IPC-4 (see **Table 4-1**), which makes isoreticular zeolites ideal models to probe the pore size effect. However, due to the complexity of synthesis parameters, the IPC-n zeolites with similar concentration of acid sites have never been achieved. In our work, Al-IPC-n zeolites were synthesized by combining the ADOR and alumination procedures. To prepare these materials, firstly, **UTL**-type zeolites with different chemical compositions were hydrothermally synthesized to provide the starting materials (that are, germanosilicate Ge-UTL and Al-containing **UTL**, Al-UTL). Then, both **UTL** zeolites were treated with aluminum nitrate solutions under optimized conditions, including the concentration of aqueous solution, temperature and time. As a result, Al-IPC-7 and Al-IPC-2 zeolites can be prepared by treating Al-UTL for 1 hour while using different $Al(NO_3)_3$ concentration and temperature. In contrast, Al-IPC-6 and Al-IPC-4 could only be prepared from Ge-UTL, which may be the presence of Al in D4R units of **UTL** preventing complete hydrolysis of **UTL**. Therefore, in order to produce a family of isoreticular zeolites with comparable Al content, it is crucial to choose suitable **UTL** zeolites and alumination conditions.

Table 4-1. Structure features of **UTL** and IPC-n zeolites.

Zeolite		Interlayer link	Channel dimension	Pore size			
IM-12	**UTL**	D4R	2D	14 R	12 R		
IPC-7	-	D4R, S4R	2D	14 R	12 R	12 R	10 R
IPC-2	**OKO**	S4R	2D			12 R	10 R
IPC-6	***PCS**	S4R, oxygen	2D		12 R	10 R	10 R 8 R
IPC-4	**PCR**	oxygen	2D				10 R 8 R

To identify the structural and textural properties of isoreticular zeolites, XRD, nitrogen adsorption and SEM characterizations were used. As shown in **Figure 4-1** of XRD pattens, Al-containing IPC zeolites possessed high crystallinity without amorphous and impurity phases. Their structures were analogous to siliceous IPC-n zeolites reported in the literatures [33, 35]. In addition, **UTL** and IPC-n showed similar positions of some diffraction peaks (e.g. 12.7° 2θ, 22.9° 2θ etc.), indicating that they have similar layers features. However, their main peaks, (200), gradually shifted to higher angles following an order: IPC-4 (9.5° 2θ) > IPC-6 (8.8° 2θ) > IPC-2 (7.6° 2θ) > IPC-7 (7.1° 2θ) > **UTL** (6.4° 2θ), which corresponds to their decreased interlayer d-spacing from **UTL** to IPC-4.
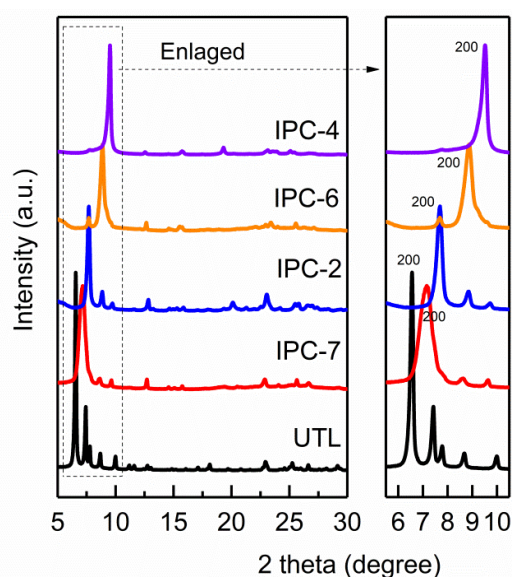
Figure 4-1. XRD patterns of Al-UTL and Al-IPC-n zeolite.

In addition, Al-UTL and all the Al-IPC-n samples showed typical type I nitrogen physisorption isotherms without hysteresis loops (**Figure 4-2**), evidencing that they are purely microporous zeolites. Moreover, their micropore volume (cm^3/g) declined in a sequence of 0.23 for **UTL** > 0.19 for IPC-7 > 0.13 for IPC-2 > 0.10 for IPC-6 > 0.08 for IPC-4 (**Table 4-2**), which agrees with the gradual decrease in the interlayer spacing and thus the pore size. Therefore, XRD and N$_2$ adsorption results confirmed that the isoreticular zeolites were synthesized successfully.
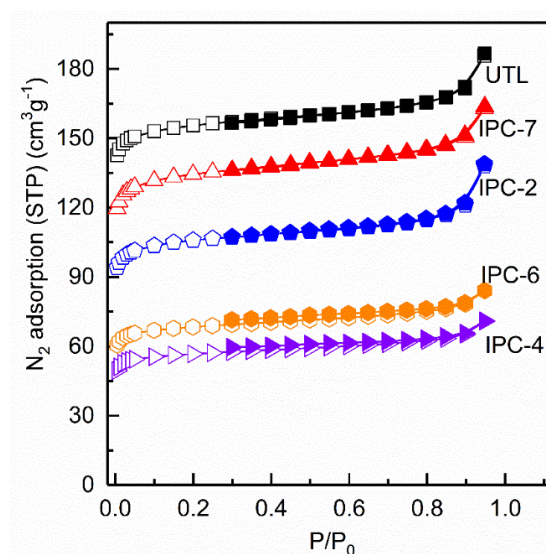

Figure 4-2. N$_2$ physisorption isotherms of calcined isoreticular zeolites at 77 K.

Table 4-2. Textural and acidic properties of isoreticular zeolites.

	V_{tot}[a]	V_{micro}[a]	S_{BET}[a]	c_B[b]	c_L[b]	c_{acid}[b]	Si/Al[c]
Al-UTL	0.289	0.231	566	0.04	0.06	0.10	64.6
Al-IPC-7	0.263	0.194	485	0.15	0.24	0.39	20.1
Al-IPC-2	0.191	0.128	325	0.17	0.20	0.37	26.2
Al-IPC-6	0.130	0.099	249	0.14	0.23	0.37	24.9
Al-IPC-4	0.110	0.082	207	0.19	0.21	0.40	20.5

[a] determined by N$_2$ adsorption. [b] given by FTIR after adsorption of ACN. $c_{acid} = c_B + c_L$. [c] Si/Al was given by ICP-OES. Units of each column: V_{tot} (cm^3/g), V_{micro} (cm^3/g), S_{BET} (m^2/g), c_B (mmol/g), c_L (mmol/g), c_{acid} (mmol/g).

Furthermore, SEM images revealed the morphology and crystal size of initial **UTL** and final isoreticular zeolites. **Figure 4-3** shows that the Al- and Ge-UTL have 2-4 μm crystals with plate-like morphology. Similarly, after the structural transformations, IPC-n zeolites inherited the morphology and crystal size of initial **UTL**, which suggested that the applied alumination treatments only caused the local structural transformation rather than affected the overall morphology of zeolite crystals.
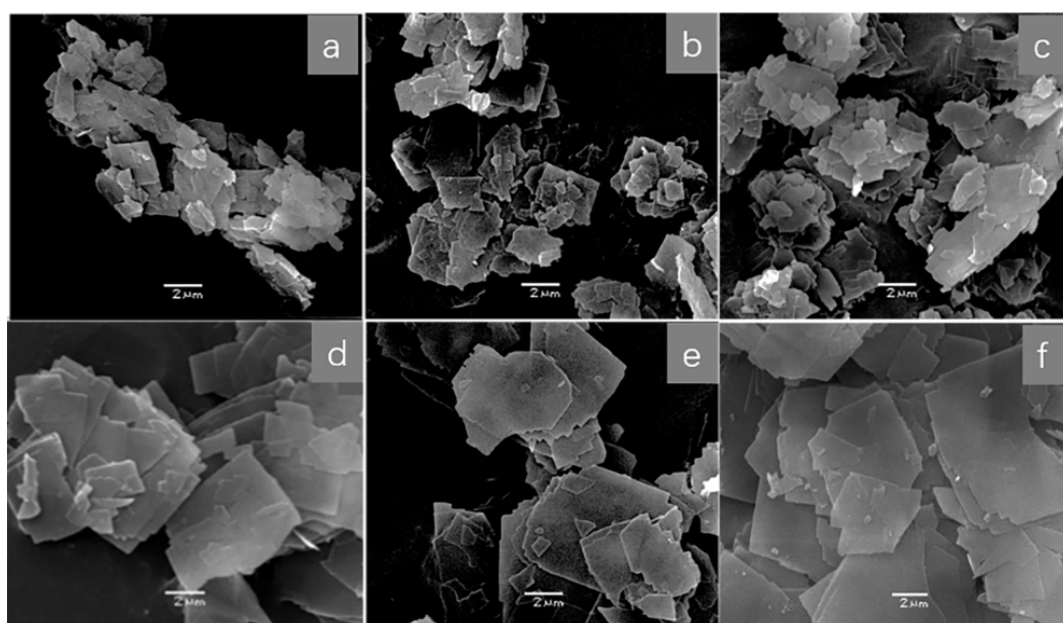

Figure 4-3. Scanning electron microscopy images of **UTL** and Al-IPC-n materials (a) Al-UTL, (b) Al-IPC-7, (c) Al-IPC-2, (d) Ge-UTL, (e) Al-IPC-6, (f) Al-IPC-4.

4.1.2. Characterization of Al^{3+} incorporation into isoreticular zeolites frameworks

To verify that the Al ions had been inserted as four-coordination in isoreticular zeolites frameworks, ^{27}Al NMR measurements were performed. In the spectra (**Figure 4-4**), all the Al-IPC-n zeolites showed dominating bands centered around 55 ppm and relatively small bands around 0 ppm. The formers were commonly allocated to tetrahedral Al on zeolite frameworks, whereas the latter were due to the extra-framework Al [101]. Therefore, ^{27}Al NMR confirmed that the majority of Al ions were introduced onto the framework positions. In addition, compared to other IPC-n (n= 7, 2, 6) materials, IPC-4 contained an apparently higher fraction

of extra-framework Al. Considering that IPC-4 structure is constructed by the direct connecting of IPC-1P layers, the higher extra-framework Al extent in IPC-4 suggests that it is more difficult to incorporate Al into the crystalline layers.
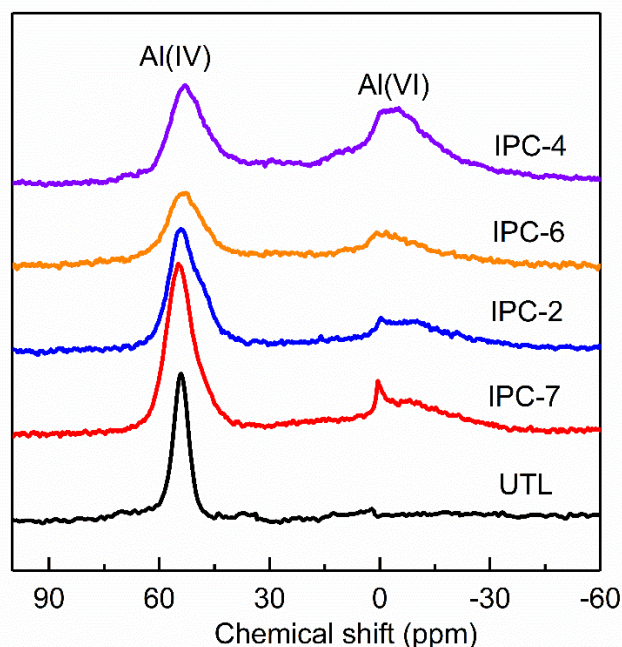

Figure 4-4. ^{27}Al NMR spectra of isoreticular zeolites.

In addition, the successful incorporation of Al ions into the frameworks of isoreticular zeolites was also confirmed by FTIR adsorption of d$_3$-acetonitrile (ACN). **Figure 4-5** shows FTIR spectra of Al-UTL and Al-IPC-n zeolites before and after ACN adsorption. Firstly, in the hydroxyl region of FTIR spectra, before ACN adsorption, all the spectra exhibited two bands (~3745 and 3620 cm^{-1}), which are corresponded to Si-OH and Si-OH-Al groups, respectively [102]. However, after ACN uptake, the ~ 3620 cm^{-1} bands disappeared and two additional bands around 2300 and 2330 cm^{-1} appeared for all the samples, indicating (i) ACN probes could access to all Si-OH-Al sites and cause the disappearance of ~ 3620 cm^{-1} bands ; (ii) these two appeared bands are associated with the interaction between ACN molecules and Brønsted/Lewis acid sites [103]. Therefore, these FTIR spectra verified that Al ions were incorporated into zeolite frameworks.
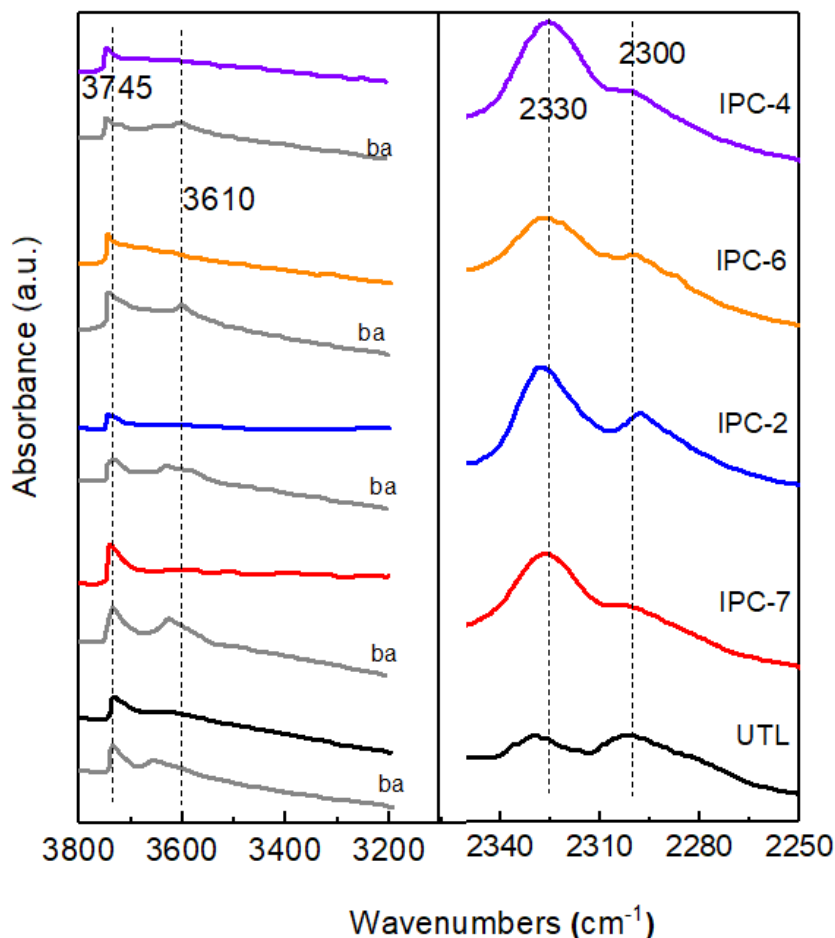
Figure 4-5. FTIR adsorption of d_3-acetonitrile spectra Al-UTL and Al-IPC-n materials. "ba" means before adsorption.

Furthermore, by analyzing the FTIR data, all the IPC-n samples had similar total acid sites concentration (~ 0.4 mmol/g), which agrees with the comparable Si/Al ratio of obtained isoreticular zeolites (Si/Al ~ 20) (**Table 4-2**). Given the distinct pore sizes among isoreticular zeolites, their locations of acid sites may differ. Based on this assumption, we developed a two-step adsorption with FTIR method to differentiate the locations of acid sites. In this method, quinoline and ACN with different kinetic diameters were sequentially adsorbed on zeolites, which distinguished the "internal" and "external" acid sites. More detailed, quinoline has a kinetic diameter of ~ 7.0 Å thus it could detect the acid sites located in large pores (>12 ring, 7.1 × 9.5 Å) and on external surfaces, which are defined as "external", while the other channels (≤12 ring) which accommodate "internal" acid sites are inaccessible for quinoline

(**Scheme 4-1**). In order to analyze the acid sites distribution, FTIR spectra for activated Al-IPC-n after ACN adsorption and those with preadsorption of quinoline and then ACN were collected and compared. ACN (~ 4.0 Å) with smaller kinetic diameter could access all acid sites and thus determines the total acid sites concentration. In contrast, quinoline preadsorption took up the "external" acid sites, then the following ACN molecules could only adsorbed at "internal" acid sites. Thus, comparing total acid sites concentration by ACN and the remaining acid sites accessible for ACN after quinoline preadsorption allowed to assess the acid sites distribution in isoreticular zeolites. **Figure 4-6** shows the acid sites distribution among IPC-n zeolites. It is observed that both "external" Brønsted and Lewis acid sites concentrations decrease was in line with zeolite pore sizes, that was, 35% (IPC-7) > 29% (IPC-2) >25% (IPC-6) > 21% (IPC-4) of total acid sites were located at the "external" positions.
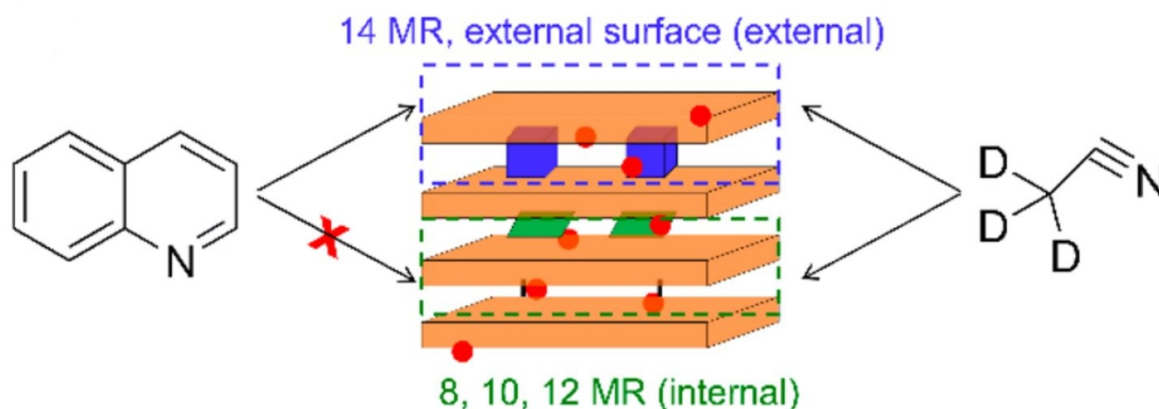
Scheme 4-1. Schematic description of acid sites locations recognized by ACN and quinoline probe molecules.
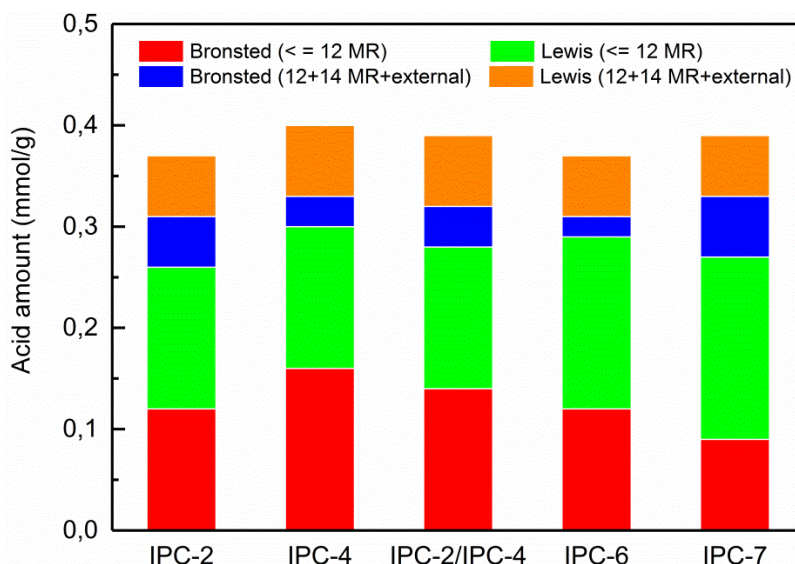
Figure 4-6. The acid sites locations of isoreticular zeolites.

### 4.1.3. Catalytic performance of isoreticular zeolite

4.1.3.1. Ethanol Dehydration

By combining the ADOR and Al isomorphous substitution methods, a group of isoreticular Al-IPC-n zeolites were synthesized. They possessed similar morphology, Al content and concentration of acid sites but continually tunable pore size, which provided a set of fairy ideal model catalysts to study the pore size effect on catalytic performance.

Alcohols (methanol/ethanol) dehydration is frequently used to investigate structure-property relationships and is one of the model reactions studying the impacts of acidity and confinement of catalyst on the rate of catalyzed reactions [104, 105]. In this aspect, ethanol dehydration can be catalyzed by Brønsted acid to produce ethylene or diethyl ether (DEE) (**Scheme 4-2**) [106]. In our work, Al-IPC-n zeolites were evaluated in the ethanol dehydration at 185 °C and ambient pressure while varied ethanol partial pressure in the range of 0-0.1 bar. **Figure 4-7** shows the ethanol dehydration reaction rate to form DEE (R_{DEE}) and ethylene ($R_{Ethylene}$) with increasing ethanol partial pressure P_{EtOH}. In the entire range of partial pressure of ethanol, the R_{DEE} over Al-IPC-n zeolites was much higher than $R_{Ethylene}$, which suggests that the ethanol dehydration over isoreticular zeolites followed the associative dehydration

mechanism [107] and diethyl ether was the main product. In the associative ethanol dehydration mechanism (**Scheme 4-2**), at first, an ethanol molecule adsorbed at Brønsted acid site forming ethanol monomer species. Then, another ethanol molecule adsorbed at the same site, producing ethanol dimer. After activating the ethanol dimer, an intermediate state (co-adsorbed state) formed. Finally, the co-adsorbed state decomposed into DEE and water [108]. In **Figure 4-7(a)**, as the ethanol partial pressure increased, the R_{DEE} firstly showed a liner increase at the lower ethanol partial pressure then an asymptotic increase at higher ethanol partial pressure, which followed the first-order and zero-order kinetics, respectively [108]. In addition, the dehydration turnover rate of DEE formation over Al-IPC-n zeolites followed the order of IPC-7 > IPC-2 > IPC-6 ≈ IPC-4. On the other hand, regarding the rate of ethylene formation (**Figure 4-7(b)**), as the P_{EtOH} increase, the $R_{ethylene}$ over IPC-7 and IPC-2 zeolites firstly increased in the range of 0 to 10 mbar but then decreased above 10 mbar because the formation of ethanol dimers prevented the ethylene synthesis at high pressures. Very similar phenomenon was observed in other large pore zeolites [108]. In contrast, when the P_{EtOH} > 10 mbar, the $R_{ethylene}$ over IPC-6/IPC-4 zeolites remained stable, which could be interpreted that both IPC-6 and IPC-4 have smaller pore size than IPC-7 and IPC-2, therefore, the ethanol dimers formation may be limited in their channels, even though higher ethanol partial pressure was applied.
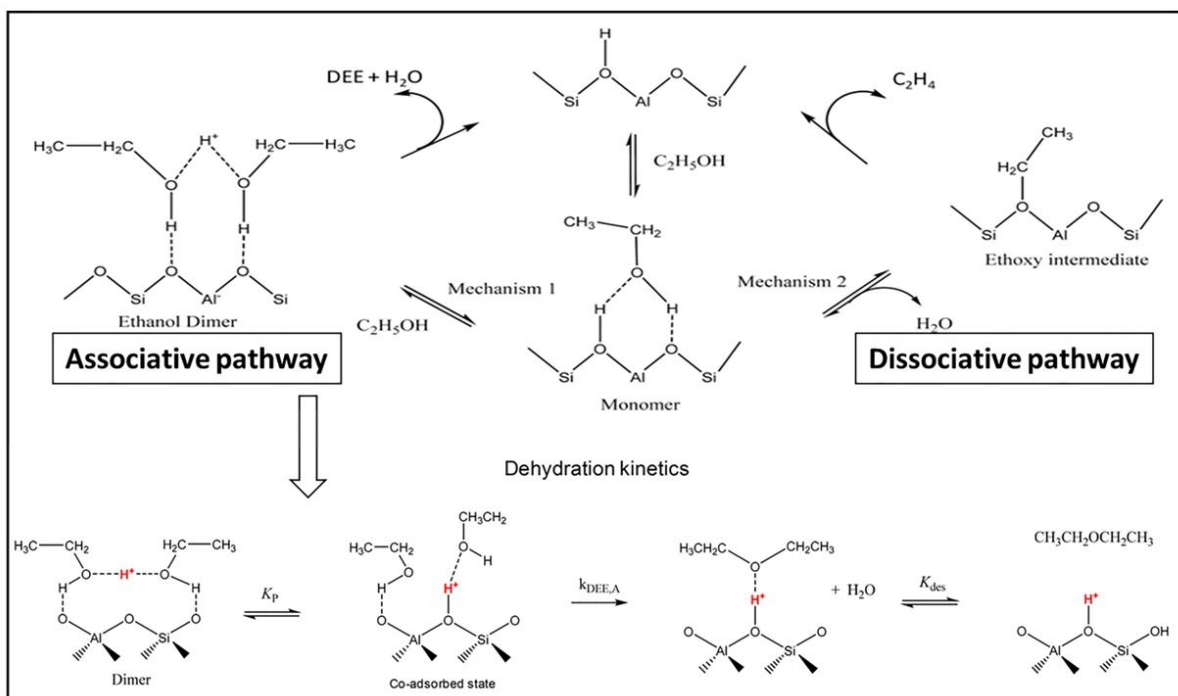
Scheme 4-2. Schematic mechanism of the ethanol dehydration pathway [102].
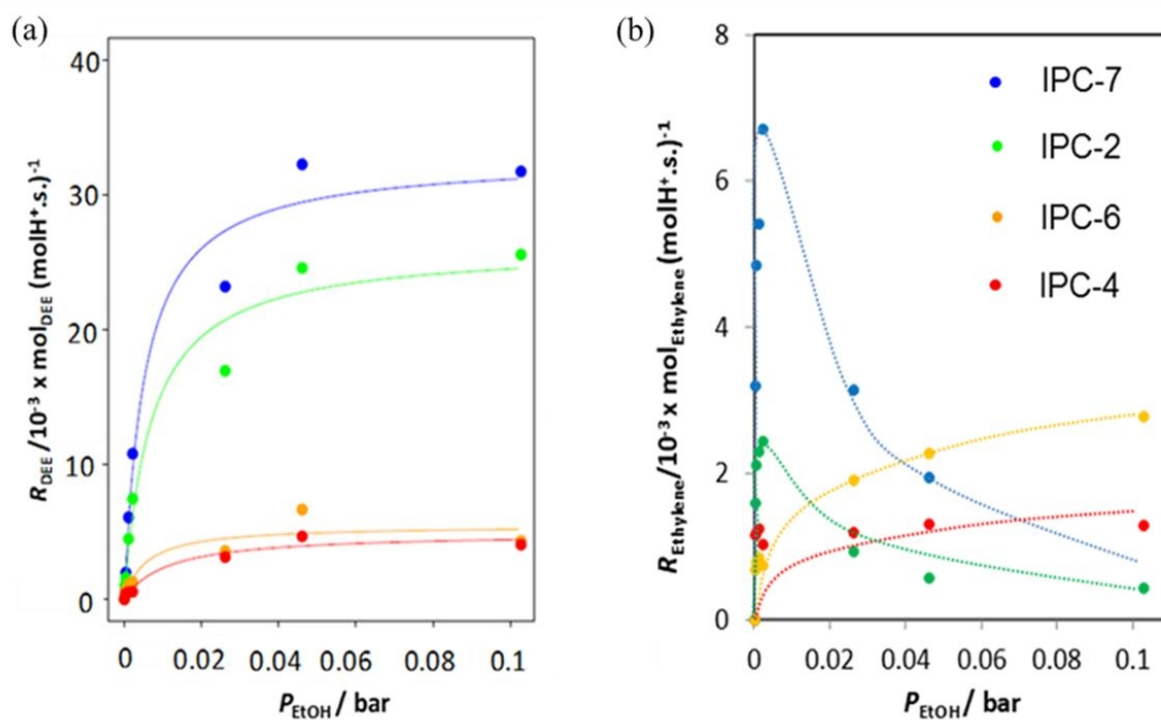
Figure 4-7. The turn-over rate of R_{DEE} (a) and $R_{Ethylene}$ (b) dependent of ethanol partial pressure (P_{EtOH}) over Al-IPC-n zeolites.

Following the associative ethanol dehydration mechanism in **scheme 4-2** and the R_{DEE} dependent of ethanol partial pressure in the literatures [108], a reaction rate expression for ethanol dehydration can be expressed as **equation 4-1**:

$$R_{DEE} = \frac{k_{DEE}\ K_P K_D P_{EtOH}}{1 + K_D P_{EtOH}}$$

(Equation 4-1)

In this equation, k_{DEE} stands for rate constant of ethanol dehydration forming diethyl ether, K_P and K_D are adsorption equilibrium constants for co-adsorbed states and ethanol dimers, respectively. P_{EtOH} is the ethanol partial pressure.

In addition, based on the method established by Carr et. al [109], **equation 4-1** could be modified to:

$$R_{DEE} = \frac{k_{first} P_{EtOH}}{1 + \frac{k_{first}}{k_{zero}} P_{EtOH}}$$

(Equation 4-2)

in **Equation 4-2**,

$$k_{first} = k_{DEE}\ K_P K_D$$

$$k_{zero} = k_{DEE}\ K_P$$

(Equation 4-3)

Where, k_{first} and k_{zero} are the apparent first-order and zero-order rate constants, respectively. The activation energy associated with k_{first} manifests energy difference between the co-adsorbed state and ethanol monomer [108]. Because these two species possess distinct charge distributions and molecular sizes, the first-order kinetic constant should be sensitive to the local environment, e.g. acid strength and pore size [109, 110]. In contrast, the activation energy associated with k_{zero} indicates the energy similarity between the same co-adsorbed state but related to the ethanol dimer [108]. Since the co-adsorbed state and ethanol dimer have

comparable molecular sizes, the difference of k_{zero} among zeolites with different pore size is expected to be insignificant.

**Figure 4-8** shows the rate constants k_{first} and k_{zero} of ethanol dehydration over Al-IPC-n materials. All the Al-IPC-n zeolite showed similar k_{zero}, while the k_{first} follows the order of IPC-7 > IPC-2 > IPC-6 > IPC-4, which is consistent of decrease in pore size. These results verified the above analysis. The dehydration first-order rate constant dependent of the pore size also observed in zeolites catalyzing the methanol dehydration, in which the zeolite catalysts with broad variation of pore sizes while comparable acid strength [110]. In addition, compared to IPC-7/IPC-2, smaller k_{first} and k_{zero} were observed over IPC-4/IPC-6, indicating the ethanol dimer and then the co-adsorbed state were more difficult to form in IPC-4 and IPC-6. Therefore, the k_{first} and k_{zero} of ethanol dehydration over Al-IPC-n suggested that larger pores (14 and 12 MR) in IPC-7 and IPC-2 zeolites could accommodate the ethanol dimer efficiently, while the smaller pore (10 and 8 MR) in IPC-6/IPC-4 lead to more limitations for formation of ethanol dimer but favor formation of ethoxide species [100, 102]. Furthermore, as shown in **Figure 4-6**, larger fraction of "external" acid sites was probed in IPC-2 than IPC-6, which may explain the lager k_{first} of IPC-2 than IPC-6 zeolite.
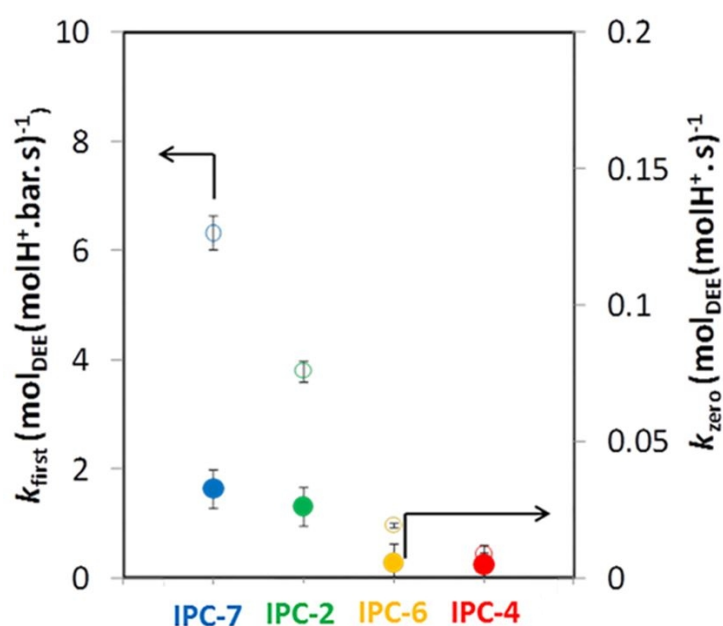
**Figure 4-8.** The rate constants k_{first} and k_{zero} of ethanol dehydration over Al-IPC-n zeolites.

4.1.3.2. Tetrahydropyranylation of Alcohols

In addition, the pore size-activity relationship of isoreticular zeolites was studied in liquid-phase tetrahydropyranylation of alcohols. Over acid catalysts, tetrahydropyranylation of organic compounds with 3,4-dihydro-2H-pyran (DHP) can produce tetrahydropyranyl ethers (**Scheme 4-3**). It is known that both Brønsted and Lewis sites could act as active centers for tetrahydropyranylation reaction [111]. In our work, Al-IPC-n zeolites possess similar concentration of acid sites, therefore their pore size effect on catalytic performance could be rationally compared. The catalytic activity of Al-IPC-n zeolites is shown in **Figure 4-9**, in terms of alcohols conversion in tetrahydropyranylation reaction. Firstly, when ethanol was used as reactant, all Al-IPC-n catalysts exhibited a complete conversion of ethanol to tetrahydropyranyl ether after 24 hours, indicating that this small reactant could be converted over all the Al-IPC-n zeolites without obvious diffusion restrictions. Then, increasing the alcohol size, significant activity differences in the tetrahydropyranylation of 1-hexanol over IPC-n zeolites was observed. The conversion of 1-hexanol after 24 hours followed an order of IPC-7 (96 %) > IPC-2 (87%) > IPC-6 (44%) > IPC-4 (36%). Furthermore, the conversions of 1-decanol were lower than 1-hexanol over all the Al-IPC-n zeolites. The conversions of 1-decanol followed the same trend of 1-hexanol and IPC-7 reached the highest conversion (78%). Considering that IPC-7 has the highest BET surface and pore volume and concentration of external acid sites among the Al-IPC-n zeolites, there is less diffusion limitation and better accessibility of the bulkier alcohol reactants, therefore, IPC-7 showed higher catalytic activity than other IPC zeolites. Overall, based on alcohols (1-hexanol or 1-decanol) conversion, the catalytic activity over Al-IPC-n catalysts was consistent with the decrease in their pore size following a sequence of IPC-7 > IPC-2 > IPC-6 > IPC-4. Therefore, tetrahydropyranylation reaction over Al-IPC-n zeolites demonstrates a unique example in which the pore size effect of zeolite on catalytic activity can be studied solely.
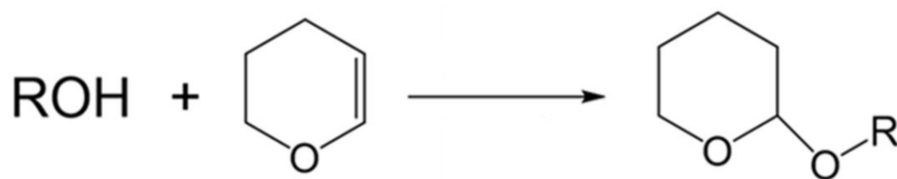
Scheme 4-3. Scheme of tetrahydropyranylation of alcohols with3, 4-Dihydro-2H-pyran (DHP).
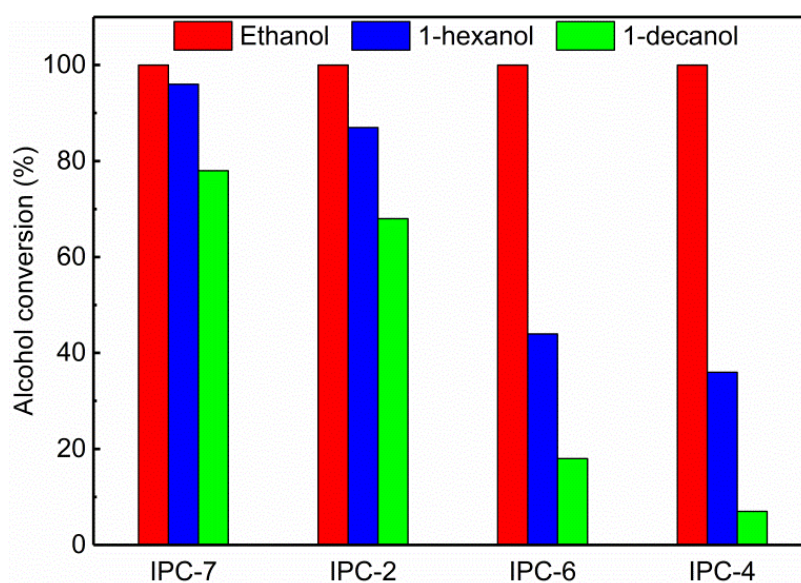
Figure 4-9. Catalytic performance of tetrahydropyranylation of alcohols over Al-IPC-n materials. Reaction conditions: Al-IPC-n catalyst (50 mg); alcohol (4.5 mmol); DHP (5.0 ml); mesitylene (0.25 g); 60 °C; 24 hours.

Furthermore, the topological structure of IPC-6 could be viewed combining IPC-2 with IPC-4. In the average structure of IPC-6, approximate 50% of the layered are connected by S4Rs and 50% by oxygen bonds (**Scheme 4-4**) [34]. Given the structural similarity among three zeolites, it is interesting to study the acid sites locations effect on the catalytic performance over zeolites with similar structures. In our work, an IPC-2/IPC-4 catalyst was prepared by physically mixing IPC-2 and IPC-4 in a weight ratio of 0.4 to 0.6, allowing to reach the textural properties and total acid site concentration practically identical to those of IPC-6 (**Table 4-3**).

Scheme 4-4. The structural relationship between IPC-6, IPC-2 and IPC-4.

Table 4-3. Textural properties and acidity of IPC-2/IPC-4 composite (40%/60% wt./wt.) and IPC-6 materials.

	S_{BET}	V_{mic}	c_{tot}
IPC-2/IPC-4	254	0.100	0.39
IPC-6	249	0.099	0.37

The unit of each column are (S_{BET}) m^2/g; (V_{mic}) cm^3/g, (c_{tol}) mmol/g.

The catalytic activity over IPC-2/IPC-4 and IPC-6 catalysts were compared in tetrahydropyranylation of different alcohols (**Figure 4-10**). Firstly, both catalysts showed very similar ethanol conversion after 6 hours (~ 90%). While for the bulkier reactants (1-hexanol and 1-decanol), higher alcohol conversions were reached over IPC-2/IPC-4 catalyst than IPC-6. Considering that both catalysts had similar morphology, microporosity and amount of acid sites, their distinct catalytic behaviors could reasonably account for location of active acid sites. The location of acid sites within IPC-2/IPC-4 and IPC-6 was assessed by FTIR with ACN and quinoline. The FTIR results showed that IPC-2/IPC-4 catalyst possesses larger fraction of "external" acid sites than IPC-6 catalyst (30% *vs.* 25%) (**Figure 4-6**), which explained the higher catalytic activity over IPC-2/IPC-4 catalyst.
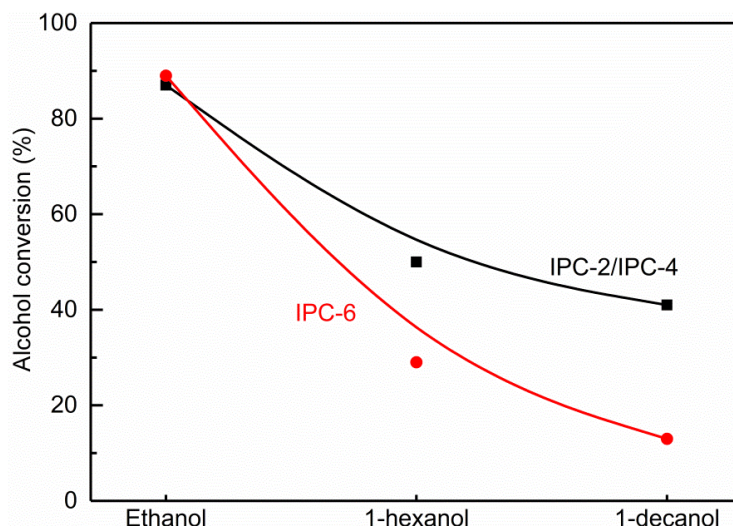
Figure 4-10. Catalytic performance of IPC-2/IPC-4 composite catalyst and IPC-6 catalyst in tetrahydropyranylation of alcohols. Reaction conditions: zeolite catalyst (50 mg); alcohol (4.5 mmol); DHP (5.0 ml); mesitylene (0.25 g); 60 °C, 6 hours.

## 4.2. Isomorphous substitution in germanosilicates for preparation of Al-enriched zeolites

4.2.1. Synthesis of Ge-AFI and Al-AFI zeolites

Zeolites with wide range of chemical compositions, for instance Si/Al, are desirable for different catalytic applications. High silica and Al-rich zeolites attract more and more attentions because of their optimized acidity, hydrophobicity and stability which lead to superior catalytic performances [112,113]. In addition, Al-rich zeolites with low Si/Al could provide large amount of acid sites as well as exchangeable cations, consequently they play important roles in catalysis, adsorption and ion exchange applications [113].

AFI zeolite has 1D parallel 12 MR pore system and finds applications in shape selective catalysis [114] and gas separation [115]. However, the Al-enriched **AFI** zeolites (Si/Al < 60), have never been achieved through both direct hydrothermal synthesis and post-synthesis. In our work, to prepare Al-enriched **AFI** zeolites, a germanosilicate with **AFI** topology (Ge-AFI, Si/Ge = 8.1) was firstly synthesized using 7, 11-dimethyl-6-azoniaspiro [5.6] undecane as structure directing agent. Taking advantage of the chemically lability of Ge in

germanosilicates, the Al-enriched **AFI** were synthesized by post-synthetic alumination of the Ge-AFI with aluminum nitrate solutions with one-step alumination (Al-AFI) or sequential degermanation-alumination two-step route (deGe-Al-AFI).

To characterize structure and crystallinity of the initial Ge-AFI, intermediate and final aluminated **AFI** materials, XRD was used firstly. The XRD patterns in **Figure 4-11** showed that all **AFI** samples had pure **AFI** phases with high crystallinity, indicating both alumination routes did not affect the **AFI** structure.
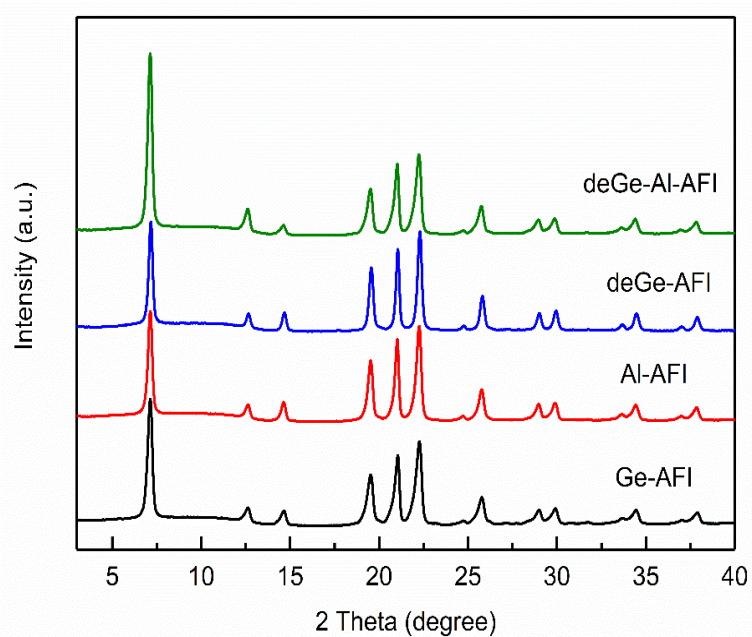
Figure 4-11. X-ray patterns of **AFI** materials.

In addition, SEM images in **Figure 4-12** showed that the calcined Ge-AFI had 3 μm needle like crystals. Compared with large hexagonal borosilicate **AFI** reported in literatures [116, 117], Ge-AFI may provide more efficient matter diffusion for post-synthetic Al introduction. As a result, the final Al-enriched **AFI** samples maintain the needle-like morphology similar to the parent Ge-AFI crystals.
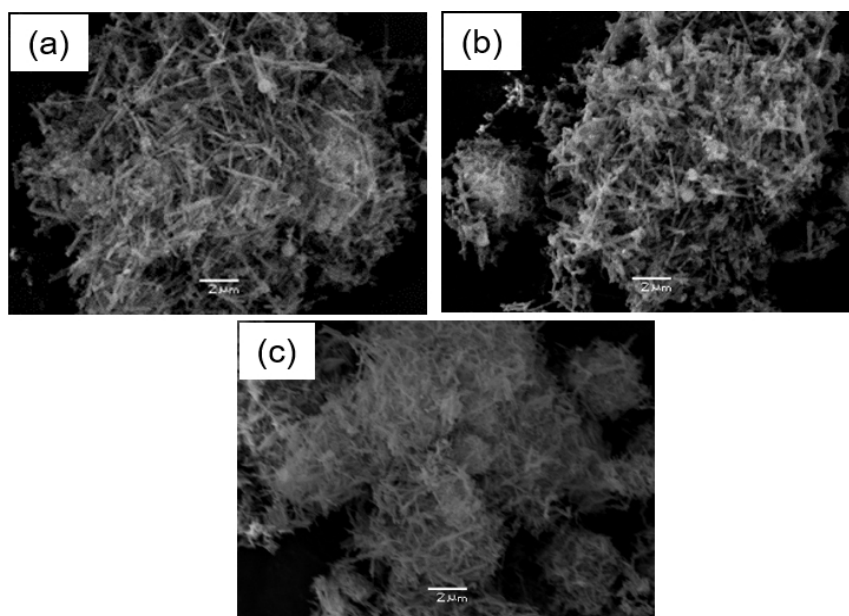
Figure 4-12. Scanning electron microscopy images of **AFI** materials. (a) Ge-AFI, (b) deGe-Al-AFI, (c) Al-AFI.

The acid-assisted degermanation is crucial for the preparation of final aluminated **AFI** zeolite maintaining the porosity, which has been shown in the alumination of other germanosilicates, e.g., **UTL**, **ITH** and **IWW** [92]. As shown in **Figure 4-13**, Ge-AFI, deGe-AFI and two Al-AFI samples exhibited I-type nitrogen adsorption/desorption isotherms, indicating that they are typical microporous materials. In addition, an increased N_2 uptake was observed at high relative pressure for all the samples, which may be caused by the disorder aggregates of small needle-like crystallites forming the interparticle voids. The initial Ge-AFI zeolite showed BET area of 306 m^2/g. And when Ge-AFI was degermanated with 0.1 M HCl solution, the resulted deGe-AFI showed BET area of 330 m^2/g, suggesting that a partial removal of framework atoms (in particular Ge) resulted in more open structure. Furthermore, Ge leaching was proved by ICP-OES results (Si/Ge changed from 8.1 in Ge-AFI to 22 in deGe-AFI). The final alumination treatment further increased the zeolite surface area, as confirmed by a higher BET area of deGe-Al-AFI (356 m^2/g) than Ge-AFI and deGe-AFI. In contrast, the direct one-step alumination resulted in deteriorated porosity of Ge-AFI: surface area of resulting Al-AFI was only 128 m^2/g (**Table 4-4**). Therefore, the N_2 adsorption results indicated that the HCl

treatment before Al incorporation is beneficial not only to remove Ge atoms from zeolite frameworks and then heal the defective vacancies by Al atoms, but also to inhibit accumulation of solid debris which may block channels of aluminated materials.
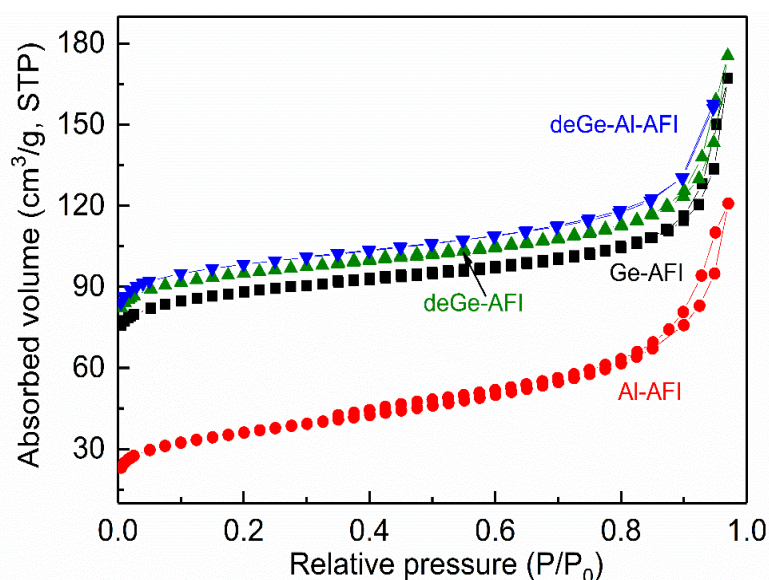
Figure 4-13. N_2 sorption isotherms of the calcined **AFI** materials.

Table 4-4. Chemical analysis and textural properties of **AFI** materials.

	channel dimension	Si/Ge[a]	Si/Al[a]	S_{BET}[b]	V_{tot}[b]	V_{micro}[b]
Ge-AFI		8.1	-	306	0.26	0.10
Al-AFI		25	53	128	0.19	0.02
deGe-AFI	1D	22	-	330	0.27	0.11
deGe-Al-AFI		38	29	356	0.24	0.12
MTW	1D	-	52	296	0.22	0.10
IPC-2	2D	-	48	390	0.20	0.16
Beta	3D	-	23	619	0.35	0.25

[a] Chemical composition was given by ICP/OES. [b] S_{BET} (m^2/g), V_{tol} (cm^3/g) and V_{micro} (cm^3/g) were estimated from N_2 physisorption.

4.2.2. Characterization of Al^{3+} in the Al-enriched AFI frameworks

In order to verify that Al^{3+} had been inserted into **AFI** zeolite framework positions, ^{27}Al NMR spectroscopy was used. In **Figure 4-14**, both Al-AFI and deGe-Al-AFI samples showed two resonances centered around 55 and 0 ppm in ^{27}Al NMR spectra. The former was dominating and commonly assigned to the tetrahedral Al in the zeolite frameworks, whereas the latter was due to the extra-framework Al species with octahedral coordination [101]. In addition, deGe-Al-AFI contained a lower fraction of extra-framework Al (integral area of resonance centered around 0 ppm) than Al-AFI. Considering the decrease in the pore volume and a higher Al content in Al-AFI (**Table 4-4**), this result supported that the extra framework Al caused the pore blockage in Al-AFI. Therefore, the ^{27}Al NMR results also showed the necessity of degermanation prior to alumination in Ge-AFI zeolite to obtain Al-enriched **AFI** with good quality (high porosity and Al content).
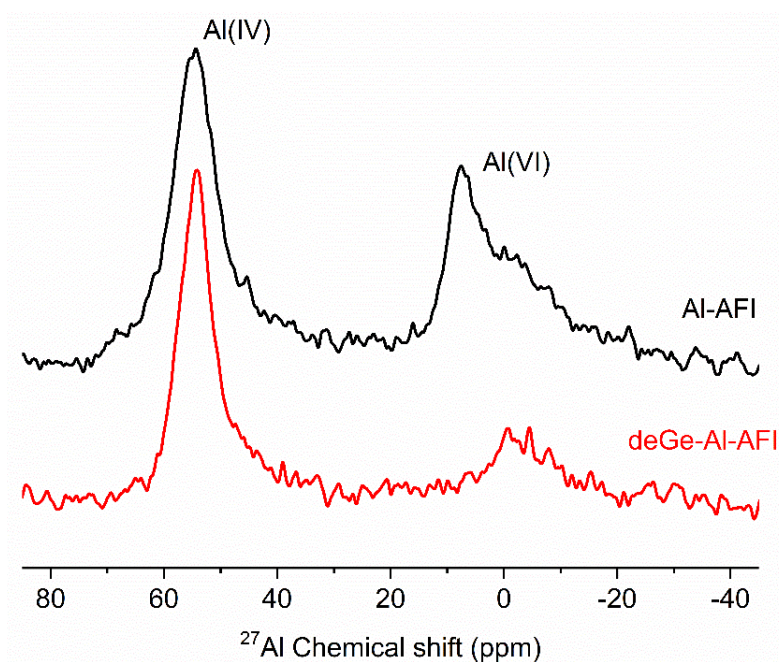
Figure 4-14. ^{27}Al NMR spectra of Al-rich **AFI** materials.

In addition, FTIR with probe molecules was employed to assess acidity of the Al-enriched **AFI** zeolites (**Figure 4-15 and Table 4-5**). Firstly, in consistency with ^{27}Al NMR, the Al-AFI displayed a small band at 3679 cm^{-1} (**Figure 4-15 (a)**), which could be assigned to non-acidic extra framework Al-O-H species [118]. Then both aluminated **AFI** zeolites showed bands around 3740 and 3608 cm^{-1} (**Figure 4-15 (a, c)**), corresponding to the Si-OH and briging $\equiv$Si-OH-Al$\equiv$ group, respectively [102]. After the adsorption of pyridine (**Figure 4-15 (b, d)**), the intensity of 3679 and 3740 cm^{-1} bands remained whereas the 3608 cm^{-1} bands disappeared, indicating that all Brønsted acid sites could be accessed by pyridine. At the same time, two new bands around 1545 and 1455 cm^{-1} appeared for both Al-rich **AFI** zeolites. They were attributed to interaction between pyridine molecules and Brønsted and Lewis acid sites, respectively [103]. Furthermore, examining pyridine desorption from acid sites at varied temperatures (150-450 °C) gave information about strength of acid sites on Al-AFI and deGe-Al-AFI zeolites. As desorption temperature increased, both bands around 1455 and 1545 cm^{-1} decreased in intensities sharply and only extremely weak bands were observed for Al-AFI at 450 °C. On the contrary, deGe-Al-AFI possessed a larger portion of strong acid sites than Al-AFI, which was proved by higher intensities of 1455 and 1545 cm^{-1} bands at higher pyridine desorption temperature.
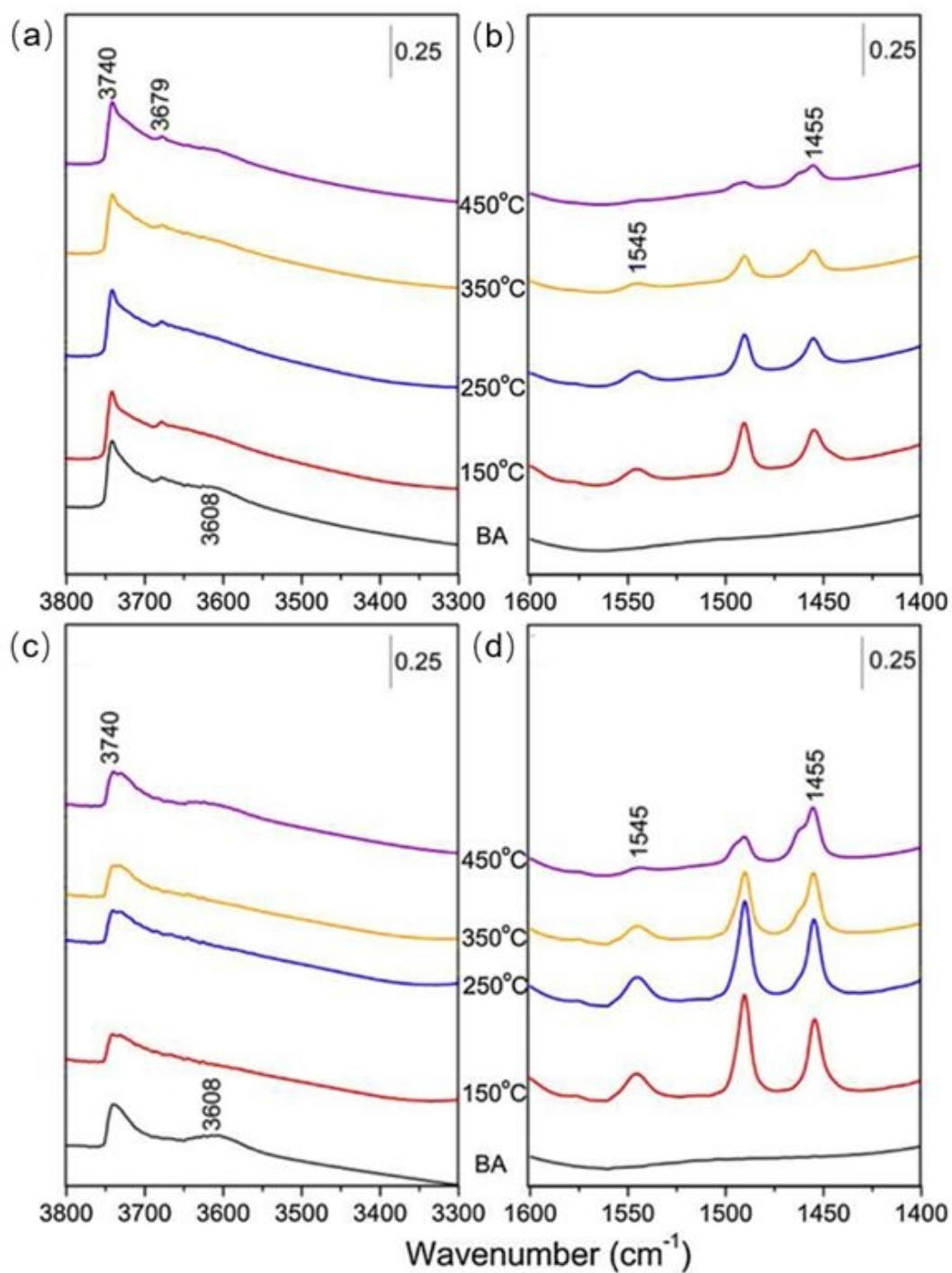
Figure 4-15. FTIR adsorption of pyridine and then desorption at different temperature. (a, b) Al-AFI, (c, d) deGe-Al-AFI.

Table 4-5. Concentration of acid sites on studied catalysts.

Catalyst	c_B	c_L	c_{tot}	B/L
Al-AFI	0.05	0.08	0.13	0.63
deGe-Al-AFI	0.11	0.15	0.26	0.73
MTW	0.11	0.03	0.14	3.67
IPC-2	0.13	0.12	0.25	1.08
Beta	0.33	0.19	0.52	1.74

Type and concentration of acid sites were determined by FTIR adsorption of pyridine at 150 °C. B/L was the ratio of Brønsted acid site concentration to Lewis acid site. Units of c_B, c_B, and c_{tol} are mmol/g.

Furthermore, the external surface acid sites concentration on Al-AFI and deGe-Al-AFI was assessed from FTIR adsorption of 2,6-di-tert-butylpyridine (DTBPy). The molecular size of DTBPy is 0.79 nm, which is larger than the pore entrance of **AFI** zeolite (0.73 nm), thus this probe molecule cannot penetrate into **AFI** channels and access to the acid sites in micropores. As shown in **Figure 4-16**, after adsorption of DTBPy, FTIR spectra of both Al-enriched **AFI** exhibited two bands around 1616 and 1530 cm^{-1}, respectively, which were attributed to the formation of DTBPyH$^+$ ions [119]. Based on the integral intensity of 1530 cm^{-1} band, it is determined that the external surface acid sites concentration on deGe-Al-AFI was 3 times higher than Al-AFI, that was, 0.03 *vs*. 0.01 mmol/g.
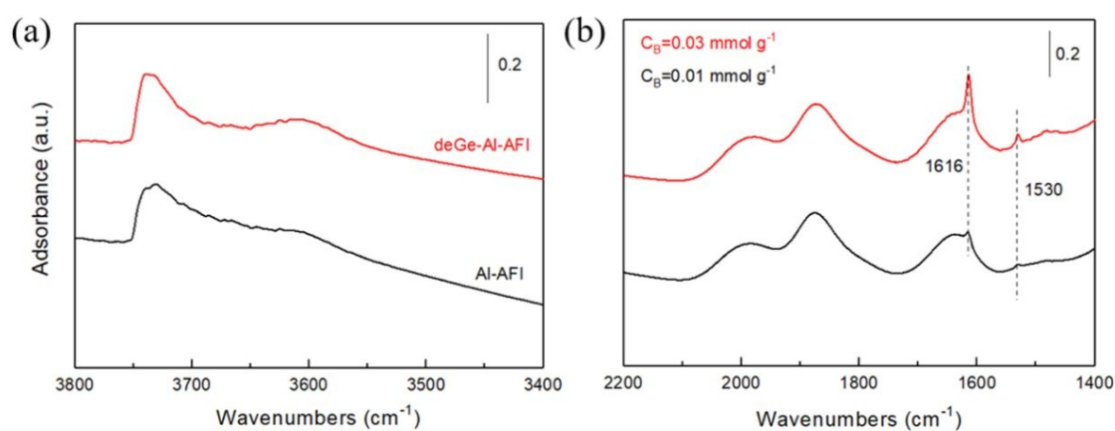
Figure 4-16. FTIR of DTBPy adsorption on Al-AFI and deGe-Al-AFI.

Overall, Al-enriched **AFI** zeolite with Si/Al about 50 was synthesized by alumination of a germanosilicate **AFI** zeolite and the majority of Al^{3+} were introduced into the framework positions. These results suggest a general way for obtaining Al-rich zeolites which cannot prepared hydrothermally.

4.2.3. Catalytic properties of Al-rich AFI catalysts.

Aromatics (benzene/toluene) alkylation is catalyzed by Brønsted acid [120] and frequently used as model reactions to study the reaction activity and products selectivity over zeolite, which reflect the textural and acidic properties of applied catalysts [120]. In addition, the catalytic behaviors of **AFI** zeolites have been vastly investigated in alkylation of polynuclear aromatics, like biphenyl, thanks to its 1D 12MR pore system showing interesting shape selective to 4,4′-diisopropylbiphenyl [114].

To evaluate the catalytic properties of the developed Al-enriched **AFI** zeolites, the Al-AFI, deGe-AFI and several selected 12 MR zeolites with different pore connectivity (**MTW** with 1D channel; IPC-2 – 2D and Beta – 3D) were compared in the toluene alkylation with isopropyl alcohol. Except Beta zeolite, other zeolites possessed similar concentration of Brønsted acid site (0.11-0.13 mmol/g) (**Table 4-5**). In addition, to avoid catalysts fast deactivation, the toluene to isopropyl alcohol molar ratio (Tol/i-PrOH) was fixed at 9.6 in the feed.

As shown in **Figure 4-17** and **Table 4-6,** the catalysts were compared in terms of: (1) reactant (toluene) conversion; (2) selectivity to cymene; (3) para-selectivity to p-cymene isomer; and (4) the iso-/n-propyltoluenes ratio in the products. The conversion of toluene after 180 minutes followed a sequence of Al-AFI < IPC-2 < deGe-Al-AFI < **MTW** ≈ Beta (**Figure 4-17 (a)**). Although the compared zeolites have different pore size and channel dimensions, the activity trend for toluene conversion was consistent with their acidity properties, e.g., B/L (the ratio of Brønsted/Lewis acid) (**Table 4-5)**. It is reported that alkylation of aromatics is associated to the carbonium ion mechanism over Brønsted acid sites [120-121]. In contrast,

the Lewis acid sites could cause negative effect to adsorb the reactants in a competitive way [122]. Therefore, the activity trend over catalysts can be rationally correlated to their B/L ratio. In addition, IPC-2 has layered-like morphology and its 2D pore system is presented in parallel to the crystal lamellae, which may cause additional restrains for reactants diffusion [46, 123]. This was maybe the reason that IPC-2 had higher B/L than deGe-Al-AFI (1.08 vs. 0.73) while showed lower toluene conversion than deGe-Al-AFI (6.0% vs. 6.4%). Finally, Al-AFI showed the lowest toluene conversion in the full range of reaction time. Based on the N_2 adsorption and FTIR analysis, Al-AFI had significantly decreased BET surface area and lower B/L ratio than other catalysts, which led to the low toluene conversion over Al-AFI zeolite.
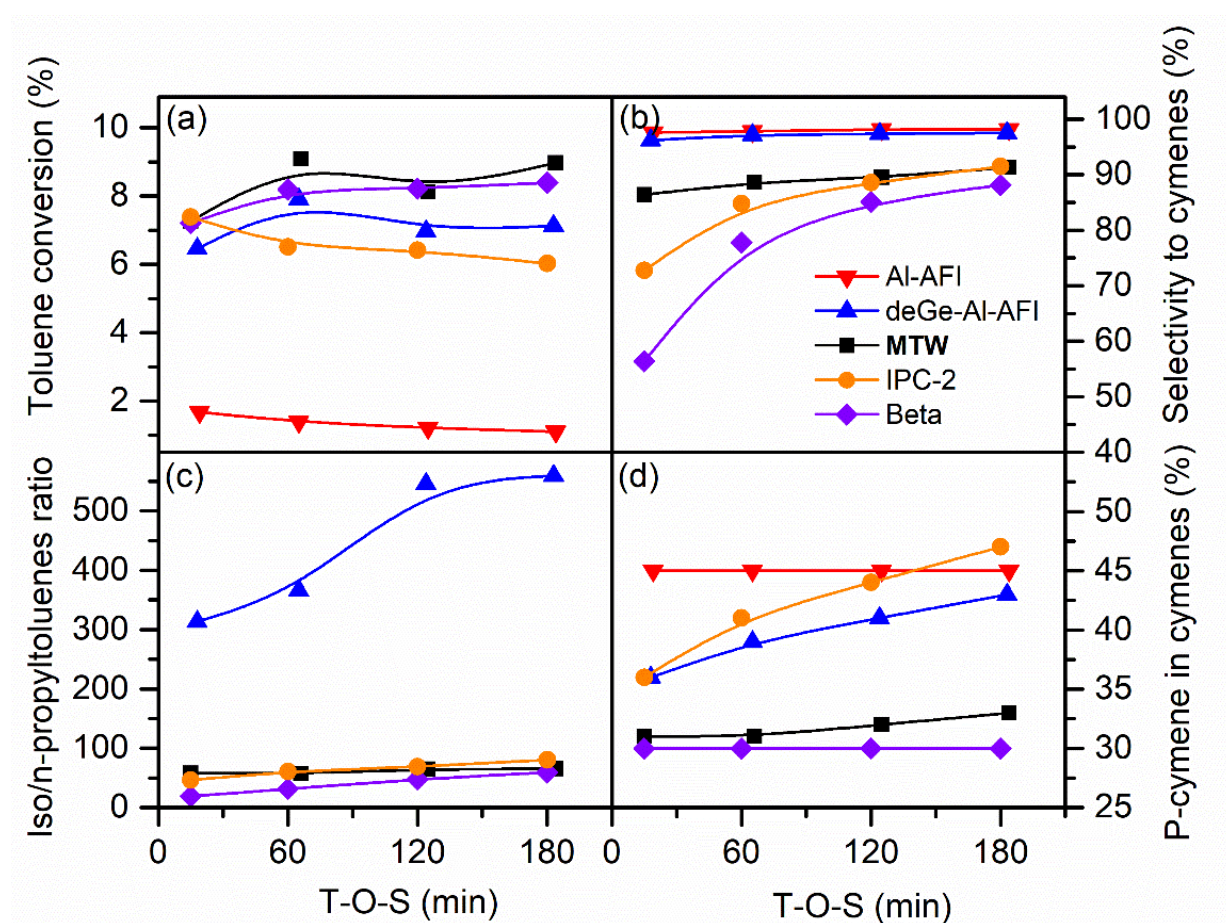
Figure 4-17. Alkylation of toluene with isopropyl alcohol over the developed Al-rich **AFI** zeolite in comparison with other reference catalysts. Reaction conditions: zeolite catalyst (0.14 g), Tol/*i*-PrOH of 9.6, weight hourly space velocity (WHSV) of 10 h^{-1}, reaction temperature 250 °C.

Table 4-6. Toluene conversion and reaction products distribution after 184 minutes.

Catalyst	Toluene Conv. (%)	p-cymene	o-cymene	m-cymene	propyl toluene	cymene Sel. (%)
Al-AFI	1.1(1.7)[a]	43.9(43.8)	24.6	30.0	0	98.5(97.6)
deGe-Al-AFI	6.4(7.2)	41.0(33.7)	11.0	45.3	0.2	97.3(95.9)
MTW	9.0(7.3)	30.0(26.5)	5.1	56.3	1.4	91.4(86.4)
IPC-2	6.0(7.4)	43.3(25.8)	1.2	47.0	1.1	91.5(72.7)
Beta	8.4(7.2)	26.3(16.7)	4.4	57.4	1.5	88.1(56.4)

[a] Numbers in parentheses are toluene conversion and products selectivity after 13 minutes. Reaction conditions: zeolite catalyst (0.14 g), Tol/*i*-PrOH of 9.6, weight hourly space velocity (WHSV) of 10 h^{-1}, reaction temperature 250 °C.

The toluene conversion over studied catalysts was mainly influenced by their B/L ratio. However, the products selectivity to cymene isomers followed another order of Beta < IPC-2 < **MTW** < Al-AFI ≈ deGe-Al-AFI (**Figure 4-17(b)**) after TOS of 180 minutes at 6-9 % conversion (except Al-AFI exhibiting < 2 % conversion over TOS = 0-180 min). This sequence agreed with the channel dimensions of the studied catalysts, that was, 3D < 2 D < 1D. Among all the catalysts, deGe-Al-AFI and Al-AFI provided > 95% product selectivity to cymenes after 13 minutes remaining high for the catalytic test duration. Compared to 1D-pore zeolites, Beta and IPC-2 showed lowered selectivity to cymenes (< 75% after 13 minutes). This may be attributed to the formation of other aromatic compounds, since n-propyl toluene and secondary alkylated di-isopropyltoluene were detected in their products (**Table 4-6**). Furthermore, the iso/n-propyltoluene ratios over **MTW**, IPC-2 and Beta were lower than 80 in the full range of reaction time. However, for the deGe-Al-AFI, the iso/n-propyltoluene ratio was 300 at the beginning and reached > 550 after 180 min (**Figure 4-17(c)**). This suggested the n-propyl toluene production mechanism and evidenced that the intersections of multiple-channel had the ability to accommodate the transition state which formed from the

bimolecular reaction of toluene and cymene products [124]. Thus, formation of n-propyltoluene could be notably suppressed over deGe-Al-AFI allowing Al-enriched AFI to outperform zeolites with multidimensional pore systems (IPC-2, Beta).

Lastly, both Al-enriched **AFI** zeolites and IPC-2 showed over 40% selectivity to p-cymene. In contrast, **MTW** (32%) and Beta (30%) showed lower para-selectivity among the cymene isomers, which may due to their B/L ratio and textural properties. Consequently, formed p-cymene in **MTW** and Beta converted to other cymene isomers on such acid sites with less steric restrictions.

4. 3. Aggregation-resistant MFI nanosized zeolites

4.3.1. Synthesis and modification of MFI nanosized zeolites

Zeolites have pore diameter less than 2 nm, which results in diffusion limitations when zeolites are used as catalysts, especially when bulky molecules are involved in the reactions. The diffusion restrictions in zeolites prohibit reactants from accessing active sites; In addition, the formed bulky intermediates or products cannot diffuse out from zeolites and thus cause deactivation by formation of coking [59]. In the aspect of shortening the diffusion paths, nanosized zeolites provide a direct solution. Besides large external surface area and short diffusion pathway, nanosized zeolites show other advantages of tunable crystal size and surface properties, diverse morphology etc. [64]. However, the nanosized zeolites prepared from alkaline conditions generally contain abundant silanols on their surface [81]. Furthermore, the spontaneous condensation of silanols during zeolites storing or utilizations lead to aggregation of zeolite nanocrystals, which would vanish the advantages of nanosized zeolites. Recently, few studies have reported the preparation of nanosized zeolites with decreased silanols (defects) concentration, for instance, by freeze drying [70], hierarchical assembly [83], isomorphous substitutions (W, Mo incorporation into the zeolite framework). Therefore, exploring other methods to reach aggregation-resistant nanosized zeolites is important and desirable.

In our work, **MFI** zeolite was selected for investigation as it is an important industrial zeolite catalyst and can be synthesized in nanosized form by different methods [125]. In addition, zeolites surface modifications with organic silanes have been widely used for reducing surface defects (silanols) concentration, which improves the tolerance of zeolite catalysts in hydrothermal conditions [126]. In order to prepare the aggregation-resistant **MFI** nanosized zeolites, mono-dispersed **MFI** nanocrystals (named as N-MFI) were first synthesized by an amino acid-mediated process [62], in which the amino acid (L-lysine) restricted the crystal growth of **MFI** zeolite. It was also reported that two-step crystallization (low temperature nucleation and high temperature crystallization) and concentrated reaction gel were necessary in this process for obtaining mono-dispersed nanosized **MFI** zeolite [62]. Then, the organic silanes that worked as protection agents against agglomeration were introduced onto the zeolite nanocrystals surface via post-synthesis silylation (silylated materials named as N-MFI-S, S stands for silane) (**Scheme 4-5**).
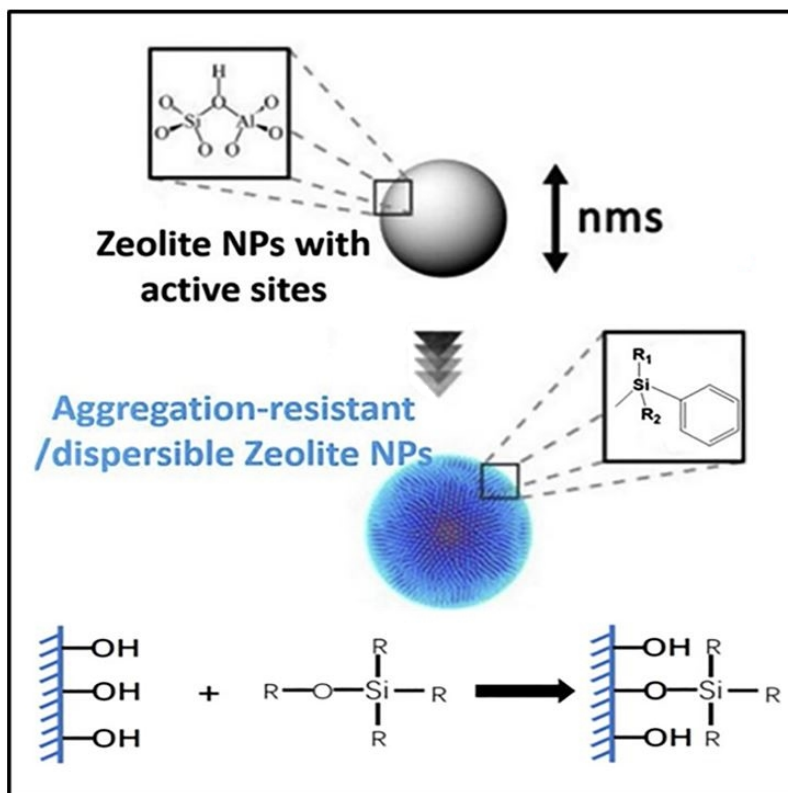

Scheme 4-5. Procedure for preparation of aggregation-resistant nanosized zeolites.

XRD was used to examine structure and crystallinity of **MFI** zeolites before and after silane modifications. **Figure 4-18** displays XRD patterns of N-MFI, N-MFI-3ES (nES stands for the initial silane containing n hydrolyzable ethoxy group(s), here 3ES, triethoxyphenylsilane), N-MFI-1ES (1ES, ethoxydimethylphenylsilane) samples. From the XRD pattens, the N-MFI exhibited broadened Bragg peaks, suggesting the crystal size for **MFI** zeolite was in nanosized range. In addition, all the samples had the same **MFI** diffraction peaks positions with high intensity and without any impurity. Therefore, the XRD patterns of **MFI** samples revealed that the grafting of organic silanes onto zeolite surface did not affect the crystalline structure and phase purity.
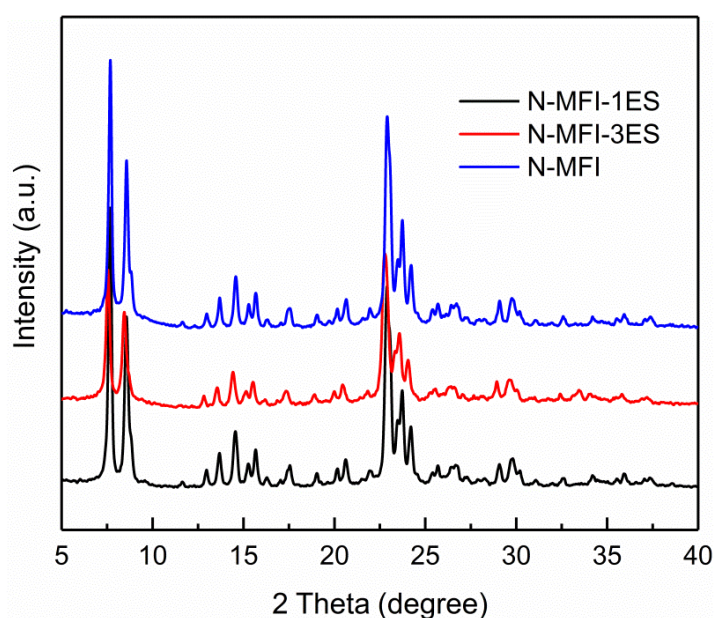
Figure 4-18. XRD patterns of **MFI** samples.

Then, TEM inspection (**Figure 4-19)** for N-MFI, M-MFI-1S and N-MFI-3S samples was used to record their crystal sizes. From TEM images, the initial N-MFI zeolite had average particle size of 67 nm (**Figure 4-19 (a)**). After modification of different silanes, the **MFI** nanocrystals almost maintained the crystal size, showing the size of 70 and 62 nm for N-MFI-3ES and N-MFI-1ES, respectively. In addition, HRTEM image (**Figure 4-19 (d)**) gave lattice spacings around 1.3 nm for N-MFI sample, which matched (001) plane of **MFI** zeolite.
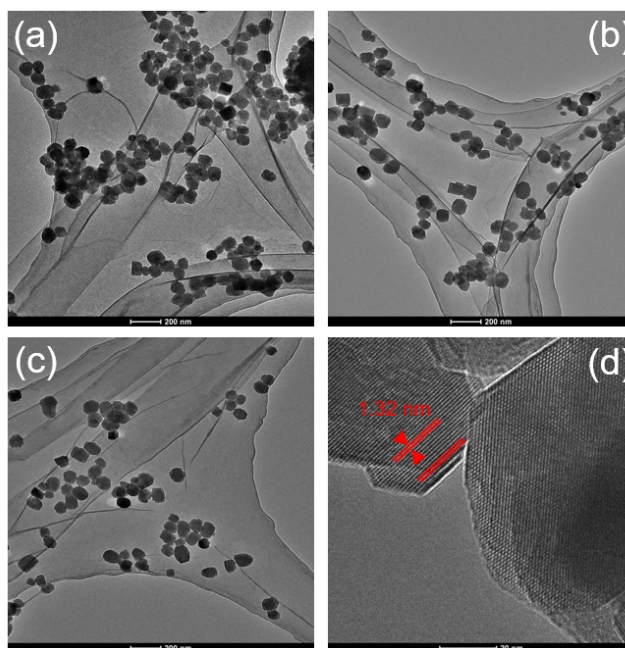
Figure 4-19. TEM images of MFI zeolites. (a, d) N-MFI, (b) N-MFI-3ES, (c) N-MFI-1ES.

Furthermore, the successful attachment of silanes onto **MFI** nanocrystals was verified by FTIR, TG and ^{29}Si MAS NMR characterizations. FTIR spectra of N-MFI and N-MFI-1ES were shown in **Figure 4-20**. Compared with N-MFI, the N-MFI-1ES displayed two additional absorption bands around 2932 and 2880 cm^{-1}, which corresponded to stretching and bending vibrational modes of CH species of grafted silanes [127].
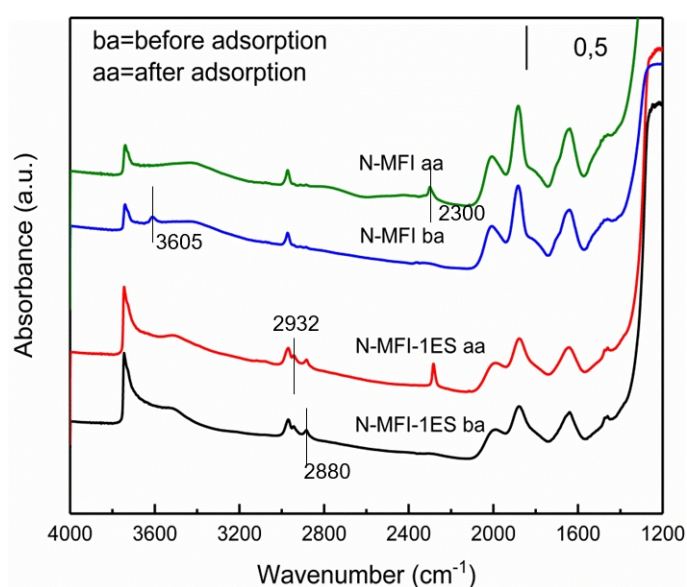
Figure 4-20. FTIR spectra of N-MFI and N-MFI-1ES materials with ACN as probe molecule.

In the TG profiles of N-MFI and silylated samples (**Figure 4-21**), N-MFI showed higher weight loss than silylated ones at temperature lower than 200 °C, which was mainly due to the water physically absorbed on the samples, suggesting that the hydrophobicity of **MFI** zeolite increased through silanes surface modifications. In addition, at higher temperature range, because of the combustion of organic functional groups, two silylated **MFI** zeolites exhibited apparently higher weight loss than N-MFI. As a result, the weight losses of silylated zeolites were 5.48% and 4.90% for N-MFI-3ES and N-MFI-1ES, respectively, suggesting the amount of organic silane appended onto the zeolite surface was similar for both samples.
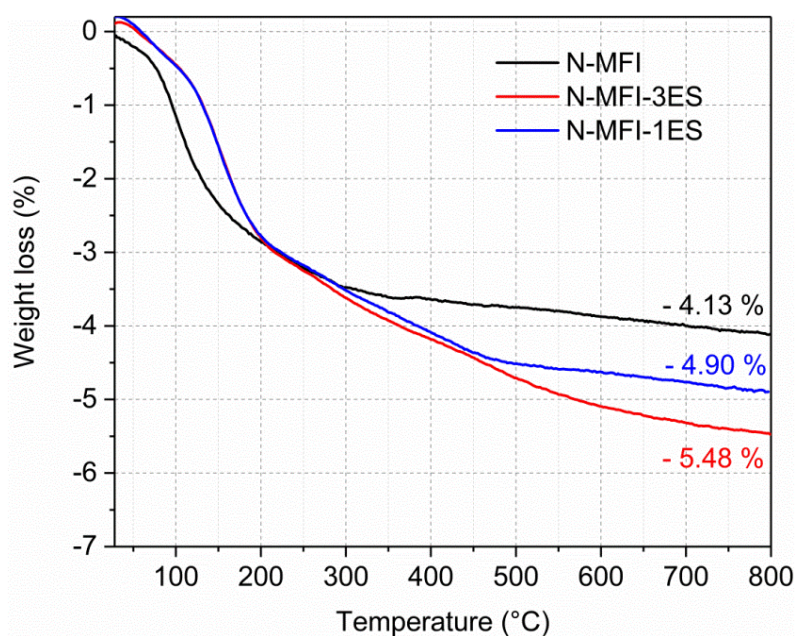

Figure 4-21. TG profiles of **MFI** zeolites.

Furthermore, in the ^{29}Si NMR spectra (**Figure 4-22 (a)**), Q3 signal was observed in N-MFI, assigning to surface $HOSi(OSi)_3$ [128], while the Q3 peaks were absent in N-MFI-3ES and N-MFI-1ES. This suggested that surface silanol groups (Si-OH) of N-MFI were consumed almost completely through interacting with alkoxysilyl groups of silanes. In addition, in the ^{27}Al NMR spectra, only tetrahedral Al (~ 60 ppm) existed for both N-MFI and silylated **MFI** zeolites (**Figure 4-22(b)**), suggesting that the silylation treatment did not influence Al coordination in **MFI** frameworks.
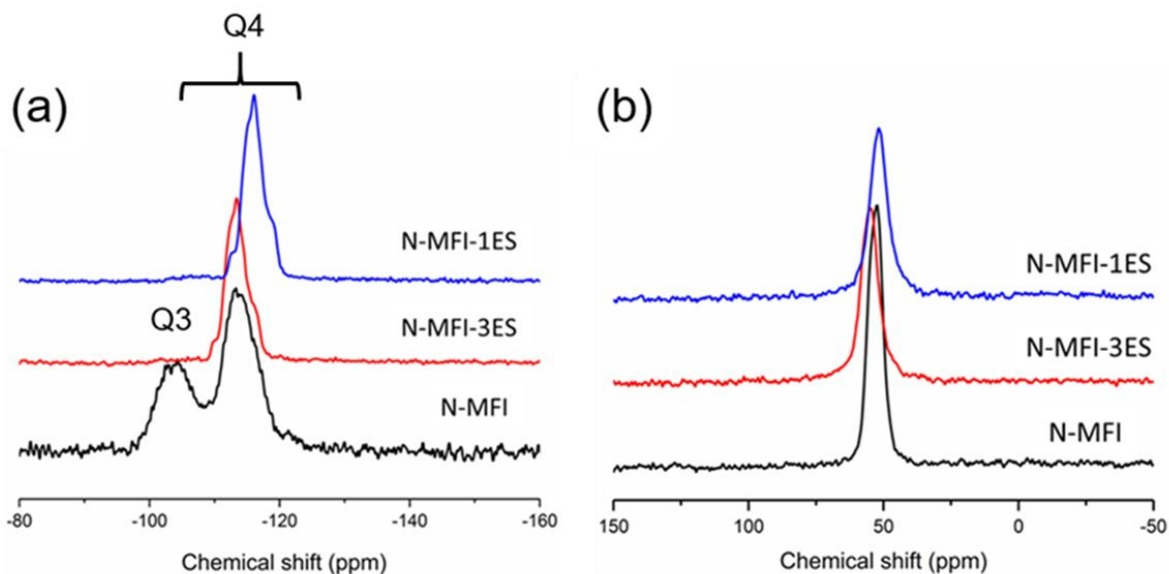
Figure 4-22. (a) solid state ^{29}Si and (b) ^{27}Al NMR spectra of N-MFI, N-MFI-3ES and N-MFI-1ES zeolites.

Moreover, N_2 adsorption and chemical analysis provided additional information about the silane modifications of nanosized **MFI** zeolites. As shown in **Figure 4-23**, both initial and silylated **MFI** samples exhibited similar (I+IV) type N_2 sorption isotherms, which agreed with the typical nanosized zeolites possessing bi-modal porosity [64]. In addition, an increased N_2 uptake was found at higher relative pressure for all samples, corresponding to the further adsorption of gas in voids formed by aggregation of zeolite nanocrystals. The N-MFI showed surface area of 378 m^2/g. After silane modifications, N-MFI-3ES and N-MFI-1ES displayed reduced surface area of 309 and 302 m^2/g respectively but similar micropore volume to N-MFI (**Table 4-7**), indicating the silylation treatment caused partial blocking the pore entrances of **MFI** zeolites and slightly decreased the resulting total pore volumes of silylated **MFI** zeolites. Furthermore, the silylation treatments increased the silicon atom fraction in the silylated samples, leading to higher Si/Al in N-MFI-3ES and N-MFI-1ES than N-MFI (**Table 4-7**).

The acidity of N-MFI and N-MFI-1ES was determined by FTIR adsorption of ACN. Since the **MFI** zeolites had low content of Al, the amounts of acid sites on N-MFI and N-MFI-1ES

were 60 and 20 μmol/g, respectively (**Table 4-7**).
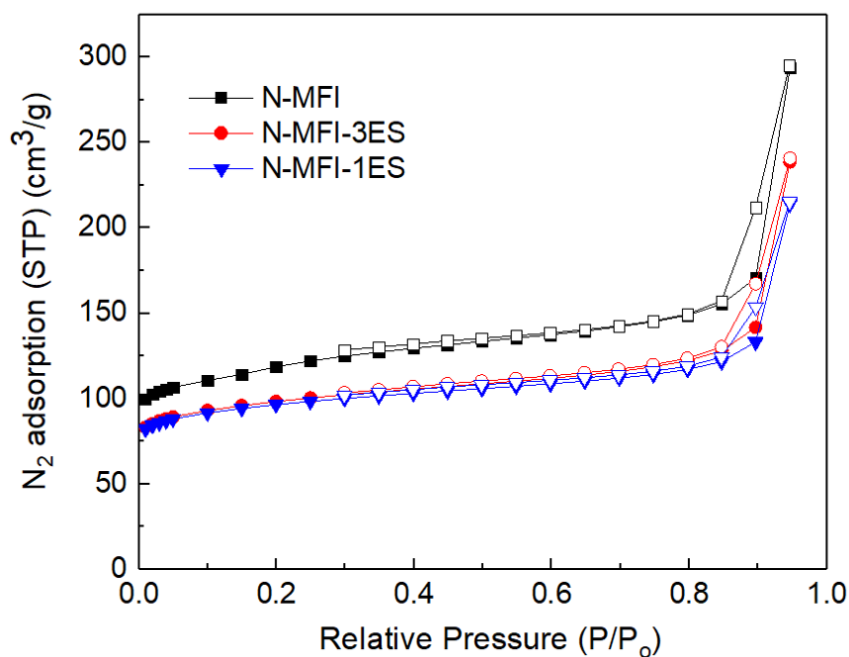
Figure 4-23. N_2 sorption isotherms of **MFI** zeolites.

Table 4-7. Physicochemical properties of materials in the investigation.

|	Si/Al[a]	S_{BET}[b]	S_{ext}[b]	V_{micro}[b]	V_{total}[b]	Partical size[c]	c_{tot}[d]
N-MFI	133	378	178	0.106	0.454	67	60
N-MFI -3ES	174	309	113	0.103	0.372	70	-
N-MFI -1ES	151	302	104	0.104	0.331	62	20
M-MFI	140	341	74	0.117	0.222	2000-4000	40

[a] Si/Al was measured by ICP-OES. [b] measured from N_2 physisorption at 77 K. [c] average size of particles was estimated from TEM and SEM images. [d] determined from FTIR adsorption of ACN; Units of each column are (S_{BET} and S_{ext}) m^2/g, (V_{micro} and V_{tot}) cm^3/g, (Particle size) nm, (c_{tol}) μmol/g.

4.3.2. Aggregation properties of nanosized MFI zeolites

The surface silanols of zeolites result in aggregation of zeolite nanocrystals due to dehydration condensation between silanols. Once the amount of surface silanols has been reduced through silane modifications, which would make zeolites higher degree of hydrophobicity. Therefore, it can be expected that the silylated zeolites would show better stability in various conditions.

The aggregation properties of **MFI** zeolites were firstly assessed by dispersion of **MFI** nanocrystals in acetone at ambient conditions. DLS and TEM were used to trace the evolution of zeolites particle size distribution (**Figure 4-24 and Figure 4-25**). For comparison, silanes with different properties (molecular size, number of hydrolyzable ethoxy group, polarity) were selected to study their influences on the stability of the silylated zeolites. In **Figure 4-24**, fresh N-MFI and silylated MFI zeolites (black curves) exhibited similar average crystal sizes around 70 nm, which was in good agreement with the observations from TEM measurements. However, except for the **MFI** modified with ethoxydimethylphenylsilane (N-MFI-1ES), N-MFI and other silylated samples failed to maintain their particle sizes after 10 days (red curves). Among them, the average particle size of N-MFI became 5 times lager than the fresh one (from around 60 to 300 nm), indicating the severe aggregation of **MFI** nanocrystals (**Figure 4-24 (a)**). In addition, **MFI** modified with the amine-containing silane (3-(ethoxydimethylsilyl)propylamine) showed the poorest stability. Compared to ethoxydimethylphenylsilane-modified **MFI** zeolite, silanes with more hydrolyzable ethoxy groups (triethoxyphenylsilane and (4-biphenyl)triethoxysilane) led to worse stability of **MFI** nanocrystals (**Figure 4-24 (b, d)**), which may be attributed to the occurrence of self-condensation of silanes. Furthermore, since the properties of used silanes (hydrophobicity/hydrophilicity, size, and denticity) were different, the concentration or location of organic groups onto the zeolite surface may vary. Therefore, the choosing of suitable silanes is crucial for the decrease in the aggregation degree of zeolite nanocrystals.
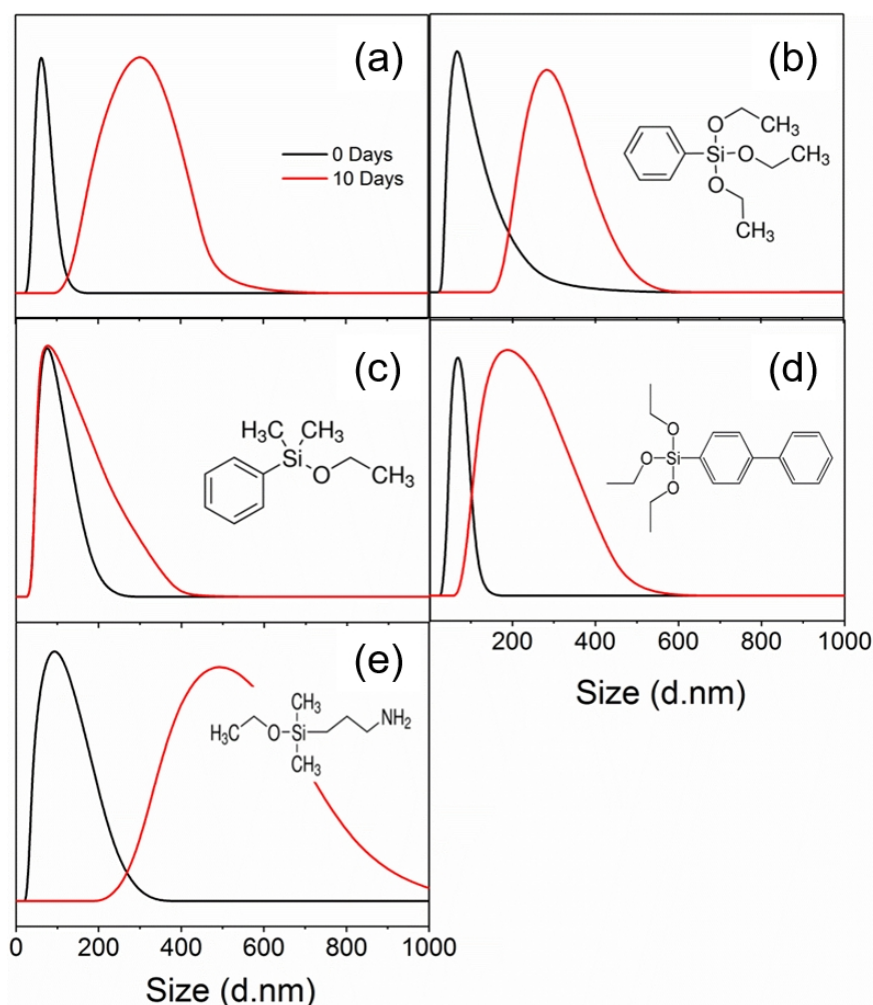
Figure 4-24. Particle size distribution of nanosized **MFI** zeolites. (a) N-MFI and N-MFI-S with different silanes: (b) triethoxyphenylsilane, (c) ethoxydimethylphenylsilane, (d) (4-biphenyl)triethoxysilane, (e) 3-(ethoxydimethylsilyl)propylamine.

In addition, in full agreement of DLS results, TEM image of N-MFI suspension after 10 days showed that **MFI** nanocrystals agglomerated into large particles (**Figure 4-25 (a)**). In contrast, under the same conditions, discrete, mono-dispersed **MFI** nanocrystals were observed for N-MFI-1ES sample (**Figure 4-25 (b)**), indicating that the nanosized **MFI** zeolite modified with ethoxydimethylphenylsilane achieved enhanced aggregation-resistant property. Furthermore, the aggregation properties of **MFI** zeolites were assessed in catalysis conditions (catalytic results are discussed in the next sub-section). Both spent N-MFI and N-MFI-1ES were recovered after acylation of p-xylene with butyryl chloride at 130 °C. Form TEM

images, spent N-MFI demonstrated closely compacted nanocrystals forming larger particles of several micrometers (**Figure 4-25 (c)**). However, though the N-MFI-1ES exhibited the aggregation to some extent after the harsh catalytic conditions as well (**Figure 4-25 (d)**), it still showed better aggregation-resistant property than MFI nanocrystals without silane modifications, in terms of the loose agglomeration of nanocrystals and the particle size.
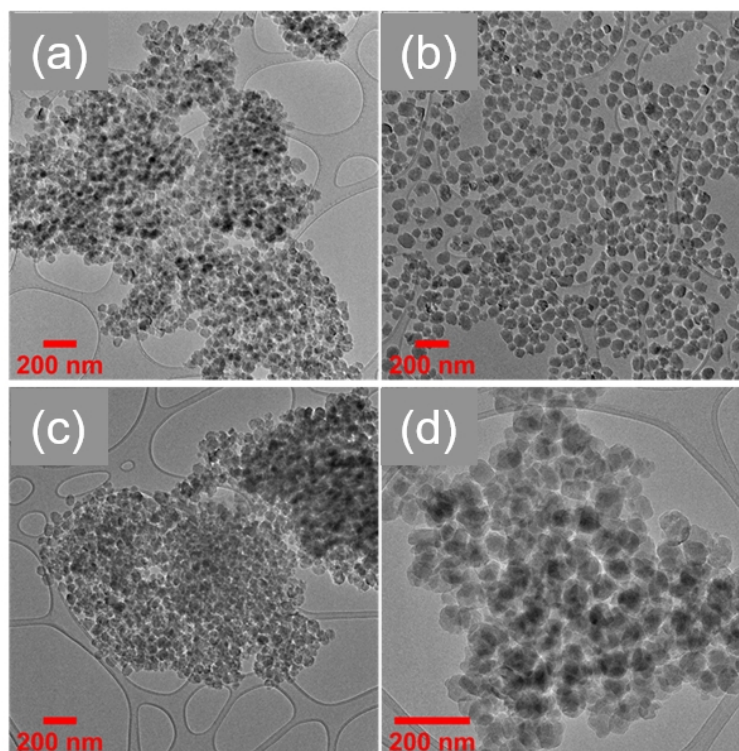
Figure 4-25. TEM images of spent **MFI** zeolites in different conditions. N-MFI dispersed in acetone for 10 days (a) and catalyzed acylation reaction (c); N-MFI-1ES dispersed in acetone for 10 days (b) and catalyzed acylation reaction (d).

4.3.3. Catalytic performance of aggregation-resistant nanosized MFI zeolite

During the catalytic reactions, the reduced aggregation of nanosized zeolites could provide better accessibility to the acid sites for reactants. Therefore, N-MFI and N-MFI-1ES related to their aggregation properties was assessed using acylation of p-xylene with butyryl chloride (**Scheme 4-6**). Acylation is one of the crucial reactions for the C-H functionalization of

aromatics [129]. The acylation of aromatics (e.g. toluene, anisole) is highly valued for the production of important platform intermediates for the further applications for perfume, pharmaceuticals, dyes and flavors etc. [130]. In addition, acylation of aromatics (benzene/toluene/p-xylene) have been frequently used as model reactions to probe the effects of structure as well as acidity of zeolites on catalytic activity and selectivity [131]. Both strong Brønsted and Lewis acid can catalyze this reaction [129, 132].
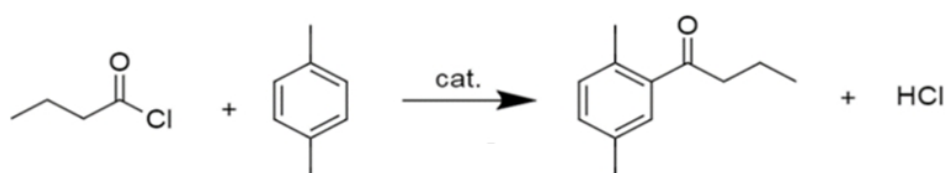
Scheme 4-6. Scheme of acylation of p-xylene under study.

The conversions of butyryl chloride as a function of time over the studied catalysts are shown in **Figure 4-26**. The commercial micron-sized **MFI** sample (M-MFI, Si/Al ~ 140) had higher chloride conversion than nanosized **MFI** catalysts. In addition, N-MFI-1ES only showed moderate butyryl chloride conversion (84%). These were due to acid sites concentration on M-MFI being 3 times higher than N-MFI-1ES (60 *vs*. 20 $\mu mol/g$) (**Table 4-7**). However, when assessing the catalysts in terms of turn-over frequency (TOF) (**Figure 4-26 (b)**), which reflects the number of butyryl chloride molecules transformed on individual active site in unit time, TOF achieved over the studied **MFI** catalysts followed a sequence of N-MFI-1ES (602 h^{-1}) > M-MFI (390 h^{-1}) > N-MFI (173 h^{-1}). Thus, there is a significant correlation between the aggregation properties and acid sites accessibility over both nanosized **MFI** zeolites. Indeed, TEM images (**Figure 4-25**) of spent **MFI** catalysts showed apparent aggregation of N-MFI nanocrystals and few micrometers aggregates formed after the catalytic reaction. N-MFI-1ES sample also did not completely maintain the initial particle size under such severe reaction conditions but the aggregation was less pronounced compared to N-MFI. Considering the vast kinds of silanes and nanosized zeolites, the method to develop aggregation-resistant nanosized zeolites here provides a facile way to tune the surface properties of nanosized zeolites, which

would improve the utilization of nanosized zeolites in more processes.
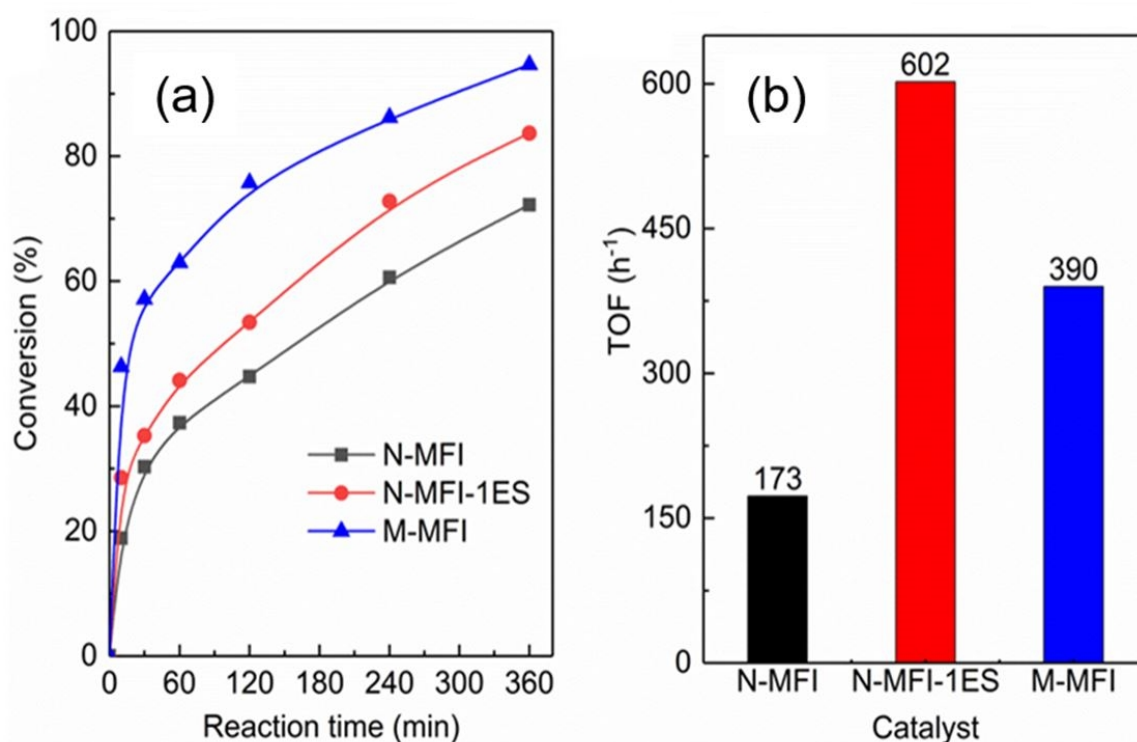
Figure 4-26. Acylation of p-xylene over **MFI** zeolites. Reaction conditions: p-xylene (5.0 ml), butyryl chloride (5.0 mmol), dodecane (0.5 g), 130 °C.

4.4. Co$_3$O$_4$/MWW for total oxidation of VOCs

4.4.1. Synthesis of Co$_3$O$_4$/MWW supported catalysts

Volatile organic compounds (VOCs) which arise from the industrial production processes and engine vehicles are the main sources of environmental pollution and are harmful to human health. Among various treatment techniques, catalytic total oxidation has been widely used to eliminate VOCs thanks to the benefits of high energy-saving, easy management, and low secondary pollution. Regarding the catalysts for combustion of VOCs, precious metal catalysts, for instance, Au, Ag, Pt etc. dispersed on suitable supports, demonstrated high activity for catalytic oxidation of VOCs [20, 22]. However, transition metal oxides are

favored because their lower cost and higher anti-sintering property compared to noble metals. On this point, among the efficient transition metal oxides for total oxidation of VOCs, Co_3O_4 shows outperformed activity and attracts a lot of interests [21]. Because the unsupported Co_3O_4 tends to agglomerate easily at higher temperatures [133], Co_3O_4 is generally loaded onto a support to strengthen thermal stability of active spinel phase as well as to increase the atomic utilization of cobalt. Therefore, a suitable support is critical, which determines the dispersity and reducibility of Co_3O_4 [21]. CeO_2, Al_2O_3, SBA-15, zeolites and activated carbons are commonly used as supports [21, 133, 134]. Among them, zeolites are desirable on account of the large surface area for dispersing Co_3O_4 and tunable properties of acid sites (nature, strength, and number) for adjusting the interaction between metal and supports. To date, almost all studied zeolite supports for VOCs oxidation catalysts are Beta and ZSM-5 [21, 133]. However, the influence of such characteristics as structure and acidity of zeolite support on dispersity, reducibility of cobalt and stability of catalyst remains unrevealed. Furthermore, in contrast to conventional 3D zeolites, the family of **MWW**-type zeolites (MCM-22, MCM-36 and MCM-56) provides the possibility to compare zeolites composed of the same layers but with different layers arrangements (**Figure 4-27**) [42, 43]. **MWW** zeolites have been not yet used as supports for the preparation of Co_3O_4 supported catalyst for total oxidation of VOCs. In addition, the acidity of **MWW** zeolites can be controlled through either adjustment of Si/Al of the reaction mixture for hydrothermal synthesis or post-synthesis treatment of the **MWW** zeolite in acidic or basic medium [43]. Therefore, using **MWW** family with different architecture and adjustable chemical composition (Si/Al) allows unraveling effects of structural and acidic properties of zeolite support on catalytic behavior of cobalt-supported materials for total oxidation of VOCs.
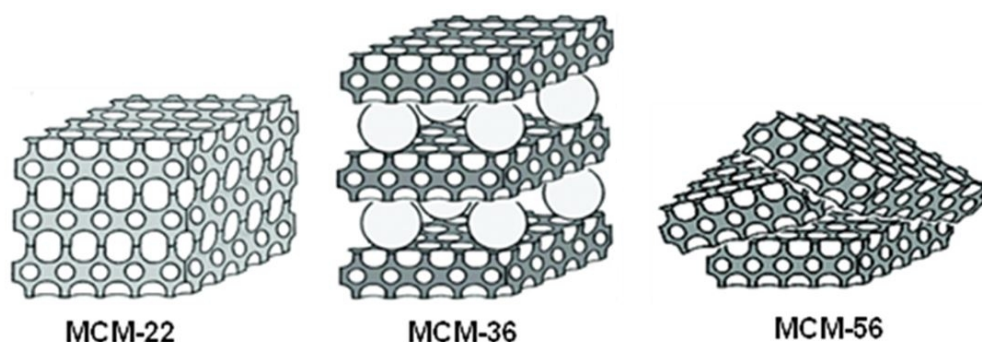
Figure 4-27. The structure models of **MWW**-type zeolites [43].

To prepare Co/MWW catalysts with optimized architecture and acidity of zeolite supports, firstly, **MWW** zeolites with different layers arrangements (MCM-22 with ordered alignment of 2D zeolite layers, MCM-36 with expanded interlayer space and MCM-56 with disordered stacking of 2D zeolite layers) and Si/Al (MCM-22(x), x presented the Si/Al of MCM-22 in synthetic gel) were synthesized. Then **MWW** zeolites were impregnated with $Co(NO_3)_2 \cdot 6H2O$ followed by calcination at 400 °C. To assess the effects of architecture and acidity of **MWW** support on the catalytic activity of Co/MWW catalysts, cobalt loading was fixed at 10 wt.%.

Different techniques were used to compare the **MWW** zeolite supports and the 10%Co/MWW after cobalt loading. In **Figure 4-28 (a)**, XRD patterns of three **MWW**-type zeolites showed the similar reflection peaks to those reported in the literature [43], indicating their phase purity. For MCM-22, after the acid or base treatments, that were MCM-22(50)-A and MCM-22(30)-B, both crystal structures were well maintained. After cobalt loading, the XRD patterns of Co supported **MWW** catalysts confirmed that the impregnation with Co did not influence the crystalline structure of the corresponding **MWW** supports (**Figure 4-28 (b)**). However, after the Co loading, additional peaks at 2θ = 19.0, 31.3, 36.8, 44.8, 59.3 and 65.2° were observed. These peaks are corresponded to crystalline planes of (111), (220), (311), (400), (511) and (440) belonged to cubic spinel Co_3O_4 phase. In addition, XRD patterns showed all Co supported materials had higher background and slightly decreased intensity relative to Co-free **MWW** zeolites, which may be attributed to the fluorescence effect caused

by the Cu X-ray [21]. Furthermore, using the (311) broadening and estimated from Scherrer equation, the average sizes of cobalt particle on Co/MWW were about 14-22 nm (**Table 4-9**).
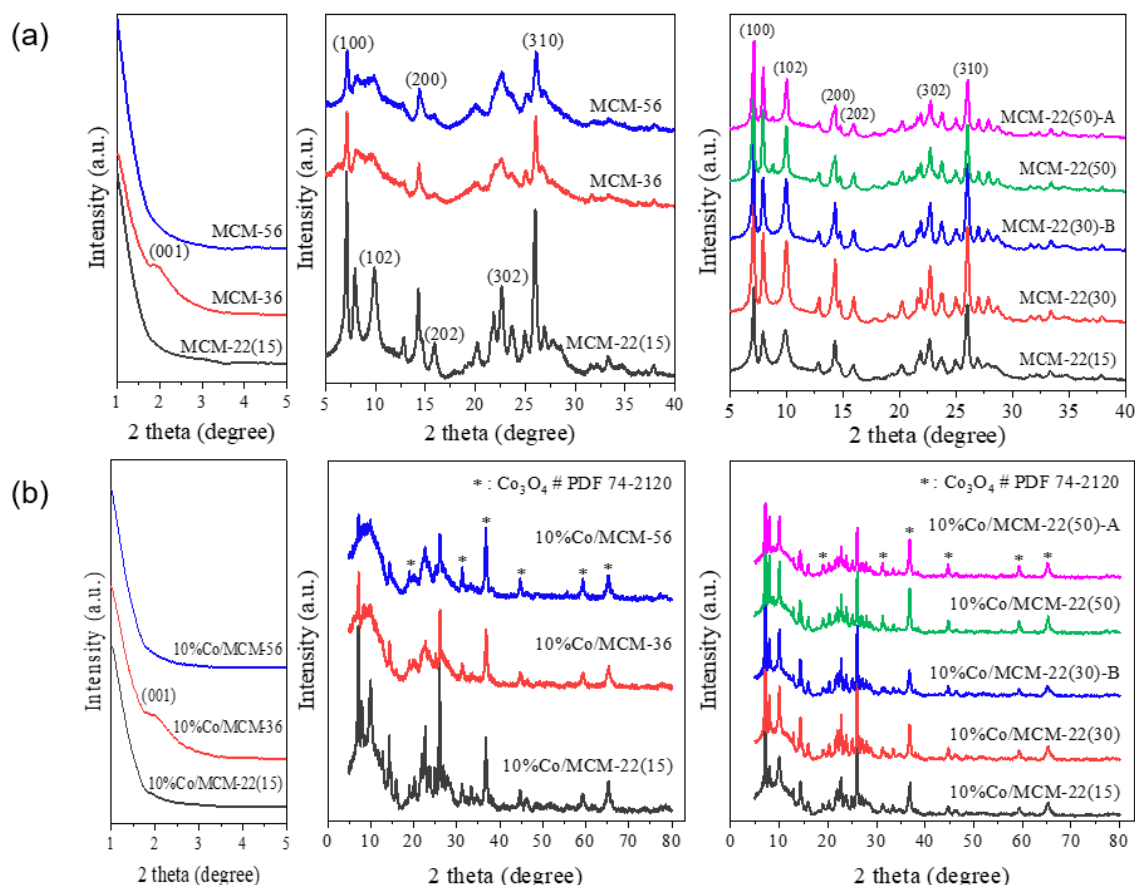
Figure 4-28. XRD patterns of (a) Co-free **MWW** zeolites supports and (b) 10%Co/MWW.

In addition, as shown in **Figure 4-29 (a)**, before the Co loading, all the **MWW** zeolites had type I+IV N_2 physisorption isotherms containing H4-type hysteresis loops stepping down at P/P_o of 0.42-0.50, suggesting the existence of interparticle mesopores. Compared to MCM-22 and MCM-56, MCM-36 showed much more N_2 adsorption at higher relative pressure and a larger hysteresis loop, confirming that the MCM-36 possesses higher mesoporosity than MCM-22 and MCM-56. Furthermore, all the **MWW** zeolites exhibited large BET area (**Table 4-8**), in the range of 400-729 m^2/g. MCM-36 showed apparently enhanced external surface area and mesopore volume but lower micropore volume than MCM-22 zeolite, which was

caused by the loss of 10-MR interlayer channels and 12 MR supercages by silica pillaring. MCM-56 also showed higher mesopore volume than MCM-22 (0.23 *vs*. 0.38 cm^3/g) (**Table 4-8**), indicating the disorder stacking of 2D layers in MCM-56 zeolite which formed meso-porosity. Moreover, the dealumination showed insignificant influence on the textural properties of MCM-22(50). While base treatment resulted MCM-22(30)-B almost exhibited double external surface area (143 vs. 77 m^2/g) as well as mesopore volume (0.21 vs. 0.11 cm^3/g) compared with MCM-22(30), which was due to the leaching of Si from zeolite framework.

After the Co loading, the shape of the N$_2$ adsorption isotherms did not change for all the 10%Co/MWW materials (**Figure 4-29 (b)**). However, their BET surface areas and micropore volumes were reduced for all the Co-supported samples, indicating that some of cobalt filled the micropores. In addition, the 10%Co/MCM-22 materials showed increased mesopore volume than the respective zeolite supports, which can be explained by the formation of Co$_3$O$_4$ interparticle mesoporosity (also see the STEM images below). In contrast, the Co-supported MCM-36 and MCM-56 showed lower mesopore volume and external surface area than Co-free **MWW** zeolite supports due to the presence of the larger Co$_3$O$_4$ particles (see SEM images below).
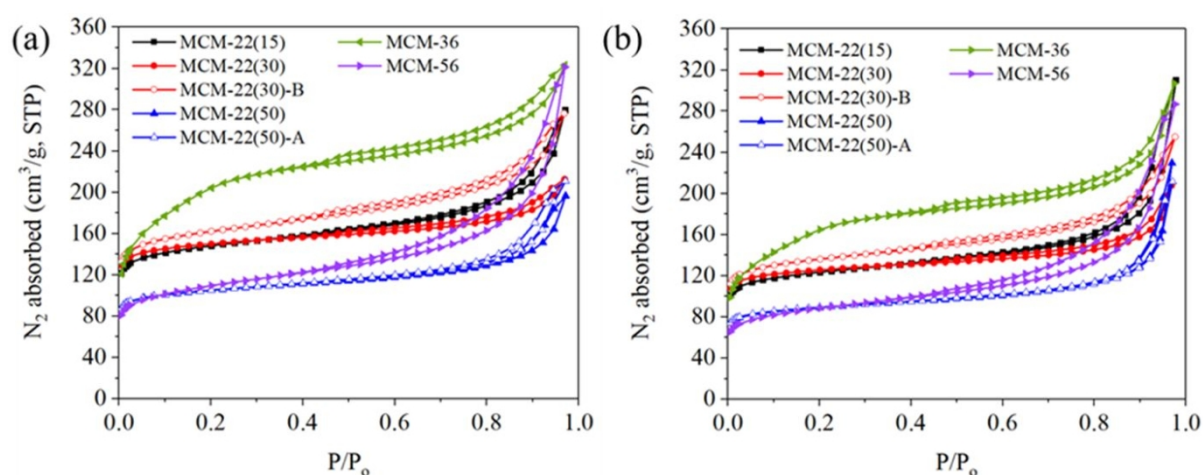
Figure 4-29. N$_2$ adsorption of (a) MWW zeolites and (b) 10%Co/MWW catalysts.

Table 4-8. Physicochemical properties of **MWW** zeolites.

	Surface area[a]		Pore volume[a]			Acidity[b]		B/L [c]	Si/Al [d]
	S_{BET}	S_{ext}	V_{total}	V_{micro}	V_{meso}	c_B	c_L		
MCM-22(15)	561	118	0.43	0.18	0.23	0.40	0.28	1.4	12
MCM-22(30)	584	77	0.33	0.20	0.11	0.33	0.21	1.6	23
MCM-22(30)-B	618	143	0.43	0.19	0.21	n.d.	n.d.	n.d.	17
MCM-22(50)	400	74	0.31	0.13	0.16	0.18	0.11	1.6	39
MCM-22(50)-A	407	78	0.33	0.13	0.18	0.12	0.10	1.2	50
MCM-36	729	596	0.50	0.06	0.31	0.34	0.20	1.7	19
MCM-56	400	140	0.50	0.11	0.38	0.26	0.18	1.4	8

[a] textural properties were given by N_2 physisorption; [b] type and amount of acid site were determined from FTIR adsorption of pyridine probe; [c] B/L, c_B/c_L; [d] Si/Al was calculated from ICP-OES. Units of (surface area), m2/g; (pore volume), cm3/g; (acid concentration), mmol/g.

Table 4-9. Co content and textural properties of 10%Co/MWW.

	Co [a]	$D_{Co_3O_4}$ [b]	Surface area[c]		Pore volume[c]		
			S_{BET}	S_{ext}	V_{total}	V_{micro}	V_{meso}
10%Co/MCM-22(15)	8.9	17	473	112	0.47	0.14	0.32
10%Co/MCM-22(30)	9.1	21	489	77	0.32	0.16	0.14
10%Co/MCM-22(30)-B	8.4	14	524	121	0.39	0.16	0.21
10%Co/MCM-22(50)	9.0	22	343	77	0.36	0.10	0.24
10%Co/MCM-22(50)-A	9.7	22	343	68	0.33	0.11	0.21
10%Co/MCM-36	8.4	17	588	473	0.48	0.05	0.26
10%Co/MCM-56	9.1	17	325	123	0.44	0.08	0.35

[a] Co content was determined from ICP-OES; [b] average size of Co_3O_4 crystallite was calculated from XRD patterns; [c] textural property was given by N_2 physisorption. Units of each column: (Co content), %; (diameter of Co_3O_4), nm; (surface area), m^2/g; (pore volume), cm^3/g.

Furthermore, in the SEM images (**Figure 4-30**), the 10%Co/MWW materials still showed the plate like morphology, which was typical for **MWW** zeolites [43]. The Co_3O_4 nanoparticles

could be observed for all the samples in a way of bright dots. However, the size of Co_3O_4 nanoparticles were different, which in consistent with the XRD estimation above. For Co-supported MCM-36 and MCM-56 materials (**Figure 4-30 (g, i)**), larger Co_3O_4 particles were presented, which may be formed by the agglomeration of Co_3O_4 crystallinities. In contrast, Co_3O_4 showed better dispersion on MCM-22 zeolites. Among 10%Co/MCM-22(x) materials, the largest Co_3O_4 particles were observed in 10%Co/MCM-22(30)-B (**Figure 4-30 (e)**), indicating the negative effect of base treatment on the zeolite support, most likely, related to the formation of mesopores upon silicon removal. However, dealumination of MCM-22 increasing the Si/Al but not affecting the textural properties of the zeolite led to more homogeneous dispersion of Co_3O_4 (**Figure 4-30 (g)**)
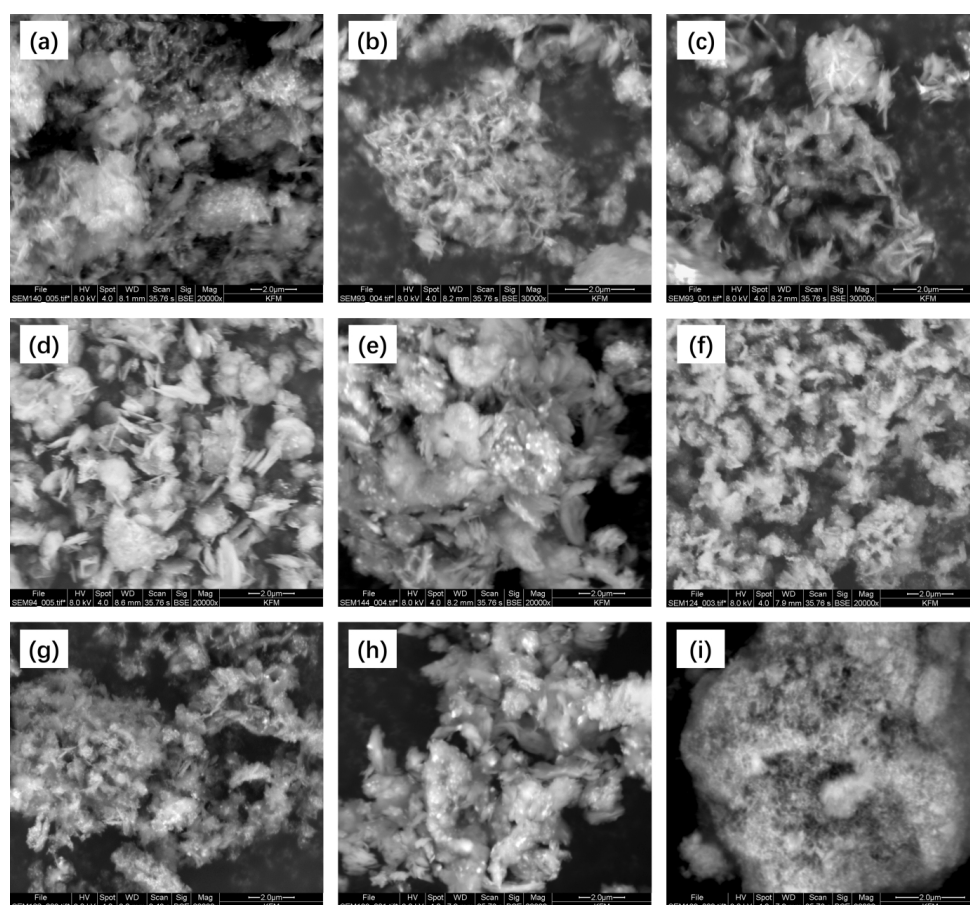
Figure 4-30. Scanning electron microscopy images of 10% Co loaded on (a, b, c) MCM-22(15), (d) MCM-22(30), (e) MCM-22(30)-B, (f) 10%Co/MCM-22(50), (g) MCM-22(50)-A, (h) MCM-36 and (i) MCM-56.

Lastly, before Co loading, FTIR spectra (**Figure 4-31 (a)**) showed that the intensity of adsorption band around 3621 cm^{-1} increased as concentration of Al atom in zeolite frameworks (or decreasing of Si/Al) (**Table 4-9**). This band is attributed to briging $\equiv$Si-OH-Al$\equiv$ group [102], indicating the concentration of Brønsted acid sites increase with decreasing of Si/Al in the zeolites. While band around 3747 cm^{-1} corresponding to external silanol groups (Si-OH) increased with external surface are (S$_{ext}$) and MCM-36 showed the highest intensity of this band.

After the Co loading, all the 10%Co/MWW materials showed reduced intensity of 3621 cm^{-1} band (**Figure 4-31 (b)**), indicating that a part of H$^+$ were replaced by Co^{2+} through ion exchange. Furthermore, the degree of H$^+$-to-Co^{2+} ion exchange enhanced as increasing the concentration of Brønsted acid site in MCM-22 zeolite supports, which followed the order of MCM-22(50)-A (38%) < MCM-22(50) (49%) < MCM-22(30) (57%) < MCM-22(15) (80%) (**Figure 4-32**). This may be related to increasing number of 2 neighboring $\equiv$Si-(OH)-Al$\equiv$ groups in zeolites with higher concentration of frameworks Al to balance the charges of Co^{2+} cations. On the other hand, among the 10%Co/MWW materials, 10%Co/MCM-36 showed the highest degree of H$^+$-to-Co^{2+} ion exchange (93%) (**Figure 4-32**), which explained by enhancement of access to Brønsted acid site of MCM-36 owing to its largest external surface area. In addition, compared with Co-free **MWW** zeolite supports, an increase in Lewis acid sites concentration was observed for all Co-supported materials (**Figure 4-32**), which should be come from the coordinatively unsaturated Co sites in Co/MWW materials.
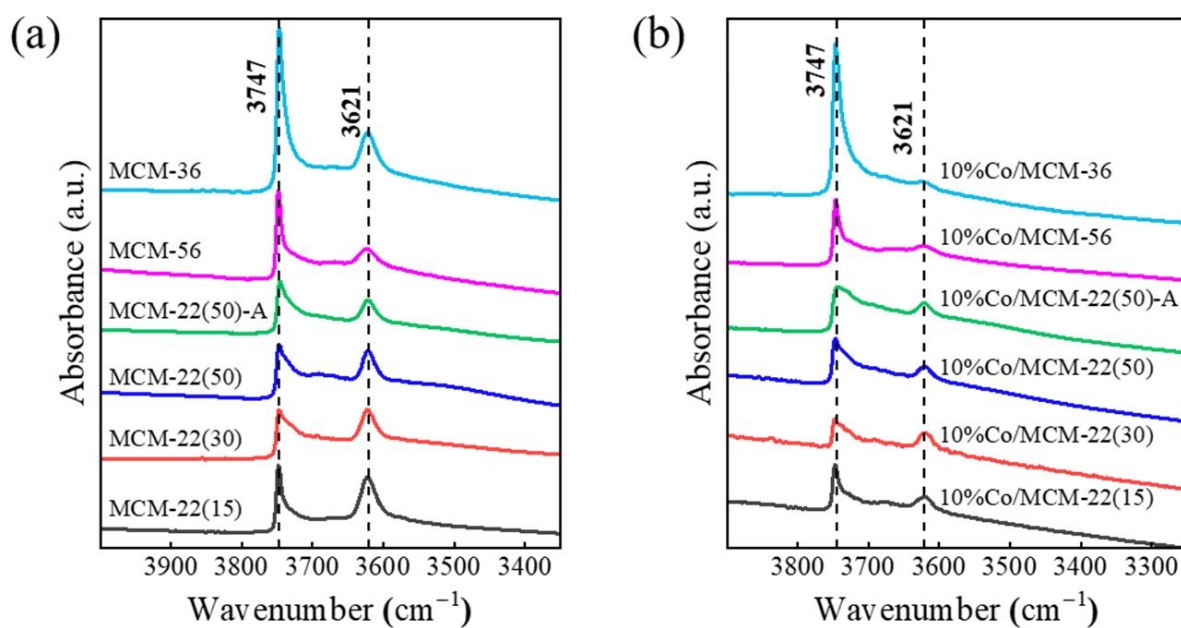
Figure 4-31. FTIR spectra of (a) MWW zeolites and 10%Co/MWW catalysts in the region of OH stretching vibration.
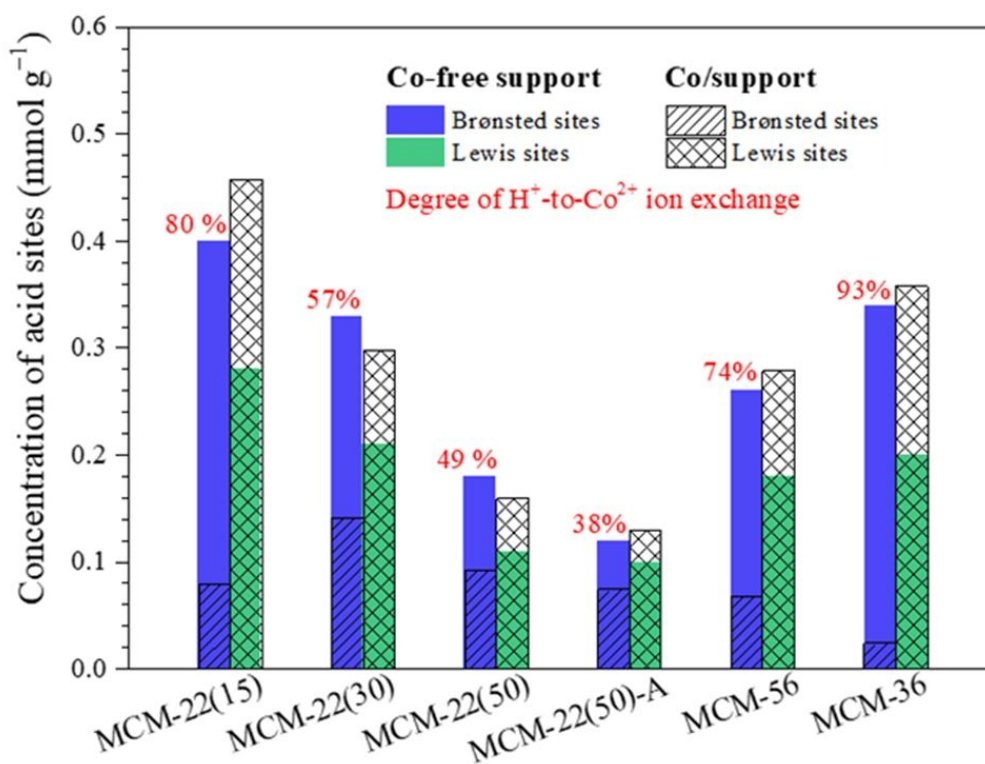
Figure 4-32. Evolution of acid sites on **MWW** zeolite supports upon impregnation with 10% cobalt.

4.4.2. Characterization of the state and reducibility of cobalt for Co₃O₄/MWW catalysts

DR UV-Vis, CO-FTIR, XPS and TEM were performed to identify the state of cobalt in Co/MWW materials.

The UV-Vis spectra (**Figure 4-33**) showed all the 10%Co/MWW contained three bands: 210 and 255 nm, assigned to Co^{2+} which resulted from ion exchange of H^+; 435 nm, assigned to octahedrally coordinated Co(III) and 720 nm corresponding to tetrahedrally coordinated Co(II) in the lattice of spinel Co_3O_4 [135].
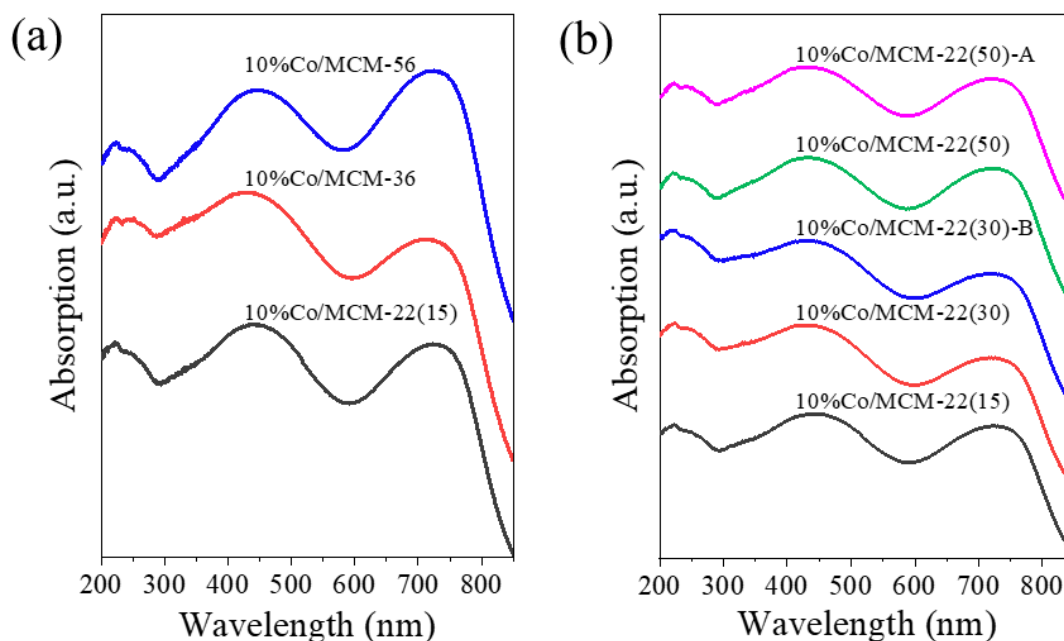
Figure 4-33. UV−vis DR spectra of the 10%Co/MWW catalysts.

In addition, in full agreement with UV-Vis characterization, the FTIR spectra of CO adsorbed in Co/MWW materials at room temperature (**Figure 4-34**) showed broad bands centered ca. 2200 cm⁻¹ accompanied by shoulders at ca. 2185 cm⁻¹. Based on the literature data, these two bands can be assigned to Co^{2+} resulted from ion exchange of H^+ and Co^{2+} in Co_3O_4, respectively [136]. Furthermore, regarding Co/MWW catalysts with different Si/Al, the absorption intensity of band around 2185 cm⁻¹ followed an order of 10%Co/MCM-22(30) ≈ 10%Co/MCM-22(15) < 10%Co/MCM-22(30) < 10%Co/MCM-22(50) < 10%Co/MCM-22(50)-A, reflecting Co^{2+} in Co_3O_4 accessible for interaction with CO probe.
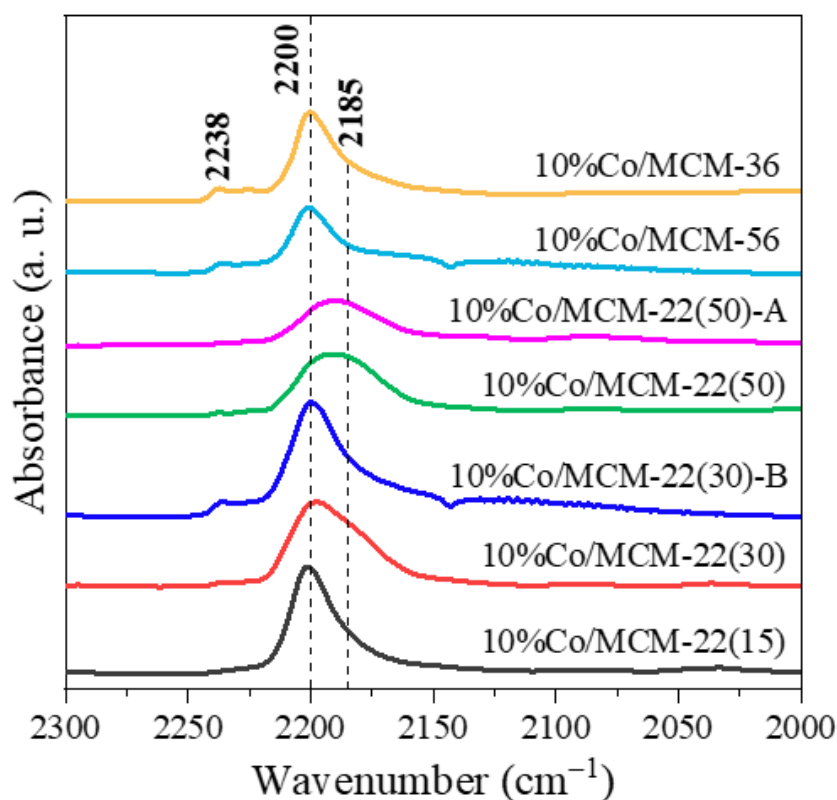
Figure 4-34. CO-FTIR spectra of the 10%Co/MWW catalysts at room temperature.

Moreover, in **Figure 4-35**, Co 2p XPS spectra of all 10%Co/MWW materials showed two peaks at ca. 781 and 796 eV, which could be assigned to Co $2p_{1/2}$ and Co $2p_{3/2}$ components [137], respectively. The presence of both peaks evidenced the main cobalt phase in Co/MWW samples were Co_3O_4.
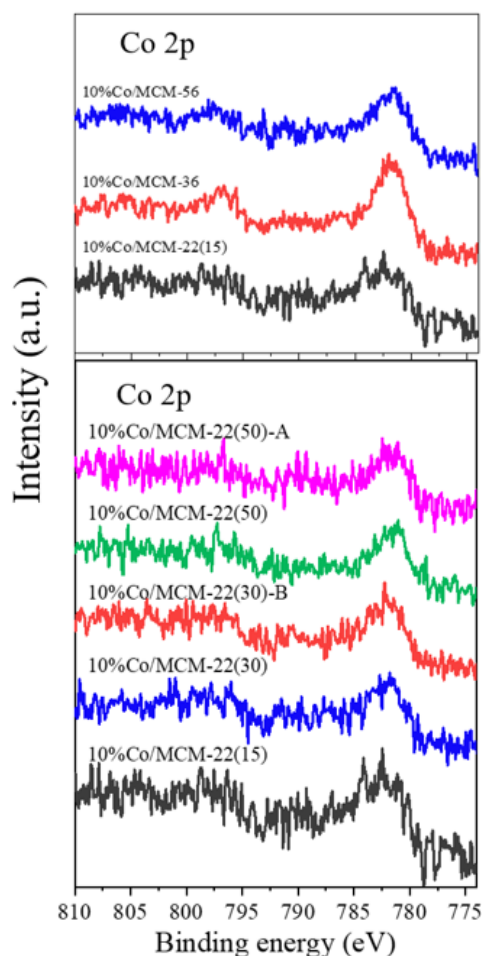
Figure 4-35. Co 2p XPS spectra of 10%Co/MWW catalysts.

Furthermore, the TEM images and elemental mapping provided additional information about the dispersion and state of Co on Co/MWW catalysts. For 10%Co/MCM-22(50)-A, Co_3O_4 nanoparticles (NPs) exhibited average particle size of 34 nm (**Figure 4-36 (a, b)**), larger than the XRD estimation (22 nm), which may be the agglomeration of smaller Co_3O_4 crystallites. In addition, lattice fringes of 0.154 nm d-spacing could be identified (**Figure 4-36 (c)**), which corresponded to the (511) planes of Co_3O_4 crystal. Moreover, the cobalt nanoparticle agglomeration formed mesopores could be observed, which may explain that the Co/MCM-22 samples showed increased mesopore volume than their Co-free supports. In consistency of SEM images, the elemental mapping of 10%Co/MCM-22(50)-A showed cobalt particle had uniform size and distribution on the MCM-22(50)-A support.
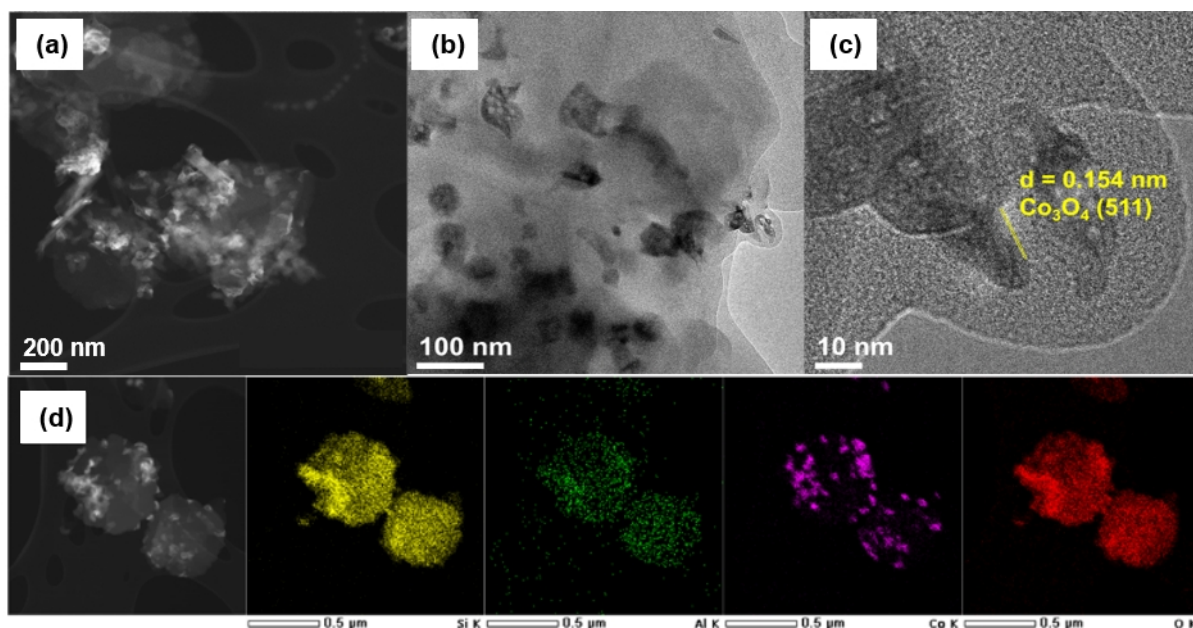
Figure 4-36. (a, b, c) TEM images and (d) elemental mapping of 10%Co/MCM-22(50)-A.

Lastly, the reducibility of Co species in Co/MWW catalysts was studied by CO-TPR. In the CO-TPR profiles (**Figure 4-37**), the CO consumption and CO_2 production curves matched very well in the temperature range. In **Figure 4-37 (a)**, all the samples showed one peak at ca. 300 and one broad peak at around 370 °C accompanied by a shoulder at around 425 °C, which can be accounted for stepwise reduction of cobalt, that were, Co(III) to Co(II), Co(II) to metallic Co respectively [138]. The shoulder peak may be related to the Co(II) species with strong interaction with the zeolite supports, which were harder to be reduced by CO. Compared to Co/MCM-22 materials, 10%Co/MCM-36 and 10%Co/MCM-56 showed higher temperature for the second reduction peak and simultaneously the shoulder peak. These results may relate to (i) an enhanced interaction of Co_3O_4 with MCM-36 and MCM-56 which contained higher fraction of surface silanols; (ii) a higher degree of H^+-to Co^{2+} ion exchange (74 and 92% for MCM-56 and MCM-36 supported samples, see **Figure 4-32**) formed more Co^{2+} species; (iii) poor dispersion of Co_3O_4 formed larger particles on MCM-36 and MCM-56 supports. In contrast, regarding Co/MCM-22 with various Si/Al, as increasing Si/Al in Co/MCM-22, the second reduction peak together with the shoulder peak shifted to lower temperatures. At the same time, the production of CO_2 increased as the increasing Si/Al. As a

result, 10%Co/MCM-22(50)-A showed the lowest reduction temperature, which may be attributed to the lowest degree of H^+-to Co^{2+} ion exchange (only 38%, see **Figure 4-32**) and very uniform dispersion of Co_3O_4 on this zeolite support.
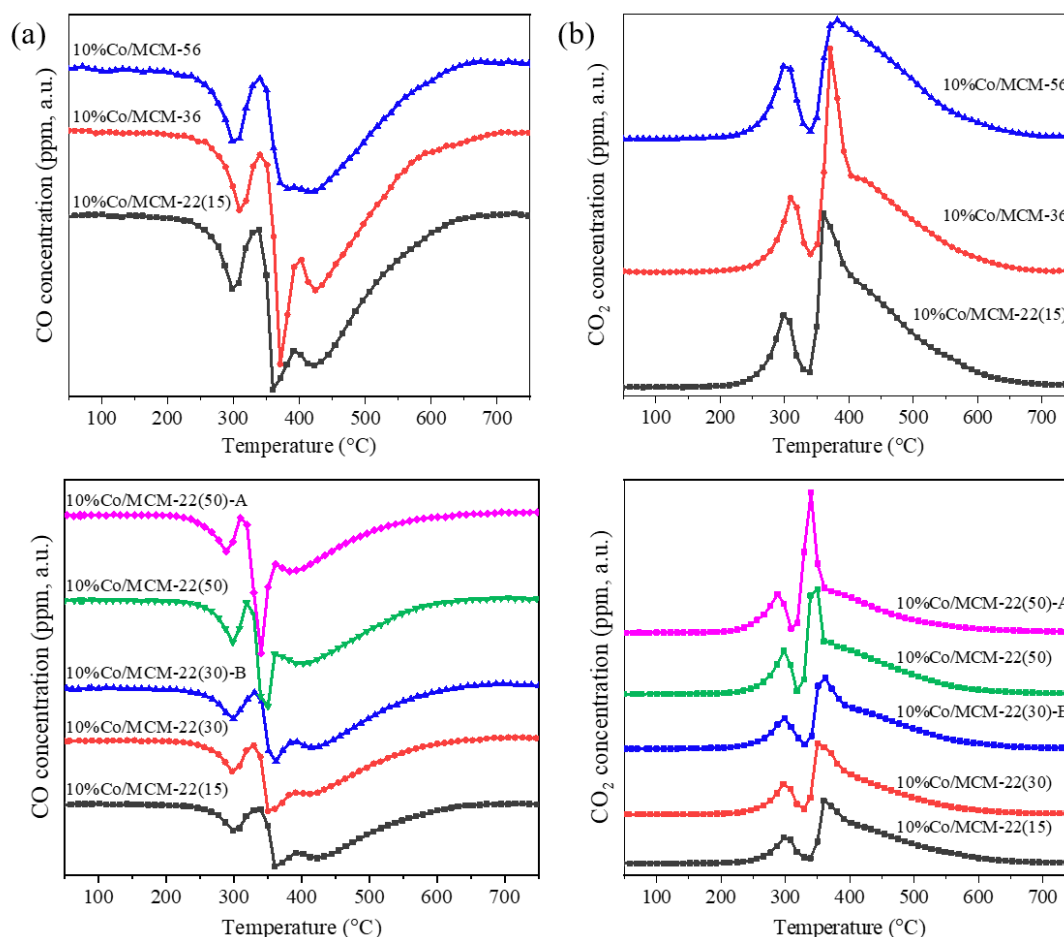
Figure 4-37. CO-TPR profiles (a) CO consumption and (b) CO_2 production of the 10%Co/MWW catalysts.

4.4.3. Catalytic performances of Co_3O_4/MWW for total oxidation of VOCs

A series of 10% Co/MWW materials characteristic of different architecture and Si/Al were prepared. It was observed that the architecture and acidity of zeolite supports showed great influences on the dispersion, phase state and reducibility of cobalt species.

10%Co/MWW materials were evaluated in total oxidation of VOCs. Toluene and propane are used as the preventatives of aromatic and alkanes to test the catalytic activity of the developed

Co/MWW materials. Catalytic performances of 10%Co/MWW for total oxidation of toluene and propane were displayed in **Table 4-10**, **4-11** and **Figure 4-38**. Three values of T_{10}, T_{50} and T_{90} are corresponded to reaction temperatures at 10%, 50% and 90% toluene or propane conversions. In the testing temperature range (150-350 °C), 10%Co/MCM-22(15), 10%Co/MCM-36 and 10%Co/MCM-56 could not reach complete conversion of toluene and propane. However, among them, 10% Co/MCM-22 showed a relatively higher activity for both toluene and propane conversion, reaching the T_{90} at 350 and 326 °C, respectively (**Table 4-10**). In contrast, 10% Co-supported on MCM-36 and MCM-56 showed higher temperature for conversion of toluene and propane under the same conditions (**Table 4-10**), suggesting the MCM-22 zeolite was a more suitable support to load cobalt than MCM-36 and MCM-56. In addition, the catalytic activity of toluene and propane oxidation over 10%Co/MCM-22(15), 10%Co/MCM-36 and 10%Co/MCM-56 was in line with the reducibility of cobalt on **MWW** supports, that was, the more reducible Co on MCM-22, the higher activity over Co/MCM-22 catalyst than MCM-36 and MCM-56 as supports.

Table 4-10. Light-off temperatures at 10, 50 and 90% toluene or propane conversions.

Catalyst	Toluene oxidation			Propane oxidation		
	T_{10}	T_{50}	T_{90}	T_{10}	T_{50}	T_{90}
10%Co/MCM-22	298	327	350	243	291	326
10%Co/MCM-36	308	334	>350	248	297	337
10%Co/MCM-56	304	331	>350	243	293	337

Regarding the 10%Co/MCM-22 with different Si/Al, dependence of toluene and propane conversion on the reaction temperature is shown in **Figure 4-38**, and their light-off temperatures of T_{10}, T_{50} and T_{90} are presented in **Table 4-11**. For all Co/MCM-22 catalysts, with regard to T_{10}, T_{50} and T_{90}, their activity for toluene and propane conversion followed the order of 10%Co/MCM-22(15) < 10%Co/MCM-22(30)-B < 10%Co/MCM-22(30) < 10%Co/MCM-22(50) < 10%Co/MCM-22(50)-A. 10% Co/MCM-22(50)-A reached the T_{90} at 307 and

295 °C for toluene and propane, respectively, which were lower temperatures achieved over other studied catalysts. Again, the conversion of toluene and propane oxidation to CO_2 over 10%Co/MCM-22 with different Si/Al (acidity) aligned perfectly with the reducibility of cobalt on MCM-22 supports. Therefore, the use of MCM-22(50)-A as Co support made it possible to prepare the Co-supported Co/MWW catalyst with the highest reducibility of Co_3O_4 and achieve the best catalytic performance in both reactions, which mainly be attributed to lack in framework Al limiting the undesirable H^+-to-Co^{2+} ion exchange and possesses low external surface area resulting in appropriate Co_3O_4 dispersion.
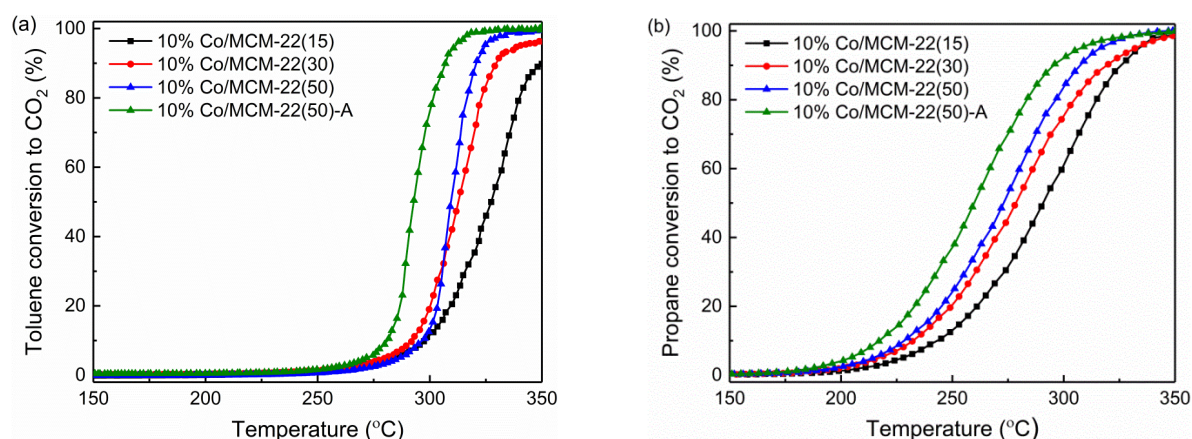
Figure 4-38. Dependence of (a) toluene and (b) propane conversions on the reaction temperature over 10%Co/MCM-22 catalysts with different Si/Al.

Table 4-11. Light-off temperatures at 10, 50 and 90% toluene or propane conversions.

Catalyst	Toluene oxidation			Propane oxidation		
	T_{10}	T_{50}	T_{90}	T_{10}	T_{50}	T_{90}
10%Co/MCM-22(15)	298	327	350	243	291	326
10%Co/MCM-22(30)	292	313	330	232	278	319
10%Co/MCM-22(30)-B	298	318	334	236	283	326
10%Co/MCM-22(50)	297	310	321	228	273	307
10%Co/MCM-22(50)-A	281	293	307	217	260	295

Overall, the investigation of the influence of zeolite properties as supports on dispersion, reducibility of catalytic active phase and following catalytic activity takes important role in design of active zeolite supported catalysts. Based on these results, in the next work, the Co/MCM-22(50)-A catalysts with different Co_3O_4 loading will be prepared and tested the activity in VOCs combustion as well.

5. Conclusions

This thesis was focused on i) designing specific zeolite materials using various synthesis methods, ii) comprehensively investigating the properties of these catalysts regarding their structure, chemical composition, and accessibility of acid sites and iii) establishing relationships between key characteristics of these materials and their catalytic performance in liquid- and gas-phase reactions.

A group of isoreticular Al-IPC-n zeolites (n = 2, 4, 6, 7) was prepared by combining ADOR structural transformations of parent **UTL** zeolites with isomorphous substitution (alumination). The resulting UTL-derived zeolites had similar morphology, Al content (Si/Al in isoreticular zeolites was around 20), and total acid sites concentrations. Simultaneously, their pore size and acid sites distributions could be adjusted by selecting an appropriate set of synthesis parameters. The results confirmed that isoreticular Al-IPC zeolites are an excellent set of model catalysts to study pore size-activity relationships. When assessing the catalytic activity, ethanol dehydration over all Al-IPC catalysts proceeded through the associative dehydration mechanism, and diethyl ether (DEE) was the main product. The rate of DEE production increased in the following order: IPC-4 < IPC-6 < IPC-2 < IPC-7. This sequence is perfectly in line with the increase in their pore size and "external" acid sites concentration, which contribute to enhancing the formation of ethanol dimer intermediates and their subsequent transformation into DEE.

In liquid-phase tetrahydropyranylation of alcohols, all Al-IPC catalysts behaved similarly in the tetrahydropyranylation of a small reactant, ethanol, providing complete conversion. When using bulkier alcohols (1-hexanol, 1-decanol) as reactants, the pore size and the concentration of "external" acid sites increased, and the conversion of the alcohols increased in the following order: IPC-4 < IPC-6 < IPC-2 < IPC-7, similarly to the ethanol dehydration test.

In summary, these FTIR and catalytic activity studies over Al-IPC-n zeolites offer direct evidence of the distribution of acid sites while simultaneously highlighting micropore size effects on their catalytic performances. Moreover, these **UTL**-derived isoreticular zeolites

could serve as perfect model catalyst to further our better understanding of catalyst pore size-activity relationships.

A new large-pore germanosilicate with **AFI** topology was also prepared and further aluminated to produce Al enriched **AFI** catalysts with Si/Al < 30, which has never been achieved using other synthesis methods, to compare the efficiency of one-step alumination and degermanation-alumination two-step routes for Al incorporation into **AFI** framework. The crystalline structure of **AFI** zeolites was not affected by the alumination treatments. However, the two-step route was more efficient in introducing Al^{3+} into framework positions and in avoiding blockage of the pore system caused by Ge leaching from the zeolite framework. In toluene alkylation with isopropyl alcohol, the two-step aluminated deGe-Al-AFI exhibited higher activity than the corresponding one-step aluminated catalyst thanks to its optimized zeolite porosity and the acidity. In addition, this two-step aluminated deGe-Al-AFI catalyst exhibited both relatively higher toluene conversion and selectivity to the *para*-isomer with higher commercial value. These results confirmed that post-synthetic isomorphous substitution is an efficient approach to tune the chemical composition of one-dimensional large-pore zeolites, thereby generating Al-enriched zeolite materials for appropriate catalytic applications.

MFI-nanosized zeolites with a crystal size of approximately 60 nm were synthesized hydrothermally and used to prepare aggregation-resistant materials by surface modification with silane agents. Surface silylation of nanosized-**MFI** maintained the zeolite crystallinity and structure. FTIR, TG analysis, NMR and N_2 adsorption confirmed that the organic silanes were successfully anchored onto the external surface of **MFI** nanocrystals, practically not affecting the pore system. Molecule size, number of hydrolyzable ethoxy groups (-O-CH_2CH_3) and hydrophobicity/hydrophilicity characteristics of silane played key roles in the resistance to aggregation of the resulting hybrid materials (static and catalytic stability). Compared with unfunctionalized **MFI** nanocrystals, the ethoxydimethylphenylsilane-modified sample showed improved stability in terms of crystal size preservation both in suspension and under harsh catalytic conditions. For p-xylene acylation with butyryl chloride,

reduced aggregation of **MFI** nanocrystals improved the accessibility of the acylation agent to acid sites, thus increasing butyryl chloride conversion. Therefore, surface modification with silanes of nanosized zeolites reduces their aggregation and consequently improves their catalytic activity, partly solving the underlying activity and stability issues of nanosized zeolites and enabling their application to a wider range of catalytic processes.

A series of cobalt containing **MWW**-type zeolite materials were synthesized through incipient wetness impregnation of $Co(NO_3)_2$ onto **MWW** zeolites with different layer arrangements (MCM-22/36/56) and chemical compositions (Si/Al ranging from 12 to 50) to understand the roles of these parameters in the catalytic elimination of VOCs. The results suggested that the architecture and acidity of **MWW**-type supports significantly affected dispersion and reducibility of cobalt species and consequently and their catalytic activity in toluene and propane oxidation reactions. Catalytic activity decreased in the following order: Co/MCM-22 > Co/MCM-36 > Co/MCM-56, in line with the reducibility of supported Co_3O_4. In addition, the reducibility of Co_3O_4 on Co/MCM-22 catalysts is positively related to the Si/Al of supports, and this trend is in good agreement with the oxidation of toluene and propane over Co/MCM-22. Therefore, among the Co/MWW catalysts, 10%Co/MCM-22(50)-A shows the highest catalytic activity at T_{90} (temperature for 90% conversion) values of 307 and 295 °C for toluene and propane, respectively. Ultimately, assessing the effects of specific properties of zeolites as supports on the dispersion and reducibility of the catalytic active phase and on the corresponding catalytic activity is crucial for the design of zeolite-supported catalysts with high activity in VOCs elimination.

In this thesis, key parameters of zeolite synthesis were correlated with their structural, textural and acidic properties and consequently with their catalytic performance (activity, selectivity and stability) over several sets of new layered and nanosized zeolites to unveil synthesis-property-activity relationships for the development and application of zeolite catalysts.

6. References

1. Database of zeolite structures. https://europe.iza-structure.org.
2. Csicsery, S. M., Shape-selective catalysis in zeolites. *Zeolites* **1984**, 4(3), 202-213.
3. Roduner, E., Understanding catalysis. *Chemical Society Reviews* **2014**, 43(24), 8226-8239.
4. van der Graaff, W. N. P., Tempelman, C. H., Pidko, E. A., Hensen, E. J., Influence of pore topology on synthesis and reactivity of Sn-modified zeolite catalysts for carbohydrate conversions. *Catalysis Science & Technology* **2017**, 7(14), 3151-3162.
5. Boronat, M., Corma, A., What is measured when measuring acidity in zeolites with probe molecules? *ACS catalysis* **2019**, 9(2), 1539-1548.
6. De, S., Dutta, S., Saha, B., Critical design of heterogeneous catalysts for biomass valorization: current thrust and emerging prospects. *Catalysis Science & Technology* **2016**, 6(20), 7364-7385.
7. Li, Y., Li, L., Yu, J., Applications of zeolites in sustainable chemistry. *Chem* **2017**, 3(6), 928-949.
8. Corma, A., From microporous to mesoporous molecular sieves materials and their use in catalysis. *Chemical Review* **1997**, 97(6), 2373–2420.
9. Vogt, E., Weckhuysen, B., Fluid catalytic cracking: Recent developments on the grand old lady of zeolite catalysis. *Chemical Society Reviews* **2015**, 44(20), 7342-7370.
10. Teng, J., Zhao, G., Xie, Z., Chen, Q., Effect of ZSM-5 zeolite crystal size on propylene production from catalytic cracking of C4 olefins. *Chinese Journal of Catalysis* **2004**, 25(8), 602-606.
11. Kloetstra, K. R., Van Bekkum, H., Base and acid catalysis by the alkali-containing MCM-41 mesoporous molecular sieve. *Journal of the Chemical Society, Chemical Communications* **1995**, 1005-1006.
12. Csihony, S., Mehdi, H., Horváth, I. T., In situ infrared spectroscopic studies of the Friedel-Crafts acetylation of benzene in ionic liquids using $AlCl_3$ and $FeCl_3$. *Green Chemistry* **2001**, 3(6), 307-309.
13. Gao, F., Walter, E. D., Karp, E. M., Luo, J., Tonkyn, R. G., Kwak, J. H., Szanyi, J., Peden, C. H., Structure-activity relationships in NH_3-SCR over Cu-SSZ-13 as probed by reaction kinetics and EPR studies. *Journal of Catalysis* **2013**, 300, 20-29.
14. Gao, F., Zheng, Y., Kukkadapu, R. K., Wang, Y., Walter, E. D., Schwenzer, B., Szanyi, J., Peden, C. H., Iron loading effects in Fe/SSZ-13 NH_3-SCR catalysts: Nature of the Fe ions and structure-function relationships. *ACS Catalysis* **2016**, 6(5), 2939-2954.
15. Iwasaki, M., Yamazaki, K., Banno, K., Shinjoh, H., Characterization of Fe/ZSM-5 $DeNO_x$ catalysts prepared by different methods: Relationships between active Fe sites and NH_3-SCR performance. *Journal of Catalysis* **2008**, 260(2), 205-216.
16. Wilken, N., Kamasamudram, K., Currier, N. W., Li, J., Yezerets, A., Olsson, L., Heat of adsorption for NH_3, NO_2 and NO on Cu-Beta zeolite using microcalorimeter for NH_3 SCR applications. *Catalysis Today* **2010**, 151, 237-243.

17. Lee, J. H., Kim, Y. J., Ryu, T., Kim, P. S., Kim, C. H., Hong, S. B., Synthesis of zeolite UZM-35 and catalytic properties of copper-exchanged UZM-35 for ammonia selective catalytic reduction. *Applied Catalysis B: Environmental* **2017**, 200, 428-438.

18. He, C., Cheng, J., Zhang, X., Douthwaite, M., Pattisson, S., Hao, Z., Recent advances in the catalytic oxidation of volatile organic compounds: A review based on pollutant sorts and sources. *Chemical Reviews* **2019**, 119(7), 4471-4568.

19. Barakat, T., Rooke, J. C., Tidahy, H. L., Hosseini, M., Cousin, R., Lamonier, J. F., Giraudon, J. M., De Weireld, G., Su, B. L., Siffert, S., Noble-metal-based catalysts supported on zeolites and macro-mesoporous metal oxide supports for the total oxidation of volatile organic compounds. *ChemSusChem* **2011**, 4(10), 1420-1430.

20. Chen, C., Wu, Q., Chen, F., Zhang, L., Pan, S., Bian, C., Zheng, X., Meng, X., Xiao, F. S., Aluminium-rich Beta zeolite-supported platinum nanoparticles for the low-temperature catalytic removal of toluene. *Journal of Materials Chemistry A* **2015**, 3(10), 5556-5562.

21. Rokicińska, A., Drozdek, M., Dudek, B., Gil, B., Michorczyk, P., Brouri, D., Dzwigaj, S., Kuśtrowski, P., Cobalt-containing BEA zeolite for catalytic combustion of toluene. *Applied Catalysis B: Environmental* **2017**, 212, 59-67.

22. Zhang, L., Xie, Y., Jiang, Y., Li, Y., Wang, C., Han, S., Luan, H., Meng, X. J., Xiao, F. S., Mn-promoted Ag supported on pure siliceous Beta zeolite (Ag/Beta-Si) for catalytic combustion of formaldehyde. *Applied Catalysis B: Environmental* **2020**, 268, 118461.

23. Roth, W. J., Nachtigall, P., Morris, R. E., Čejka, J., Two-dimensional zeolites: Current status and perspectives. *Chemical Reviews* **2014**, 114(9), 4807-4837.

24. Roth, W. J., Gil, B.; Makowski, W., Marszalek, B., Eliášová, P., Layer like porous materials with hierarchical structure. *Chemical Society Reviews* **2016**, 45(12), 3400-3438.

25. Xu, L., Sun, J., Recent Advances in the synthesis and application of two-dimensional zeolites. *Advanced Energy Materials* **2016**, 6(17), 1600441.

26. Ikeda, T., Kayamori, S., Mizukami, F., Synthesis and crystal structure of layered silicate PLS-3 and PLS-4 as a topotactic zeolite precursor. *Journal of Materials Chemistry* **2009**, 19(31), 5518-5525.

27. Moteki, T., Chaikittisilp, W., Shimojima, A., Okubo, T., Silica sodalite without occluded organic matters by topotactic conversion of lamellar precursor. *Journal of the American Chemical Society* **2008**, 130(47), 15780-15781.

28. Leonowicz, M. E., Lawton, J. A., Lawton, S. L., Rubin, M. K., MCM-22: A molecular sieve with two independent multidimensional channel systems. *Science* **1994**, 264(5167), 1910-1913.

29. Choi, M., Na, K., Kim, J., Sakamoto, Y., Terasaki, O., Ryoo, R., Stable single-unit-cell nanosheets of zeolite MFI as active and long-lived catalysts. *Nature* **2009**, 461(7261), 246-249.

30. Shvets, O. V., Konysheva, K. M., Shamzhy, M. V., Opanasenko, M. V., Yaremov, P. S., Xiao, C., Zou, X., Čejka, J., Mordenite nanorods and nanosheets prepared in presence of gemini type surfactants. *Catalysis Today* **2019**, 324, 115-122.

31. Eliášová, P., Opanasenko, M., Wheatley, P. S., Shamzhy, M., Mazur, M., Nachtigall, P., Roth, W. J., Morris, R. E., Čejka, J., The ADOR mechanism for the synthesis of new zeolites. *Chemical Society Reviews* **2015**, 44(20), 7177-7206.

32. Trachta, M., Bludský, O., Čejka, J., Morris, R. E., Nachtigall, P., From double-four-ring germanosilicates to new zeolites: In silico investigation. *ChemPhysChem* **2014**, 15(14), 2972-2976.

33. Roth, W. J., Nachtigall, P., Morris, R. E., Wheatley, P. S., Seymour, V. R., Ashbrook, S. E., Chlubná, P., Grajciar, L., Položij, M., Zukal, A., Čejka, J., A family of zeolites with controlled pore size prepared using a top-down method. *Nature Chemistry* **2013**, 5(7), 628-633.

34. Morris, S. A., Bignami, G. P., Tian, Y., Navarro, M., Firth, D. S., Čejka, J., Wheatley, P. S., Dawson, D. M., Slawinski, W. A., Wragg, D. S., In situ solid-state NMR and XRD studies of the ADOR process and the unusual structure of zeolite IPC-6. *Nature Chemistry* **2017**, 9(10), 1012-1018.

35. Wheatley, P. S., Chlubná-Eliášová, P., Greer, H., Zhou, W., Seymour, V. R., Dawson, D. M., Ashbrook, S. E., Pinar, A. B., McCusker, L. B., Opanasenko, M., Čejka, J., Morris, R. E., Zeolites with continuously tunable porosity. *Angewandte Chemie International Edition* **2014**, 53(48), 13210-13214.

36. Mazur, M., Wheatley, P. S., Navarro, M., Roth, W. J., Položij, M., Mayoral, A., Eliášová, P., Nachtigall, P., Čejka, J., Morris, R. E., Synthesis of 'unfeasible' zeolites. *Nature Chemistry* **2016**, 8(1), 58-62.

37. Wu, P., Ruan, J., Wang, L., Wu, L., Wang, Y., Liu, Y., Fan, W., He, M., Terasaki, O., Tatsumi, T., Methodology for synthesizing crystalline metallosilicates with expanded pore windows through molecular alkoxysilylation of zeolitic lamellar precursors. *Journal of the American Chemical Society* **2008**, 130(26), 8178-8187.

38. Xu, H., Fu, L., Jiang, J., He, M., Wu, P., Preparation of hierarchical MWW-type titanosilicate by interlayer silylation with dimeric silane. *Microporous Mesoporous Materials* **2014**, 189, 41-48.

39. Yang, B., Jiang, J. G., Xu, H., Wu, H., He, M., Wu, P., Synthesis of extra-large-pore zeolite ECNU-9 with intersecting 14*12-ring channels. *Angewandte Chemie-International Edition* **2018**, 130(30), 9659-9663.

40. Xu, H., Yang, B., Jiang, J., Jia, L., He, M., Wu, P., Post-synthesis and adsorption properties of interlayer-expanded PLS-4 zeolite. *Microporous and Mesoporous Materials* **2013**, 169, 88-96.

41. Mazur, M., Kubů, M., Wheatley, P. S., Eliášová, P., Germanosilicate UTL and its rich chemistry of solid-state transformations towards IPC-2 (OKO) zeolite. *Catalysis Today* **2015**, 243, 23-31.

42. Roth, W., Kresge, C., Vartuli, J., Leonowicz, M., Fung, A., McCullen, S., MCM-36: The first pillared molecular sieve with zeolite properties, *Studies in Surface Science and Catalysis*. Beyer, H. K., Karge, H. G., Kiricsi, I., Nagy, J. B., *Elsevier*, **1995**, Vol. 94, 301-308.

43. Kikhtyanin, O., Chlubná, P., Jindrová, T., Kubička, D., Peculiar behavior of MWW

materials in aldol condensation of furfural and acetone. *Dalton Transactions* **2014**, 43(27), 10628-10641.

44. Corma, A., Fornes, V., Pergher, S., Maesen, T. L., Buglass, J., Delaminated zeolite precursors as selective acidic catalysts. *Nature* **1998**, 396(6709), 353-356.

45. Ogino, I., Nigra, M. M., Hwang, S. J., Ha, J. M., Rea, T., Zones, S. I., Katz, A., Delamination of layered zeolite precursors under mild conditions: synthesis of UCB-1 via fluoride/chloride anion-promoted exfoliation. *Journal of the American Chemical Society* **2011**, 133(10), 3288-3291.

46. Žilková, N., Eliášová, P., Al-Khattaf, S., Morris, R. E., Mazur, M., Čejka, J., The effect of UTL layer connectivity in isoreticular zeolites on the catalytic performance in toluene alkylation. *Catalysis Today* **2016**, 277, 55-60.

47. Přech, J., Čejka, J., UTL titanosilicate: An extra-large pore epoxidation catalyst with tunable textural properties. *Catalysis Today* **2016**, 277, 2-8.

48. Zhou, Y., Kadam, S. A., Shamzhy, M., Čejka, J., Opanasenko, M., Isoreticular UTL-derived zeolites as model materials for probing pore size-activity relationship. *ACS Catalysis* **2019**, 9(6), 5136-5146.

49. Opanasenko, M. V., Roth, W. J., Čejka, J., Two-dimensional zeolites in catalysis: Current status and perspectives. *Catalysis Science & Technology* **2016**, 6(8), 2467-2484.

50. Corma, A., Fornes, V., Martınez-Triguero, J., Pergher, S., Delaminated zeolites: Combining the benefits of zeolites and mesoporous materials for catalytic uses. *Journal of Catalysis* **1999**, 186(1), 57-63.

51. Seo, Y., Cho, K., Jung, Y., Ryoo, R., Characterization of the surface acidity of MFI zeolite nanosheets by ^{31}P NMR of adsorbed phosphine oxides and catalytic cracking of decalin. *ACS Catalysis* **2013**, 3(4), 713-720.

52. Gong, P., Li, B., Kong, X., Liu, J., Zuo, S., Well-dispersed Ni nanoclusters on the surfaces of MFI nanosheets as highly efficient and selective catalyst for the hydrogenation of naphthalene to tetralin. *Applied Surface Science* **2017**, 423, 433-442.

53. Kim, W., Ryoo, R., Probing the catalytic function of external acid sites located on the MFI nanosheet for conversion of methanol to hydrocarbons. *Catalysis Letters* **2014**, 144(7), 1164-1169.

54. Hu, S., Shan, J., Zhang, Q., Wang, Y., Liu, Y., Gong, Y., Wu, Z., Dou, T., Selective formation of propylene from methanol over high-silica nanosheets of MFI zeolite. *Applied Catalysis A: General* **2012**, 445, 215-220.

55. Na, K., Jo, C., Kim, J., Ahn, W. S., Ryoo, R., MFI titanosilicate nanosheets with single-unit-cell thickness as an oxidation catalyst using peroxides. *ACS Catalysis* **2011**, 1(8), 901-907.

56. Wang, L., Wang, Y., Liu, Y., Chen, L., Cheng, S., Gao, G., He, M., Wu, P., Post-transformation of MWW-type lamellar precursors into MCM-56 analogues. *Microporous and Mesoporous Materials* **2008**, 113, 435-444.

57. Liu, G., Jiang, J., Yang, B., Fang, X., Xu, H., Peng, H., Xu, L., Liu, Y., Wu, P., Hydrothermal synthesis of MWW-type stannosilicate and its post-structural transformation to MCM-56 analogue. *Microporous and Mesoporous Materials* **2013**,

165, 210-218.

58. Luo, H. Y., Bui, L., Gunther, W. R., Min, E., Román-Leshkov, Y., Synthesis and catalytic activity of Sn-MFI nanosheets for the Baeyer-Villiger oxidation of cyclic ketones. *ACS Catalysis* **2012**, 2(12), 2695-2699.

59. Hartmann, M., Hierarchical zeolites: A proven strategy to combine shape selectivity with efficient mass transport. *Angewandte Chemie International Edition* **2004**, 43(44), 5880-5882.

60. Chen, L. H., Li, X. Y., Rooke, J. C., Zhang, Y. H., Yang, X. Y., Tang, Y., Xiao, F. S., Su, B. L., Hierarchically structured zeolites: synthesis, mass transport properties and applications. *Journal of Materials Chemistry* **2012**, 22(34), 17381-17403.

61. Millini, R., Zou, X., Strohmaier, K., Schwieger, W., Eliasova, P., Morris, R. E., Weckhuysen, B., Zhou, W., Abdo, S., Martinez, A., Zeolites in catalysis: properties and applications. *Royal Society of Chemistry*, **2017**, 527.

62. Zhang, Q., Chen, G., Wang, Y., Chen, M., Guo, G., Shi, J., Luo, J., Yu, J., High-quality single-crystalline MFI-type nanozeolites: A facile synthetic strategy and MTP catalytic studies. *Chemistry of Materials* **2018**, 30(8), 2750-2758.

63. Zhang, Q., Xiang, S., Zhang, Q., Wang, B., Mayoral, A., Liu, W., Wang, Y., Liu, Y., Shi, J., Yang, G., Breaking the Si/Al limit of nanosized Beta zeolites: Promoting catalytic production of lactide. *Chemistry of Materials* **2020**, 32(2), 751-758.

64. Mintova, S., Grand, J., Valtchev, V., Nanosized zeolites: Quo vadis? *Comptes Rendus Chimie* **2016**, 19, 183-191.

65. Mintova, S., Gilson, J. P., Valtchev, V., Advances in nanosized zeolites. *Nanoscale* **2013**, 5(15), 6693-6703.

66. de Moor, P. P. E., Beelen, T. P., Komanschek, B. U., Beck, L. W., Wagner, P., Davis, M. E., van Santen, R. A., Imaging the assembly process of the organic-mediated synthesis of a zeolite. *Chemistry–A European Journal* **1999**, 5(7), 2083-2088.

67. Valtchev, V. P., Tosheva, L., Bozhilov, K. N., Synthesis of zeolite nanocrystals at room temperature. *Langmuir* **2005**, 21(23), 10724-10729.

68. Dimitrov, L., Valtchev, V., Nihtianova, D., Kalvachev, Y., Submicrometer zeolite a crystals formation: Low-temperature crystallization versus vapor phase gel transformation. *Crystal Growth & Design* **2011**, 11(11), 4958-4962.

69. Ng, E. P., Chateigner, D., Bein, T., Valtchev, V., Mintova, S., Capturing ultrasmall EMT zeolite from template-free systems. *Science* **2012**, 335(6064), 70-73.

70. Awala, H., Gilson, J. P., Retoux, R., Boullay, P., Goupil, J. M., Valtchev, V., Mintova, S., Template-free nanosized faujasite-type zeolites. *Nature Materials* **2015**, 14(4), 447-451.

71. Majano, G., Darwiche, A., Mintova, S., Valtchev, V., Seed-induced crystallization of nanosized Na-ZSM-5 crystals. *Industrial & Engineering Chemistry Research* **2009**, 48(15), 7084-7091.

72. Iyoki, K., Kamimura, Y., Itabashi, K., Shimojima, A., Okubo, T., Synthesis of MTW-type zeolites in the absence of organic structure-directing agent. *Chemistry Letters* **2010**, 39(7), 730-731.

73. Yokoi, T., Yoshioka, M., Imai, H., Tatsumi, T., Diversification of RTH-type zeolite and

its catalytic application. *Angewandte Chemie International Edition* **2009**, 48(52), 9884-9887.

74. Majano, G., Delmotte, L., Valtchev, V., Mintova, S., Al-rich zeolite beta by seeding in the absence of organic template. *Chemistry of Materials* **2009**, 21(18), 4184-4191.

75. Louis, B., Vicente, A., Fernandez, C., Valtchev, V., Crystal size-acid sites relationship study of nano-and micrometer-sized zeolite crystals. *The Journal of Physical Chemistry C* **2011**, 115(38), 18603-18610.

76. Lee, J. Y., Park, S. M., Saha, S. K., Cho, S. J., Seo, G., Liquid-phase degradation of polyethylene (PE) over MFI zeolites with mesopores: Effects of the structure of PE and the characteristics of mesopores. *Applied Catalysis B: Environmental* **2011**, 108, 61-71.

77. Zhang, H., Ma, Y., Song, K., Zhang, Y., Tang, Y., Nano-crystallite oriented self-assembled ZSM-5 zeolite and its LDPE cracking properties: Effects of accessibility and strength of acid sites. *Journal of Catalysis* **2013**, 302, 115-125.

78. Konno, H., Tago, T., Nakasaka, Y., Ohnaka, R., Nishimura, J., Masuda, T., Effectiveness of nano-scale ZSM-5 zeolite and its deactivation mechanism on catalytic cracking of representative hydrocarbons of naphtha. *Microporous and Mesoporous Materials* **2013**, 175, 25-33.

79. Choo, M. Y., Juan, J. C., Oi, L. E., Ling, T. C., Ng, E. P., Noorsaadah, A. R., Centi, G., Lee, K. T., The role of nanosized zeolite Y in the H_2-free catalytic deoxygenation of triolein. *Catalysis Science & Technology* **2019**, 9(3), 772-782.

80. Mintova, S., Jaber, M., Valtchev, V., Nanosized microporous crystals: Emerging applications. *Chemical Society Reviews* **2015**, 44(20), 7207-7233.

81. Grand, J., Talapaneni, S. N., Vicente, A., Fernandez, C., Dib, E., Aleksandrov, H. A., Vayssilov, G. N., Retoux, R., Boullay, P., Gilson, J. P., One-pot synthesis of silanol-free nanosized MFI zeolite. *Nature Materials* **2017**, 16(10), 1010-1015.

82. Guo, Z., Li, X., Hu, S., Ye, G., Zhou, X., Coppens, M. O., Understanding the role of internal diffusion barriers in Pt/Beta zeolite catalyzed isomerization of n-Heptane. *Angewandte Chemie International Edition* **2020**, 132(4), 1564-1567.

83. Shang, C., Wu, Z., Wu, W. D., Chen, X. D., Chemical crosslinking assembly of ZSM-5 nanozeolites into uniform and hierarchically porous microparticles for high-performance acid catalysis. *ACS Applied Materials & Interfaces* **2019**, 11(18), 16693-16703.

84. Dubray, F., Moldovan, S., Kouvatas, C., Grand, J., Aquino, C., Barrier, N., Gilson, J. P., Nesterenko, N., Minoux, D., Mintova, S., Direct evidence for single molybdenum atoms incorporated in the framework of MFI zeolite nanocrystals. *Journal of the American Chemical Society* **2019**, 141(22), 8689-8693.

85. Chen, H., Zhou, Y., Tošner, Z., Čejka, J., Opanasenko, M., Synthesis of aggregation-resistant MFI nanoparticles. *Catalysis Today* **2019**, 10.1016/j.cattod.2019.10.026.

86. Breck, D. W., Sieves, Z. M., Zeolite Molecular Sieves: Structure, chemistry and use. *Wiley, New York* **1974**, 772.

87. Shamzhy, M., Opanasenko, M., Concepción, P., Martínez, A., New trends in tailoring active sites in zeolite-based catalysts. *Chemical Society Reviews* **2019**, 48(4), 1095-

1149.

88. Tang, B., Dai, W., Sun, X., Guan, N., Li, L., Hunger, M., A procedure for the preparation of Ti-Beta zeolites for catalytic epoxidation with hydrogen peroxide. *Green Chemistry* **2014**, 16(4), 2281-2291.

89. Dessau, R., Kerr, G., Aluminum incorporation into high silica zeolites. *Zeolites* **1984**, 4(4), 315-318.

90. Sulikowski, B., Rakoczy, J., Hamdan, H., Klinowski, J., Structural and catalytic consequences of isomorphous substitution of silicon by aluminum and vice versa in the framework of pentasil zeolites. *Journal of the Chemical Society, Chemical Communications* **1987**, 20, 1542-1543.

91. Chen, C. Y., Zones, S. I., Post-synthetic treatment and modification of zeolites. *Zeolites and Catalysis: Synthesis, Reactions and Applications* **2010**, 155-170.

92. Shamzhy, M. V., Eliašová, P., Vitvarová, D., Opanasenko, M. V., Firth, D. S., Morris, R. E., Post-synthesis stabilization of germanosilicate zeolites ITH, IWW, and UTL by substitution of Ge for Al. *Chemistry–A European Journal* **2016**, 22(48), 17377-17386.

93. Zhou, Y., Žilková, N., Shamzhy, M., Avadhut, Y., Hartmann, M., Čejka, J., Opanasenko, M., Novel approach towards Al-rich AFI for catalytic application. *Applied Catalysis A: General* **2019**, 577, 62-68.

94. Gao, F., Jaber, M., Bozhilov, K., Vicente, A., Fernandez, C., Valtchev, V., Framework stabilization of Ge-rich zeolites via postsynthesis alumination. *Journal of the American Chemical Society* **2009**, 131(45), 16580-16586.

95. Bai, R., Sun, Q., Wang, N., Zou, Y., Guo, G., Iborra, S., Corma, A., Yu, J., Simple quaternary ammonium cations-templated syntheses of extra-large pore germanosilicate zeolites. *Chemistry of Materials* **2016**, 28(18), 6455-6458.

96. Jiang, J., Jorda, J. L., Diaz-Cabanas, M. J., Yu, J., Corma, A., The Synthesis of an extra-large-pore zeolite with double three-ring building units and a low framework density. *Angewandte Chemie International Edition* **2010**, 49(29), 4986-4988.

97. Shvets, O. V., Zukal, A., Kasian, N., Žilková, N., Čejka, J., The role of crystallization parameters for the synthesis of germanosilicate with UTL topology. *Chemistry–A European Journal* **2008**, 14(32), 10134-10140.

98. Shvets, O., Kasian, N., Zukal, A., Pinkas, J., Čejka, J., The role of template structure and synergism between inorganic and organic structure directing agents in the synthesis of UTL zeolite. *Chemistry of Materials* **2010**, 22(11), 3482-3495.

99. Shamzhy, M. V., Shvets, O. V., Opanasenko, M. V., Yaremov, P. S., Sarkisyan, L. G., Chlubná, P., Zukal, A., Marthala, V. R., Hartmann, M., Čejka, J., Synthesis of isomorphously substituted extra-large pore UTL zeolites. *Journal of Materials Chemistry* **2012**, 22(31), 15793-15803.

100. Kadam, S. A., Shamzhy, M. V., IR operando study of ethanol dehydration over MFI zeolite. *Catalysis Today* **2018**, 304, 51-57.

101. Hsien-Ming, K., Chen Y. C., ^{27}Al and ^{19}F solid-state NMR studies of zeolite H-β dealuminated with ammonium hexafluorosilicate. *The Journal of Physical Chemistry B* **2003**, 107(15), 3367-3375.

102. Ryczkowski, J., IR spectroscopy in catalysis. *Catalysis Today* **2001**, 68(4), 263-381.

103. El-Malki, E. M., Van Santen, R. A., Sachtler, W. M. H., Introduction of Zn, Ga, and Fe into HZSM-5 cavities by sublimation: Identification of acid sites. *The Journal of Physical Chemistry B* **1999**, 103(22), 4611-4622.

104. Rutkowska, M., Macina, D., Mirocha-Kubień, N., Piwowarska, Z., Chmielarz, L., Hierarchically structured ZSM-5 obtained by desilication as new catalyst for DME synthesis from methanol. *Applied Catalysis B: Environmental* **2015**, 174, 336-343.

105. Takahara, I., Saito, M., Inaba, M., Murata, K., Dehydration of ethanol into ethylene over solid acid catalysts. *Catalysis Letters* **2005**, 105, 249-252.

106. Chiang, H., Bhan, A., Catalytic consequences of hydroxyl group location on the rate and mechanism of parallel dehydration reactions of ethanol over acidic zeolites. *Journal of Catalysis* **2010**, 271(2), 251-261.

107. Blaszkowski, S. R., van Santen, R. A., Theoretical study of C-C bond formation in the methanol-to-gasoline process. *Journal of the American Chemical Society* 1997, 119(21), 5020-5027.

108. Kadam, S. A., Shamzhy, M. V., IR operando study of ethanol dehydration over MFI zeolites: Structure-activity relationships. *The Journal of Physical Chemistry C* **2018**, 122(42), 24055-24067.

109. Carr, R. T., Neurock, M., Iglesia, E., Catalytic consequences of acid strength in the conversion of methanol to dimethyl ether. *Journal of Catalysis* **2011**, 278(1), 78-93.

110. Jones, A. J., Zones, S. I., Iglesia, E., Implications of transition state confinement within small voids for acid catalysis. *The Journal of Physical Chemistry C* **2014**, 118(31), 17787-17800.

111. Naik, S., Gopinath, R., Patel, B. K., Tetrabutylammonium tribromide (TBATB)-promoted tetrahydropyranylation/depyranylation of alcohols. *Tetrahedron Letters* **2001**, 42(43), 7679-7681.

112. Martínez-Franco, R., Paris, C., Martínez-Armero, M. E., Martínez, C., Moliner, M., Corma, A., High-silica nanocrystalline Beta zeolites: Efficient synthesis and catalytic application. *Chemical Science* **2016**, 7(1), 102-108.

113. Zhang, H., Wang, L., Zhang, D., Meng, X., Xiao, F. S., Mesoporous and Al-rich MFI crystals assembled with aligned nanorods in the absence of organic templates. *Microporous and Mesoporous Materials* **2016**, 233, 133-139.

114. Ito, A., Maekawa, H., Kawagoe, H., Komura, K., Kubota, Y., Sugi, Y., Shape-selective alkylation of biphenyl over H-[Al]-SSZ-24 zeolites with AFI topology. *Bulletin of the Chemical Society of Japan* **2007**, 80(1), 215-223.

115. Liu, Y., Zhang, B., Liu, D., Sheng, P., Lai, Z., Fabrication and molecular transport studies of highly c-oriented AFI membranes. *Journal of Membrane Science* **2017**, 528, 46-54.

116. Bandyopadhyay, R., Kubota, Y., Sugimoto, N., Fukushima, Y., Sugi, Y., Synthesis of borosilicate zeolites by the dry gel conversion method and their characterization. *Microporous and mesoporous materials* **1999**, 32, 81-91.

117. Lobo, R. F., Davis, M. E., Synthesis and characterization of pure-silica and boron-

substituted SSZ-24 using N (16) methylsparteinium bromide as structure-directing agent. *Microporous Materials* **1994**, 3, 61-69.

118. Roberge, D. M., Hausmann, H., Hölderich, W. F., Dealumination of zeolite beta by acid leaching: A new insight with two-dimensional multi-quantum and cross polarization ^{27}Al MAS NMR. *Physical Chemistry Chemical Physics* **2002**, 4(13), 3128-3135.

119. Corma, A., Fornés, V., Forni, L., Márquez, F., Martınez-Triguero, J., Moscotti, D., 2, 6-Di-tert-butyl-pyridine as a probe molecule to measure external acidity of zeolites. *Journal of Catalysis* **1998**, 179(2), 451-458.

120. Portilla, M. T., Llopis, F. J., Martínez, C., Valencia, S., Corma, A., Structure-reactivity relationship for aromatics transalkylation and isomerization process with TNU-9, MCM-22 and ZSM-5 zeolites, and their industrial implications. *Applied Catalysis A: General* **2011**, 393, 257-268.

121. Čejka, J., Kapustin, G. A., Wichterlová, B., Factors controlling iso-/n- and para-selectivity in the alkylation of toluene with isopropanol on molecular sieves. *Applied Catalysis A: General* **1994**, 108(2), 187-204.

122. Zhu, Z., Chen, Q., Zhu, W., Kong, D., Li, C., Catalytic performance of MCM-22 zeolite for alkylation of toluene with methanol. *Catalysis Today* **2004**, 93, 321-325.

123. Perego, C., Ingallina, P., Combining alkylation and transalkylation for alkylaromatic production. *Green Chemistry* **2004**, 6(6), 274-279.

124. Wichterlova, B., Čejka, J., Mechanism of n-propyltoluene formation in C3 alkylation of toluene: The effect of zeolite structural type. *Journal of Catalysis* **1994**, 146(2), 523-529.

125. Mohammadparast, F., Halladj, R., Askari, S., The crystal size effect of nano-sized ZSM-5 in the catalytic performance of petrochemical processes: A review. *Chemical Engineering Communications* **2015**, 202(4), 542-556.

126. Zhang, L., Chen, K., Chen, B., White, J. L., Resasco, D. E., Factors that determine zeolite stability in hot liquid water. *Journal of the American Chemical Society* **2015**, 137(36), 11810-11819.

127. Zhang, K., Lively, R. P., Noel, J. D., Dose, M. E., McCool, B. A., Chance, R. R., Koros, W. J., Adsorption of water and ethanol in MFI-type zeolites. *Langmuir* **2012**, 28(23), 8664-8673.

128. Thomas, J. M., Klinowski, J., Ramdas, S., Hunter, B. K., Tennakoon, D. T., The evaluation of non-equivalent tetrahedral sites from ^{29}Si NMR chemical shifts in zeolites and related aluminosilicates. *Chemical Physics Letters* **1983**, 102, 158-162.

129. De Castro, C., Primo, J., Corma, A., Heteropolyacids and large-pore zeolites as catalysts in acylation reactions using α, β-unsaturated organic acids as acylating agents. *Journal of Molecular Catalysis A: Chemical* **1998**, 134, 215-222.

130. Yadav, G. D., Pujari, A. A., Friedel-Crafts acylation using sulfated zirconia catalyst. *Green Chemistry* **1999**, 1(2), 69-74.

131. Bejblova, M., Prochazkova, D., Čejka, J., Acylation reactions over zeolites and mesoporous catalysts. *ChemSusChem: Chemistry & Sustainability Energy & Materials* **2009**, 2(6), 486-499.

132. Kurfiřtová, L., Seo, Y. K., Hwang, Y. K., Chang, J. S., Čejka, J., High activity of iron containing metal-organic-framework in acylation of p-xylene with benzoyl chloride. *Catalysis Today* **2012**, 179(1), 85-90.

133. Zhu, Z., Lu, G., Zhang, Z., Guo, Y., Guo, Y., Wang, Y., Highly active and stable Co_3O_4/ZSM-5 catalyst for propane oxidation: Effect of the preparation method. *ACS Catalysis* **2013**, 3(6), 1154-1164.

134. Hu, F., Peng, Y., Chen, J., Liu, S., Song, H., Li, J., Low content of CoO_x supported on nanocrystalline CeO_2 for toluene combustion: The importance of interfaces between active sites and supports. *Applied Catalysis B: Environmental* **2019**, 240, 329-336.

135. Chen, Y., Zhang, Y., Fu, S., Synthesis and characterization of Co_3O_4 hollow spheres. *Materials Letters* **2007**, 61(3), 701-705.

136. Sun, X., Sartipi, S., Kapteijn, F., Gascon, J., Effect of pretreatment atmosphere on the activity and selectivity of Co/meso HZSM-5 for Fischer-Tropsch synthesis. *New Journal of Chemistry* **2016**, 40(5), 4167-4177.

137. Si, J., Xiao, S., Wang, Y., Zhu, L., Xia, X., Huang, Z., Gao, Y., Sub-nanometer Co_3O_4 clusters anchored on TiO_2 (B) nano-sheets: Pt replaceable Co-catalysts for H_2 evolution. *Nanoscale* **2018**, 10(5), 2596-2602.

138. Potoczna-Petru, D., Kępiński, L., Reduction study of Co_3O_4 model catalyst by electron microscopy. *Catalysis Letters* **2001**, 73(1), 41-46.

7. Enclosures

1. Yong Zhou, Shashikant A. Kadam, Mariya Shamzhy, Jiří Čejka, Maksym Opanasenko. Isoreticular UTL-derived zeolites as model materials for probing pore size-activity relationship. ACS Catalysis, 9(2019), 5136-5146. doi.org/10.1021/acscatal.9b00950.

2. Yong Zhou, Naděžda Žilková, Mariya Shamzhy, Yamini Avadhut, Martin Hartmann, Jiří Čejka, Maksym Opanasenko. Novel approach towards Al-rich AFI for catalytic application. Applied Catalysis A: General, 577(2019), 62-68. doi.org/10.1016/j.apcata.2019.03.015

3. Hua Chen, Yong Zhou, Zdeněk Tošner, Jiří Čejka, Maksym Opanasenko. Synthesis of aggregation-resistant MFI nanoparticles. Catalysis Today, (2019). doi.org/10.1016/j.cattod.2019.10.026.

# Isoreticular UTL-Derived Zeolites as Model Materials for Probing Pore Size−Activity Relationship

Yong Zhou, Shashikant A. Kadam, Mariya Shamzhy,* Jiří Čejka, and Maksym Opanasenko*

Department of Physical and Macromolecular Chemistry, Faculty of Science, Charles University in Prague, Hlavova 8, 128 43 Prague 2 Czech Republic

S *Supporting Information*

ABSTRACT: The relationship between the chemical composition and the activity of zeolites has been unambiguously established and used to optimize some reactions. However, the relationship between the micropore size and the activity of catalysts remains elusive. Here, we report the combination of the ADOR approach and postsynthetic alumination for the preparation of isoreticular Al−IPC materials as model catalysts to assess the effect of micropore size on their catalytic activity. XRD, SEM, N_2 ad-/desorption, chemical analysis, ^{27}Al NMR, and FTIR spectroscopy of adsorbed acetonitrile-d_3 show that the prepared isoreticular Al−IPC zeolites have similar Al content and coordination states as well as similar types and total numbers of acid sites but differ in micropore size, decreasing in the following order: Al−IPC-7 (14, 12, and 10-ring channels) > Al−IPC-2 (12 and 10) > Al−IPC-6 (12, 10, and 8) > Al−IPC-4 (10 and 8). Furthermore, the kinetic study of gas-phase ethanol-to-diethyl ether transformation evidenced a lack of confinement in ethanol dimers of IPC-6 and IPC-4 (k_{first} = 0.4−0.9 mol_{DEE} $(mol_{H_+}\cdot s)^{-1}$) compared with IPC-2 (k_{first} = 3.8 mol_{DEE} $(mol_{H_+}\cdot s)^{-1}$) and IPC-7 (k_{first} = 6.3 mol_{DEE} $(mol_{H_+}\cdot s)^{-1}$) zeolites. The catalytic activity of IPC-zeolites in liquid-phase tetrahydropyranylation was correlated with the relative concentration of acid sites on the external surface of Al−IPC-*n* crystals, both increasing in the following order: IPC-4 (35% of "external" acid sites) < IPC-6 (29%) < IPC-2 (25%) < IPC-7 (21%). The use of Al−IPC-*n* as model catalysts in important acid-catalyzed reactions can shed a light on the fundamental structure−activity relationship and help to improve or optimize existing catalytic processes.

KEYWORDS: *UTL zeolite, ADOR, acid sites, ethanol dehydration, tetrahydropyranylation*
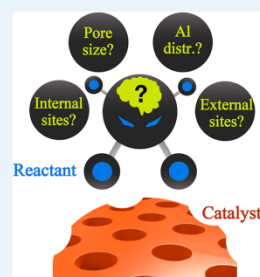
1. INTRODUCTION

Zeolites are a class of porous materials traditionally applied in industrial processes, such as fluid catalytic cracking,[1,2] hydro-cracking[3] and alkylation.[4] Recently emerging applications of zeolites have been extended to the production of fine chemicals.[5,6] The performance of zeolite catalysts (activity, selectivity) largely depends on both pore size/connectivity (e.g., 8-, 10-, and 12-rings or even larger pore openings and one-, two-, or three-dimensional channel systems) and framework composition (e.g., Si/Al ratios).[7–10] The relationship between the chemical composition and the activity of zeolites has been unambiguously established and used to optimize some processes, such as dehydrogenation,[7,8] esterification,[9] and methanol to olefin (MTO) reactions.[10] In contrast, the effect of the distribution of active centers among pores of different sizes (which plays a role, e.g., in the stabilization of particular intermediates and products) on the catalytic performance of zeolites has been difficult to establish because variations in zeolite pore structure are necessarily accompanied by changes in zeolite topology. On the other hand, the comparison of the catalytic activity of zeolites with the same structure and chemical composition but with different micropore sizes enables a fair analysis of the role of micropore size in a specific reaction.

The recently developed unconventional zeolite synthesis method, ADOR (assembly disassembly organization−reassem-bly),[11–13] is an appropriate method for designing zeolites with predefined structure and porosity.[14–19] In particular, the ADOR transformation of UTL germanosilicate is a facile route to produce a set of isoreticular IPC zeolites[17–20] (Table 1), i.e., zeolites with the same crystalline layers but with different interlayer connectivity, represented by simple building units, as shown in Figure 1.
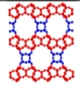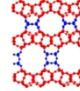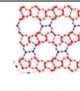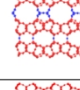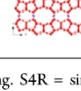
The UTL framework can be regarded as silicon-rich layers connected by germanium-rich, double-four-ring units (D4R).[21,22] The outcome of the UTL transformation via the ADOR process strongly depends on the acidity of the reaction medium because two competing processes are involved: rearrangement and deintercalation.[12,18] High acidity favors the rearrangement of silica at the interlayer sites, thus leading to the IPC-2 zeolite with single four-ring (S4R) interlayer connections.[17,23] Complete removal of species from the interlayer space, facilitated under neutral or mild acidic conditions, results in the formation of the IPC-4 zeolite with only oxygen bridges between layers.[17] When optimized conditions were applied, other new zeolites combining D4Rs, S4Rs, and oxygen bridges could be produced (Table 1). The IPC-7 zeolite containing both

Table 1. Structure of UTL and IPC-*n* Zeolites[a]

Zeolite		Interlayer connection	Channel size, Å					
			14-ring	12-ring	12-ring	10-ring	10-ring	8-ring
UTL		D4R	9.5× 7.1	8.5× 5.5				
IPC-7		D4R, S4R	9.5× 7.1	8.5× 5.5	6.6× 6.2	5.4× 5.3		
IPC-2		S4R			6.6× 6.2	5.4× 5.3		
IPC-6		S4R, oxygen			6.6× 6.2	5.4× 5.3	5.8× 3.8	4.5× 3.6
IPC-4		oxygen					5.8× 3.8	4.5× 3.6

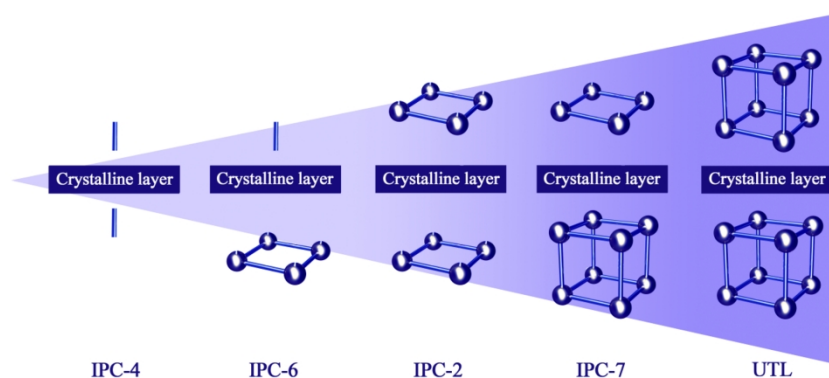[a]D4R = double four-ring. S4R = single four-ring.

Figure 1. Examples of the alternating units that connect layers of the same structure in isoreticular zeolites. Spheres depict T atoms (Si, Al, Ge), whereas lines depict oxygen bridges.

D4Rs and S4Rs in a 1:1 ratio can be synthesized in acidic solutions at approximately $[H^+]$ = 3 M, whereas the IPC-6 zeolite containing both S4Rs and oxygen bridges units can be synthesized at approximately $[H^+]$ = 1.5 M.[18]

A comprehensive study of UTL and IPC-*n* zeolites by X-ray powder diffraction, transmission electron microscopy, Ar physisorption, and annihilation lifetime spectroscopy[24] showed the isoreticular character of the IPC-*n* family. The structure and composition identity of IPC-*n* zeolites with various micropore sizes enabled us to assess the effect of micropore structure on carbon dioxide adsorption.[25] This family of isoreticular zeolites with tunable porosity may also be used to address the effect of micropore size on the catalytic performance.[26,27]

Žilková et al.[28] have attempted to address the effect of UTL layer connectivity in isoreticular zeolites on their catalytic performance in toluene alkylation. However, significant differ-

ences in Al content (Si/Al = 13−109) with a large fraction of extra-framework Al atoms in IPC-*n* catalysts prevented them from reaching clear conclusions on the micropore structure–activity relationship. Therefore, the synthesis of isoreticular IPC catalysts with Al atoms predominantly located at framework positions and with similar Al content and acidity remains a considerable challenge.

Conversely, the specific location of the acid sites is known to affect the catalytic activity and selectivity of Al-containing zeolites.[29−32] Since the structure of IPC zeolites prepared under different conditions varies, the location of acid sites within individual zeolites could also vary. Matsunaga et al.[33,34] studied the location of Brønsted and Lewis acid sites in several MCM-22-type zeolites using IR methods with N_2, CO, hexamethylenimine, or pivalonitrile as probe molecules and found that the reactivity of MWW catalysts in the MPV reduction of different ketones depends on the location of active Lewis acid sites. Wang et al.[35−37] revealed that Al atoms preferably occupy intersectional T sites in H-ZSM-5. In contrast, these atoms are mainly located in the straight 10-ring channel of H-ZSM-11, as shown by several spectroscopy methods, *p*-xylene isomerization, and DFT calculations. These results clearly show that Al siting or the distribution of acid sites strongly affects the catalytic performance in MTO. Therefore, the effects of the location of acid sites and of the types of Al species in frameworks with different pore systems on the catalytic activity of the respective zeolites must be assessed to improve or optimize the corresponding catalytic processes.

In this work, we report the combination between the ADOR approach and postsynthetic alumination for the preparation of isoreticular Al−IPC zeolites without extra-framework Al and with a similar concentration of acid sites in micropores of different sizes. The structural and textural properties of the materials were characterized using XRD, N_2 ad-/desorption, SEM, and ^{27}Al NMR. The distribution of acid sites among the pores in Al−IPC was thoroughly characterized by FTIR spectroscopy of adsorbed probe molecules with different sizes (acetonitrile-d_3) and by ethanol-to-diethyl ether kinetic analysis. Lastly, the catalytic behavior of aluminosilicate isoreticular zeolites in a liquid-phase batch-type reaction (tetrahydropyranylation with alcohols) was tested and discussed on the basis of their pore structure and on the location of acid sites.

2. EXPERIMENTAL SECTION

2.1. Zeolite Synthesis. *2.1.1. Synthesis of UTL Zeolites.* Germanosilicate UTL zeolite was synthesized using (6*R*,10*S*)-6,10-dimethyl-5-azoniaspiro[4,5]decane hydroxide as the structure-directing agent (SDA).[38] The molar composition of the reaction mixture was 0.6−0.8SiO_2/0.4−0.6GeO_2/0.4SDA/30H_2O. Aluminum-containing UTL (Al−UTL) was synthesized using 7-ethyl-6-azoniaspiro[5.5]undecane hydroxide as SDA[39] from the reaction gel with a molar ratio of 0.788SiO_2/0.4GeO_2/0.012$AlO_{1.5}$/0.4SDA/30H_2O. Typically, germanosilicate UTL was prepared by dissolving germanium dioxide (Sigma-Aldrich, 99.99%) in the aqueous solution of SDA. After 30 min, silica (Cab-O-Sil M5, Supelco Analytical) was added to the solution, and the mixture was stirred at room temperature. Subsequently, the resulting fluid gel was charged into 25 mL Teflon-lined stainless-steel autoclaves and heated to 175 °C for 7 days under agitation. The as-synthesized solid product was recovered by filtration, washed with distilled water, and dried overnight at 65 °C. For the Al-containing UTL sample, Al(OH)$_3$

(Sigma-Aldrich) was dissolved first in the aqueous solution of SDA and then in germanium dioxide, subsequently adding silica. Finally, the above mixture remained under vigorous stirring to adjust the pH of the gel to 12 according to ref 39. The resulting fluid gel was charged into 25 mL of Teflon-lined stainless-steel autoclaves and heated to 175 °C for 22 days under agitation. To remove the SDA, the as-synthesized zeolites were calcined in air at 550 °C, 1 °C/min for 6 h. The calcined samples were used as the starting material of postsynthetic alumination to synthesize Al−IPC zeolites according to the following procedures.

2.1.2. Synthesis of Al−IPC-n Isoreticular Zeolites. **Al−IPC-7:** 1 g of calcined Al−UTL zeolite was mixed with 100 mL of a 3 M aqueous Al(NO$_3$)$_3$ solution at 60 °C for 16 h. After alumination, the solid was isolated by centrifugation, washed with 0.01 M HCl and water, dried at 65 °C overnight, and calcined at 550 °C for 6 h.

Al−IPC-2: 1 g of calcined Al−UTL zeolite was mixed with 100 mL of 1 M aqueous Al(NO$_3$)$_3$ solution at room temperature for 16 h. After alumination, the solid was isolated by centrifugation, washed with 0.01 M HCl and water, dried at 65 °C overnight, and calcined at 550 °C for 6 h.

Al−IPC-6: 1 g of calcined UTL zeolite (Si/Ge = 2 in gel) was stirred in a mixture of 150 mL of 1 M acetic acid and 100 mL of 1 M Al(NO$_3$)$_3$ solutions at 95 °C for 16 h. The solid was isolated by centrifugation, washed with 0.01 M HCl and water, dried at 65 °C overnight, and treated with octylamine (solid-to-liquid ratio = 1:50 w/w) at 60 °C for 16 h. The final product was calcined at 550 °C for 6 h.

Al−IPC-4: 1 g of calcined UTL zeolite (Si/Ge = 1 in gel) was stirred in a mixture of 150 mL of 1 M acetic acid and 100 mL of 1 M Al(NO$_3$)$_3$ solutions at 95 °C for approximately 16 h. The solid was isolated by centrifugation, thoroughly washed with 0.01 M HCl and water, dried, and then treated with octylamine (solid-to-liquid ratio = 1:50 w/w) at 60 °C for 16 h. The final product was calcined at 550 °C for 6 h.

2.2. Characterization of the Catalysts. The structure and phase purity of the catalysts were validated using X-ray powder diffraction (XRD). The XRD patterns were measured with a Bruker AXS-D8 Advance diffractometer equipped with a graphite monochromator and a position sensitive detector (Vantec-1) at a scan rate of 0.25° (2θ per minute) using Cu Kα radiation. The chemical composition of zeolites was analyzed by ThermoScientific iCAP 7000 ICP/OES. The crystal morphology was assessed by scanning electron microscopy (SEM) using a JEOL JSM-5500 LV microscope. An ASAP 2020 (Micrometeritics) static volumetric apparatus was used to measure N_2 ad-/desorption isotherms at T = −196 °C (liquid nitrogen temperature). Prior to the N_2 adsorption, zeolites were activated at T = 250 °C for 4 h while being degassed with a turbomolecular pump. The concentrations of Lewis (c_L) and Brønsted (c_B) acid sites were evaluated using FTIR spectroscopy of adsorbed acetonitrile-d_3 (ACN). The zeolites were pressed into self-supporting wafers with a density of 8−10 mg·cm^{-2} and activated in situ at T = 450 °C and at P < 1 × 10^{-4} Torr for 4 h. This was followed by desorption at the same temperature for 30 min. The spectra were recorded with a resolution of 4 cm^{-1} using a Nicolet 6700 FT-IR spectrometer equipped with a transmission MCT/B detector. ACN adsorption was performed at T = 25 °C and at a partial pressure p_{AN} = 3.0 Torr for 30 min. c_B and c_L were evaluated based on the intensity of the bands at 2300 cm^{-1} ($\mathcal{E}$(B) = 2.05 ± 0.1 cm·μmol^{-1}[40]) and 2330 cm^{-1} ($\mathcal{E}$(L) = 3.6 ± 0.2 cm·μmol^{-1}[40]), respectively.
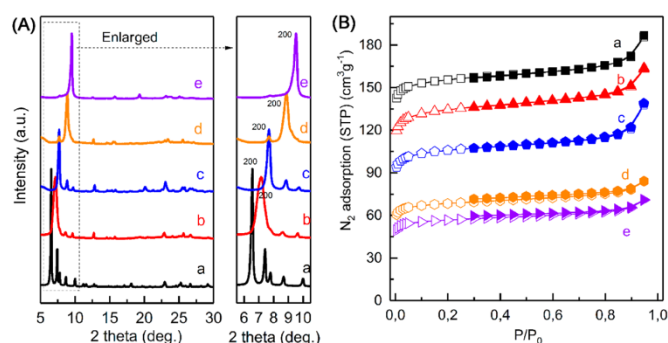
Figure 2. (A) XRD patterns; (B) N_2 adsorption and desorption isotherms of the parent Al−UTL and isoreticular Al-containing IPC-7 (b), IPC-2 (c), IPC-6 (d), and IPC-4 (e) zeolite catalysts.

Table 2. Physicochemical Properties of the Parent UTL and Al−IPC Samples

material	Si/Al^a ratio	V_{tot} (cm^3 g^{-1})	V_{micro}^{b} (cm^3 g^{-1})	S_{BET}^{c} (m^2 g^{-1})	$c_{Brønsted}$^{d} (mmol g^{-1})	c_{Lewis}^{d} (mmol g^{-1})	c_{acid} (mmol g^{-1})
UTL		0.301	0.213	580			
Al−UTL	64.6	0.289	0.231	566	0.04	0.06	0.10
Al−IPC-7	20.1	0.263	0.194	485	0.15	0.24	0.39
Al−IPC-2	26.2	0.191	0.128	325	0.17	0.20	0.37
Al−IPC-6	24.9	0.130	0.099	249	0.14	0.23	0.37
Al−IPC-4	20.5	0.110	0.082	207	0.19	0.21	0.40

^{a}Measured by ICP. ^{b}Calculated using the t-plot method. ^{c}Specific surface area (BET) given by N_2 adsorption at −196 °C. ^{d}Measured by FTIR after ACN adsorption.

"Internal" acid sites were discriminated from those located in extra-large pores and on the external surface ("external" acid centers) of Al−IPC-*n* zeolites by coadsorption of bulky quinoline and ACN. Quinoline adsorption was performed according to refs 41 and 42. Subsequently, the amount of "internal" acid centers being inaccessible for quinoline was probed by AN, as described above.

An Agilent DD2 500WB spectrometer was used for collecting ^{27}Al MAS NMR spectra at a resonance frequency of 130.24 MHz using a sample spinning rate of 15 kHz.

2.3. Catalytic Tests. *2.3.1. Tetrahydropyranylation of Alcohols.* The liquid-phase tetrahydropyranylation reaction was performed under atmospheric pressure at 60 °C in a multiexperiment workstation Star-Fish (Radleys Discovery Technologies). Before the catalytic test, 50 mg of the zeolite was activated for 90 min at T = 450 °C. Typically, alcohol (4.5 mmol), internal standard (0.25 g of mesitylene), and the catalyst were added to a two-necked flask equipped with a thermometer. 3,4-Dihydro-2*H*-pyran (DHP, 10 mL) was added to the flask when the required temperature was reached. Probes of the reaction mixture were taken periodically and analyzed using a gas chromatograph (Agilent 6859) equipped with a DB-WAX column (20 m × 0.18 mm × 0.3 μm) and with an FID detector.

2.3.2. Ethanol Dehydration. Steady-state gas-phase ethanol dehydration reaction over Al−IPC zeolites was performed at 185 °C under atmospheric pressure while varying partial pressures of ethanol nonmonotonically. First, the catalyst was activated under an oxygen flow (30 cm^3/min) at 450 °C for 5 h. Ethanol partial pressure was adjusted by changing (i) the temperature in the saturator (7 and 30 °C for lower and higher ethanol partial pressure, respectively) and (ii) the degree of ethanol dilution with N_2.

The products were analyzed on an online Agilent 6850 GC equipped with a DB-5 column (50 m × 0.32 mm × 1 μm) and with an FID detector. Ethanol conversion did not exceed 10%, and catalyst deactivation was not observed under used experimental conditions.

3. RESULTS AND DISCUSSION

3.1. Physicochemical Properties of Zeolites. By combining the ADOR approach with postsynthetic alumination, four Al-containing isoreticular IPC zeolites (IPC-7, IPC-2, IPC-6, and IPC-4) were synthesized using Al−UTL (for IPC-7 and IPC-2) or germanosilicate UTL (for IPC-6 and IPC-4) as starting materials.

3.1.1. Structure and Textural Properties. The XRD patterns of all synthesized Al−IPC-*n* zeolites (Figure 2A) matched those of silica analogues reported in the literature,[17,18] thus showing the phase purity of all samples. Similar profiles (e.g., 12.7°, 15.7°, 22.9°, 25.2° 2θ) of the intralayer reflections observed in all samples confirmed the identity of their intralayer structure. Conversely, the shift of the interlayer peak (200) to 2θ higher values shows decreasing interlayer *d*-spacing in the following order of zeolites: UTL (6.1 2θ) > IPC-7 (6.9 2θ) > IPC-2 (7.8 2θ) > IPC-6 (8.5 2θ) > IPC-4 (9.7 2θ).

N_2 adsorption/desorption isotherms of Al−UTL and Al−IPC-*n* samples (Figure 2B) belong to type-I zeolites without a hysteresis loop, thus demonstrating purely microporous materials. Micropore volume decreases in the following order (Table 2): UTL (0.23 cm^3 g^{-1}) > IPC-7 (0.19 cm^3 g^{-1}) > IPC-2 (0.13 cm^3 g^{-1}) > IPC-6 (0.10 cm^3 g^{-1}) > IPC-4 (0.08 cm^3 g^{-1}). This order matches the gradual decrease in interlayer spacing and hence in micropore size.

114
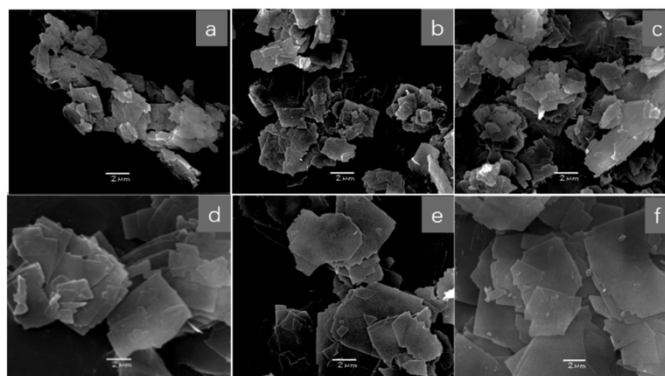
Figure 3. SEM of the parent Al−UTL (a), Ge−UTL (d), and isoreticular Al-containing IPC-7 (b), IPC-2 (c), IPC-6 (e), and IPC-4 (f) zeolite catalysts.
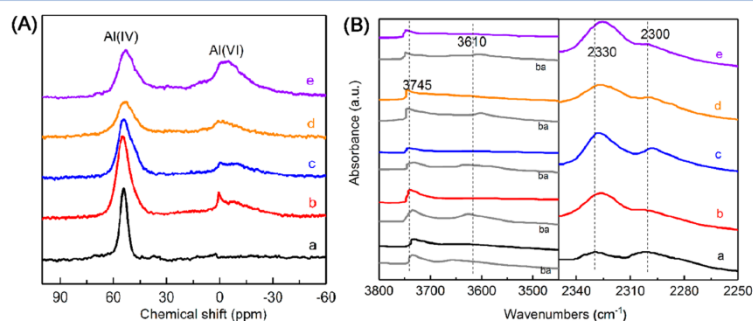
Figure 4. (A) ^{27}Al MAS NMR and (B) FTIR spectra of AN adsorbed in the parent Al−UTL (a) and isoreticular Al-containing IPC-7 (b), IPC-2 (c), IPC-6 (d), IPC-4 (e), and zeolite catalysts. Gray lines (ba) show the spectra of the respective samples after activation.

SEM images reveal that the crystals maintain their shape and size upon UTL-to−IPC transformation (Figure 3). Al−IPC-6 (Figure 3e) and Al−IPC-4 (Figure 3f) materials showed uniform platelike crystals ($2−4$ μm) similar to those of the parent UTL (Figure 3d) germanosilicate zeolite, whereas the crystal sizes of Al−IPC-2 (Figure 3c) and Al−IPC-7 (Figure 3b) samples were slightly smaller than that of the parent Al−UTL ($\sim$2 μm, Figure 3a).

^{27}Al NMR spectra showing a dominating peak of tetrahedrally coordinated Al atoms at 55 ppm and a small reflex of octahedrally coordinated Al at 0 ppm clearly showing the incorporation of most Al atoms into the framework positions of IPC-n zeolites (Figure 4A). Importantly, the duration of zeolite treatment with 0.01 M HCl had no effect on the intensity of the peak at 55 ppm corresponding to tetrahedrally coordinated aluminum for all Al−IPC-n zeolites. Simultaneously, complete removal of octahedrally coordinated Al from the IPC-7 zeolite required prolonging the washing treatment to 25 min (Figure S1). In accordance with the chemical analysis, the Si/Al ratio of IPC-7 increased from 13 to 20.1 upon acid treatment.

Thus, the results clearly show that the concentration of extra-framework Al species in IPC samples can be changed by modulating the acid-washing period, thereby preparing a set of

isoreticular zeolites with similar Si/Al ratios of approximately 20 (Table 1).

3.1.2. Type and Concentration of Acid Sites. The type and total concentration of acid sites in Al−IPC-n samples are determined by FTIR of adsorbed ACN with a kinetic diameter (4.0 Å) small enough to access acid sites, even in 8-ring channels. As shown in Figure 4B, before ACN adsorption ("ba"), all samples show bands around 3745 and 3620 cm^{-1} assigned to silanol and acidic bridging OH groups ($\equiv$Sdadsori−OH-Al$\equiv$), respectively. The adsorption of ACN removed the band around 3620 cm^{-1}, whereas new characteristic absorption bands appeared at 2300 and 2330 cm^{-1}, thus indicating that ACN molecules interact with Brønsted and Lewis acid sites, respectively.

All Al−IPC samples under investigation have similar concentrations of both Brønsted and Lewis acid sites (Table 2), exceeding 3−4 times the values characteristic of Al−UTL zeolites. The markedly lower number of acid sites in Al−UTL is caused by the narrow field of pure UTL phase crystallization in Al-containing reaction mixtures, as shown in ref 39.

Although we used ACN to probe the total concentration of acid sites in Al−IPC zeolites (Table 2 and Figure 4B), sequential adsorption of quinoline and ACN was applied to differentiate acid sites located in small (8-ring), medium (10-ring), and large

(12 ring) pore containing channel systems ("internal" acid sites) from those located in extra-large pores and on the external surface ("external" acid sites). A previous study has shown that quinoline can be adopted to determine acid sites located on the external surface and in extra-large pores of zeolites albeit without penetrating deep inside pores with a diameter smaller than 0.7 nm.[43] IR spectra of ACN adsorbed in activated Al–IPC-2, IPC-4, and IPC-6 and those collected after quinoline preadsorption are compared in Figure S2. In all samples, quinoline preadsorption unsurprisingly decreased the intensities of the peaks attributed to the interaction between ACN and Brønsted (2300 cm^{−1}) and Lewis (2315 and 2325 cm^{−1}) acid sites. Thus, the comparison between the total concentration of acid sites (Table 2) and the number of acid centers accessible for ACN after quinoline preadsorption allowed the selective determination of the Al siting of both noninterconnected pore systems of the IPC-7 zeolite and of pore systems located on the external surface and in the micropores of IPC-2, IPC-6, and IPC-4 zeolites (Figure 5B). The concentrations of Brønsted and Lewis
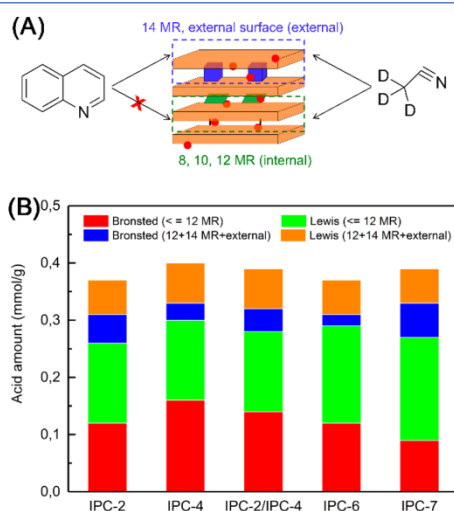

Figure 5. (A) Schematic description of quinoline and acetonitrile on Al–IPC zeolites and (B) distribution of acid sites of Al–IPC zeolites.

acid sites located on the external surface and in extra-large pores decrease with the increase in the crystal size of the catalysts, e.g., accounting for 35%, 29%, 25%, and 21% of the total number of acid sites of IPC-7, IPC-2, IPC-6, and IPC-4, respectively.

Thus, the chemical analysis, ^{27}Al NMR, and FTIR spectroscopy results showed the similarity between isoreticular Al–IPC zeolites with respect to the content and coordination state of Al and to the type and total number of acid sites, whereas the distribution of acid sites among micropores and the external surface of catalyst crystals slightly varies, thus reflecting differences in their size. Concomitantly, isoreticular IPC zeolites have micropores with markedly different sizes, ranging from the ones restricted with 8- to 14-ring channels, which is reflected in the decrease in the micropore volume in the following order: Al–IPC-7 > Al–IPC-2 > Al–IPC-6 > Al–IPC-4.

3.2. Catalytic Performance of Al–IPC Zeolites in Ethanol Dehydration.

To shed light on the siting of acid sites in micropores of different sizes, we further analyzed the performance of Al–IPC catalysts in the Brønsted acid-catalyzed ethanol dehydration reaction known to occur through a unimolecular route to produce ethylene or through a bimolecular pathway to generate diethyl ether (DEE). The choice of this reaction also allows us to experimentally validate the confinement effect on reaction rates by studying structure–activity relationships in the Al–IPC zeolite family.[44−46] Figure 6 shows the turnover rates of DEE (R_{DEE}) and ethylene ($R_{ethylene}$) formation as a function of ethanol partial pressure at 185 °C. Figure 6 also shows that DEE is a major product in the whole range of ethanol partial pressures for all catalysts tested (Figure 6a). Ethylene production over IPC-7 and IPC-2 catalysts follows the well-established trend for a number of medium- and large-pore zeolites.[44,45] The increase in $R_{ethylene}$ with ethanol pressure at $0 < p_{EtOH} < 10$ mbar and the decrease in $R_{ethylene}$ with the increase in p_{EtOH} at $p_{EtOH} > 10$ mbar was explained by the inhibition of ethylene synthesis via the formation of ethanol dimers at high pressures. Interestingly, $R_{ethylene}$ remained stable in IPC-6 and IPC-4 when p_{EtOH} was increased to >0.01 bar, thus suggesting a limited formation of ethanol dimers in catalyst channels, even at high p_{EtOH}.

The analysis of the variation of ethanol-to-DEE dehydration turnover rates (R_{DEE}, normalized per total concentration of Brønsted sites determined from ACN adsorption) as a function of p_{EtOH} over Al–IPC zeolites (Figure 6A) shows a linear increase in R_{DEE} with p_{EtOH} (the first order kinetic) at low ethanol partial pressures (0.15−2.14 mbar) and an asymptotic, nonlinear R_{DEE} vs p_{EtOH} function (zero order kinetic) at higher ethanol pressures (2.14−102 mbar). Such function suggests that ethanol dehydration followed the associative dehydration pathway in all studied Al–IPC zeolites, yielding diethyl ether as a major product. The associative dehydration mechanism involves the adsorption of an ethanol molecule over the Brønsted acid site (ethanol monomer) followed by the adsorption of a second ethanol molecule over the same Brønsted acid site, thereby forming an ethanol dimer.[46] The activation of dimer results in the formation of transition state, which decomposes into water and adsorbed diethyl ether species. These species desorb, thus regenerating the Brønsted acid sites (Scheme 1). This sequence of elementary steps leads to following rate expression (the full derivation is shown in ref 47)

$$R_{DEE,A} = \frac{k_{first}P_{EtOH}}{1 + \frac{k_{first}}{k_{zero}}P_{EtOH}} \tag{1}$$

where

$$k_{first} = k_{DEE,A}K_{P}K_{D} \tag{2}$$

and

$$k_{zero} = k_{DEE,A}K_{P} \tag{3}$$

where $K_{DEE,A}$ is a rate constant and K_{P} and K_{D} are the adsorption equilibrium constants for coadsorbed state and dimer formation, respectively. K_{first} and K_{zero} are the apparent first-order and zero-order rate constants for the associative dehydration pathway.

The activation energy associated with the apparent first-order rate constants (k_{first}) reflects the energy difference between the transition state of the reaction of ether formation and the hydrogen-bonded ethanol monomer. Since the transition state and the ethanol monomer differ in charge distribution and size,
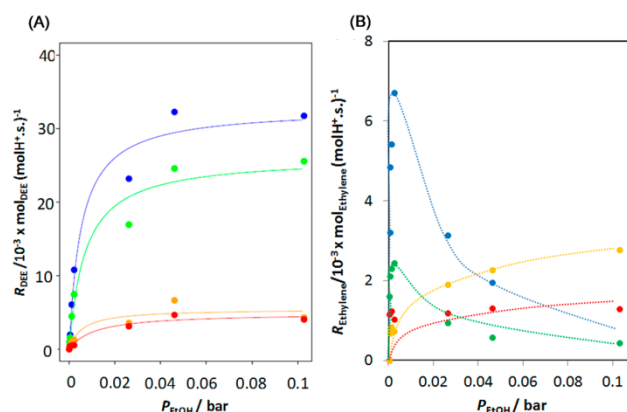
116

Figure 6. (A) Ethanol-to-DEE (R_{DEE}/mol_{DEE} (mol H$^+$·s)$^{-1}$) (data fitted to eq 1) and (B) ethanol-to-ethylene ($R_{ethylene}/mol_{ethylene}$(mol H$^+$·s)$^{-1}$) dehydration turnover rates (lines are the guide to the eye) over IPC-7 (blue), IPC-2 (green), IPC-6 (orange), and IPC-4 (red) at 185 °C.

Scheme 1. Schematic Representation of the Associative Ethanol Dehydration Pathway Showing Elementary Adsorption and Reaction Steps as Well as the Respective Adsorption Equilibrium and Rate Constants (Adapted from Kadam and Shamzhy[46])
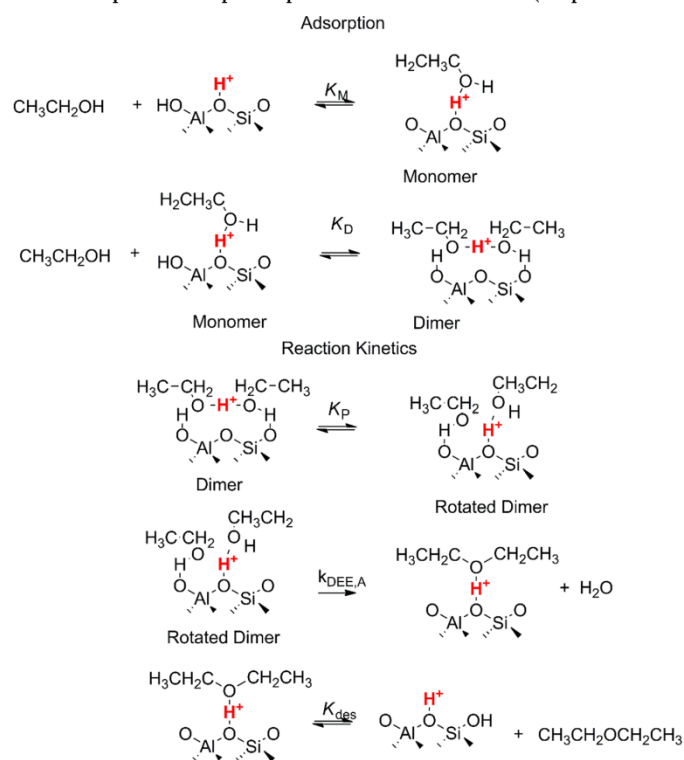
k_{first} is sensitive to differences in both acid strength and porosity.[48,49] Conversely, the activation energy associated with the apparent zero-order rate constants (k_{zero}) reflects the energy of same transition state but relative to that of a protonated dimer. In contrast to k_{first}, k_{zero} remains similar among zeolites with different pore sizes because the protonated dimers and transition

117

state of the reaction of dimethyl ether formation are similar in size and thus in their van der Waals interactions with the zeolite wall.[49]

The data shown in Figure 6A were fitted to eq 1, and the values of k_{first} and k_{zero} were extracted (Figure 7). The values of

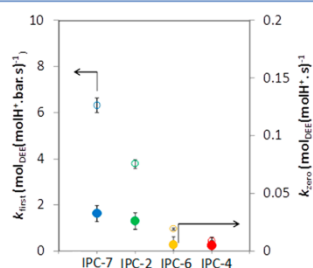**Figure 7.** Rate constants k_{first} (P_{EtOH} < 2.14mbar) and k_{zero} (P_{EtOH} > 2.14 mbar) of Al−IPC catalysts.

zero-order rate constants (close symbols, Figure 7) k_{zero} remain almost similar when comparing IPC-7 with IPC-2 and IPC-6 with IPC-4, but IPC-6 and IPC-4 have significantly lower constants than IPC-7 and IPC-2. Smaller k_{first} and k_{zero} clearly indicate space restrictions in the formation of ethanol dimers and in the corresponding transition state when comparing IPC-6 and IPC-4 vs IPC-7 and IPC-2. Figure 6B confirms this explanation, as shown by the variation in the turnover rate of ethylene formation ($R_{ethylene}$) as a function of p_{EtOH}. The turnover rates of ethylene formation over IPC-7 and IPC-2 gradually decrease with the increase in pressure due to the formation of ethanol dimers in the larger pores (14R and 12R) of the aforementioned zeolites.[46−49] However, the $R_{ethylene}$ of IPC-6 and IPC-4 remain constant, albeit slightly increasing at higher ethanol pressures. It confirms a limited dimer formation and the protection of ethoxide species, which are formed in the smaller pores (10R and 8R) of IPC-6 and IPC-4.[49] The higher value of k_{first} for Al−IPC-6 vs Al−IPC-4 is consistent with a better van der Waals stabilization of the transition state (rotated dimer in Scheme 1) than of H-bonded C_2H_5OH molecule in 10 × 12-ring channels of Al−IPC-6.[49] Higher concentration of acid sites in 10 × 12-ring channels of IPC-2 vs IPC-6 naturally resulted in a further increase in the k_{first} value. In accordance with refs 45−49, the k_{first} value of IPC-7 is 1.5 times higher than that of IPC-2 at similar k_{zero} values for both catalysts, which may be explained by the higher concentration of Al atoms in the 10-ring channels of the IPC-7 zeolite.

Thus, the present data represent a predictive analysis of the structure−function relationship between Al siting and resulting kinetics. The present kinetic data contributes to developing methods for Al siting estimation in a given zeolite structure using the marked effects of active sites and surrounding confinement on kinetic rate constants, which are sensitive to such environments.

3.3. Catalytic Performance of Al−IPC Zeolites in Tetrahydropyranylation of Alcohols. *3.3.1. Al−IPC catalysts.* The effect of the distribution of acid sites among pores of different sizes on the catalytic behavior of Al−IPC zeolites was investigated in liquid-phase tetrahydropyranylation of alcohols with DHP, which is known to be catalyzed by both Brønsted and Lewis acid sites (Scheme 2).[50,51]

Scheme 2. Tetrahydropyranylation of Alcohols
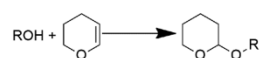
When a small ethanol molecule was used as reactant, all IPC catalysts showed similar activity, completely converting the substrate into the target product after 24 h (Figure 8). In
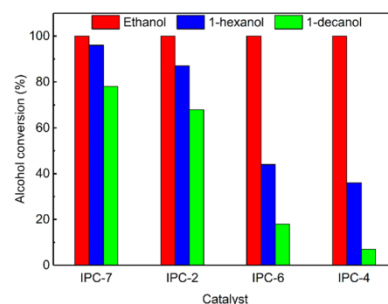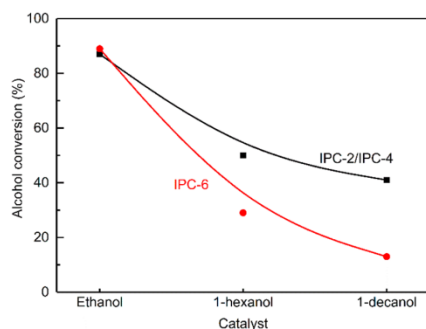

Figure 8. Alcohol conversion for the tetrahydropyranylation of ethanol, 1-hexanol, and 1-decanol after 24 h with DHP over Al−IPC catalysts under the following reaction conditions: 50 mg of catalyst, 4.5 mmol pf alcohol, 5 mL of DHP, and 0.25 g of mesitylene at 60 °C.

contrast, when using 1-hexanol, the IPC-4 catalyst reached only 36% conversion after 24 h, whereas the reactant conversion substantially increased when using IPC-7 as catalyst (over 90% conversion after 24 h, Figure 8). The four zeolites were also applied in the tetrahydropyranylation of 1-decanol, which provided further information on the effect of catalyst pore structure on its performance. Although lower conversion rates of 1-decanol vs 1-hexanol were assessed over all Al−IPC catalysts under investigation, IPC-7 was again the most active catalyst (78% conversion after 24 h). In general, the catalytic activity of zeolites in the tetrahydropyranylation of either 1-hexanol or 1-decanol correlates with the relative concentration of "external" acid sites, i.e., decreases with micropore size/volume in the following order: IPC-7 > IPC-2 > IPC-6 > IPC-4. These results suggest that, due to diffusion limitations, bulky reagents have limited access to the internal active sites of IPC zeolites and that IPC-4 has the lowest porosity has is the zeolite most affected by diffusion limitations.

3.3.2. Al−IPC-6 vs Al−IPC-2/IPC-4 catalyst. The average structure of the IPC-6 zeolite can be considered a combination of IPC-2 and IPC-4 (Figure S3). This makes it possible to compare materials with the same morphology, textural properties, and total concentration of acid sites but differing in structural organization, i.e., Al−IPC-6 (intergrown IPC-4 and IPC-2 frameworks) and the physical mixture of Al−IPC-4 and Al−IPC-2. We were able to prepare the physical mixture of IPC-2/IPC-4 catalysts (40% IPC-2 and 60% IPC-4), which has similar morphology to and the same porosity and number of acid sites as IPC-6 (Table S1). The distribution of acid sites in IPC-2/IPC-4 and in IPC-6 is different, as shown by acetonitrile-IR preadsorbed with quinoline. The composite catalyst IPC-2/IPC-4 has a higher concentration of external acid sites than the IPC-6 zeolite, 0.11 mmol/g (30%) and 0.08 mmol/g (25%), respectively (Figure 5).

We compared the behavior of the IPC-6 zeolite with that of the mechanical mixture of IPC-2/IPC-4 to further understand the effect of the distribution of acid sites on the catalytic performance of zeolites in the tetrahydropyranylation of different alcohols. IPC-6 and IPC-2/IPC-4 showed the same ethanol conversion rates, whereas the conversion rates of bulkier 1-hexanol and 1-decanol were significantly higher than those of IPC-2/IPC-4 (Figure 9). Considering the similar morphology,

Figure 9. Conversion rates of the tetrahydropyranylation of ethanol, 1-hexanol, and 1-decanol with DHP over IPC-2/IPC-4 and IPC-6 catalysts at 6 h. Reaction conditions: 50 mg of catalyst, 4.5 mmol of alcohol, 5 mL of DHP, and 0.25 g of mesitylene at 60 °C.

porosity, and total concentration of acid sites of both catalysts, such a difference in their performance can be attributed to differences in the distribution of acid sites in IPC-6 vs IPC-2/IPC-4, i.e., to the lower concentration of "external" acid sites in IPC-6.

4. CONCLUSIONS

A set of isoreticular Al−IPC-n aluminosilicate zeolites with similar morphology, crystal size, Al content, and concentration of acid sites (0.37−0.40 mmol g^{-1}) but with different distributions of acid sites and gradually smaller channel sizes has been synthesized for the first time. FTIR spectroscopy of adsorbed probe molecules of variable size (d_3-acetonitrile, quinoline) revealed an increasing concentration of acid sites located on the external surface and in extra-large pores ("external" acid sites) in the following order: IPC-4 (21%) < IPC-6 (25%) < IPC-2 (29%) < IPC-7 (35%). Ethanol-to-diethyl ether kinetic study showed a lack of confinement of ethanol dimers in IPC-6 and IPC-4 (k_{first} = 0.4−0.9 mol$_{DEE}$ (mol$_{H+}$·s)$^{-1}$) compared with IPC-2 (k_{first} = 3.8 mol$_{DEE}$ (mol$_{H+}$·s)$^{-1}$) and especially with IPC-7 (k_{first} = 6.3 mol$_{DEE}$ (mol$_{H+}$·s)$^{-1}$) zeolites. The better van der Waals stabilization of the transition state than that of H-bonded C$_2$H$_5$OH molecule in IPC-7 vs IPC-2 zeolite explains the higher concentration of Al atoms in 10-ring channels of the former catalyst. The comparison between the catalytic behavior of model catalysts (i.e., the IPC-6 zeolite and a mechanical mixture of IPC-2/IPC-4) with similar textural properties and total concentration of acid sites but with different distributions of acid centers allowed us to correlate catalyst activity in the tetrahydropyranylation of bulky 1-decanol with the number of "external" acid sites. Furthermore, while performing similarly in reactions with ethanol, the catalytic activity of IPC-n zeolites in the tetrahydropyranylation of bulky

1-decanol differed drastically and decreased with the concentration of "external" acid sites: IPC-7 > IPC-2 > IPC-6 > IPC-4. IPC-6 has fewer "external" acid sites, thus showing lower activity than IPC-2/IPC-4 catalysts, even though they have the same textural properties and total concentration of acid sites. The findings of this study not only provide evidence of the direct effects of the location of acid sites and micropore structure of zeolites on their catalytic performance but also show that the use of Al−IPC-n as model catalysts in important acid-catalyzed reactions helps to explain the fundamental structure−activity relationship and to improve existing catalytic processes.

■ ASSOCIATED CONTENT

⑤ Supporting Information

The Supporting Information is available free of charge on the ACS Publications website at DOI: 10.1021/acscatal.9b00950.

N$_2$ adsorption and desorption isotherms and ^{27}Al MAS NMR spectra of aluminated IPC-7 zeolites washed with 0.01 M HCl at different times; FTIR spectra of IPC-2, IPC-4, and IPC-6 before adsorption and after adsorption of acetonitrile-, quinoline-, or quinoline-preabsorbed followed by acetonitrile; scheme of the average structure of IPC-6; physicochemical properties of the IPC-2/IPC-4 composite and IPC-6 catalyst (PDF)

■ AUTHOR INFORMATION

Corresponding Authors
*E-mail: mariya.shamzhy@natur.cuni.cz.
*E-mail: maksym.opanasenko@natur.cuni.cz.

ORCID ⓞ
Shashikant A. Kadam: 0000-0002-4298-4074
Mariya Shamzhy: 0000-0002-1979-6817

Notes
The authors declare no competing financial interest.

■ REFERENCES

(1) Vogt, E. T. C.; Weckhuysen, B. M. Fluid Catalytic Cracking: Recent Developments on the Grand Old Lady of Zeolite Catalysis. *Chem. Soc. Rev.* **2015**, *44*, 7342−7370.

(2) Corma, A.; Huber, G. W.; Sauvanaud, L.; O'connor, P. Processing Biomass-derived Oxygenates in the Oil Refinery: Catalytic Cracking (FCC) Reaction Pathways and Role of Catalyst. *J. Catal.* **2007**, *247*, 307−327.

(3) Cheng, K.; Kang, J.; Huang, S.; You, Z.; Zhang, Q.; Ding, J.; Wang, Y. Mesoporous Beta Zeolite-Supported Ruthenium Nanoparticles for Selective Conversion of Synthesis Gas to C5−C11 Isoparaffins. *ACS Catal.* **2012**, *2*, 441−449.

(4) Xue, Y.; Li, J.; Wang, S.; Cui, X.; Dong, M.; Wang, G.; Fan, W. Co-reaction of Methanol with Butene over a High-silica H-ZSM-5 Catalyst. *J. Catal.* **2018**, *367*, 315−325.

(5) Čejka, J., Morris, R. E., Nachtigall, P., Eds. *Zeolites in Catalysis: Properties and Applications*; Royal Society of Chemisty: UK, 2017; Chapter 11, pp 409−440.

(6) Opanasenko, M. V.; Roth, W. J.; Čejka, J. Two-dimensional Zeolites in Catalysis: Current Status and Perspectives. *Catal. Sci. Technol.* **2016**, *6*, 2467−2484.

(7) Simon-Masseron, A.; Marques, J. P.; Lopes, J. M.; Ribeiro, F. R.; Gener, L.; Guisnet, M. Influence of the Si/Al Ratio and Crystal Size on the Acidity and Activity of HBEA Zeolites. *Appl. Catal., A* **2007**, *316*, 75−82.

(8) Zhang, J.; Zhao, C. Development of a Bimetallic Pd-Ni/HZSM-5 Catalyst for the Tandem Limonene Dehydrogenation and Fatty Acid Deoxygenation to Alkanes and Arenes for Use as Biojet Fuel. *ACS Catal.* **2016**, *6*, 4512−4525.

(9) Peters, T. A.; Benes, N. E.; Holmen, A.; Keurentjes, J. T. Comparison of Commercial Solid Acid Catalysts for the Esterification of Acetic Acid with Butanol. *Appl. Catal., A* **2006**, *297*, 182−188.

(10) Dusselier, M.; Deimund, M. A.; Schmidt, J. E.; Davis, M. E. Methanol-to-Olefins Catalysis with Hydrothermally Treated Zeolite SSZ-39. *ACS Catal.* **2015**, *5*, 6078−6085.

(11) Eliášová, P.; Opanasenko, M.; Wheatley, P. S.; Shamzhy, M.; Mazur, M.; Nachtigall, P.; Roth, W. J.; Morris, R. E.; Čejka, J. The ADOR Mechanism for the Synthesis of New Zeolites. *Chem. Soc. Rev.* **2015**, *44*, 7177−7206.

(12) Morris, S. A.; Bignami, G. P.; Tian, Y.; Navarro, M.; Firth, D. S.; Čejka, J.; Wheatley, P. S.; Dawson, D. M.; Slawinski, W. A.; Wragg, D. S.; Morris, R. E. In Situ Solid-state NMR and XRD Studies of the ADOR Process and the Unusual Structure of Zeolite IPC-6. *Nat. Chem.* **2017**, *9*, 1012−1018.

(13) Bignami, G. P. M.; Dawson, D. M.; Seymour, V. R.; Wheatley, P. S.; Morris, R. E.; Ashbrook, S. E. Synthesis, Isotopic Enrichment, and Solid-State NMR Characterization of Zeolites Derived from the Assembly, Disassembly, Organization, Reassembly Process. *J. Am. Chem. Soc.* **2017**, *139*, 5140−5148.

(14) Chlubná, P.; Tian, Y.; Pinar, A. B.; Kubů, M.; Čejka, J.; Morris, R. E. The Assembly-Disassembly-Organization-Reassembly Mechanism for 3D-2D-3D Transformation of Germanosilicate IWW Zeolite. *Angew. Chem., Int. Ed.* **2014**, *53*, 7048−7052.

(15) Kasneryk, V.; Shamzhy, M.; Opanasenko, M.; Wheatley, P. S.; Morris, S. A.; Russell, S. E.; Mayoral, A.; Trachta, M.; Čejka, J.; Morris, R. E. Expansion of the ADOR Strategy for the Synthesis of Zeolites: The Synthesis of IPC-12 from Zeolite UOV. *Angew. Chem., Int. Ed.* **2017**, *56*, 4324−4327.

(16) Firth, D. S.; Morris, S. A.; Wheatley, P. S.; Russell, S. E.; Slawin, A. M. Z.; Dawson, D. M.; Mayoral, A.; Opanasenko, M.; Položij, M.; Čejka, J.; Nachtigall, P.; Morris, R. E. Assembly−Disassembly−Organization−Reassembly Synthesis of Zeolites Based on cfi-Type Layers. *Chem. Mater.* **2017**, *29*, 5605−5611.

(17) Roth, W. J.; Nachtigall, P.; Morris, R. E.; Wheatley, P. S.; Seymour, V. R.; Ashbrook, S. E.; Chlubná, P.; Grajciar, L.; Polozij, M.; Zukal, A.; Shvets, O.; Čejka, J. A Family of Zeolites with Controlled Pore Size Prepared Using a Top-down Method. *Nat. Chem.* **2013**, *5*, 628−633.

(18) Wheatley, P. S.; Chlubná- Eliášová, P.; Greer, H.; Zhou, W.; Seymour, V. R.; Dawson, D. M.; Ashbrook, S. E.; Pinar, A. B.; McCusker, L. B.; Opanasenko, M.; Čejka, J.; Morris, R. E. Zeolites with Continuously Tuneable Porosity. *Angew. Chem., Int. Ed.* **2014**, *53*, 13210−13214.

(19) Mazur, M.; Wheatley, P.; Navarro, M.; Roth, W. J.; Mayoral, A.; Eliášová, P.; Nachtigall, P.; Čejka, J.; Morris, R. E.; Položij, M. Synthesis of 'Unfeasible' Zeolites. *Nat. Chem.* **2016**, *8*, 58−62.

(20) Roth, W. J.; Shvets, O. V.; Shamzhy, M.; Chlubná, P.; Kubů, M.; Nachtigall, P.; Čejka, J. Postsynthesis Transformation of Three-Dimensional Framework into a Lamellar Zeolite with Modifiable Architecture. *J. Am. Chem. Soc.* **2011**, *133*, 6130−6133.

(21) Paillaud, J. L.; Harbuzaru, B.; Patarin, J.; Bats, N. Extra-large-pore Zeolites with Two-dimensional Channels Formed by 14 and 12 Rings. *Science* **2004**, *304*, 990−992.

(22) Corma, A.; Diaz-Cabanas, M. J.; Rey, F.; Nicolopoulus, S.; Boulahya, K. ITQ-15: The First Ultralarge Pore Zeolite with a Bi-directional Pore System Formed by Intersecting 14- and 12-ring

Channels, and Its Catalytic Implications. *Chem. Commun.* **2004**, *12*, 1356−1357.

(23) Verheyen, E.; Joos, L.; Van Havenbergh, K.; Breynaert, E.; Kasian, N.; Gobechiya, E.; Houthoofd, K.; Martineau, C.; Hinterstein, M.; Taulelle, F.; Van Speybroeck, V. Design of Zeolite by Inverse Sigma Transformation. *Nat. Mater.* **2012**, *11*, 1059−1064.

(24) Jagiello, J.; Sterling, M.; Eliášová, P.; Opanasenko, M.; Zukal, A.; Morris, R. E.; Navaro, M.; Mayoral, A.; Crivelli, P.; Warringham, R.; Mitchell, S.; Pérez-Ramírez, J.; Čejka, J. Structural Analysis of IPC Zeolites and Related Materials Using Positron Annihilation Spectroscopy and High-resolution Argon Adsorption. *Phys. Chem. Chem. Phys.* **2016**, *18*, 15269−15277.

(25) Zukal, A.; Shamzhy, M.; Kubů, M.; Čejka, J. The Effect of Pore Size Dimensions in Isoreticular Zeolites on Carbon Dioxide Adsorption Heats. *J. CO₂ Util.* **2018**, *24*, 157−163.

(26) Přech, J.; Morris, R. E.; Čejka, J. Selective Oxidation of Bulky Organic Sulphides over Layered Titanosilicate Catalysts. *Catal. Sci. Technol.* **2016**, *6*, 2775−2786.

(27) Přech, J.; Čejka, J. UTL Titanosilicate: An Extra-large Pore Epoxidation Catalyst with Tunable Textural Properties. *Catal. Today* **2016**, *277*, 2−8.

(28) Žilková, N.; Eliášová, P.; Al-Khattaf, S.; Morris, R. E.; Mazur, M.; Čejka, J. The Effect of UTL Layer Connectivity in Isoreticular Zeolites on the Catalytic Performance in Toluene Alkylation. *Catal. Today* **2016**, *277*, 55−60.

(29) Dědeček, J.; Sobalík, Z.; Wichterlová, B. Siting and Distribution of Framework Aluminium Atoms in Silicon-Rich Zeolites and Impact on Catalysis. *Catal. Rev.: Sci. Eng.* **2012**, *54*, 135−223.

(30) Jones, A. J.; Carr, R. T.; Zones, S. I.; Iglesia, E. Acid Strength and Solvation in Catalysis by MFI Zeolites and Effects of the Identity, Concentration and Location of Framework Heteroatoms. *J. Catal.* **2014**, *312*, 58−68.

(31) Vjunov, A.; Fulton, J. L.; Huthwelker, T.; Pin, S.; Mei, D.; Schenter, G. K.; Govind, N.; Camaioni, D. M.; Hu, J. Z.; Lercher, J. A. Quantitatively Probing the Al Distribution in Zeolites. *J. Am. Chem. Soc.* **2014**, *136*, 8296−8306.

(32) Chen, J.; Liang, T.; Li, J.; Wang, S.; Qin, Z.; Wang, P.; Huang, L.; Fan, W.; Wang, J. Regulation of Framework Aluminum Siting and Acid Distribution in H-MCM-22 by Boron Incorporation and Its Effect on the Catalytic Performance in Methanol to Hydrocarbons. *ACS Catal.* **2016**, *6*, 2299−2313.

(33) Matsunaga, Y.; Yamazaki, H.; Imai, H.; Yokoi, T.; Tatsumi, T.; Kondo, J. N. Hexamethyleneimine and Pivalonitrile as Location Probe Molecules of Lewis Acid Sites on MWW-type Zeolites. *Microporous Mesoporous Mater.* **2015**, *206*, 86−94.

(34) Onida, B.; Geobaldo, F.; Testa, F.; Crea, F.; Garrone, E. FTIR Investigation of the Interaction at 77 K of Diatomic Molecular Probes on MCM-22 Zeolite. *Microporous Mesoporous Mater.* **1999**, *30*, 119−127.

(35) Wang, S.; Wang, P.; Qin, Z.; Chen, Y.; Dong, M.; Li, J.; Zhang, K.; Liu, P.; Wang, J.; Fan, W. Relation of Catalytic Performance to the Aluminum Siting of Acidic Zeolites in the Conversion of Methanol to Olefins, Viewed via a Comparison between ZSM-5 and ZSM-11. *ACS Catal.* **2018**, *8*, 5485−5505.

(36) Liang, T.; Chen, J.; Qin, Z.; Li, J.; Wang, P.; Wang, S.; Wang, G.; Dong, M.; Fan, W.; Wang, J. Conversion of Methanol to Olefins over H-ZSM-5 Zeolite: Reaction Pathway Is Related to the Framework Aluminum Siting. *ACS Catal.* **2016**, *6*, 7311−7325.

(37) Wang, S.; Li, S.; Zhang, L.; Qin, Z.; Dong, M.; Li, J.; Wang, J.; Fan, W. Insight into the Effect of Incorporation of Boron into ZSM-11 on Its Catalytic Performance for Conversion of Methanol to Olefins. *Catal. Sci. Technol.* **2017**, *7*, 4766−4779.

(38) Shvets, O. V.; Zukal, A.; Kasian, N.; Žilková, N.; Čejka, J. The Role of Crystallization Parameters for the Synthesis of Germanosilicate with UTL Topology. *Chem. - Eur. J.* **2008**, *14*, 10134−10140.

(39) Shamzhy, M. V.; Shvets, O. V.; Opanasenko, M. V.; Yaremov, P. S.; Sarkisyan, L. G.; Chlubná, P.; Čejka, J. Synthesis of Isomorphously Substituted Extra-large Pore UTL Zeolites. *J. Mater. Chem.* **2012**, *22*, 15793−15803.

120

(40) Wichterlová, B.; Tvarůšková, Z.; Sobalík, Z.; Sarv, P. Determination and Properties of Acid Sites in H-ferrierite: A Comparison of Ferrierite and MFI Structures. *Microporous Mesoporous Mater.* **1998**, *24*, 223−233.

(41) Lawton, S. L.; Leonowicz, M. E.; Partridge, R. D.; Chu, P.; Rubin, M. K. Twelve-ring Pockets on the External Surface of MCM-22 Crystals. *Microporous Mesoporous Mater.* **1998**, *23*, 109−117.

(42) Štekrová, M.; Kubů, M.; Shamzhy, M.; Musilová, Z.; Čejka, J. α-Pinene Oxide Isomerization: Role of Zeolite Structure and Acidity in the Selective Synthesis of Campholenic Aldehyde. *Catal. Sci. Technol.* **2018**, *8*, 2488−2501.

(43) Corma, A.; Fornés, V.; Rey, F. Quinoline as a Probe Molecule for Determination of External Brönsted and Lewis Acidity in Zeolites. *Zeolites* **1993**, *13*, 56−59.

(44) Chiang, H.; Bhan, A. Catalytic Consequences of Hydroxyl Group Location on the Rate and Mechanism of Parallel Dehydration Reactions of Ethanol over Acidic Zeolites. *J. Catal.* **2010**, *271*, 251−261.

(45) Kadam, S. A.; Shamzhy, M. V. IR Operando Study of Ethanol Dehydration over MFI zeolite. *Catal. Today* **2018**, *304*, 51−57.

(46) Kadam, S. A.; Shamzhy, M. V. IR Operando Study of Ethanol Dehydration over MFI Zeolites: Structure-Activity Relationships. *J. Phys. Chem. C* **2018**, *122*, 24055−24067.

(47) Di Iorio, J. R.; Nimlos, C. T.; Gounder, R. Introducing Catalytic Diversity into Single-Site Chabazite Zeolites of Fixed Composition via Synthetic Control of Active Site Proximity. *ACS Catal.* **2017**, *7* (10), 6663−6674.

(48) Carr, R. T.; Neurock, M.; Iglesia, E. Catalytic Consequences of Acid Strength in the Conversion of Methanol to Dimethyl ether. *J. Catal.* **2011**, *278*, 78−93.

(49) Jones, A. J.; Zones, S. I.; Iglesia, E. Implications of Transition State Confinement within Small Voids for Acid Catalysis. *J. Phys. Chem. C* **2014**, *118*, 17787−17800.

(50) Naik, S. G. R.; Patel, B. K. Tetrabutylammonium Tribromide (TBATB)-promoted Tetrahydropyranylation/depyranylation of Alcohols. *Tetrahedron Lett.* **2001**, *42*, 7679−7681.

(51) Chandrasekhar, S. T. M.; Reddy, Y. R.; Mohapatra, S.; Rao, C. R.; Reddy, K. V. TaCl$_5$-silicagel and TaCl$_5$ as New Lewis Acid Systems for Selective Tetrahydropyranylation of Alcohols and Thioacetalisation, Trimerisation and Aldolisation of Aldehydes. *Tetrahedron* **1997**, *53*, 14997−15004.

121

Enclosure 2

Novel approach towards Al-rich AFI for catalytic application

Yong Zhou, Naděžda Žilková, Mariya Shamzhy, Yamini Avadhut, Martin Hartmann, Jiří Čejka, Maksym Opanasenko, Applied Catalysis A: General, 577(2019), 62-68.

Contents lists available at ScienceDirect

Applied Catalysis A, General

Novel approach towards Al-rich AFI for catalytic application

Yong Zhou[a,b], Naděžda Žilková[a], Mariya Shamzhy[b], Yamini Avadhut[c], Martin Hartmann[c], Jiří Čejka[b], Maksym Opanasenko[b,*]

[a] J. Heyrovsky Institute of Physical Chemistry, Czech Academy of Sciences, Dolejškova 3, 182 23, Prague 8, Czech Republic
[b] Department of Physical and Macromolecular Chemistry, Faculty of Science, Charles University in Prague, Hlavova 8, 128 43, Prague 2, Czech Republic
[c] Erlangen Catalysis Resource Center, Friedrich-Alexander-Universität Erlangen-Nürnberg, Egerlandstr. 3, 91058, Erlangen, Germany

ABSTRACT

A new germanosilicate structural analogue of **AFI** zeolite (Ge-AFI) was hydrothermally synthesized. One- and two-step alumination of the Ge-AFI zeolites were used to modify their structure and acidic properties traced using XRD, N_2 adsorption, ICP-OES, ^{27}Al NMR, and FTIR spectroscopy. Two-step aluminated sample (deGe-Al-AFI) provided a higher Al content, stronger acid sites and a higher micropore volume than one-step aluminated sample (Al-AFI). Extensive evaluation of the catalytic performance of these **AFI** zeolites compared with reference conventional zeolite catalysts for alkylation of toluene with isopropyl alcohol showed that deGe-Al-AFI exhibited relatively high toluene conversion and selectivity to valuable p-cymene due to the optimized textural and acidic properties.

1. Introduction

Synthesis of zeolites with large (12-ring) and extra-large (> 12-ring) pores is of a great interest and importance due to their ability to accommodate bulky molecules in adsorption and catalysis [1–3]. As an example, zeolite and zeotype materials with the **AFI** framework type have been investigated in such as shape-selective catalysis and gas separation [4–8] because of their unique one-dimensional parallel 12-ring pore opening of 7.3 Å [9].

The synthesis of the pure silica **AFI** zeolite (SSZ-24) was reported over 20 years ago by Zones et al. [10], however, the direct hydrothermal crystallization of Al containing SSZ-24 has never been achieved. Later, the success in the synthesis of borosilicate SSZ-24 provided a chance to incorporate heteroatoms, e.g. Al and Fe, into the SSZ-24 framework for preparation of the desirable shape-selective catalysts [5,11,12]. B-SSZ-24 can be synthesized either using a calcined borosilicate Beta as the boron and silica sources [11] or using N(16)-methylsparteinium as structure directing agent (SDA) [12]. However, only a limited amount of Al (Si/Al > 63) or Ti (Si/Ti > 200) can be incorporated into the **AFI** framework when using B-SSZ-24 precursor by isomorphous substitution [7,13]. In contrast to the conversion of B-Beta into B-SSZ-24 followed by alumination, Hiroyoshi et al. reported the hydrothermal synthesis of Al-SSZ-24 with Si/Al = 70 from Al-Beta zeolite precursor [14]. In order to improve the potential of substituted

SSZ-24 zeolites as catalyst increasing the content of active sites, the new method to prepare heteroatom-containing SSZ-24 is still highly desirable.

Over the last decade, many new large- and extra-large- pore zeolites have been synthesized in the germanosilicate form [15–18]. Germanium acts as inorganic structure-directing-agent (SDA) stabilizing the formation of small building units, e.g. double four rings (d4r) or double three rings (d3r), having high geometric constraints [19]. On the other hand, germanosilicates possess hydrolytic lability of Ge–O bonds, which stimulated researchers developed methods to incorporate heteroatoms, e.g. B, Al, Ga, Ti, Sn, into the frameworks of germanosilicates by post-synthetic synthesis, such as BEC [20], UTL [21–23], IWW and ITH [21], IWR [24], and ITQ-33 [25]. Such isomorphous substitution with tri-valent or tetravalent heteroatoms into the zeolite framework not only stabilizes the zeolite structure but also introduce the active sites into the frameworks. Therefore, the synthesis of germanosilicate **AFI** zeolite followed by the post-synthetic substitution could be a desirable way to obtain **AFI** zeolite with reasonably high content of catalytically active sites.

In the present work, we report the synthesis of a new gemanosilicate SSZ-24 (Ge-AFI) zeolite and utilization of this germanosilicate for post-synthetic isomorphous substitution via either one-step or two-step alumination procedures. The catalytic properties of aluminated **AFI** materials were evaluated in the alkylation of toluene with isopropyl

* Corresponding author at: Department of Physical and Macromolecular Chemistry, Faculty of Science, Charles University in Prague, Hlavova 8, 128 43, Prague 2, Czech Republic.

E-mail address: maksym.opanasenko@natur.cuni.cz (M. Opanasenko).

alcohol.

2. Experimental

2.1. Materials and synthesis

2.1.1. Materials

1,5-dibromopentane (97%, Sigma Aldrich), cis-2,6-dimethylpiper-idine(98%, Sigma Aldrich), NaOH (98%, Lanchner), Sodium sulfate (Sigma Aldrich), Chloroform (Lanchner), Diethyl ether (Lanchner), Ambersep® 900(OH) (Alfa Aesar), Germanium oxide (99.99%, Sigma Aldrich), Cab-O-Sil M-5 (Supelco Analytical), Aluminum nitrate non-ahydrous (99.4%, Lanner), Hydrochloric acid (37 wt. % in H_2O, Lanchner).

2.1.2. Synthesis

2.1.2.1. Structure directing agent (SDA). The 7, 11-dimethyl-6-azoniaspiro [5.6] undecane was synthesized with the method similar to that described in the literature [26]. 140 ml of distilled water, 5.68 g NaOH, and 32.65 g 1, 5-dibromopentane were mixed in a glass flask. Then, 16.07 g of (2R, 6S)-2, 6-dimethylpiperidine was added dropwise under reflux. The mixture was under very intensive stirring to prepare a milk-like suspension and then cooled in an ice bath. Another small amount of NaOH was added very slowly under vigorous stirring and cooling by ice until the appearance of the oil products. Further stirring for 1 h led to the formation of the crystalline phase, which was recovered by filtration and extracted with 300 ml chloroform. The organic fractions were dried using anhydrous sodium sulfate and partially evaporated. The ammonium salt was precipitated and washed out with diethyl ether. The salt was converted into hydroxide form by ion exchange with Ambersep® 900(OH) anion exchange resin.

2.1.2.2. Ge-AFI. The germanosilicate **AFI** zeolite (referred to as **Ge-AFI**) was synthesized from a gel using 7, 11-dimethyl-6-azoniaspiro [5.6] undecane as SDA with a molar composition: $0.96\ SiO_2 : 0.24\ GeO_2 : 0.4\ SDA : 30\ H_2O$. The gel was prepared by dissolving germanium oxide in the solution of SDAOH followed by addition of silica into the solution and the mixture was stirred at room temperature for 30 min. Hydrothermal crystallization was conducted at 175 °C for 7 days under agitation.

The ranges of compositions yielding the germanosilicate **AFI** can be varied:

$$0.9-0.96\ SiO_2 : 0.24-0.3\ GeO_2 : 0.4\ SDA : 30\ H_2O.$$

The solid products were recovered by filtration with water and then dry at 65 °C overnight. To remove the SDA from the zeolites, the as-synthesized samples were calcined in air at 550 °C for 6 h.

2.1.2.3. Al-AFI. Al containing **AFI** catalyst synthesized though one-step alumination of calcined Ge-AFI is referred to as **Al-AFI**. 1 g of calcined zeolite was treated with 100 ml of 1 M $Al(NO_3)_3$ solution at 80 °C for 48 h. The aluminated sample was subsequently centrifuged and washed with 0.01 M HCl and water and then dried at 65 °C overnight.

2.1.2.4. deGe-Al-AFI. Al containing **AFI** catalyst synthesized though two-step alumination of calcined Ge-AFI is referred to as **deGe-Al-AFI**. 1 g of calcined zeolite was treated with 100 ml of 0.1 M HCl solution at 80 °C for 16 h. After the treatment, the zeolite was centrifuged and washed with water to $_pH = 7$. The alumination was conducted by addition of 100 ml of 1 M $Al(NO_3)_3$ solution at 80 °C for 48 h. The aluminated sample were subsequently centrifuged and washed with 0.01 M HCl and water and then dried at 65 °C overnight.

All the aluminated samples were calcined at 450 °C for 4 h prior further characterization.

2.2. Characterization

The structure and crystallinity of zeolites were determined by powder X-ray diffraction (XRD) using a Bruker AXS D8 Advance diffractometer with Cu Kα radiation in Bragg-Brentano geometry. The chemical composition was determined an inductively coupled plasma-optical emission spectrometry (ICP/OES) (ThermoScientific Icap7000). Crystal size and shape of all the samples were assessed using a JSM-5500LV microscope. Nitrogen adsorption measurements were carried out on a Micromeritics GEMINI II 2370 volumetric Surface Area Analyzer at −196 °C to determine BET area and pore volume.

Concentration of Lewis (c_L) and Brønsted (c_B) acid sites was determined after adsorption of pyridine (PyR) by Fourier-transform infrared spectroscopy (FTIR) on Nicolet 6700 FTIR with MCT/B detector. Zeolites were pressed into self-supporting wafers with a density of 8.0–12 mg/cm² and activated in situ at 450 °C overnight. Pyridine adsorption was carried out at 150 °C for 20 min at partial pressure 600–800 Pa, followed by desorption for 20 min. Before adsorption pyridine was degassed by freezing and thawing cycles. All spectra were recorded with a resolution of 4 cm⁻¹ by collecting 128 scans for a single spectrum at room temperature. Spectra were calculated on wafer density of 10 mg cm⁻². Concentration of c_L and c_B were evaluated from the integral intensities of bands at 1454 cm⁻¹ (c_L) and at 1545 cm⁻¹ (c_B) using molar absorption coefficients, $\varepsilon(L) = 2.22$ cm μmol⁻¹, and $\varepsilon(B) = 1.67$ cm μmol⁻¹ [27]. For the determination of the strength of different acid sites, desorption of pyridine was carried out at 150, 250, 350 and 450 °C followed by FTIR measurements. A relatively large probe molecule 2,6-di-tert-butyl-pyridine (DTBP) was used to determine the accessibility of acid sites within prepared zeolites [28]. The adsorption of DTBP took place at 150 °C and at equilibrium probe vapour pressure with the zeolite wafer for 15 min. Desorption proceeded at the same temperature for 1 h followed by collection of spectra at room temperature. Molar absorption coefficient from Ref [27]. was used for evaluation of c_B accessible for DTBPy using integral intensity of absorption band ca. 1530 cm⁻¹.

The solid state ²⁷Al nuclear magnetic resonance (NMR) spectra were recorded under magic angle spinning (MAS) with a commercial 3.2 mm triple resonance MAS probe spinning at 15 kHz on an Agilent DD2 500WB spectrometer operating a at resonance frequency of 130.24 MHz.

2.2.1. Catalytic test

Toluene alkylation with isopropyl alcohol was investigated in a vapor phase continuous down-flow glass micro-reactor with a fixed bed of catalyst under atmospheric pressure. Before the catalytic run, all the zeolite catalysts studied were activated at 500 °C in nitrogen stream for 120 min. The reaction was performed at 250 °C with toluene to iso-propyl alcohol (Tol/i-PrOH) molar ratio of 9.6 and weight hour space velocity (WHSV) based on toluene equal to 10 h⁻¹. The reaction products were analyzed using an Agilent 6890 Plus "on-line" gas chromatograph with flame ionization detector and a high-resolution capillary DB-5 column (length 50 m, diameter 0.32 mm, and film thickness 1 μm). After 15 min of the time-on-stream (T-O-S), the first analysis was done, followed by further sampling of the reaction products at approx. 50 min interval.

3. Results and discussion

3.1. Synthesis and characterization of aluminated AFI zeolites by using Ge-AFI as precursors

Germanosilicate Ge-SSZ-24 (Ge-AFI) with Si/Ge of 8.1 in the framework (Table 1) was prepared under hydrothermal conditions using 7, 11-dimethyl-6-azoniaspiro [5.6] undecane as SDA in this study. The synthesis of Ge-AFI is sensitive to the Ge content in the gel mixture (Fig. S1). At Si/Ge ratio ≤ 2, germanosilicate UTL is the main phase, while at

63

124

Table 1

Physicochemical and textural properties of Ge- or Al-zeolites under investigation.

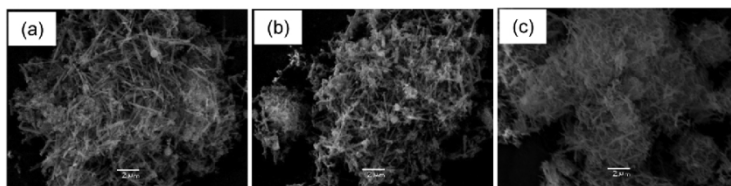| Catalyst	Pore system dimension	Si/Ge[a]	Si/Al[a]	S_{BET}[b] $/m^2 g^{-1}$	V_{tot} $/cm^3 g^{-1}$	V_{micro}[c] $/cm^3 g^{-1}$
Ge-AFI	1 D	8.1	–	306	0.26	0.10
Al-AFI		25	53	128	0.19	0.02
deGe-AFI		22	–	330	0.27	0.11
deGe-Al-AFI		38	29	356	0.24	0.12
MTW	1D	–	52	296	0.22	0.10
IPC-2	2D	–	48	390	0.20	0.16
Beta	3D	–	23	619	0.35	0.25

[a] Measured by ICP/OES. [b] Specific surface area (BET) given by N_2 adsorption at −196 °C. [c] Calculated by t-plot method.
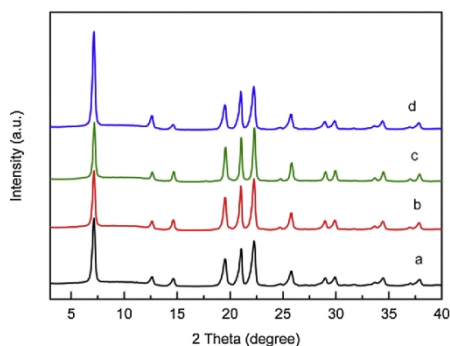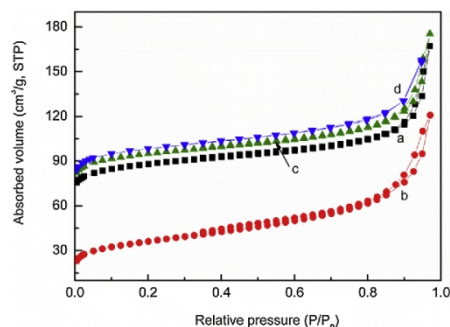

Fig. 1. XRD patterns of Ge-AFI (a), Al-AFI (b), deGe-AFI (c), and deGe-Al-AFI (d) zeolites.

Si/Ge ratio ≥ 3, pure Ge-AFI could be obtained. For further incorporation of Al into AFI zeolite, direct alumination (denoted as Al-AFI) and two-step degermanation-alumination (deGe-Al-AFI) were performed in order to evaluate the necessity for the careful acidic leaching of Ge prior the introduction of Al into the framework.

The structures of starting, intermediate and final **AFI** samples were investigated with XRD. Fig. 1 shows that the calcined Ge-AFI had high crystallinity and no impurities at detectable level. Both aluminated **AFI** samples obtained by the one- or two-step alumination retained topology typical for **AFI** (Fig. 1) The crystals of synthesized Ge-AFI precursor have the needle shape (3 μm x 0.2 μm) and form aggregates of several μm size (Fig. 2, a). It is worth to note that the morphology of obtained **AFI** zeolite significantly differs from that of B-SSZ-24 having much larger hexagonal crystals [12]. This feature of Ge-AFI can potentially provide more efficient post-synthesis isomorphous substitution due to the decreased diffusional restrictions in tiny needle-like crystals in comparison with bulky ones. After post-synthetic alumination, needle-shape crystal morphology typical for Ge-AFI was preserved in the deGe-Al-AFI and Al-AFI samples (Fig. 2b and c). These results indicate the

Fig. 3. N_2 adsorption and desorption isotherms of the calcined Ge-AFI precursor (a), Al-AFI (b), deGe-AFI (c), and deGe-Al-AFI (d) samples at −196 °C.
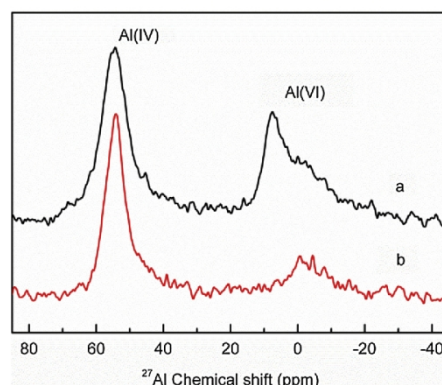
Fig. 4. ^{27}Al NMR spectra of Al-AFI (a) and deGe-Al-AFI (b).

applied alumination treatments have almost no impact on the crystal structure and morphology of substituted **AFI** zeolites.

All AFI samples showed similar and typical type I adsorption/desorption isotherms (Fig. 3) with gradual increase in the adsorbate uptake in the range 0.1 – 0.9 p/p_0 probably due to the very small size of the crystals and an enhanced nitrogen uptake at high relative pressure $p/p_0 > 0.9$ may be ascribed to the existence of interparticle voids of different size generated from the disordered agglomeration of crystallites. Compared to the Ge-AFI precursor, Al-AFI sample demonstrated a significantly lower BET area and the pore volume (Table 1) that could be caused by the deposition of inorganic remnants in the pores of Al-AFI. The source of these residues can be either the former framework domains formed during leaching of Ge from the structure or aluminum-containing species formed during the treatment with $Al(NO_3)_3$ solution; however, they could not be traced by XRD because of small size of these

Fig. 2. SEM images of Ge-AFI (a), deGe-Al-AFI (b), and Al-AFI (c) zeolites.
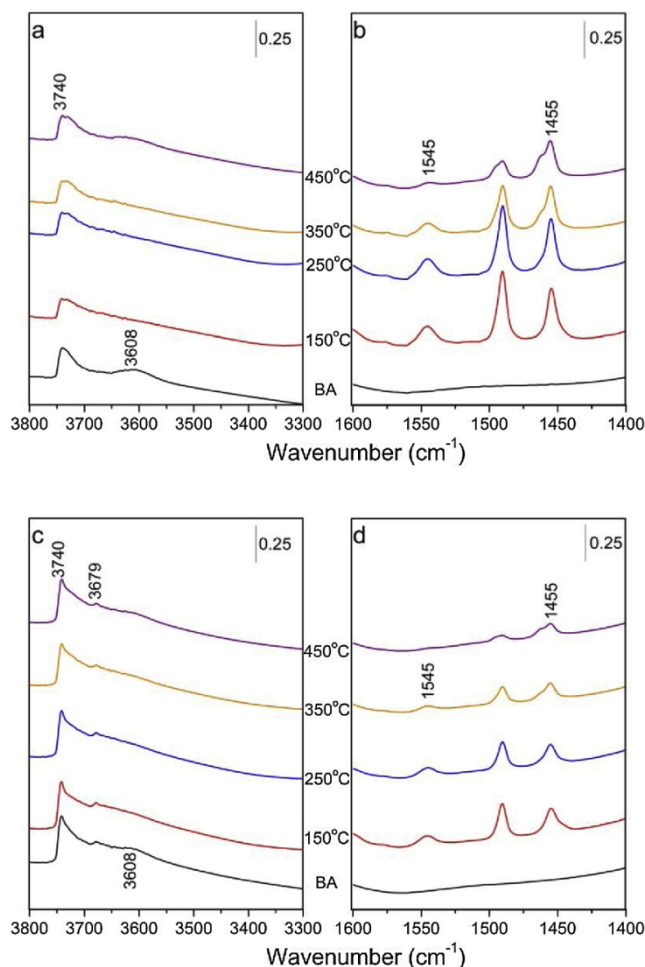
125

Fig. 5. FTIR spectra of (a, b) deGe-Al-AFI and (c, d) Al-AFI before (BA), and after pyridine adsorption, followed by desorption at 150 °C, 250 °C, 350 °C, and 450 °C.

Table 2
Acidic properties of catalysts determined by pyridine-IR at 150 °C.

Catalyst	Brønsted[a] /mmol g^{-1}	Lewis[b] /mmol g^{-1}	Total /mmol g^{-1}	B/L ratio
Al-AFI	0.05	0.08	0.13	0.63
deGe-Al-AFI	0.11	0.15	0.26	0.73
MTW	0.11	0.03	0.14	3.67
IPC-2	0.13	0.12	0.25	1.08
Beta	0.33	0.19	0.52	1.74

[a] Calculated from the area of the band located at around 1545 cm^{-1}. [b] Calculated from the area of the band located at around 1455 cm^{-1}.

species. On the other hand, textural characteristics of the sample obtained by two-step treatment were similar to that of Ge-AFI. Intermediate HCl-treated Ge-AFI sample (deGe-AFI) exhibited increased BET area (from 306 to 330 m^2 g^{-1}) and micropore volume (from 0.10 to 0.11 cm^3 g^{-1}) (Table 1), which may be caused by removal of the Ge

species from the framework (in agreement with the chemical analysis showing the increase in the Si/Ge molar ratio from 8.1–22) and formation of the silanol nests. The following Al incorporation healed the defects and the resulting deGe-Al-AFI possessed a BET area and pore volume comparable to the parent Ge-AFI. These results suggest that the acid treatment prior to alumination is i) more benificial for generation of hydroxyl nests by removal of germaniun atoms from the framework, which weakens the steric hindrance for the insertion of Al isomorphously into the framework and ii) necessary to decrease the deposition of solid species that block the pores in final zeolite. According to the analysis of mesopore size distribution (Fig. S2), no significant changes in their characteristics were detected indicating that alumination affect mainly microporous system of AFI zeolite under conditions used.

To evaluate the state of Al atoms in the frameworks of zeolites obtained by different approaches, ^{27}Al NMR spectra of Al-AFI and deGe-Al-AFI were investigated (Fig. 4). The spectra consist of two groups of
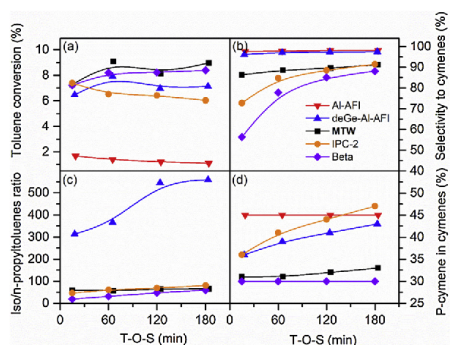
Fig. 6. Time-on-stream dependence of (a) toluene conversion, (b) selectivity to cymenes, (c) iso-/n-propyltoluenes ratio and (d) para-cymene selectivity in toluene alkylation with isopropyl alcohol over Al-AFI, deGe-Al-AFI, **MTW**, IPC-2 and Beta catalysts at 250 °C. Toluene to isopropyl alcohol (Tol/i-PrOH) molar ratio of 9.6 and WHSV based on toluene equal to 10 h $^{-1}$.

peaks centered around 55 and 0–10 ppm, which are assigned to tetrahedrally coordinated Al and extra-framework (penta-coordinated, octahedral or distorted octahedral) Al, respectively. deGe-Al-AFI possessed significantly lower fraction of extra-framework Al (about 10% of that in Al-AFI sample), which is consistent with the adsorption results and further confirms the necessity of an additional degermanation step prior to alumination, maybe the large amount of extra framework Al as pore blockage leaded to decrease in the pore volume in Al-AFI sample. Although, the ^{27}Al NMR spectra indicated the presence of extra framework Al, Al^{3+} is mainly incorporated into the tetrahedral framework positions by both alumination procedures.

In full agreement with ^{27}Al NMR results, FTIR spectrum of Al-AFI showed the band at 3679 cm^{-1} attributed to Al-O–H groups of small non-acidic extra-framework aluminum species [29,30] (Fig. 5c), while both Al-AFI and deGe-Al-AFI possess the bands at 3740 and 3608 cm^{-1} assigned to silanol and bridging hydroxyl ≡Si-(OH)-Al≡ groups [31] (Fig. 5a,c). To provide a detailed information about the type, amount, and strength of acid sites in deGe-Al-AFI and Al-AFI, FTIR spectroscopy of adsorbed pyridine was used. After pyridine adsorption, the intensities of the bands ca. 3740 and 3679 cm^{-1} remained almost unchanged, while the band at 3608 cm^{-1} assigned to bridging hydroxyl groups of acid character disappeared, evidencing the accessibility of all Brønsted acid centres for pyridine in the investigated samples. On the other hand, the adsorption of pyridine in Al-AFI and deGe-Al-AFI was accompanied with the appearance of a typical set of adsorption bands in the region 1400 – 1600 cm^{-1} attributed to the probe molecule interacting either with Lewis or Brønsted acid sites. Fig. 5 shows the evolution of the absorption bands centered around 1455 and 1545 cm^{-1} (related to pyridine molecules adsorbed on the Lewis and Brønsted acid sites, respectively) after desorption of pyridine from

deGe-Al-AFI (Fig. 5b) and Al-AFI (Fig. 5d) zeolites at different temperatures. The fraction of strong acid sites (calculated as the amount of pyridine molecules remaining adsorbed after heating at 623 K) was higher for deGe-Al-AFI sample (70%) in comparison with Al-AFI (54%). Only low intensive bands at 1455 and 1545 cm^{-1} can be seen in the spectra of Al-AFI when the desorption temperature was increased to 723 K. In addition, the acid sites located at the external surface were assessed with DTBPy as probe molecule (Fig. S3) with the kinetic diameter of 0.79 nm [28], being higher than the diameter of 12-ring channels in AFI zeolite. Indeed, the adsorption of DTBP on either Al-AFI or deGe-Al-AFI does not remove, but only slightly decreases intensity of the band at 3608 cm^{-1} corresponding to bridging hydroxyl groups, which indicates a small fraction of Brønsted acid centers are accessible for DTBPy. The bands at 1616 and 1530 cm^{-1} can detected in the region of chemisorbed DTBPy were attributed to the formation of DTBPyH$^+$ ions [28]. The absence of a band at 1545 cm^{-1} confirms no dealkylation of the probe molecule used. Based on the integral intensity of absorption band ca. 1530 cm^{-1}, the concentration of acid sites at external surface of Al-AFI (0.01 mmol g^{-1}) was evaluated to be 3 times lower compared to deGe-Al-AFI (0.03 mmol g^{-1}).

3.2. Catalytic performance of aluminated AFI zeolites

Aromatic alkylation reactions are widely employed as model reactions for the characterization of zeolite structures. Their activity and selectivity can be correlated to the textural and acidic properties of zeolites. [32–36] The catalytic performance of two aluminated **AFI** zeolites in the alkylation of toluene with isopropyl alcohol was compared with conventional zeolites possessing pore entrances of a size similar to **AFI** (12-ring channels) but different pore connectivity: **MTW** with 1-dimensional (1D) pore system (12-ring), IPC-2 with intersecting 12- and 10-ring channels (2D) and Beta zeolite possessing 3-dimensional (3D) pore system with 12-ring windows (Tables 1,2, Fig. 6). For the reference zeolites (except Beta), the concentration of Brønsted acid sites responsible for catalytic activity in the alkylation reaction [32,37,38] was kept similar to that of the most promising deGe-Al-AFI (0.11 – 0.13 mmol g^{-1}) to exclude the influence of this parameter on the overall catalytic activity. The catalysts were compared in terms of i) toluene conversion; ii) selectivity to cymene isomers; iii) para-selectivity to p-cymene; iv) iso/n-propyl ratio in cymenes (Fig. 6 and Table 4). Toluene conversion decreased in the order **MTW** ≈ Beta > deGe-Al-AFI > IPC-2 > Al-AFI (Fig. 6a). This result agrees with the Brønsted/Lewis acid ratio (B/L ratio) in the catalysts investigated (Table 2). Alkylation of toluene with alcohols catalyzed by zeolites is commonly considered to proceed via carbonium ion mechanisms [37,38] and the Brønsted acid sites are active sites of the reaction [32]. Lewis acid centers can act as the additional adsorption sites [39] slowing down the overall rates of reactants/products diffusion. Therefore, lower B/L ratio leads to lower catalytic activities. In spite of 12-ring in IPC-2, smaller 10-ring channels cause diffusion limitations similar to that found for MFI zeolite [34]. Additionally, IPC-2 zeolite had the plate-like morphology and relatively large crystals (Fig. S4) which

Table 3

Catalyst activity and products distribution in the alkylation of toluene with isopropyl alcohol on catalysts under study after 13 min of T-O-S.

Catalyst	Toluene Conv. (%)	p-cymene	o-cymene	m-cymene	propyl toluene	other	cymene Sel. (%)
		Products selectivity (%)					
Al-AFI	1.7	43.8	22.0	31.8	0	2.4	97.6
deGe-Al-AFI	7.2	33.7	6.9	55.3	0.4	3.7	95.9
MTW	7.3	26.5	4.5	55.4	1.5	12.1	86.4
IPC-2	7.4	25.8	1.3	45.6	1.6	25.7	72.7
Beta	7.2	16.7	2.8	36.9	2.9	40.7	56.4

Reaction conditions: toluene / i-PrOH molar ratio = 9.6, catalyst = 0.14 g, temperature = 250 °C, TOS = 13 min.

Table 4
Catalyst activity and products distribution in the alkylation of toluene with isopropyl alcohol on catalysts under study after 184 min of T-O-S.

Catalyst	Toluene Conv. (%)	Products selectivity (%)					cymene Sel. (%)
		p-cymene	o-cymene	m-cymene	propyl toluene	other	
Al-AFI	1.1	43.9	24.6	30.0	0	1.5	98.5
deGe-Al-AFI	6.4	41.0	11.0	45.3	0.2	2.5	97.3
MTW	9.0	30.0	5.1	56.3	1.4	7.2	91.4
IPC-2	6.0	43.3	1.2	47.0	1.1	7.4	91.5
Beta	8.4	26.3	4.4	57.4	1.5	10.4	88.1

Reaction conditions: toluene / i-PrOH molar ratio = 9.6, catalyst = 0.14 g, temperature = 250 °C, TOS = 184 min.

can only be accessed from the rim of the crystal plates, this could also result in diffusion limitations and hampers the efficient use of the catalyst [35]. These maybe the reason why deGe-Al-AFI (B/L = 0.73) outperform the IPC-2 (B/L = 1.08). Al-AFI exhibited the lowest toluene conversion, its relatively poor catalytic activity is caused by a partial blockage of the pores during one-step alumination treatment and this severe decrease in the pore volume led to poor diffusion of reactants and products.

In contrast to conversion, the most important selectivity parameters (selectivity to cymenes, p-selectivity, and iso/n-propyl ratio) significantly differed for the materials with different structural properties. Selectivity to cymenes, the primary reaction (o- and p-cymenes) and isomerization (m-cymene) products, strongly depended on the dimensions and connectivity of the zeolite channels and decreased in the sequence of 1D > 2D > 3D (Fig. 6b). In the case of two aluminated AFI samples, selectivity to cymenes is rather constant and close to 100% within 184 min T-O-S indicating that cymenes are almost exclusively formed (Table 3). Relatively lower selectivity to cymenes for IPC-2, and Beta mainly caused by formation of n-propyl toluene (Tables 3 and 4) and secondary alkylation of primarily formed cymenes to other aromatic compounds, e.g. di-isopropyltoluene.

The isopropyl (cymene)/ n-propyl toluene ratio did not exceed 80 for MTW, IPC-2 and Beta zeolites in the course of the reaction during 184 min T-O-S (Fig. 6c). In contrast, for deGe-Al-AFI this ratio was found to be higher than 300 at the low T-O-S values and increased to > 550 at 184 min T-O-S. This is in line with the proposed mechanism of n-propyl toluene formation [40], evidencing the decisive role of 10-ring (10–12) channel intersections being able to accommodate the transition state of the bimolecular isomerization reactions between toluene and primarily formed cymene. Based on the results above, thus, the selectivity towards valuable branched products can be significantly increased over deGe-Al- AFI zeolites in comparison with conventional zeolites possessing either 1D (MTW) or multidimensional (IPC-2, Beta) pore system.

The selectivity to p-cymene over Beta and MTW was only 30% and 32%, respectively (Fig. 6d), which is lower than the values found for deGe-Al-AFI (41%), IPC-2 (43%) and Al-AFI (44%). Relatively low para-selectivity of Beta and MTW can be attributed to the higher B/L ratios or porosity for these zeolites. As a result, the kinetically favored p-cymene can be transformed to o- or m-cymene on the acid sites without steric limitation.

Therefore, the deGe-Al-AFI catalyst showed advantages to reach both relatively higher toluene conversion and commercially valuable p-cymene selectivity in the alkylation of toluene with isopropyl alcohol.

4. Conclusions

In the present work, new germanosilicate AFI zeolite with Si/Ge molar ratio equal to 8 was synthesized using 7, 11-dimethyl-6-azoniaspiro [5.6] undecane as SDA. This AFI zeolite was treated by one-step alumination or two-step degermanation/alumination and final products were investigated from the structure and acidity point of

views. The catalytic performance of these aluminated AFI zeolites was evaluated in alkylation of toluene with isopropyl alcohol. Incorporation of Al did not change the crystalline structure of the zeolite precursors, however, compared to two-step process, the pore-volume, BET area, and concentration and strength of acid sites were significantly lower for the zeolite obtained by one-step alumination. These results indicated that the degermanation step is necessary prior to the incorporation of aluminum due to the creation of hydroxyl nests by removal of germaniun atoms from the framework.

The modification protocol of deGe-Al-AFI catalyst showed distinctive advantages in the alkylation of toluene with isopropyl alcohol to reach both relatively higher toluene conversion and selectivity to commercially valuable p-cymene due to the appropriate size of the zeolite channels and optimized B/L ratio. These factors cause more efficient formation of cymenes, especially p-cymene, by suppressing the secondary alkylation of cymenes and isomerization of p-cymene to o- or m-cymenes.

References

[1] J. Martinez-Triguero, M.J. Diaz-Cabanas, M.A. Camblor, V. Fornes, T.L. Maesen, A. Corma J. Catal. 182 (1999) 463–469.
[2] J. Jiang, J. Yu, A. Corma, Angew. Chem. Int. Ed 49 (2010) 3120–3145.
[3] R. Bai, Q. Sun, N. Wang, Y. Zou, G. Guo, S. Iborra, A. Corma, J. Yu, Chem. Mater. 28 (2016) 6455–6458.
[4] C.W. Jones, S.I. Zones, M.E. Davis, Appl. Catal. A Gen. 181 (1999) 289–303.
[5] H. Kawagoe, K. Komura, J.-H. Kim, G. Seo, Y. Sugi, J. Mol. Catal. A Chem. 350 (2011) 1–8.
[6] H.X. Zhang, A. Chokkalingam, P.V. Subramaniam, S. Joseph, S. Takeuchi, M.D. Wei, A.M. Al-Enizi, H.-G. Jang, J.-H. Kim, G. Seo, K. Komura, Y. Sugi, A. Vinu, J. Mol. Catal. A Chem. 412 (2016) 117–124.
[7] A. Ito, H. Maekawa, H. Kawagoe, K. Komura, Y. Kubota, Y. Sugi, Bull. Chem. Soc. Jpn. 80 (2007) 215–223.
[8] E. Hu, Y.L.W. Huang, Q. Yan, D. Liu, Z. Lai, Microporous Mesoporous Mater. 126 (2009) 81–86.
[9] http://www.iza-structure.org/databases/.
[10] U.S. Patent (Ed.), Process for Preparing Molecular Sieves Using Adamantane Template, S.I. Zones, US, 1987.
[11] S.I. Zones, Y. Nakagawa, Microporous Mesoporous Mater. 2 (1994) 543–555.
[12] R.F. Lobo, M.E. Davis, Microporous Mesoporous Mater. 3 (1994) 61–69.
[13] J. Přech, D. Vitvarová, L. Lupínková, M. Kubů, J. Čejka, Microporous Mesoporous Mater. 212 (2015) 28–34.
[14] H. Maekawa, Y. Kubota, Y. Sugi, Chem. Lett. 33 (2004) 1126–1127.
[15] Y. Yun, M. Hernandez, W. Wan, X. Zou, J.L. Jorda, A. Cantin, F. Rey, A. Corma, Chem. Commun. 51 (2015) 7602–7605.
[16] J.H. Kang, D. Xie, S.I. Zones, S. Smeets, L.B. McCusker, M.E. Davis, Chem. Mater. 28 (2016) 6250–6259.
[17] A. Corma, M.J. Diaz-Cabanas, J.L. Jorda, C. Martinez, M. Moliner, Nature 443 (2006) 842–845.

[18] J. Sun, C. Bonneau, A. Cantin, A. Corma, M.J. Díaz-Cabanas, M. Moliner, D. Zhang, M. Li, X. Zou, Nature 458 (2009) 1154–1157.

[19] J. Jiang, Y. Xu, P. Cheng, Q. Sun, J. Yu, A. Corma, R. Xu, Chem. Mater. 23 (2011) 4709–4715.

[20] F. Gao, Maguy Jaber, Krassimir Bozhilov, Aurelie Vicente, Christian Fernandez, V. Valtchev, J. Am. Chem. Soc. 45 (2009) 16580–16586.

[21] M.V. Shamzhy, P. Eliasova, D. Vitvarova, M.V. Opanasenko, D.S. Firth, R.E. Morris, Chem.Eur. J. 22 (2016) 17377–17386.

[22] X. Liu, H. Xu, L. Zhang, L. Han, J. Jiang, P. Oleynikov, L. Chen, P. Wu, ACS Catal. 6 (2016) 8420–8431.

[23] M.V. Shamzhy, O.V. Shvets, M.V. Opanasenko, P.S. Yaremov, L.G. Sarkisyan, P. Chlubná, A. Zukal, V.R. Marthala, M. Hartmann, J. Čejka, J. Mater. Chem. 22 (2012) 15793.

[24] M. Shamzhy, F.Sd.O. Ramos, Catal. Today 243 (2015) 76–84.

[25] A. Rodríguez-Fernández, F.J. Llopis, C. Martínez, M. Moliner, A. Corma, Microporous Mesoporous Mater. 267 (2018) 35–42.

[26] O.V. Shvets, N. Kasian, A.T. Zukal, J.I. Pinkas, J. Čejka, Chem. Mater. 22 (2010) 3482–3495.

[27] C.A. Emeis, J. Catal. 141 (1993) 347–354.

[28] A. Corma, V. Fornés, L. Forni, F. Márquez, J. Martínez-Triguero, D. Moscotti, J. Catal. 179 (1998) 451–458.

[29] D.M. Roberge, H. Hausmann, W.F. Holderich, Phys. Chem. Chem. Phys. 4 (2002) 3128–3135.

[30] M.V. Shamzhy, C. Ochoa-Hernández, V.I. Kasneryk, M.V. Opanasenko, M. Mazur, Catal. Today 277 (2016) 37–47.

[31] S. Bordiga, C. Lamberti, F. Bonino, A. Travert, F. Thibault-Starzyk, Chem. Soc. Rev. 44 (2015) 7262–7341.

[32] M.T. Portilla, F.J. Llopis, C. Martínez, S. Valencia, A. Corma, Appl. Catal. A Gen. 393 (2011) 257–268.

[33] M. Osman, S. Al-Khattaf, U. Díaz, C. Martínez, A. Corma, Catal. Sci. Technol. 6 (2016) 3166–3181.

[34] N. Žilková, P. Eliášová, S. Al-Khattaf, R.E. Morris, M. Mazur, J. Čejka, Catal. Today 277 (2016) 55–60.

[35] C. Perego, P. Ingallina, Green Chem. 6 (2004) 274–279.

[36] B. Wichterlová, J. Čejka, N. Žilková, Microporous Mesoporous Mater. 6 (1996) 405–414.

[37] J. Čejka, G.A. Kapustin, B. Wichterlová, Appl. Catal. A Gen. 108 (1994) 187–204.

[38] J. Čejka, A. Vondrová, B. Wichterlová, G. Vorbeck, R. Fricke, Zeolites 14 (1994) 147–153.

[39] Z.R. Zhu, Q.L. Chen, W. Zhu, D.J. Kong, C. Li, Catal. Today 93 (2004) 321–325.

[40] B. Wichterlová, J. Čejka, J. Catal. 146 (1994) 523–529.

Enclosure 3

Synthesis of aggregation-resistant MFI nanoparticles

Synthesis of aggregation-resistant MFI nanoparticles

Hua Chen, Yong Zhou, Zdeněk Tošner, Jiří Čejka*, Maksym Opanasenko*

Department of Physical and Macromolecular Chemistry, Faculty of Science, Charles University, Hlavova 8, Prague 2, Czech Republic

A B S T R A C T

Zeolites with particles of nm-scale size and restricted aggregation propensity were designed by decoration of zeolite surface with specific functional groups to address the problem of irreversible aggregation of respective nanoparticles. Highly crystalline MFI nano zeolites synthesized using hydrothermal method were functionalized with silanes of different nature (monodentate vs. polydentate, hydrophobic vs. hydrophilic) to investigate the influence of the type of surface functional groups on the stability of zeolite nanoparticles against aggregation in solution, accessibility of acid sites located in zeolite framework, and catalytic properties of resulting hybrid materials. The as-prepared materials were characterized by XRD, DLS, nitrogen adsorption, and adsorption of acetonitrile followed by FTIR, solid state ^{29}Si and ^{27}Al NMR, ICP-OES, TEM. Finally, we investigated the catalytic performance of designed materials in acylation of p-xylene to demonstrate that surface functionalization does not lead to deterioration of catalytic activity of the zeolite nanoparticles. Characterization data and catalytic results confirmed the improved stability of prepared nanoparticles with reasonable accessibility of acid sites. This finding can be used for preparation of aggregation-resistant zeolites dispersible in liquid-phase reaction mixtures in order to mimic homogeneous catalytic systems.

1. Introduction

Zeolites have been widely used in ion-exchange, gas adsorption and heterogeneous catalysis (e.g. in petrochemistry) [1–3], which is due to their unique structural features, such as pore size, channel dimensionality, and acidity [4,5]. Heterogeneous catalysis is essentially important in industrial chemistry because of easier separation of products, formation of a lower volume of waste substances and usually lower toxicity [6,7]. With the increasing demand for industrial chemicals and the pressure of the environmental issues, seeking for more effective, safe and environmentally friendly solutions, design and synthesis of novel catalysts, is highly desirable.

Utilization of zeolites as heterogeneous catalysts is restricted due to the limited size of the micropores (< 2 nm). The narrow pore openings and channels of conventional zeolites hinder the mass transport of bulky reactants [8,9]. To overcome this limitation, an effective way is to prepare zeolites possessing extra-large pores (> 8.0 Å) [10–14]. However, most of extra-large pore zeolites are germanosilicates. The high cost, low thermal and chemical stability restrict their applications. On the other hand, great efforts also have been undertaken to introduce meso- or macro porosity into zeolites to design hierarchical zeolites [15–18]. The synthetic strategies toward hierarchical zeolites include "top-down" and "bottom-up" methods, which involve partial removal of framework atoms (Si, or Al) by acid or basic solution treatments [19–21], or using of soft (surfactants, polymers), hard (carbon nanostructures) templates as porogens [22,23]. However, the top-down approach can result in decreasing crystallinity and lowering thermal and chemical stability of resulting materials. On the other hand, producing hierarchical zeolites with templates will increase the cost, and uncontrollable mesopore size limits their large-scale application of respective materials as well [26].

Alternatively, a straightforward solution to overcome diffusion limitation in zeolite catalysts is to decrease the crystal size [24,25]. Compared with the micron-sized counterparts, the decrease in the zeolite crystal size to nanometer scale can endow zeolites with outstanding characteristics, such as the short diffusion path and large external surface area, which can well overcome the bulky reagents mass transport limitation [26,27]. These characteristics not only provide new possibilities for traditional applications in heterogeneous catalysis and molecular separation processes, but also lead to the expansion of their use to other emerging fields, such as chemical sensing, optical devices, biomedical and biological analyses [28]. However, nanosized zeolites suffer from aggregation because of high specific surface energy, which restricts their utilization [29]. The aggregation of zeolite nanoparticles can be prevented by adding emulsifying agents like detergents or surfactants [30]. Functionalization or coating of silica and zeolite

nanoparticles surface with organosilane reagents to reduce the aggregation has been reported as well [31,32]. However, only additional mesopores are formed by close packing of nanoparticles upon calcination [32]. Therefore, the obtained materials were not real aggregation-resistant catalysts, which significantly limit the utilization of such materials as reusable catalysts with predictable surface properties and activity. Resasco and other researchers did a lot of attempts to functionize the surface of zeolite crystals with organosilanes and tune the hydrophobic properties of zeolites [33,34]. Their works inspired us to design and synthesis of aggregation-resistant zeolite catalyst by careful silylation of nanosized zeolite crystals.

In this work, we have developed a new strategy for the synthesis of aggregation-resistant zeolite by silylation of the MFI nanocrystals. Four organosilanes with different size and nature were tested. Compared to the conventional zeolites with bulk crystals and non-functionalized nm-size zeolites, the resulting hybrid materials showed significantly less aggregation under both static (for 10 days) and catalytic (acylation of p-xylene with butyryl chloride) conditions, which suggested that they can be considered as good candidates for pseudo-homogeneous catalytic systems.

2. Experimental

2.1. Materials

For synthesis of MFI type nanosized zeolite, tetraethylorthosilicate (TEOS, 98%), tetrapropylammonium hydroxide solution (TPAOH, 40 wt %), sodium aluminate (NaAlO$_2$), and L-lysine (C$_6$H$_{14}$N$_2$O$_2$, 98%), ethoxydimethylphenylsilane (98%), triethoxyphenylsilane (98%), (4-biphenyl)triethoxysilane (98%) and 3-(ethoxydimethylsilyl)propylamine (98%), acetone (99%) were supplied by Sigma Reagent Company. Sodium hydroxide (NaOH, 98%) was purchased from VWR Reagent Company, p-xylene (99.5%), butyryl chloride (99%), dodecane (99%) were supplied by Sigma-Aldrich.

2.2. Preparation of catalysts

2.2.1. Synthesis of nanosized MFI zeolites

The molar compositions of the mixture was 1.0 SiO$_2$/0.45 TPAOH/0.003Al$_2$O$_3$/0.015 Na$_2$O/0.1L-lysine/9 H$_2$O. The synthesis procedure followed the Zhang's experiment [35]. Typically, TEOS was mixed with TPAOH and deionized water at room temperature with fast stirring until completely hydrolyzed, followed by the addition of NaAlO$_2$ to the reaction mixture with fast stirring for another 30 min. Then L-lysine was added to the uniform solution. The gel mixture was continuously stirred to evaporate the excess water to get required water-to-silica ratio and then transferred into a Teflon-lined stainless steel autoclave for crystallization. The crystallization was conducted in a conventional oven initially at 80 °C for 2 days and subsequently at 170 °C for 1 day under static conditions. The as-synthesized solid products were centrifuged, washed with water several times, and then dried at 80 °C in the oven overnight, followed by calcination at 550 °C for 6 h.

2.2.2. Ion-exchange

Aqueous 1 M NH$_4$NO$_3$ solution was used (1 g zeolites with 30 mL solution) with fast stirring in 80 °C for 2 h. Ion exchange procedure was repeated 3 times. After filtration, sample was dried at 80 °C in the oven followed by calcination at 550 °C for 4 h. Obtained sample was denoted as N-MFI [36].

2.2.3. Functionalization of N-MFI

Firstly, 50 mg of N-MFI was added to 10 mL of acetone. Further, the solution was sonicated to form a suspension. After addition of required silane (0.04 mol/g), reaction mixture was sonicated 3 times 10 min. per time in an ice bath. Then centrifuge the solution and washed the solid products with acetone 3 times. The final solid products were dried at 80 °C. The N-MFI functionalized by triethoxyphenylsilane and ethoxydimethylphenylsilane were denoted as N-MFI-S1and N-MFI-S2, respectively.

2.3. Characterization

The structure and crystallinity of nanozeolites were assessed using Bruker AXS D8 Advance diffractometer with Cu Kα radiation (λ =0.154nm) in the 2θ range of 5–50° at a scanning rate of 4°/min

The elemental analysis was carried out using Thermo Scientific ICAP 7000 inductive coupled plasma-optical emission spectroscopy (ICP-OES). Prior to the measurement, samples were mineralized in a mixture of concentrated hydrochloric, nitric and hydrofluoric acid.

The nitrogen adsorption and desorption measurements were carried out at −196 °C using the Micromeritics GEMINI II 2370 volumetric Surface Area Analyzer. Before the sorption measurements, all samples were degassed at 150 °C in a Micromeritics FlowPrep 060 instrument, (heating rate 10 °C /min) for 4 h. The surface area was evaluated using BET method. The t-plot method was applied to determine the volume of micropores. The adsorbed amount at relative pressure p/p$_0$ = 0.98 reflects the total adsorption capacity. The pore size distributions were calculated using the BJH model from the desorption branch of the isotherms.

The concentration and type of acid sites were determined by adsorption of acetonitrile as a probe molecule followed by FTIR spectroscopy (Nicolet iS50 FT-IR) using the self-supported wafer technique. Prior to adsorption of the probe molecule, the wafers of zeolite samples were activated by overnight evacuation at temperature 250 °C.

High-resolution transmission electron microscopy (HRTEM) were carried out on a JEOL JEM-2011 electron microscope operating at an accelerating voltage of 200 kV. The HRTEM images were recorded using a 9 Gatan 794 CCD camera.

Dynamic light scattering (DLS) was used to identify particles size distribution. Prior the measurement, 10 mg of zeolite was introduced in 10 mL of the acetone and mixture was sonicated for 10 min.

Solid-state ^{27}Al and ^{29}Si NMR spectra were obtained using a Bruker Avance III HD spectrometer working with a 9.4 T standard-bore superconducting magnet (27Al Larmor frequency of 104.26 MHz). The samples were packed into a thin-wall 3.2 mm zirconia rotor, and rotated at a MAS rate of 15 kHz using a Bruker 3.2 mm HX CP-MAS probe. A pulse of 1.0 μs (B1 field approx. 95 kHz) with a relaxation delay of 1 s was applied and 2048 transients were averaged. The spectra were referenced to saturated solution of Al(NO$_3$)$_3$ in D$_2$O. ^{29}Si spectra (79.49 MHz) were acquired employing the pulse length of 2.0 μs (B1 field approx. 63 kHz) and repetition time of 15 s. For referencing, tetramethylsilane solution was used. The spectra were averaged over 512 or 4096 transients, depending on the sample. In all cases, no proton decoupling was applied.

2.4. Aggregation test

Catalyst was dispersed in acetone (1 g/L), under sonication in ice bath for 10 min (3 sonication cycles). Then, 1 mL of the homogeneous solution was taken to evaluate the particle size by DLS.

2.5. Catalytic test

The catalytic test was performed in the liquid phase at 130 °C and at atmospheric pressure in a multi-experiment workstation StarFish. Prior to reaction, the catalysts were activated at 150 °C for 90 min with the rate of 10 °C min. In all cases, 50 mg of catalyst powder, p-xylene (5 ml, 40 mmol), butyryl chloride (5 mmol) and 0.5 g of dodecane (internal standard) were added to the two-necked flask equipped with a condenser and a thermometer. The samples of the reaction mixture were taken periodically and analyzed using Agilent 6850 GC equipped a polar DB-WAX column (length 20 m, diameter 0.180 mm, and film

thickness 0.3 μm) and flame ionization detector.

Turnover frequency was calculated based on following formula:

$$TOF = \frac{N * Con.}{(CL + CB) * M * t}$$

Where *N* stands for 5 mmol of butyryl chloride, *Con.* is the conversion after reaction time *t*, *(CL + CB)* is the concentration of acid sites based on acetonitrile adsorption followed by FTIR and *M* is the weight of the catalyst (50 mg).

3. Results and discussion

In order to optimize the aggregation properties of nanosized zeolite particles four types of silanes were chosen:

- tridentate (able to form three bonds per one molecule) small-(containing phenyl group) and large-size (with biphenyl group) silanes were selected to investigate the influence of π-π interaction between aromatic groups and size of these groups on the degree of nanoparticles aggregation;

- material synthesized using monodentate silane (ethoxydimethylphenylsilane) was compared with that prepared using triethoxyphenylsilane to confirm the necessity to limit the cross-linking capacity of the functionalizing agent;

- silane containing relatively hydrophilic amino-group was chosen for comparison with silanes containing exclusively alkyl- and aryl-groups and providing high hydrophobicity of the resulting nanoparticles.

Proposed concept is chemically very simple (Scheme 1) and related to the well-known modification of silanols on the surface of zeolite crystals with organic groups using organosilanes [37,38].

Dynamic light scattering (DLS) was applied to investigate the particle size distribution of the zeolite samples obtained. The DLS data demonstrated that functionalization of the zeolite particles did not change significantly average size (Fig. 1. black curves), which slightly increased from about 65 nm for N-MFI to 70–95 nm for the modified species. For evaluation of aggregation behavior of both purely zeolitic and functionalized nanoparticles, the particle size change after 10 days static state (Fig. 1. red curves) was chosen as the criterion. From the DLS results, the average size of non-functionalized N-MFI crystals increased almost 5 times (398% increase, Fig. 1A) after 10 days that indicate severe aggregation of the nanoparticles due to the high surface free energy. TEM of N-MFI after 10 days provided additional evidence of the aggregation of nanocrystals, which shown in Fig. 5A. The N-MFI functionalized with ethoxydimethylphenylsilane showed remarkable aggregation resistance with almost no shift of the maximum on DLS curve and only minor increase in the average particle size (37%) caused by the formation of the particles of > 100 nm size (shoulder on the red plot, Fig. 1C), the TEM image of N-MFI-S2 again showed the discrete MFI nanoparticles uniformly dispersed in acetone after 10 days (Fig. 5B). This result can be explained by the optimum hydrophobicity

of the dimethylphenylsilyl groups allowing to avoid the aggregation of the nanoparticles under conditions used as well as the inability of initial silane to form more than one covalent bond with silanol groups that provide the absence of interparticle linkages. In contrast, when N-MFI was functionalized with tridentate triethoxyphenylsilane and especially (4-biphenyl)triethoxysilane, the aggregation behavior was just slightly better (215% average particle size increase after 10 days, Fig. 1B) or comparable (397% increase, Fig. 1D) to the non-modified sample. In the latter case, the aggregation resistance was the worst despite the largest size of substituent among the tested silanes, this is probably caused by π–π interaction of biphenyl rings with each other facilitating interparticle conjugation more efficiently in compared with phenyl counter silane. When more hydrophilic functionalization agent (e.g. amino-containing) was used, even low denticity of initial silane does not provide sufficient stability of the resulting nanoparticles in the solution (207% average particle size increase after 10 days, Fig. 1E). Difference in the concentration or distribution of functional groups over the surface of zeolite particles caused by the differences in the properties of used silanes (hydrophilicity, presence of aromatic rings, possibility to form intermolecular H-bonds) can be additional factor for the distinction in the properties of functionalized samples. Based on the DLS results, N-MFI functionalized by phenylsilyl- (N-MFI-S1, reference sample) and dimethylphenylsilyl-groups (N-MFI-S2, sample most stable against aggregation) was chosen for further study and comparison with N-MFI.

TG analysis was carried out in order to assess the amount of organosilanes attached to the zeolite nanocrystals (see Fig. 2). The total weight loss in the tested samples are 5.48% and 4.90% for N-MFI-S1 and N-MFI-S2 respectively, which suggested the amount of two silanes attached during the silylation treatment was comparable. The TG results confirmed the better stability of N-MFI-S2 was mainly attributed to the monodentate property of ethoxydimethylphenylsilane instead of the amount of silane capped on the nanoparticles.

The preservation of zeolite structure and crystallinity of the synthesized materials was evaluated by X-ray powder diffraction. Fig. 3. shows the diffraction patterns of N-MFI, N-MFI-S1 and N-MFI-S2. Sharp diffraction peaks at 7.6°, 8.5°, 23°, 23.9° and 24.4° of 2θ, which are the typical characteristic diffraction peaks of MFI zeolite [35], were observed in the N-MFI sample. This result confirms the MFI structure and high crystallinity of this as-synthesized sample. After the functionalization, the structure of zeolites did not change (both peak positions and intensities in XRD patterns were the same when compared with N-MFI, Fig. 3), which means that the introduction of organic functional groups did not influence the structure of zeolites.

The TEM images were in agreement with the DLS and XRD data of the samples studied (Fig. 4). Observed nanoparticles are uniform and of similar size in the range 60–70 nm for N-MFI, N-MFI-S1 and N-MFI-S2 samples. Average particle sizes are slightly lower in comparison with those estimated using DLS. The reason is that in the latter case the existence of even small fraction of aggregated particles with the
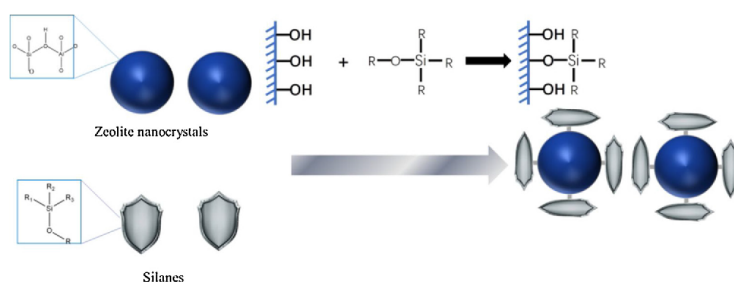
Scheme 1. Concept of approach for the synthesis of aggregation-resistant zeolites using silane as aggregation prohibit.
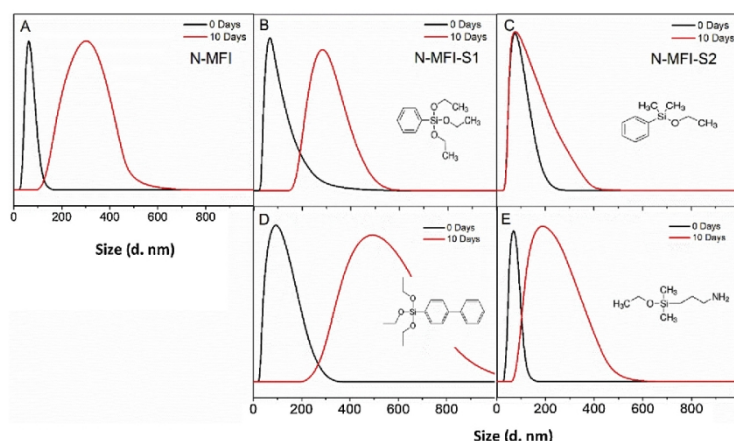
3

Fig. 1. DLS curves of the as-synthesized nanosized MFI and different silanes modified samples after 10 days static state: (A) non-functionalized N-MFI, (B) triethoxyphenylsilane (N-MFI-S1), (C) ethoxydimethylphenylsilane (N-MFI-S2), (D) (4-biphenyl)triethoxysilane, (E) 3-(ethoxydimethylsilyl)propylamine.
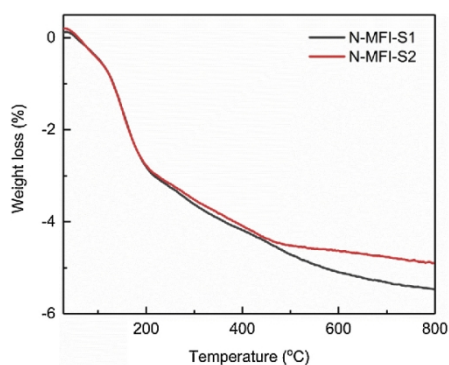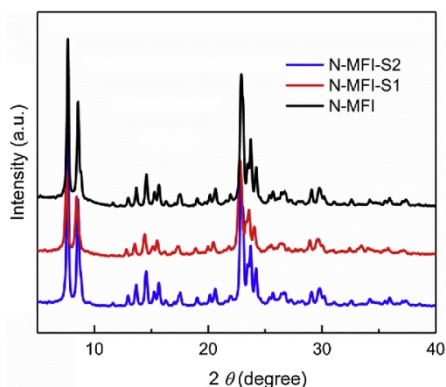

Fig. 2. TG analyses of N-MFI-S1 and N-MFI-S2.

Fig. 3. XRD of N-MFI, N-MFI-S1 and N-MFI-S2.

size > 100 nm, which were not spotted on TEM images, resulting in the shift of the median of the size distribution. From TEM images on Fig. 4, modification of the surface of MFI nanoparticles with substituted silanes practically does not affect the size, morphology and crystallinity of functionalized nano zeolites. HRTEM images (Fig. 4B, D, F) revealed that all samples have good crystallinity and microporosity. The results of HRTEM indicated that the lattice spacing around 1.3 nm was associated to the (001) lattice plane of the MFI type zeolite, which corresponds to the literature data [39].

Blocking of the pore entrances by functionalization agent can proceed during surface modification of porous materials resulting in deterioration of textural properties of the final material. Therefore, adsorption characteristics of all functionalized samples were examined using nitrogen as probe molecule and compared with N-MFI (Fig. S-1 and Table 1). All the isotherms exhibit the same type (I + IV) and similar shape (Fig. S-1). A sharp uptake at $p/p_0 > 0.8$ corresponds to the adsorption in the interparticle voids of the mesopore scale. The same values of the micropore volume for N-MFI ($V_{micro} = 0.106$ cm^3/g) and functionalized samples ($V_{micro} = 0.103 - 0.104$ cm^3/g) evidences the absence of pore blocking phenomena under conditions used. At the same time, BET area decreased (Table 1) after functionalization due to the condensation of silanes with silanols on the external surface. The drop in S_{BET} value (69–76 m^2/g) roughly corresponds to the decrease in S_{ext} (65–74 m^2/g). However, the porosity of N-MFI, N-MFI-S1 and N-MFI-S2 after activation at the relatively high temperature (250 °C) dramatically changed (Fig. S-2). For non-functionalized samples, aggregation at 250 °C resulted in a decrease in the external surface area accompanied by increase in the micropore volume due to the collapse of interparticle mesoporous system. In the case of functionalized materials, the apparent decrease in the BET area (from > 300 to about 60 m^2/g) and micropore volume (from 0.1 to < 0.005 cm^3/g) was observed. This is probably caused by the degradation of organic groups due to the high-temperature pre-treatment causing the coking and plugging of the channel in the samples (Table S-1). Utilization of the interparticle voids limited by external surface of zeolite nanoparticles as the reaction space for anchoring of functional groups lead also to the decrease of total pore volume (Table 1).

For N-MFI sample, the Si/Al ratio obtained by ICP/OES (Table 1) was slightly lower in comparison with the Si/Al ratio used for the synthesis (133 and 167, respectively). Functionalization using silylation agents naturally resulted in the increase in the silicon atoms fraction and thus increases in Si/Al ratio up to 174 (Table 1).
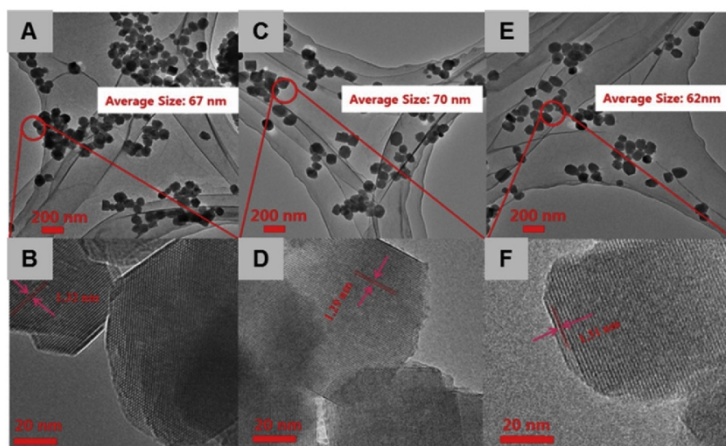
4

Fig. 4. TEM images of N-MFI (A, B), N-MFI-S1(C, D) and N-MFI-S2 (E, F).

In typical IR spectra of functionalized samples (Fig. S-3), the bands related C—H stretching (2982, 2943, 2884 cm-1) and bending (1478/1460, 1385 cm^{-1}) vibrations can be found [40]. The band at around 3745 cm^{-1} corresponds to the terminal OH groups bound to silicon framework atoms. Intensity of this line was significantly reduced in comparison with that of the parent N-MFI sample due to the consumption of the fraction of surface silanol groups for condensation with functionalized silanes. The number of Brønsted sites and Lewis sites determined using acetonitrile as probe molecule were 50 and 10 μmmol/g for N-MFI, while totaled 10 and 10 μmmol/g for N-MFI-S2, 30
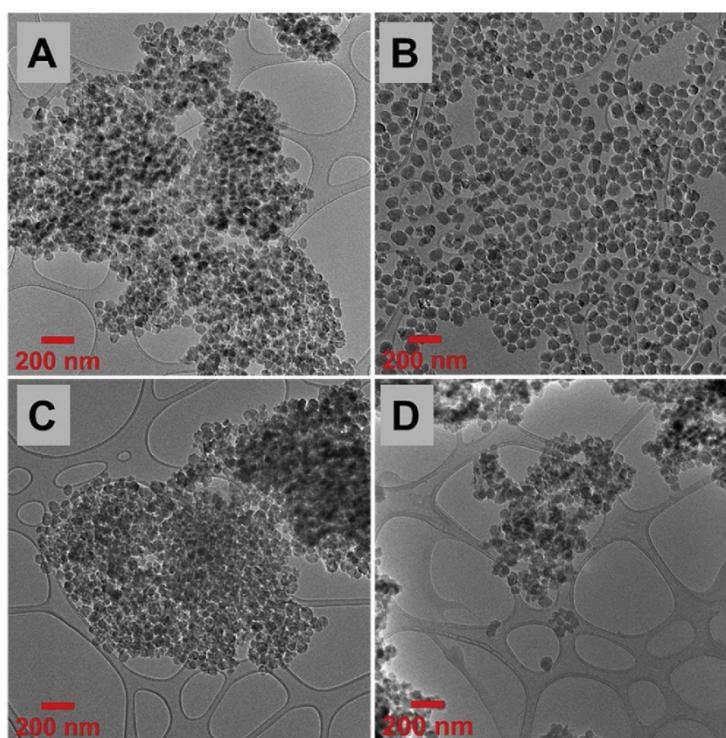

Fig. 5. TEM images of N-MFI (A, C) and N-MFI-S2 (B, D) dispersed in acetone for 10 days (A, B) or after catalytic reaction (C, D).

5

Table 1

Chemical composition and textural properties of N-MFI, N-MFI-S1, N-MFI-S2 and commercial MFI.

	Si/Al[a]	S_{BET} $(m^2/g)^b$	S_{ext} (m^2/g)	V_{micro} $(cm^3/g)^c$	V_{total} (cm^3/g)
N-MFI	133	378	178	0.106	0.454
N-MFI -S1	174	309	113	0.103	0.372
N-MFI –S2	151	302	104	0.104	0.331
C-MFI [40]	140	378	n.d.	0.192	n.d.

[a] Measured by ICP/OES. [b] Specific surface area (BET) given by N_2 adsorption at −196 °C. [c] Calculated by t-plot method. n.d.: not determined.

and 10 μmmol/g for commercial MFI, respectively. In the case of N-MFI-S1, concentration of acidic sites was below the FTIR detection limit. We assumed two main reasons for the lower (for N-MFI-S2) or even negligible (for N-MFI-S1) concentration of acid sites determined by FTIR in comparison with parent N-MFI: 1) the change of the Al state during functionalization treatment either because of partial breaking of Si–O–Al bonds or due to the interaction of Al with silylating agent; 2) degradation of organic part of functionalized samples due to the high-temperature pre-treatment (required for evacuation of adsorbed molecules prior the IR measurement) resulting in the lower accessibility of acid sites by probe molecules in the following experiment.

To check the first assumption, we performed ^{27}Al and ^{29}Si MAS-NMR spectroscopy measurements for the samples before and after functionalization (Fig. 6). The line located at 56 ppm in ^{27}Al MAS-NMR spectra is assigned to framework tetrahedral Al atoms [42]. No other peaks (e.g. related to the extra-framework octahedral aluminum) were detected for both the initial and modified zeolites (Fig. 6A) evidencing the maintenance of Al positions upon functionalization, and exclusively framework location of aluminum atoms for all the samples studied. In contrast, the surrounding of Si atoms was substantially changed after anchoring organosilanes to the surface of zeolite nanoparticles (Fig. 6B). Two dominating resonance peaks in the ^{29}Si-MAS NMR spectra of N-MFI were observed. The signal at -114 ppm can be assigned to Si*(OSi)₄ sites (Q4) in the framework, while broad resonance peak around -109 ppm is typically ascribed to HOSi*(OSi)₃ sites (Q3) [43]. The dramatic decrease in the intensity of Q3 peak occurred in the spectra of N-MFI-S1 and N-MFI-S2 samples that indicates the complete condensation of surface silanol groups with alkoxysilyl groups of silanes. As a result, both ^{27}Al and ^{29}Si NMR spectra of functionalized materials contain the single peak of Q4 evidencing the uniformity of the atoms in the frameworks.

The catalytic activity of N-MFI-S2 was evaluated in acylation of p-xylene with butyryl chloride (Fig. 7). Since the reaction under study can proceed over both Brønsted and Lewis acid sites, the evaluation of the catalyst activity (turnover frequency values, TOF) was done using the total concentration of active sites. The commercial MFI (Si/Al = 140, designated as C-MFI) with chemical composition similar to the samples under investigation was selected for comparison. C-MFI has clearly discrete spherical morphology with mean diameter of particles about 2 μm (see Fig. S-4). The results of catalytic test indicate that C-MFI reached the highest butyryl chloride conversion (Fig. 7A) because it contains more acid sites (60 μmmol/g), while in terms of TOF (Fig. 7B), N-MFI-S2 exhibited the highest activity (TOF =602 h⁻¹). The non-functionalized N-MFI (TOF =173 h⁻¹) did not surpass the efficiency of commercial sample (TOF =390 h⁻¹). Taking into account the aggregation stability of the samples used (see discussion above), the agglomeration of the nanoparticles is the most probable explanation of relatively low activity of the N-MFI material. The results of DLS for N-MFI sample recovered after full catalytic run (Fig. S-5) showed the increase of the average particle size from 65 to 210. TEM images (see Fig. 5C) of used N-MFI showed severe aggregation of nanocrystals, larger clusters of nanoparticles had size around 1 μm, which confirms the assumption made. N-MFI-S2 sample also suffers from aggregation under relatively severe conditions of activation and reaction resulting in the particle size increase (Fig. 5D and Fig. S-5), however, this increase was moderate in comparison with non-functionalized zeolite evidencing the advantage of modified catalysts in terms of both activity and stability.

4. Conclusions

We have demonstrated a new method to prepare aggregation-resistant MFI zeolites with nm-scale size around 70 nm. Among the tested silanes with different nature and size, ethoxydimethylphenylsilane was found to be the best reagent to functionalize the nanosized zeolites. The ethoxydimethylphenylsilane-silylated sample (N-MFI-S2) almost preserved their crystal size both in dispersion in acetone for 10 days and after catalytic test in acylation of p-xylene under harsh reaction conditions, which exhibited obviously improved aggregation-resistant performances. Together with the relatively better catalytic activity, this proof of concept work showed the design and preparation of aggregation-resistant zeolites dispersible in liquid-phase reaction mixtures, and this kind of catalyst could be potentially used in quasi-homogeneous
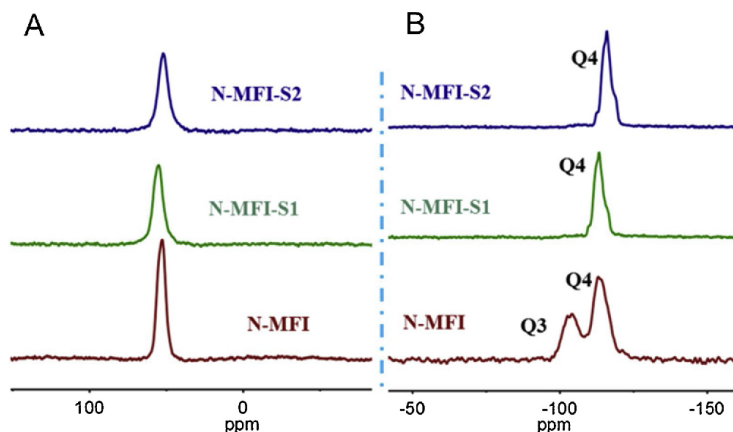

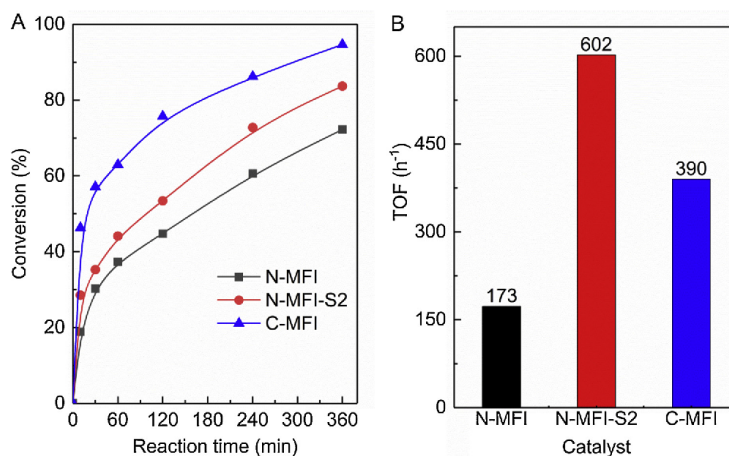**Fig. 6.** (A) ^{27}Al and (B) ^{29}Si MAS NMR spectra of N-MFI, N-MFI-S1 and N-MFI-S2.

Fig. 7. (A) Conversion of butyryl chloride with reaction time and (B) TOF over N-MFI, N-MFI-S2 and C-MFI catalysts in acylation of p-xylene. Conditions: 5 ml p-xylene, 5 mmol butyryl chloride, 0.5 g dodecane (internal standard), 130 °C.

catalytic systems.

References

[1] J. Prech, P. Pizarro, D.P. Serrano, J. Cejka Chem. Soc. Rev. 47 (2018) 8263–8306.
[2] D.P. Serrano, J.A. Melero, G. Morales, J. Iglesias, P. Pizarro Catal. Rev.: Sci. Eng. 60 (2018) 1–70.
[3] M. Shamzhy, M. Opanasenko, P. Concepcion, A. Martinez Chem. Soc. Rev. 48 (2019) 1095–1145.
[4] M. Moliner, T. Willhammar, W. Wan, J. Gonzalez, F. Rey, J.L. Jorda, X. Zou, A. Corma, J. Am. Chem. Soc. 134 (2012) 6473–6478.
[5] W. Schwieger, A.G. Machoke, T. Weissenberger, A. Inayat, T. Selvam, M. Klumpp, A. Inayat, Chem. Soc. Rev. 45 (2016) 3353–3376.
[6] A. Galadima, O. Muraza, J. Ind. Eng. Chem. 31 (2015) 1–14.
[7] B.M. Weckhuysen, J. Yu, Chem. Soc. Rev. 44 (2015) 7022–7024.
[8] W.J. Roth, P. Nachtigall, R.E. Morris, J. Cejka Chem. Rev. 114 (2014) 4807–4837.
[9] M. Opanasenko, M. Shamzhy, F. Yu, W. Zhou, R.E. Morris, J. Cejka Chem. Sci. 7 (2016) 3589–3601.
[10] B. Yang, J. Jiang, H. Xu, H. Wu, M. He, P. Wu Angew.Chem. 130 (2018) 659–9663.
[11] M. Hartmann, W. Schwieger Chem. Soc. Rev. 45 (2016) 3311–3322.
[12] B. Chen, M. Eddaoudi, S.T. Hyde, M. O'Keeffe, O.M. Yaghi Science 291 (2001) 1021–1023.
[13] J.L. Paillaud, B. Harbuzaru, J. Patarin, N. Bats Science 304 (2004) 990–992.
[14] J. Jiang, J.L. Jorda, M.J. Diaz-Cabanas, J. Yu, A. Corma Angew. Chem. In. Ed 49 (2010) 4986–4988.
[15] J. Ramirez, C.H. Christensen, K. Egeblad, C.H. Christensen, J.C. Groen Chem. Soc. Rev. 37 (2008) 2530–2542.
[16] D.P. Serrano, J. Aguado, J.M. Escola, J.M. Rodriguez, A. Peral Chem. Mater. 18 (2006) 2462–2464.
[17] D.P. Serrano, J.M. Escola, P. Pizarro Chem. Soc. Rev. 42 (2013) 4004–4035.
[18] K. Li, J. Valla, J. Martinez ChemCatChem 6 (2014) 46–66.
[19] J. Perez-Ramirez, C.H. Christensen, K. Egeblad, C.H. Christensen, J.C. Groen, Chem. Soc. Rev. 37 (2008) 2530–2542.
[20] M. Opanasenko, W. Parker Jr, M. Shamzhy, E. Montanari, M. Bellettato, M. Mazur, R. Millini, J. Čejka, J. Am. Chem. Soc. 136 (2014) 2511–2519.
[21] H. Hernando, I. Moreno, J. Fermoso, C. Ochoa-Hernández, P. Pizarro, J.M. Coronado, J. Čejka, D.P. Serrano, Biomass Convers. Bior 7 (2017) 289–304.
[22] K. Zhu, K. Egeblad, C.H. Christensen, Eur. J. Inorg. Chem. 2007 (2007) 3955–3960.
[23] Z.P. Wang, C. Li, H.J. Cho, S.C. Kung, M.A. Snyder, W. Fan, Direct J. Mater. Chem. A 3 (2015) 1298–1305.
[24] G.H. Yang, X.F. Zhang, S.Q. Liu, K.L. Yeung, J.Q. Wang, J. Phys. Chem. Solids 68 (2007) 26–31.
[25] G. Reding, T. Maurer, B. Czarnetzki, Microporous Mesoporous Mater. 57 (2003) 83–92.
[26] F. Mohammadparast, R. Halladj, S. Askari, Chem. Engin.Commun. 202 (2015) 542–556.
[27] S.M. Alipour, Chin. J. Catal. 37 (2016) 671–680.
[28] S. Mintova, M. Jaber, V. Valtchev, Chem. Soc. Rev. 44 (2015) 7207–7233.
[29] V.S. Raghuwanshi, U.M. Garusinghe, J. Ilavsky, W.J. Batchelor, G. Garnier, J. Colloid Interface Sci. 510 (2018) 190–198.
[30] X. Su, R. Kanjanawarut, ACS Nano 3 (2009) 2751–2759.
[31] R.P. Bagwe, L.R. Hilliard, W. Tan, Langmuir 22 (2006) 4357–4362.
[32] D.P. Serrano, J. Aguado, G. Morales, J.M. Rodriguez, A. Peral, M. Thommes, J.D. Epping, B.F. Chmelka, Chem. Mater. 21 (2009) 641–654.
[33] P.A. Zapata, J. Faria, M.P. Ruiz, R.E. Jentoft, D.E. Resasco, J. Am. Chem. Soc. 134 (2012) 8570–8578.
[34] K. Chen, J. Kelsey, J.L. White, L. Zhang, D. Resasco, ACS Catal. 5 (2015) 7480–7487.
[35] Q. Zhang, G.R. Chen, Y.Y. Wang, M.Y. Chen, G.Q. Guo, J. Shi, J. Luo, J.H. Yu, Chem. Mater. 30 (2018) 2750–2758.
[36] G.L. Wang, W. Wu, W. Zan, X.F. Bai, W.J. Wang, X. Qi, O.V. Kikhtyanin, Trans. Nonferrous Met. Soc. China 25 (2015) 1580–1586.
[37] Y.P. Guo, H.J. Wang, Y.J. Guo, L.H. Guo, L.F. Chu, C.X. Guo, Chem. Eng. J. 166 (2011) 391–400.
[38] P.A. Zapata, Y. Huang, M.A. Borja, D.E. Resasco, J. Catal. 308 (2013) 82–97.
[39] N. Wang, W. Qian, K. Shen, C. Su, F. Wei, Chem. Commun. (Camb.) 52 (2016) 2011–2014.
[40] K. Zhang, R.P. Lively, J.D. Noel, M.E. Dose, B.A. McCool, R.R. Chance, W.J. Koros, Langmuir 28 (2012) 8664–8673.
[42] A.W.S. Guarino, R.A.S. San Gil, H. Polivanov, S.M.C. Menezes, J. Braz. Chem. Soc. 8 (1997) 581–586.
[43] W. Song, R.E. Justice, C.A. Jones, V.H. Grassian, S.C. Larsen, Langmuir 20 (2004) 8301–8306.